UNIVERSITY OF BIRMINGHAM

Fabrication of composite materials with addition of graphene platelets

By

Jian Liu

A thesis submitted to

The University of Birmingham

for the degree of

DOCTOR OF PHILOSOPHY

School of Mechanical Engineering

University of Birmingham

Abstract

Structural ceramics, such as alumina, are widely used in the materials industry and have potential applications covering high speed cutting tools, dental implants, chemical and electrical insulators, wear resistance parts and various coatings. These applications arise from their high hardness, chemical inertness and high electrical and thermal insulation properties. However, they bear the disadvantage of low fracture toughness which has seriously limited their further applications. Ceramics with improved fracture toughness are therefore desired in many engineering fields.

Radioactive materials are extensively used in a variety of applications such as medicine, weapons, and power generation. Once these materials lose their commercial value they are considered radioactive waste. The safe disposal of radioactive waste requires that the waste be isolated from the environment until radioactive decay has reduced its toxicity to innocuous levels for plants, animals, and humans. Mild steels due to their excellent mechanical and corrosion resistant properties have been used for storing the radioactive waste. However, to ensure a safe storage, steels with improved corrosion performance are preferred.

This PhD project set out to tackle the disadvantages of brittleness and low corrosion resistance that ceramics and mild steel bear respectively by developing ceramic and metallic nanocomposites using nanostructured fillers. Graphene platelets (GPLs) as newly emerging carbon materials were chosen as the reinforcing fillers. Two types of nanocomposites were fabricated and their mechanical or corrosion resistant properties were characterized. Alumina

(Al_2O_3) based nanocomposites reinforced with GPLs were sintered and GPL/Nickel (Ni) nanocomposites were produced using an electrodeposition technique.

The research can be divided into four sections. In the first section, zirconia (ZrO_2) toughened Al_2O_3 nanocomposites (ZTA) reinforced with GPLs were sintered in a spark plasma sintering (SPS) furnace and the effects of the sintering temperature on the mechanical properties of the GPL/ZTA composites were investigated. The results show that GPLs are widely dispersed in the ceramic matrix and the optimum sintering temperature for consolidating the GPL/ZTA bulk composites is 1550 ˚C. At this temperature, nearly fully densified GPL/ZTA samples with significantly improved fracture toughness can be obtained. The addition of only 0.81 vol% GPLs into the ZTA matrix results in a 40% increase in fracture toughness. Toughening mechanisms such as pull-out, crack bridging and crack deflection are observed and are responsible for the significant increase in fracture toughness.

In the second section, GPL/Al_2O_3 and GPL-silicon carbide (SiC)/Al_2O_3 nanocomposites were sintered using the SPS technique and the effects of the content of the GPLs and SiC nanoparticles on the mechanical properties of the nanocomposites were characterized. The results indicate that GPLs result in a decrease in the grain size of the matrix microstructures due to the pinning effect caused by GPLs on the grain boundaries and higher contents of GPLs lead to smaller grain sizes of the ceramic matrices. The addition of SiC nanoparticles together with GPLs causes further refinement in the ceramic matrix microstructures. The refined microstructures contribute to the hardness and flexural strength of the GPL-reinforced ceramic composites and enhance the toughening effect of GPLs by increasing the contact area and anchoring sites between the GPLs and the matrix. Raman studies show that agglomeration of GPLs takes place during the ball milling process and a higher content of

GPLs is likely to cause the formation of thicker GPL aggregates. The addition of SiC nanoparticles prevents the formation of the GPL aggregates and the higher percentage of SiC nanoparticles results in thinner GPLs after ball milling. Thinning of GPLs during the SPS process occurs because of the interaction between the GPLs and the ceramic matrix at high temperatures. For GPL/Al_2O_3 composites, the addition of 0.38 vol% GPLs results in significant improvement in the mechanical properties of the Al_2O_3 matrix. Approximately a 31% and a 27% increase in flexural strength and fracture toughness have been achieved respectively. The addition of dual fillers of GPLs and SiC nanoparticles causes the further improvement in mechanical properties of the Al_2O_3 matrix. Approximately a 36 % increase in hardness, a 40% increase in flexural strength and a 50% increase in fracture toughness have been achieved by introducing 0.38 vol% GPLs and 1 vol% SiC nanoparticles.

In the third section, for the first time GPL/Al_2O_3 nanocomposites were sintered in a pressureless way under flowing inert gases and the effects of the content of GPLs on the mechanical properties of the nanocomposites were studied. It has been found that some GPLs are well protected after sintering while some GPLs are damaged. The optimum processing paramters for consolidating the GPL/Al_2O_3 nanocomposites are: heating rate: 6 ℃/min, sintering temperature:1650 ℃, sintering time: 3h, sintering atmoshpere: forming gas and flowing rate: 8L/min. GPL/Al_2O_3 composites containing 0, 0.75, 1.3 and 1.48 vol% GPLs were nearly fully densified under the optimum processing parameters and densities of the composites decrease with the increasing percentage of GPLs. The grain sizes of Al_2O_3 ceramic matrices decrease from 4.31 to 2.87 μm with increasing percentage of GPLs from 0 to 1.48 vol% GPLs. A maximum increase of approximately 60% in flexural strength and 70% in fracture toughness are achieved by introducing 0.75 vol% GPLs.

In the fourth section, pure Ni and GPL/Ni coatings were electrodeposited onto mild steel. The microstructures and corrosion resistance of the coatings were investigated. The results show that the introduction of GPLs results in the significant decrease in average grain size of the Ni matrix and a considerable increase in the hardness of the coatings. In addition, the GPL/Ni composite coatings with higher percentages of GPLs have smaller grain size and greater hardness. Electrochemical tests indicate that compared to a pure Ni coating, GPL/Ni composite coatings have higher corrosion potential and impedances, which implies significantly improved corrosion resistance. Additionally, better corrosion resistance can be obtained by introducing a relatively higher percentage of GPLs.

Dedicated to my Family

Acknowledgements

Above all, I would like to express my sincere appreciation to my research supervisor, Professor Kyle Jiang for his guidance, idea and support during my PhD study. The stringent manner in which he approaches science and work and the constructive advices he gives will certainly exhibit significant influence on my future career and life.

I would also like to thank our collaborator, Dr Haixue Yan at the Queen Mary University of London for his technical support on the spark plasma sintering furnace. Without his support, most of the work in this thesis could not possibly have been carried out. I owe my sincere thanks to Dr Mike Keeble at the Buehler Ltd for this kind help with the hardness tests. I would also like to thank my friend, Weichen Xu for his support on SEM characterization and electrochemical tests and thank the members of the Micro Engineering and Nanotechnology Group for being kind and supportive. I thank my colleagues Hany, Susan, Ali, Hossein, Guang, Yang, Jiang and Majid for sharing their knowledge and expertise and for their helpful suggestions and support throughout the completion of my PhD thesis. Most of all, I would like to thank my family, my father and my mother for their support throughout my graduate study journey. They have always been there as a sounding board during my hard times.

Table of Contents

Abstract ..... **i**
Acknowledgements ..... **vi**
Table of Contents ..... **vii**
List of Figures ..... **xii**
List of Tables ..... **xxvi**
Abbreviations ..... **xxviii**
Nomenclatures ..... **xxx**
List of Publications ..... **xxxiii**
Chapter 1: Introduction of the thesis **1**
1.1 Introduction 1
1.2 Aims and objectives 2
1.3 Thesis structure 4
Chapter 2: Literature review **7**
2.1 Introduction 7
2.2 Properties of graphene 7
2.2.1 Structure of graphene. 8
2.2.2 Mechanical properties 9
2.2.3 Thermal Properties 11
2.2.4 Electrical properties 14
2.3 Fabrication approaches of graphene and GPLs 16
2.3.1 Exfoliation and cleavage 16
2.3.2 Epitaxial growth on SiC substrates 17
2.3.3 Chemical Vapour Deposition (CVD) 19
2.3.4 Chemical conversion of graphite 21
2.4 Toughening mechanisms in ceramics and ceramic composites 22
2.4.1 Particle dispersion toughening 23
2.4.2 Phase transformation toughening 32
2.4.3 Multilayer toughening 36
2.4.4 Fibre toughening 40
2.4.5 Toughening in CNT/ceramic composites 42

2.4.6 Controversial fracture toughness evaluated using the indentation technique. ...44
2.4.7 Toughening in graphene/ceramic composites ...45
2.5 Sintering techniques ...48
2.5.1 Conventional sintering ...48
2.5.2 SPS ...49
2.5.3 HIP ...52
2.5.4 SLS ...53
2.5.5 Self-propagating high-temperature synthesis plus quick pressing (SHS/QP) ...55
2.5.6 Microwave sintering ...55
2.6 Composite coatings for corrosion protection ...57
2.6.1 Electroplating deposition ...58
2.6.2 Electropheric deposition (EPD) ...60
2.6.3 Electroless deposition ...61
2.7 Potential applications of graphene based materials ...62
2.7.1 Field effect transistors ...62
2.7.2 Graphene thin film as transparent electrodes ...63
2.7.3 Solar cell ...65
2.7.4 Electrochemical sensors and biosensors ...67
2.7.5 Graphene composite for energy storage. ...68
2.8 Summary ...72
Chapter 3: SPS and characterization of GPL/ZTA composites ...75
3.1 Introduction ...75
3.2 Experiments of the fabrication process ...75
3.2.1 Powders ...76
3.2.2 Composite powder preparation and sintering ...78
3.2.3 Material characterisations ...81
3.2.3.1 Density measurement ...81
3.2.3.2 X-ray fluorescence (XRF) analysis ...81
3.2.3.3 X-Ray diffraction (XRD) analysis ...82
3.2.3.4 SEM observation ...83
3.2.3.5 Raman study ...83
3.2.3.6 Micro hardness measurement ...84
3.2.3.7 Fracture toughness measurement ...85

3.3 Results and discussion....87
3.3.1 Selection of dispersants....87
3.3.2 Densities of the powder mixtures....89
3.3.3 SPS behaviours of the GPL/ZTA composites....91
3.3.4 XRD patterns of the sintered samples....95
3.3.4 Raman spectra of GPLs in the sintered GPL/ZTA composites. 96
3.3.5 Microstructures of the 'as-prepared' samples....98
3.3.6 Mechanical properties of the sintered samples....100
3.3.7 Toughening mechanisms in the GPL/ZTA ceramic composites....103
3.3.8 Indentation fracture toughness of the pure ZTA and GPL/ZTA composites...105
3.4 Summary....108
Chapter 4: SPS and characterization of GPL/Al_2O_3 and GPL-SiC/Al_2O_3 composites .110
4.1 Introduction....110
4.2 Experiments of fabrication process....111
4.2.1 Powders....111
4.2.2 Composite powder preparation and sintering....112
4.2.3 Material Characterizations....114
4.2.3.1 Bending tests....115
4.2.3.2 Micro hardness measurement....116
4.3 Results and discussion....117
4.3.1 GPL-reinforced Al_2O_3 ceramic nanocomposites....117
4.3.1.1 Sintering behaviours of the samples during SPS....117
4.3.1.2 Microstructures of the ceramic composites....119
4.3.1.3 Mechanical properties of sintered samples....121
4.3.1.4 Effects of GPLs in the GPL/Al_2O_3 composites....125
4.3.1.5 Porosity induced by GPLs in the GPL/Al_2O_3 composites....127
4.3.2 Al_2O_3 composites reinforced with GPLs and SiC nanoparticles. 128
4.3.2.1 Raman spectra of the GPLs in the powder mixtures and sintered samples..129
4.3.2.2 Microstructures of the sintered GPL-SiC/Al_2O_3 composites....133
4.3.2.3 Grain sizes and mechanical properties of the sintered Al_2O_3 composites...135
4.3.2.4 Dispersion of SiC nanoparticles and its effects in the composites....140
4.4 Summary....143
Chapter 5: Pressureless sintering and characterization of GPL/Al_2O_3 composites 146

5.1 Introduction 146
5.2 Experiments of fabrication 147
5.2.1 Powder mixture preparation 147
5.2.2 Formation of green compacts using CIP 147
5.2.3 Sintering of the GPL/Al_2O_3 composites with different content of GPLs 149
5.2.4 Material characterizations 150
5.2.4.1 TGA of the GPL/Al_2O_3 powder mixtures 150
5.3 Results and discussion 153
5.3.1 Microstructures and densities of the GPL/Al_2O_3 composites sintered under various processing parameters. 153
5.3.2 Effects of content of GPLs on the microstructures and mechanical properties of GPL/Al_2O_3 composites. 159
5.3.2.1 The GPLs content in the sintered GPL/Al_2O_3 composites. 160
5.3.2.2 Microstructures of the sintered samples 160
5.3.2.3 Raman spectra of the pristine GPL and GPLs after ball milling and sintering. 163
5.3.2.4 XRD patterns of the pristine GPL and the sintered samples 166
5.3.2.5 Mechanical properties of the pressureless sintered pure Al_2O_3 and GPL/Al_2O_3 composites 168
5.3.2.6 Effects of GPLs on the mechanical properties of the GPL/Al_2O_3 composites 172
5.4 Summary 173
Chapter 6: Electrodeposition and characterization of GPL/Ni composite coatings 176
6.1 Introduction 176
6.2 Experiments of fabrication 176
6.2.1 Starting materials 176
6.2.2 Electrodeposition 177
6.2.3 Material Characterizations 178
6.2.3.1 Electrochemical measurement 179
6.3 Results and discussion 180
6.3.1 Surface morphologies and microstructures of the coatings 180
6.3.2 Raman spectra of the GPLs in the coatings 184
6.3.3 Grain sizes and texture coefficients of the electrodeposited coatings 185
6.3.4 Corrosion resistant properties of the electrodeposited coatings 191

6.4 Summary 195
Chapter 7: Conclusions and future work 197
7.1 Introduction 197
7.2 Contributions 197
7.3 Conclusions 199
7.4 Suggestions for future work 201
References 205

List of Figures

Figure 2.1. Publications on graphene over the years. Source: Web of Science **8**

Figure 2.2. Graphene as a 2D building block for constructing 0D buckyballs, 1D nanotubes or 3D graphite. **9**

Figure 2.3. A SEM image of graphene with circular holes (a) and a schematic illustration of nanoindentation on graphene using AFM (b). **11**

Figure 2.4. Schematic of an experiment showing laser light focusing on single layer graphene. **12**

Figure 2.5. Variation of the thermal conductivities of carbon materials with temperature. **13**

Figure.2.6. Thermal conductivities of graphene sheet as a function of the number of atomic planes. **13**

Figure 2.7. Schematic diagrams of band gaps in graphene. (a) and (b) indiate monolayer and bilayer grapheme respectively. (c) indicates a band gap can be opened in bilayer graphene when an electric field is imposed perpendicular to the bilayer. **15**

Figure 2.8. Mechanical exfoliation of graphene using scotch tape **17**

Figure 2.9. Scanning transmission electron microscope (STEM) images of graphene prepared by epitaxial growth. M and B indicate monolayer and bilayer graphene. (b) and (c) are the 3 dimensional view of monolayer and bilayer graphene respectively. **18**

Figure 2.10. Schematic diagrams of mechanisms for formation of graphene on metal substrates by CVD. (a) and (b) indicate formation of graphene on Ni and Cu substrates respectively. **19**

Figure 2.11. Schematic of fabrication of graphene devices through roll-to-roll process. (a) Production of graphene on Cu substrates. (b) Transfer of graphene films to polymer films. (c) A transparent large graphene film transferred on a target polymer film. (d) An assembled graphene/polymer touch panel. **20**

Figure 2.12. SEM and TEM images of acid intercalated graphite (a) and graphene sheets (b). **22**

Figure 2.13. Schematic illustrations of particle toughening mechanisms in ceramic composites. (a) Particle bridging. (b) Crack deflection. **23**

Figure 2.14. SEM images of thermally etched surfaces of pure Al_2O_3 (a) sintered at 1400 ˚C and Cr/ Al_2O_3 nanocomposite (b) sintered at 1450 ˚C. **24**

Figure 2.15. A SEM image of an indentation crack in the Cr/ Al_2O_3 nanocomposite **24**

Figure 2.16. TEM images of sintered Al_2O_3 (a) and Ni/Al_2O_3 nanocomposite (b). **25**

Figure 2.17. A SEM image of an indentation crack in the sintered Ni/Al_2O_3 nanocomposites. **26**

Figure 2.18. SEM images of the fractured surface of pure Al_2O_3 (a) and 20%SiC/Al_2O_3 nanocomposite (b) sintered at 1200 and 1400˚C respectively. **27**

Figure 2.19. A TEM image of crack shielding and stress-induced micro cracking around a secondary particle in the SiC/Al_2O_3 nanocomposite. **27**

Figure 2.20. A model of intra-type nanostructure. Tmax is the maximum shear stress. **.....29**

Figure 2.21. Dislocations after sintering (a) and after annealing (b). **.....30**

Figure 2.22. A schematic illustration of FPZ and bridging in ceramics with R-curve behaviour. **.....31**

Figure 2.23. Schematic illustrations of the toughening mechanism in nanocomposites. (a) Nanostructure of the ceramic composites after annealing. (b) Creation of FPZ. **.....32**

Figure 2.24. Phase transformation of ZrO_2 with temperature **.....34**

Figure 2.25. A schematic illustration of stress-induced transformation toughening process. **.35**

Figure 2.26. SEM images of ZTA composites sintered at 1600 ˚C for 2 hours. (a) Al_2O_3, (b) Al_2O_3+10% ZrO_2, (c) Al_2O_3+20% ZrO_2 and (d) Al_2O_3+30% ZrO_2. **.....36**

Figure 2.27. Typical load deflection diagram of a layered structure with weak interfaces. The steps show the failure of individual layers and the crack propagation along the interface. A schematic side view of a broken specimen showing crack deflection into the weak layers is shown in the inset. The failure of a monolithic is also shown for comparison. **.....37**

Figure 2.28. An optical image showing the path of a crack across a laminated sample containing a notch. **.....38**

Figure 2.29. Fracture surface of Si_3N_4/ Si_3N_4-50% wt.%TiN composite. (a) and (c) are SEM images. (b) and (d) are backscattered images. **.....39**

Figure 2.30. SEM images of the monolithic (a) and laminated (b and c) ceramic specimens after bending tests. **.....40**

Figure 2.31. A SEM image of fracture surface of the carbon fibre reinforced TiC composites. **.....41**

Figure 2.32. Fracture behaviour of carbon fibre/Ti ceramic composites. (a) A crack initiates in the ceramic matrx, (b) A crack meets with a fibre and debonding occurs between matrix and fibre, (c) Crack bridging and (d) Pullout and bridging of the fibres. **.....41**

Figure 2.33. SEM images of fracture surfaces of the CNT/Al_2O_3 composites. **.....43**

Figure 2.34. SEM images of fracture surfaces for monolithic Al_2O_3 (a) Al_2O_3–4vol% CNT nanocomposites (b). **.....43**

Figure 2.35. SEM images of the Vicker indentation sites. (a) dense Al_2O_3, showing radial cracks. (b) and (c) are CNT/Al_2O_3 and graphite/Al_2O_3 composites, showing no evidence of radial cracks. **.....45**

Figure 2.36. SEM images of the fracture surface of the GPL/Si_3N_4 composite (a) and an indentation crack (b). **.....46**

Figure 2.37. SEM images of the fracture surface of the GPL/Si_3N_4 composite, showing crack propagates and climbs over the graphene sheets, implying three dimensional toughening mechanism. **.....47**

Figure 2.38. Images of conventional furnaces. (a) is box furnace and (b) is tube furnace. **.....49**

Figure 2.39. A schematic illustration of SPS (a) and an image of SPS (b). **.....50**

Figure 2.40. Relative density of ZrO_2 produced by SPS as a function of pressure. **.....52**

Figure 2.41. A schematic illustration of HIP (a) and an image of HIP (b). **.....53**

Figure 2.42. A schematic illustration of SLS process.....**54**

Figure 2.43. Images of components produced by SLS. (a) is a part of a turbine blade. (b) and (c) are ceramic parts.....**54**

Figure 2.44. A schematic representation of SHS experiment process.....**55**

Figure 2.45. Heating patterns in conventional (a) and microwave (b) furnaces.....**56**

Figure 2.46. A schematic illustration of the electroplating deposition.....**58**

Figure 2.47. A schematic illustration of the electropheric deposition.....**60**

Figure 2.48. A schematic illustration of electroless deposition with reducing agent R as the source of electrons.....**61**

Figure 2.49. Schematic illustrations of back gated (a) and top gated (b) graphene field effect devices.....**63**

Figure 2.50. Optical and electrical properties of GO and RGO films on quartz. (a) Images of a GO (leftmost) and four RGO films with increasing thickness. (b) Optical transmittance of the films in (a) with the film thickness indicated. (c) Sheet resistance of the films prepared using two different methods as a function of optical transmittance at 550 nm light. (d) Film conductivity as a function of transmittance for films shown in (c).....**64**

Figure 2.51. Schematic of the dye-sensitized solar cell (a) and variation of current density with the voltage (b). The four layers from bottom to top in (a) are gold, dye-sensitized heterojunction, compact titanium oxide, and graphene film. Black and red lines in (b) indicate graphene-based cell and fluorine doped tin oxide (FTO)-based cell respectively.....**65**

Figure 2.52.Schematic illustrations of the photovoltaic device structures. (a) ITO/GO/P3HT:PCBM/A and (b) ITO/PEDOT:PSS/P3HT:Graphene/LiF/Al. **67**

Figure 2.53. Electrochemical properties of a half-cell composed of Mn_3O_4/RGO and Li. (a) Charge and discharge curves of Mn_3O_4/RGO at a current density of 40 mA/g. (b) Charge and discharge curves of Mn_3O_4/RGO at various current densities. (c) Capacity retention of Mn_3O_4/RGO at various current densities. (d) Capacity retention of Mn_3O_4 at a current density of 40 mA/g. **69**

Figure 2.54. Images of graphene papers. **72**

Figure 3.1. SEM images of the Al_2O_3 powders. (b) is a magnified image of (a). **76**

Figure 3.2. SEM (a-b) and AFM (c-d) images of GPLs. (b) is the magnified part of the square area in (a). (d) is the three dimensional topography image of GPL. **77**

Figure 3.3. SEM images of powder mixtures. (a) SEM images of small GPLs. (b) low and (c) higher resolution SEM images of a large GPL. **79**

Figure 3.4. SPS facility by FCT Systeme, Germany. (a) SPS facility and (b) SPS at 1550˚C. **79**

Figure 3.5. Sintering profiles for GPL/ZTA composites. **80**

Figure 3.6. An image of XRF Spectrometer **82**

Figure 3.7. An image of the Bruker D8 Advance Diffractometer **83**

Figure 3.8. An image of the Raman Microscope **84**

Figure 3.9. A schematic illustration of the typical Vickers' indent. **85**

Figure 3.10. An image of the Instron mechanical tester **86**

Figure 3.11. A schematic illustration of the SENB test. **87**

Figure 3.12. Comparison of colloidal dispersion stability of GPLs in different solvents after 1 hour ultrasonication. (A), (B) and (C) indicate dispersion of GPLs in ethanol, DMF and NMP. The concentration for all cases is 0.008 g/ml. **88**

Figure 3.13. Densities of the powder mixtures **89**

Figure 3.14. Temperature and displacement profiles of the sintered samples. (a), (b) and (c) are for samples sintered at 1450, 1550 and 1650 ˚C respectively. **92**

Figure 3.15. Variation of shrinkage rate with heating temperature. (a), (b) and (c) are for samples sintered at 1450, 1550 and 1650 ˚C respectively. **94**

Figure 3.16. XRD patterns of ZTA and GPL/ZTA ceramic composites. **95**

Figure 3.17. Raman spectra of the pristine GPL and the GPLs in the composites **96**

Figure 3.18. SEM images of fracture surfaces of the samples sintered at 1550˚C (a) is the sample without GPLs and (b) is with GPLs. **99**

Figure 3.19. SEM images of the thermally etched surfaces. (a) pure ZTA (b) GPL/ZTA composites. **99**

Figure 3.20. SEM images of fracture surfaces for GPL-reinforced ZTA composite sintered at 1650˚C, (b), (c) and (d) are the magnified parts of square, hexagonal and circular areas in (a). The white arrows point at GPLs. **100**

Figure 3.21. Relative densities of the sintered ZTA and GPL/ZTA composites **101**

Figure 3.22. Hardness of the sintered ZTA and GPL/ZTA composites. **.....102**

Figure 3.23. Fracture toughness of the sintered ZTA and GPL/ZTA composites. **.....102**

Figure 3.24. SEM images of fracture surfaces of GPL/ ZTA composite sintered at 1650˚C. **.....103**

Figure 3.25. SEM images of fracture surfaces of GPL/ZTA composite sintered at 1450˚C (a-b) and 1650˚C (c-d). (b) is the magnified GPL in (a). (d) shows the magnified GPL in (c). The solid and dashed lines in (a) indicate the crack paths with or without GPL. White arrows point at GPLs. **.....104**

Figure 3.26. Indentation fracture toughness of the pure ZTA and GPL/ZTA ceramic composites. **.....105**

Figure 3.27. SEM images of a micro hardness indent (a) and radial cracks (b-f). (c) is magnified part of the square area in (b). **.....106**

Figure 3.28. Schematic illustrations of toughening mechanisms in GPL-reinforced ceramic composites with micro and nano scale ceramic matrices. **.....108**

Figure 4.1. SEM images of Al_2O_3 (a-b) and SiC (c-d) powders. (b) and (d) are the magnified images of (c) and (d). **.....112**

Figure 4.2. The flow chart of the preparation of the powder mixtures. **.....113**

Figure 4.3. SEM images of the GPL/Al_2O_3 (a) and GPL-SiC/Al_2O_3 (b) powder mixtures. **...114**

Figure 4.4. Schematic illustrations of three-point bending configurations for the measurements of the flexural strength (a) and fracture toughness (b). **.....115**

Figure 4.5. Temperature and displacement profiles for the pure Al_2O_3 and 0.38vol% GPL/Al_2O_3 composite. **118**

Figure 4.6. Profiles of shrinkage rates for the pure Al_2O_3 and 0.38vol% GPL/Al_2O_3 composite **119**

Figure 4.7. SEM images of fracture surfaces of the pure Al_2O_3 samples (a), 0.38 vol% GPL/Al_2O_3 composite (b), 0.76 vol% GPL/Al_2O_3 composite (c) and 1.33 vol% GPL/Al_2O_3 composite (d). The arrows point at GPLs. **120**

Figure 4.8. Hardness of the GPL/Al_2O_3 composites as a function of GPLs content **122**

Figure 4.9. Flexural strength of the GPL/Al_2O_3 composites as a function of GPLs content **123**

Figure 4.10. Fracture toughness of the GPL/Al_2O_3 composites as a function of GPLs content. **123**

Figure 4.11. SEM images and optical images of notches before (a-b) and after (c-d) the bending test. **124**

Figure 4.12. SEM images of fracture surfaces of GPL-reinforced Al_2O_3 composites showing the toughening and reinforcing mechanisms. **126**

Figure 4.13. SEM images of fracture surfaces of GPL-reinforced Al_2O_3 composites showing the pores and aggregates of GPLs. (b) and (d) are the magnified part of white square areas in (a) and (c). **127**

Figure 4.14. Raman spectra of the pristine GPL and GPLs in the composites **130**

Figure 4.15. Raman spectra of the GPLs in the GPL-SiC/Al_2O_3 powder mixture and the sintered composite. **132**

Figure 4.16. SEM images of fracture surfaces of the sintered pure Al_2O_3 (a), GPL/Al_2O_3 composite (b), 1vol% SiC-GPL/Al_2O_3 composite (c), 3vol% SiC-GPL/Al_2O_3 composite (e) and 5vol% SiC-GPL/Al_2O_3 (g) composite. (d), (f) and (h) are the magnified images of (c), (e) and (g) respectively. White arrows indicate the GPLs. **.....134**

Figure 4.17. Grain sizes of the pure Al_2O_3 and GPL-SiC/Al_2O_3 composites as a function of SiC content.**.....135**

Figure 4.18. SEM images of fracture surfaces of the sintered pure Al_2O_3 (a), GPL/Al_2O_3 composite (b), 1vol% SiC-GPL/Al_2O_3 composite (c), 3vol% SiC-GPL/Al_2O_3 composite (d) and 5vol% SiC-GPL/Al_2O_3 composites (e). **.....136**

Figure 4.19. Densities of the GPL-SiC/Al_2O_3 composites as a function of SiC content.**.....137**

Figure 4.20. Hardness of the GPL-SiC/Al_2O_3 composites as a function of SiC content.**.....138**

Figure 4.21. Flexural strength of the GPL-SiC/Al_2O_3 composites as a function of SiC content. **.....139**

Figure 4.22. Fracture toughness of the GPL-SiC/Al_2O_3 composites as a function of SiC content.**.....139**

Figure 4.23. SEM images of fracture surfaces of the GPL-SiC/Al_2O_3 composites.**.....140**

Figure 4.24. SEM images of fracture surfaces (a-b) and polished surfaces (c-d) of GPL-SiC/Al_2O_3 composites. White and black arrows indicate GPLs and SiC nanoparticles respectively. **.....141**

Figure 4.25 A schematic illustration of the strengthened grain boundaries induced by SiC nanopartilces **……142**

Figure 5.1. An image of the soft mould. **148**

Figure 5.2. Images of the hydraulic press. (a) the hydraulic press and cylinder assembly (b) hydraulic cylinder. **148**

Figure 5.3. An image of the typical green compacts formed by CIP. White is the pure Al_2O_3 and blue is the GPL/Al_2O_3 sample. **148**

Figure 5.4. An image of the tube furnace for sintering. **149**

Figure 5.5. An image of a sintered sample. **150**

Figure 5.6. An image of the instrument for TGA. **151**

Figure 5.7. An image of four-point bending configuration (a) and schematic illustrations of four-point bending configurations for the measurements of flexural strength (b) and fracture toughness (c). **152**

Figure 5.8. Fracture surfaces of the sintered GPL/Al_2O_3 composites processed under the following parameters: heating rate: 3 ℃/s; sintering temperature: 1200 ℃; sintering time: 2.5 hours; sintering atmosphere: nitrogen; flowing rate of nitrogen: 3L/min. **154**

Figure 5.9. Fracture surfaces of the GPL/Al_2O_3 composites processed under the following parameters: heating rate: 5 ℃/s; sintering temperature: 1300 ℃; sintering time: 2.5 hours; sintering atmosphere: nitrogen; flowing rate of nitrogen: 6 L/min. **154**

Figure 5.10. Fracture surfaces of the GPL/Al_2O_3 composites processed under the following parameters: heating rate: 5 ℃/s; sintering temperature: 1400 ℃; sintering time: 3 hours; sintering atmosphere: nitrogen; flowing rate of nitrogen: 6 L/min. **155**

Figure 5.11. Fracture and polished surfaces of the GPL/Al_2O_3 composites processed under the following parameters: heating rate: 5 ℃/s; sintering temperature: 1400 ℃; sintering time: 3 hours; sintering atmosphere: forming gas; flowing rate of forming gas: 6 L/min. **.....156**

Figure 5.12. Fracture surfaces of the GPL/Al_2O_3 composites processed under the following parameters: heating rate: 5 ℃/s; sintering temperature: 1650 ℃; sintering time: 3 hours; sintering atmosphere: forming gas; flowing rate of forming gas: 8 L/min. White arrows indicate GPLs. **.....157**

Figure 5.13. Fracture surfaces of the GPL/Al_2O_3 composites processed under the following parameters: heating rate: 5 ℃/s; sintering temperature: 1770 ℃; sintering time: 2.5 hours; sintering atmosphere: nitrogen gas; flowing rate of nitrogen gas: 8 L/min. (b) and (c) are the magnified circle and square areas in (a). White arrows indicate GPLs. **.....158**

Figure 5.14. TGA for the sintered samples with different GPLs content. **.....160**

Figure 5.15. Fracture surfaces of the sintered samples. (a) Al_2O_3, (b) 0.75 vol% GPL/Al_2O_3, (c) 1.3 vol% GPL/Al_2O_3 and (d) 1.48 vol% GPL/Al_2O_3. **.....161**

Figure 5.16. SEM images of the polished and thermally etched surfaces of the sintered samples. (a) Al_2O_3, (b) 0.75 vol% GPL/Al_2O_3, (c) 1.3 vol% GPL/Al_2O_3 and (d) 1.48 vol% GPL/Al_2O_3. **.....162**

Figure 5.17. Grain sizes of Al_2O_3 matrices as a function of GPLs content. **.....163**

Figure 5.18. Raman spectra of the pristine GPL and GPLs in powder mixtures. **.....164**

Figure 5.19. Raman spectra of the pristine GPL and GPLs after sintering. **.....166**

Figure 5.20. XRD pattens of the pristine GPL, pure Al_2O_3 and GPL/Al_2O_3 composites. **.....167**

Figure 5.21. Densities of the GPL/Al_2O_3 samples as a function of GPLs content **.....168**

Figure 5.22. Hardness of the GPL/Al_2O_3 samples as a function of GPLs content. **.....169**

Figure 5.23. Flexural strength of the GPL/ Al_2O_3 samples as a function of GPLs content. **..170**

Figure 5.24. Fracture toughness of the GPL/Al_2O_3 samples as a function of GPLs content. **171**

Figure 5.25. A SEM image of the typical notch tip. **.....171**

Figure 5.26. Fracture surfaces of GPL/Al_2O_3 composites **.....173**

Figure 6.1. A schematic illustration of the electrodeposition process. **.....178**

Figure 6.2. An image of electrochemical analyzer. **.....179**

Figure 6.3. Schematic of three-electrode cell. **.....180**

Figure 6.4. Surface morphologies and elemental composition of electrodeposited coatings. (a) pure nickel, (b) 1-GPL/Ni and (d) 2-GPL/Ni. (c) and (e) are the EDS results of the square areas in (b) and (d). **.....181**

Figure 6.5. Schematic illustrations of the deposition process of Ni (a) and GPL/Ni (b) coatings. **.....182**

Figure 6.6. Surface morphologies (a-d) and elemental composition (e) of the electrodeposited GPL/Ni composite coatings. (e) is the EDS result of the square area in (d). **.....183**

Figure 6.7. Raman spectra of the pristine GPL and the GPLs in the electrodeposited GPL/Ni. **.....184**

Figure 6.8. XRD patterns of pure Ni and GPL/Ni composite coatings. (a) pure Ni, (b) 1-GPL-Ni and (c) 2-GPL-Ni. **186**

Figure 6.9. XRD patterns of the pure Ni and GPL/Ni coatings. **187**

Figure 6.10. Texture coefficients of the pure Ni and GPL/Ni coatings. **188**

Figure 6.11. Hardness of the pure Ni and GPL/Ni coatings. **190**

Figure 6.12. Polarization curves of the pure Ni and GPL/Ni coatings. **192**

Figure 6.13. Surface morphologies of the GPL/Ni coatings. (b) is the magnified part of the square area in (a). White arrows indicate GPLs. **193**

Figure 6.14. Impedance spectra of the mild steel, pure Ni and GPL/Ni coatings in 3.5% NaCl solution. **194**

Figure 7.1. Images of sintered sample (left) and the green compact (right). **203**

Figure 7.2. SEM images of the Al_2O_3 micro gear (a-b) and the surface morphology (c) of the micro gear. **204**

List of Tables

Table 2.1. Properties of different engineering fibres **16**

Table 2.2. A summary of the fracture toughness of composites reinforced with CNTs or GPLs **47**

Table 2.3. A summary of the mechanical properties of ceramics..... **57**

Table 2.4. Properties of graphene-based transparent electrodes. **65**

Table 2.5. Photovoltaic properties of solar cells containing RGO. **67**

Table 2.6. RGO based chemical sensors and biosensors **68**

Table 2.7. Performances of graphene based lithium ion battery materials **70**

Table 2.8. Properties of graphene based supercapacitors **71**

Table 3.1. Composition of the powder mixtures. **90**

Table 3.2. Content of the oxides in the powder mixtures **90**

Table 3.3. Theoretical density and composition of the powder mixtures **90**

Table 3.4. Raman parameters of the pristine GPL and the GPLs in the composites. **97**

Table 4.1. Densities of the sintered samples. **121**

Table 4.2. Raman parameters of the pristine GPL and the GPLs in powder mixtures. **131**

Table 4.3. Raman parameters of the pristine GPL and the GPLs in the sintered sample. **.....132**

Table 5.1. A summary of densities of the sintered samples under various processing parameters **.....159**

Table 5.2. Raman parameters of the pristine GPL and the GPLs in the powder mixtures **....165**

Table 6.1. Raman parameters of the pristine GPL and the GPLs in the composite coatings. **185**

Table 6.2. Corrosion potentials and corrosion current densities of the electrodeposited coatings **.....192**

Abbreviations

GPL	Graphene platelet
CNTs	Carbon nanotubes
SPS	Spark plasma sintering
HIP	Hot isostatic pressing
SLS	Selective laser sintering
AFM	Atomic force microscopy
GNR	Graphene nanoribbon
CVD	Chemical Vapour Deposition
SEM	Scan electron microscopy
XRD	X-ray diffraction
TEM	Transmission electron microscopy
SEVNB	Single edge V-notched beam
SENB	Single-edge notched beam
AM	Additive manufacturing
SHS/QP	Self-propagating high-temperature synthesis plus quick pressing
EPD	Electropheric deposition
RGO	Reduced graphene oxide

ITO	Indium doped tin oxide
LIBs	Lithium ion batteries (LIBs)
PANI	Polyaniline
P3HT	Poly(3-hexylthiophene)
PEDOT	Poly(3,4-ethylene dioxythiophene)
PSS	Poly(styrene sulfonate)
PCBM	Phenyl-C61-butyric acid methyl ester
XRF	X-ray fluorescence
FWHM	Full width at half maximum
E_{ccor}	Corrosion potential
I_{ccor}	Corrosion current densities

Nomenclatures

τ_{cb}	Critical resolved shear stresses for basal slip planes.
τ_{cp}	Critical resolved shear stresses for basal and prism slip planes.
$K_R(\Delta a)$	Fracture toughness of the material exhibiting R-curve behaviour,
K_i	Intrinsic fracture toughness
$\Delta K_R(\Delta a)$	Extrinsic increase in the fracture toughness
ρ_A	Actual density of the sintered sample
ρ_w	Density of distilled water
m_A	The weight of the sintered sample measured in air
m_w	The weight of the sintered sample measured in distilled water
H	Hardness
P	Load
d	Average length of indentation diagonals
k_c	Indentation fracture toughness.
C	Half of the mean radial crack length
L	Span of the specimen
B	Width of the specimen

W	Depth of the specimen
c	Depth of the notch
a	V notch depth
Y	Stress intensity shape factor
K_{Ic}	Fracture toughness
L_1	Outer span
L_2	Inner span
α	V-notch depth
Q	Average crystallite size
K	Scherrer constant
λ	Wave length
β	FWHM
θ	Diffraction angle
$I_{(hkl)}$	Intensity of the reflection for the examined sample
$I_{o(hkl)}$	Intensity of the reflection from the standard oriented sample.
μ	Modulus of the matrix materials
b	Burger's vector
f_v	Volume fraction of the particulate phase
d_p	Size of the particulate phase

M	Taylor factor

List of Publications

Journal papers:

[1] Liu J, Yan HX, Reece MJ, Jiang K. Toughening of zirconia/alumina composites by the addition of graphene platelets. J Eur Ceram Soc 2012;32(16):4185-93.

[2] Liu J, Yan HX, Jiang K. Mechanical properties of graphene platelet-reinforced alumina ceramic composites. Ceram Int 2013;39(6):6215-21.

[3] Liu J, Zheng Li, Yan HX, Jiang K. Spark Plasma Sintering of Alumina Composites with Graphene Platelets and Silicon Carbide Nanoparticles. Adv. Eng. Mater.2014. In press.

Chapter 1: Introduction of the thesis

1.1 Introduction

This thesis presents an investigation into fabrication and characterization of ceramic and metallic composite materials reinforced with GPLs. The research described in this thesis was driven jointly by the needs for further improvement on the brittleness of ceramics and the low corrosion resistance of mild steel using carbon nanostructured fillers. The opportunity to achieve these improvements is emerging with the appearance of graphene materials.

Ceramics, such as Al_2O_3, are widely used in various applications due to their excellent mechanical properties, thermal stability and chemical inertness. However, the brittleness of the ceramics has seriously limited their further applications. To overcome this problem, various strategies and processing approaches have been proposed. Among them the addition of secondary strong and tough nano fillers has become popular for a significant improvement in the mechanical properties of the ceramic matrices can be achieved by introducing a small percentage of these nano fillers. Carbon fillers, such as carbon nanotubes (CNTs) and carbon fibres have been extensively studied as strong reinforcements due to their remarkable Young's modulus. However, the high cost of these carbon fillers make them less competitive when mass production of related composites is considered. Graphene since its discovery in 2004 has received widespread attention and its excellent electrical and mechanical properties make it a suitable candidate to be used in a variety of applications. Compared to monolayer graphene, GPLs are stacked graphene with thickness of up to approximately 100nm [1]. It is reported that the Young's modulus of GPLs with thickness of 2-8 nm is approximately

0.5Tpa [2], which is higher than 380Gpa for alumina. Therefore, it is expected that the strength and toughness of the ceramic matrices can be considerably improved using GPLs as reinforcements. In this thesis, two types of sintering approaches were employed to fabricate the GPL-reinforced ceramic composites. One approach involves a SPS furnace, which can introduce high temperature and high pressure and achieve the densification process of the ceramic composites within just a few minutes. The other approach concerns a tube furnace, by which the pressureless sintering can be carried out under flowing inert gases. Bending tests and characterization tools such as X-ray fluorescence (XRF), X-Ray diffraction (XRD), Scan electron microscopy (SEM) and Raman spectroscopy were used to examine the microstructures and mechanical properties of the GPL/ceramic composites.

On the other hand, metal/CNT and polymer/GPL composite coatings have shown significantly improved corrosion resistance. In order to explore GPLs as potential reinforcements for corrosion resistant applications, an electrodeposition technique was used to produce GPL/Ni composite coatings. Polarization curves and impedances of the composite coatings were obtained by electrochemical tests and compared with those of the pure Ni and mild steel.

1.2 Aims and objectives

The aims of this PhD thesis are to fabricate GPL-reinforced ceramic and metallic composites and improve their mechanical or corrosion resistant properties. The significance of this research is to investigate the effects of GPLs on the properties of the fabricated composites. In particular, for GPL/ceramic composites, flexural strength and fracture toughness of the

ceramic matrices enhanced by GPLs are investigated. For GPL/metal composites, the improvement in corrosion resistant properties induced by GPLs is studied.

The research in this thesis poses several challenges. The first is to find a simple and feasible way to disperse the GPLs in ceramic powder particles during the ball milling process. The second is to design a composite system comprised of Al_2O_3 matrix and nano fillers, in which hardness, flexural strength and fracture toughness of the Al_2O_3 matrix can be improved simultaneously by the nano fillers after sintering. The third is to find the suitable processing parameters for consolidating GPL/Al_2O_3 powder compacts during pressureless sintering.

In order to achieve the research aims mentioned above, the objectives of the thesis are set out below:

1. Review the recent progress of fabrication and characterization of Al_2O_3, ZTA, CNT-reinforced ceramic and metallic composite materials.

2. Find an effective dispersion process to prevent the formation of GPL aggregates and to enable a wide distribution of GPLs in the ceramic particles.

3. Perform SPS experiments and related characterizations and find the optimum sintering temperature to densify the GPL/ZTA composites.

4. Perform SPS experiments and related characterizations and find the optimum GPLs content where mechanical properties of the GPL/Al_2O_3 ceramic composites are considerably enhanced.

5. Perform SPS experiments and characterization of GPL-SiC/Al_2O_3 composites and find the optimum content of the nano fillers where hardness, flexural strength and fracture toughness of the Al_2O_3 matrix can be significantly improved.

6. Perform a series of pressureless sintering experiments and find the suitable processing parameters to consolidate the GPL/Al_2O_3 powder compacts.

7. Perform electrodeposition experiments and characterization of GPL/Ni coatings and find the influence of the GPLs on the corrosion properties of the coatings.

1.3 Thesis structure

This thesis consists of seven chapters. Chapter 1 introduces the research topic covered by this thesis. It includes the project aims, objectives and thesis structure.

Chapter 2 reviews the properties of the graphene, the graphene fabrication techniques, the state of the art composite technologies and the potential applications of the graphene. It starts with an introduction of the structure, properties and fabrication approaches of graphene, followed by a review of sintering techniques and toughening mechanisms in ceramic

composites. Afterwards, a literature survey covering fabrication techniques of the composite coatings and applications of the graphene is presented. In this chapter, mechanical properties of the graphene and ceramic matrix composites are primarily introduced. However, in order to give a comprehensive introduction of graphene, its functional properties and potential applications are reviewed as well.

Chapter 3 introduces fabrication and characterization of GPL/ZTA composites processed by SPS. N-Dimethylformamide (DMF) is used for dispersing GPLs in the ceramic particles. To achieve dense sample easily, micro-sized powders are used. The effects of the sintering temperature on the densification of GPL/ZTA composites are studied and discussed. A single edge notched beam (SENB) method is used to examine the fracture toughness of the pure ZTA and GPL/ZTA composites. The toughening mechanisms induced by the GPLs are discussed. Structural changes of the GPLs with the sintering temperature are analyzed by Raman spectroscopy.

Chapter 4 introduces fabrication and characterization of GPL/Al_2O_3 and GPL-SiC/Al_2O_3 composites processed by SPS. The effects of GPLs content on the microstructures and mechanical properties of the fabricated composites are investigated. In particular, fracture toughness of the pure Al_2O_3, GPL/Al_2O_3 and GPL-SiC/Al_2O_3 composites is determined by a single edge V-notched beam (SEVNB) method and then compared. Structural changes of GPLs after ball milling and SPS processing are analyzed and discussed. Also discussed are the effects of SiC nanoparticles on the Raman spectra of GPLs and the effects of GPLs and SiC nanoparticles on the microstructures and mechanical properties of the composites.

Chapter 5 for the first time introduces fabrication and characterization of GPL/Al_2O_3 composites processed by pressureless sintering. Various processing parameters are used to consolidate the powder compacts of GPL/Al_2O_3 prepared by cold isostatic pressing (CIP). Suitable processing parameters are determined by comparing the densities of the sintered composites and the morphologies of the GPLs within the composites. The effects of GPLs content on the microstructures and mechanical properties of the pressureless-sintered composites are investigated and discussed. Structural changes of the GPLs after pressureless sintering over a long period of time are characterized by Raman spectroscopy.

Chapter 6 introduces the electrodeposition of Ni and GPL/Ni composite coatings and characterization of the fabricated coatings. The effects of GPLs content on the hardness, grain size and corrosion resistant properties of composite coatings are studied and discussed.

Chapter 7 concludes the complete research work of the thesis. The major findings obtained from the study are summarised. Possible future research topics are suggested.

Chapter 2: Literature review

2.1 Introduction

This chapter presents a literature review of graphene, toughening mechanisms in ceramic materials, sintering techniques, composite coating for corrosion resistance and potential applications of graphene. The review concerning the structure and properties of graphene is presented in Section 2.2. Fabrication approaches of graphene and GPLs are reviewed in Section 2.3. Toughening mechanisms in ceramics and ceramic composites are reviewed in Section 2.4, in which CNT/ceramic composites and GPL/ceramic composites are discussed. Sintering techniques including SPS, selective laser sintering (SLS) and hot isostatic pressing (HIP) are reviewed in Section 2.5. Section 2.6 outlines fabrication techniques of composite coatings for corrosion resistance. Potential applications of graphene are reviewed in Section 2.7. Finally the literature review is summarized in Section 2.8.

2.2 Properties of graphene

Since it was produced and characterised in 2004 by Geim and Novoselo, graphene has become a hot topic and attracted attention globally. As shown in Figure.2.1, the last decade has seen a dramatic increase of publications concerning graphene. Particularly in 2013, there were almost 30 publications produced by researchers each day. So much effort is put into graphene research because of its remarkable mechanical and electrical properties which make it a good candidate to replace CNT. It is believed to have great potential to revolutionize

many industries, such as electronics. Many related fields such as bioscience and medical science are expected to be benefited from the research of graphene.

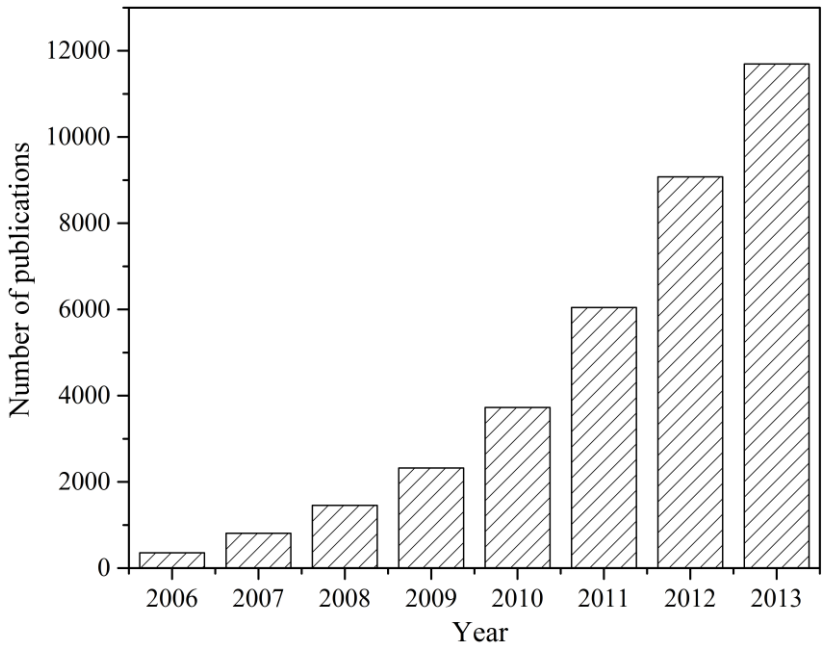

Figure 2.1. Publications on graphene over the years. Source: Web of Science

2.2.1 Structure of graphene.

Graphene is a flat monolayer of carbon atoms tightly packed into a two-dimensional (2D) honeycomb lattice and is a basic building block for graphitic materials of all other dimensionalities [3]. Graphene is one of several single layer allotropes of carbon. The other allotropes of carbon include 0D fullerenes, 1D carbon nanotubes and 3D graphite, as shown in Figure 2.2. The carbon-carbon bond length in graphene is about 0.142 nm. Graphene can appear in many different ways, i.e., functionalised and stacked containing different structural defects. Each type of graphene has its own advantages and disadvantages and can be used for specific applications. Compared to monolayer graphene, GPLs are multilayer graphene

formed by the stacking of graphene and have a thickness of up to approximately 100 nm and interplanar spacing of 0.335 nm [4].

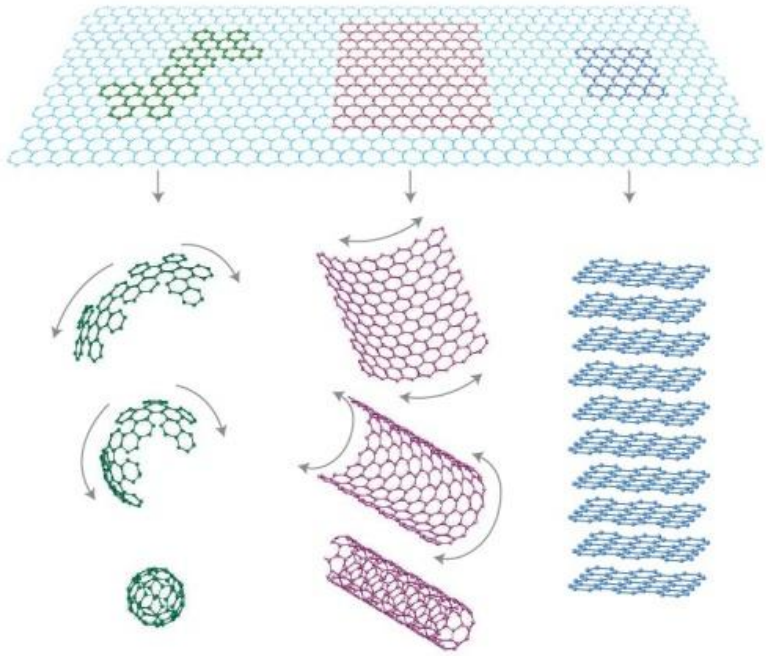

Figure 2.2. Graphene as a 2D building block for constructing 0D buckyballs, 1D nanotubes or 3D graphite.

2.2.2 Mechanical properties

When graphene was produced, it impressed the scientific community with its remarkable flexibility. Researchers then became interested in exploring its mechanical properties and expected that it could be as strong as the CNT. The initial studies on the mechanical properties of the monolayer graphene were carried out by numerical simulations [5, 6]. Van Lier et.al simulated the mechanical behavior of the graphene and concluded that elastic modulus of graphene could be around 1.11 GPa [5]. Reddy et al. used a continuum mechanics method and modelled the deformation of graphene sheets in terms of Brenner's potential [6].

The elastic modulus of the graphene was estimated to be 0.669 TPa in their results. In recent years researchers have developed experimental methods to reveal the true elastic modulus. These experiments are primarily based on the utilization of atomic force microscopy (AFM). For example, AFM was employed to measure the force-displacement on a strip of graphene and the elastic modulus of a few layers of graphene [2]. Characterization of circular membranes of few-layer graphene was also made through force volume measurement by AFM [7]. In a recent report, the elastic properties and breaking strength of the monolayer graphene were determined by nanoindentation using AFM, as shown in Figure 2.3 [8]. It was reported that the elastic modulus and fracture strength obtained were 1 TPa and 130 GPa respectively. Elastic properties of the graphene sheets produced by chemical method were also studied [9]. The elastic modulus of the monolayer graphene was determined through deformation experiments induced by the tip of an AFM and the reported elastic modulus of the graphene was 0.25 TPa. Examination was also carried out on multilayer graphene with a thickness of 2-8 nm and it was found that its elastic modulus was approximately 0.5 TPa [2].

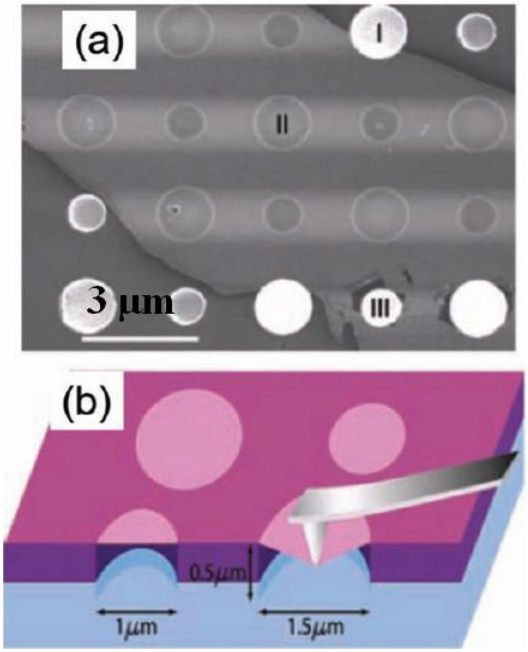

Figure 2.3. A SEM image of graphene with circular holes (a) and a schematic illustration of nanoindentation on graphene using AFM (b).

2.2.3 Thermal Properties

Carbon and its allotropes such as CNT, graphite and diamond possess very good thermal conductivities and are widely utilized in various applications. The emergence of graphene enriches the carbon family and provides an alternative in fields where good thermal conductivity is highly valued.

Generally thermal conductivity of graphene is dominated by phonon transport at high temperature and ballistic conduction at low temperature [10]. Simulation work was firstly performed to predict the thermal conductivity of the monolayer graphene and the reported value is 6000 W $m^{-1}K^{-1}$at room temperature [11]. Work was later carried out to obtain the

true thermal conductivity of the graphene and the examined in-plane thermal conductivity of graphene was reported to be 2000-4000 W $m^{-1}K^{-1}$ [12-14] . In a recent report, an optical method was used to measure the thermal conductivity of graphene (Figure 2.4) and the obtained thermal conductivity is about 5000 W $m^{-1}K^{-1}$ [15].

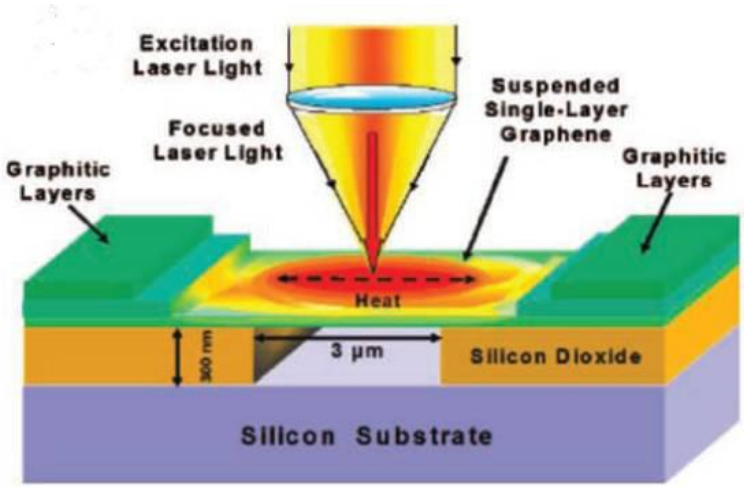

Figure 2.4. Schematic of an experiment showing laser light focusing on single layer graphene.

Figure 2.5 shows the thermal conductivity of different materials as a function of temperature [14]. It can be seen that graphene presents a very good thermal conductivity, which is higher than that of graphene nanoribbon (GNR) and comparable to conductivities of diamond, graphite or CNT (Figure 2.5a). In particular, suspended graphene exhibits the highest thermal conductivity among all conductive materials at room temperature (Figure 2.5b). It was implied that the heat transfer through the cross-plane direction in graphite was seriously affected by interplaner van der Waals force [14] and the thermal conductivity of graphene sheets decreases with the increase of layers, as shown in Figure 2.6 [16]. It is expected that thermal properties of graphene can be tuned and will be beneficial to heat-sinking and thermoelectric applications.

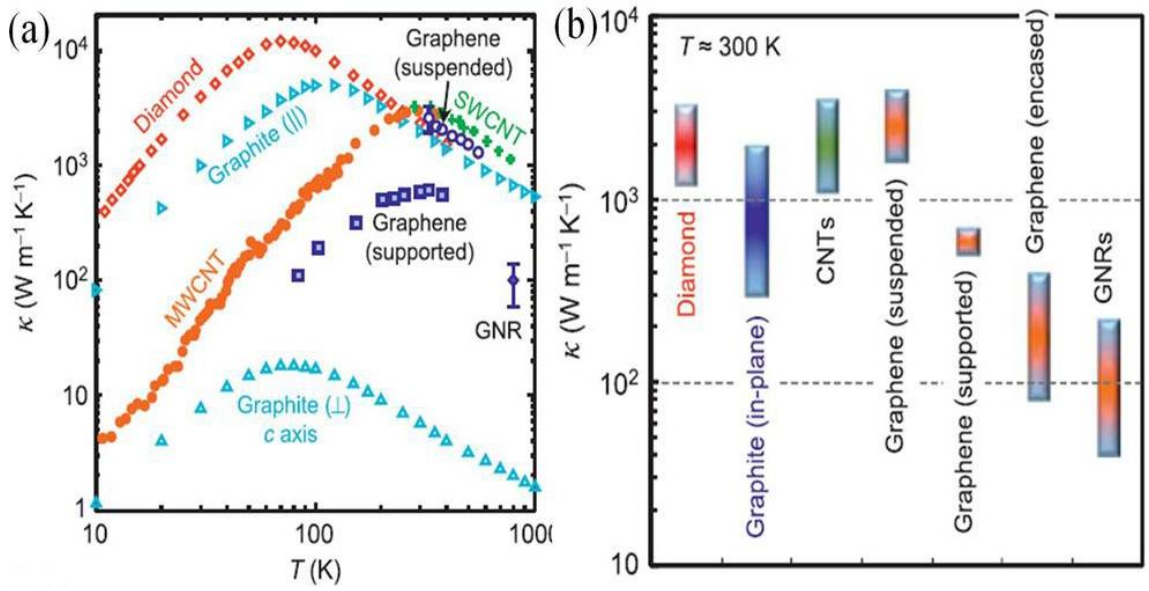

Figure 2.5. Variation of the thermal conductivities of carbon materials with temperature.

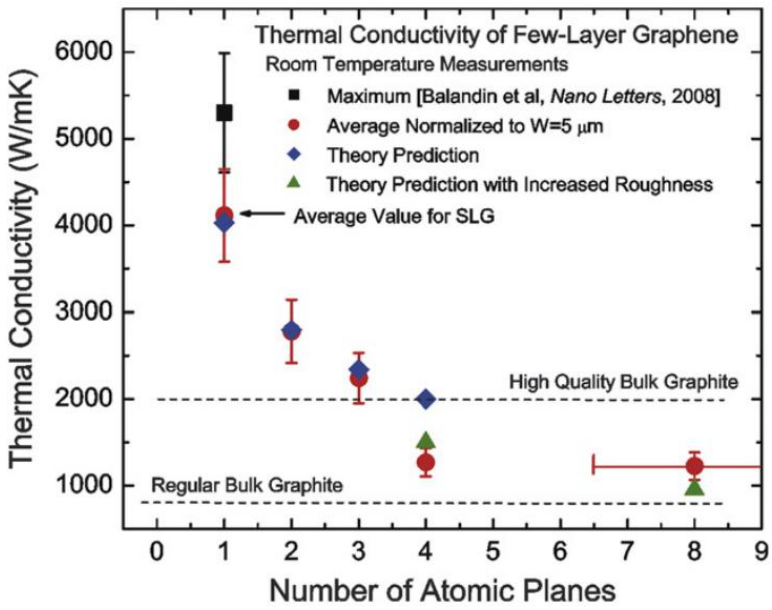

Figure.2.6. Thermal conductivities of graphene sheet as a function of the number of atomic planes.

2.2.4 Electrical properties

In comparison with three dimensional conductive materials graphene possesses unique electrical properties. To understand graphene's electronic structure will establish the fundamental knowledge for band structure of graphite and pave the way for the development of new electronic industries. Geim et al. first carried out transport experiments and reported that at room temperature graphene had a marvellous electron mobility of higher than 15,000 $cm^2 \cdot V^{-1} s^{-1}$ [3]. Charlier et al. performed symmetrical experiments to examine the conductance and their results indicated that holes and electrons had nearly the same mobilities [17].

Intrinsically graphene is a zero-gap semiconductor (Figure.2.7) [18]. Morozov et al. investigated electrons' mobility as a function of temperature and found the effect of temperature was negligible in the range from 10K to 100K [19, 20], which implies that defect scattering plays a vital role in electron mobility. By controlling the impurity scattering, mobilities higher than 200,000 $cm^2 \cdot V^{-1} s^{-1}$ can be obtained in suspended graphene [21]. Correspondingly, the resistivity of graphene is $10^{-6}\ \Omega \cdot cm$. Such a resistivity is lower than that of silver and graphene is considered the material with the lowest room temperature resistivity ever known so far.

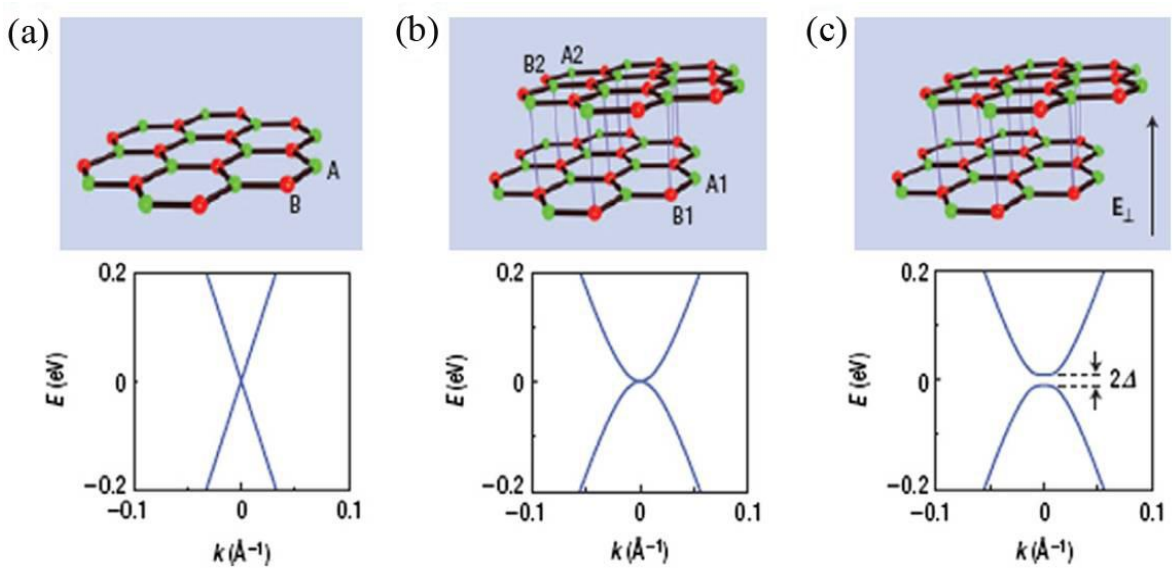

Figure 2.7. Schematic diagrams of band gaps in graphene. (a) and (b) indiate monolayer and bilayer graphene respectively. (c) indicates a band gap can be opened in bilayer graphene when an electric field is imposed perpendicular to the bilayer.

Mechanical and functional properties of graphene are summarized in Table 2.1 and compared with those of other materials [3, 22-31]. It can be seen that graphene is superior to many materials in various ways and is considered to have great potential to spark a revolution in a variety of industrial fields. It can be imagined that life will be changed due to the application of such a wonder material.

Table 2.1. Properties of different engineering fibres

Fibres	Density (g/cm^3)	Diameter or Thickness	Young's Modulus (GPa)	Tensile Strength (GPa)	Thermal Conductivity (W/mK)	Electrical Conductivity (S/m)
Graphene	1.3-2.1	0.33-100 nm	500-1000	130	4840-5300	10^{7}-10^{8}
CNT	1.3-2.1	0.01-0.04 µm	1300	20-63	1800-6000	10^{7}
Glass	2.56	11 µm	76	2	0.05-13	10^{-6}-10^{-12}
Boron	2.6	2.3-2.5 µm	400	4	38	10^{-4}-10^{-2}
Al_2O_3	3.4	3-20 µm	300	2	5	10^{-13}

2.3 Fabrication approaches of graphene and GPLs

Since graphene was produced, various approaches have been developed and tried to fabricate the monolayer or multilayer graphene in large quantities. These approaches include mechanical exfoliation, epitaxial growth and graphene oxide reduction. Each approach has its advantages and disadvantages. A suitable fabrication process of graphene can be adopted for specific applications.

2.3.1 Exfoliation and cleavage

Graphene sheets were first produced by Andre Geim and Konstantin Novoselov in 2004. They used scotch tape to separate layers of graphene from graphite (Figure 2.8). After repeating the process a dozen times, they obtained the monolayer graphene with the aid of a Raman spectrometer. Such an approach bears the advantage of simple operation but suffers from low production [18].

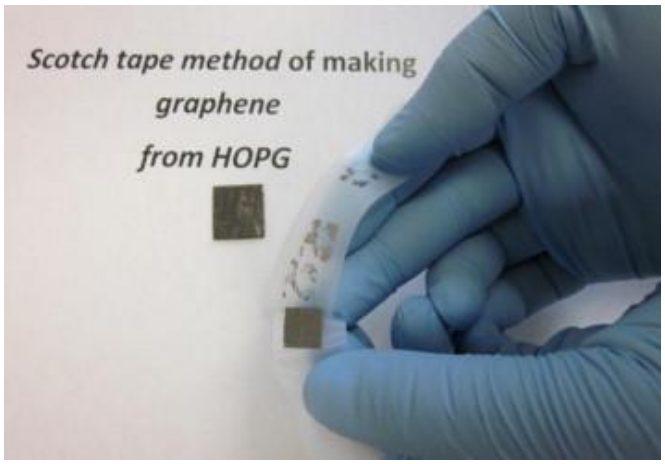

Figure 2.8. Mechanical exfoliation of graphene using scotch tape

2.3.2 Epitaxial growth on SiC substrates

Epitaxial growth attracts widespread attention for high quality and large graphene can be obtained through the process. Moreover, standard nanolithography can be used for patterning the epitaxial graphene, which puts the method in an advantageous position since it can be compatible with the current semiconductor technology. Using this method graphene is produced by controlling sublimation of the silicon from single crystalline SiC. The SiC is usually heated up to a high temperature (>1,100 ℃) under low pressures (~10^{-6} torr) and Si will then sublimate at high temperature. As a result, free carbon species tend to rearrange on the surface in a way to achieve minimum energy [32]. An example of morphology of the epitaxial graphene is shown in Figure 2.9 [33].

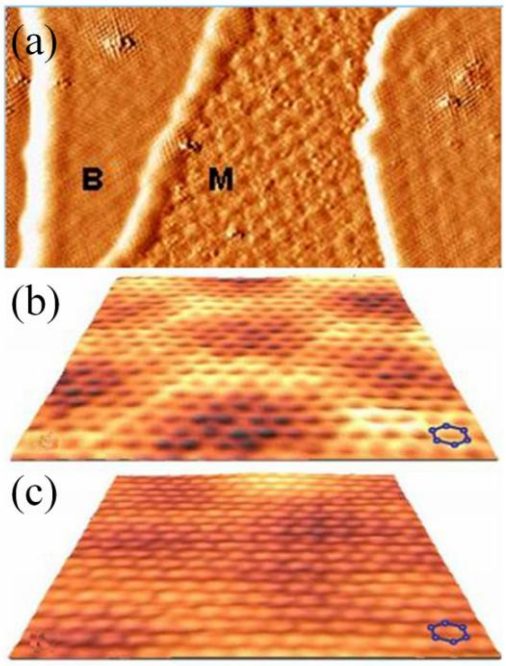

Figure 2.9. Scanning transmission electron microscope (STEM) images of graphene prepared by epitaxial growth. M and B indicate monolayer and bilayer graphene. (b) and (c) are the 3 dimensional view of monolayer and bilayer graphene respectively.

The epitaxial growth process can produce graphene with dimensions dependent upon the size of the SiC substrate. The thickness and electrical properties of the graphene are primarily affected by the face of the SiC. It has been proved that high quality graphene prepared by epitaxial growth has great potential in various applications such as a transistor, resonator and actuator [18]. However, the experimental process involves high temperature and ultra-high vacuum conditions, making this approach less desirable when energy efficiency and cost are considered. On the other hand, in most cases the graphene transfer process is required to realize the applications of electronics. The strong bonding in the interface between graphene and SiC make it difficult to transfer graphene from SiC to other substrates, restricting its further application [34].

2.3.3 Chemical Vapour Deposition (CVD)

CVD is a popular technique to grow large area graphene on such metal substrates as copper (Cu) and Ni. The general procedure of CVD is such that a carbon source, such as methane, is introduced in an environment where metal substrates, Cu or Ni as catalysts, are heated to a high temperature and the carbon source will be decomposed during the process. As indicated in Figure 2.10, different metal substrates cause different mechanisms for the formation of graphene [35]. When Ni substrate is used, the carbon will be absorbed by the metal and graphene is formed when precipitation of carbon take places, while for Cu substrate, formation of graphene can occur as a surface process. A high quality graphene can be obtained by controlling the cooling rate, carbon exposure time, flowing rate and carbon source [35].

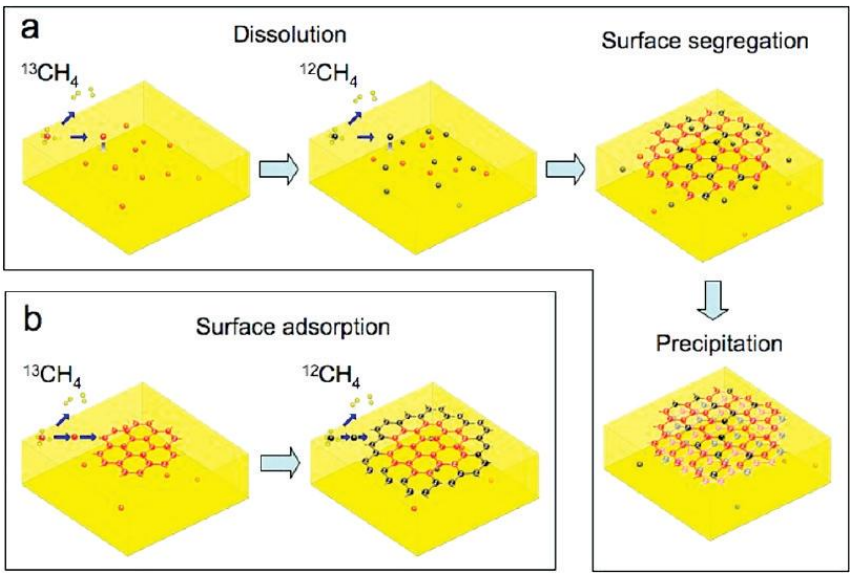

Figure 2.10. Schematic diagrams of mechanisms for formation of graphene on metal substrates by CVD. (a) and (b) indicate formation of graphene on Ni and Cu substrates respectively.

The main advantage of CVD is that large graphene can be produced at a relatively low cost and in a scalable way. For example, Bae et al. developed a roll-to-roll process to produce 30-inch graphene on ultra large Cu substrate [36]. Figure 2.11 shows the CVD preparation process for such large size graphene. It can be noticed that the fabrication process includes adhesion of polymer supports to the graphene, Cu etching and dry transfer-printing on target substrate. The obtained large graphene monolayer films have very low resistance and half integer quantum hall effect, suggesting great potential to replace commercial transparent electrodes such as indium tin oxides[18].

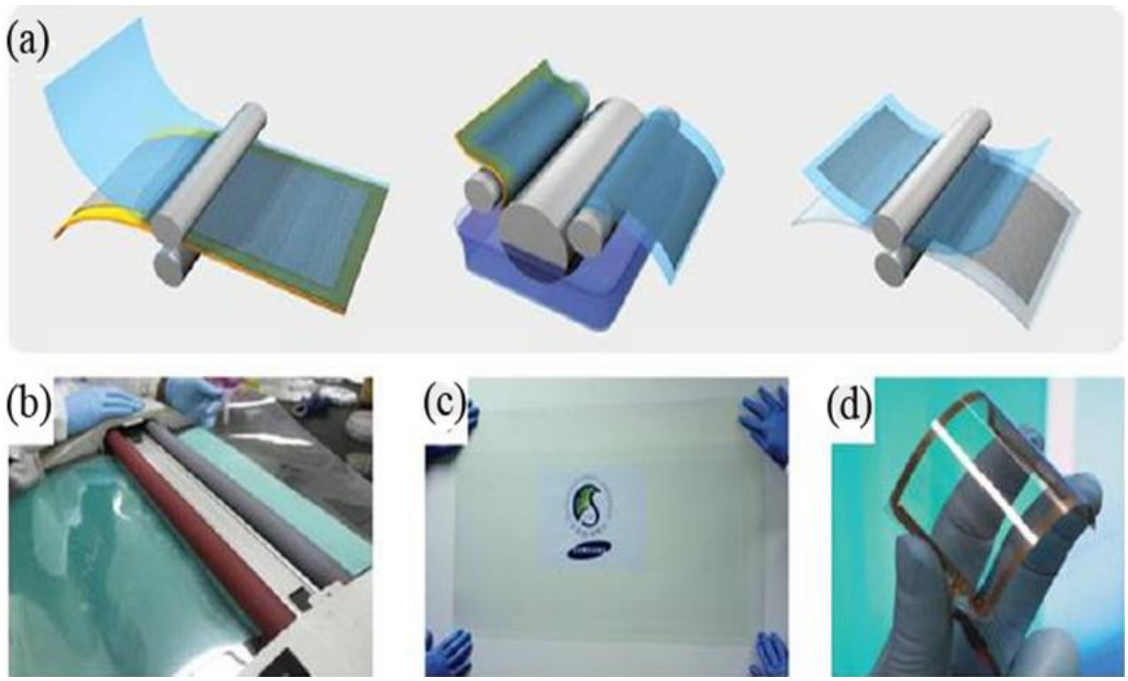

Figure 2.11. Schematic of fabrication of graphene devices through roll-to-roll process. (a) Production of graphene on Cu substrates. (b) Transfer of graphene films to polymer films. (c) A transparent large graphene film transferred on a target polymer film. (d) An assembled graphene/polymer touch panel.

2.3.4 Chemical conversion of graphite

At present, chemical conversion of graphite to graphene has become a feasible way to produce GPLs in large quantities [18]. A graphite oxide reduction method is one of the common ways to prepare graphene sheets. This method involves oxidation of graphite, exfoliation of graphite oxide and a reduction process to form the graphene sheets. The formation of graphite oxide is often obtained by modified Hummer's method [18, 37]. Graphite oxide exfoliation is achieved by rapid heating and an ultrasonication process. Reducing agents such as hydrazine and dimethylhydrazine are commonly used for the reduction process. However, the toxicity of these reducing agents have made this method undesirable and many other less toxic agents such as sodium borohydride and strong alkalis are proposed as replacements [18].

Another chemical way to produce the graphene sheets is through rapid thermal expansion and exfoliation of graphite. This method was developed by the Drzal group at Michigan State University [38]. In the preparation process, sulfuric acid is used to intercalate the graphite (Figure 2.12a). The graphite is first rapidly heated in a microwave environment, which causes the entrapped intercalants to vaporize and the graphite flake particles to undergo significant expansion. Strong ultrasonication is then employed to break down the expanded graphite. As a result, graphene sheets with thickness up to 10 nm are obtained (Figure 2.12b).

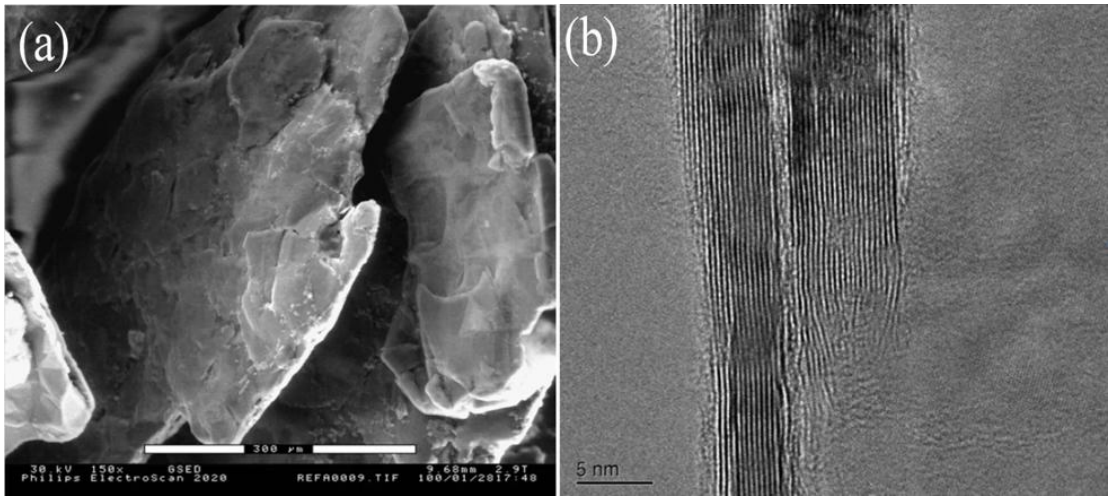

Figure 2.12. SEM and TEM images of acid intercalated graphite (a) and graphene sheets (b).

2.4 Toughening mechanisms in ceramics and ceramic composites

Structural ceramic materials have quite a few unique properties such as high melting points, high hardness, stable chemical inertness and good corrosion resistance. However, they suffer from low fracture toughness, which seriously limits their application. Various approaches have been proposed to overcome this problem. Among them there are three main toughening techniques which have proven very effective to increase ceramics' toughness. They are (i) particle dispersion toughening, (ii) multilayer toughening and (iii) phase transformation toughening [39-43].

2.4.1 Particle dispersion toughening

A particle toughening technique is a typical way to improve the toughness of ceramic matrix materials and it is based on the concept of mixing ceramic particles with a small portion of ductile nanoparticles. The ductile phase can contribute to the fracture toughness in two ways, as shown in Figure 2.13 [44]. In one way, it can act as bridging ligaments in the crack wake, which increases the extrinsic toughness (Figure 2.13a). In the other way, it can deflect the crack propagation direction, which forms a long and tortuous crack path, helping release the stress (Figure 2.13b).

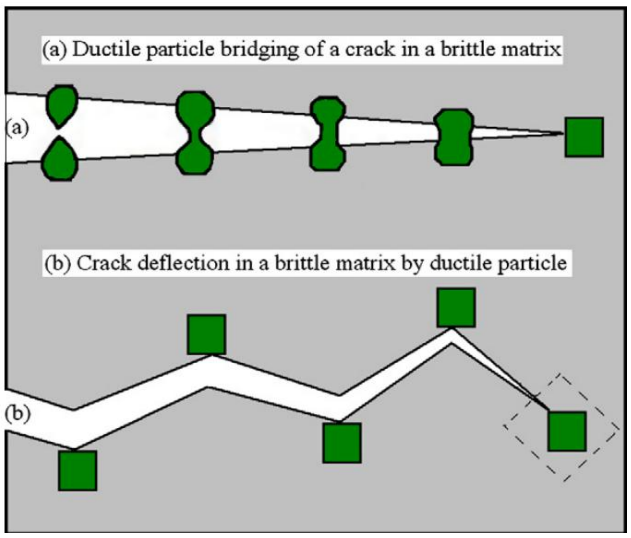

Figure 2.13. Schematic illustrations of particle toughening mechanisms in ceramic composites. (a) Particle bridging. (b) Crack deflection.

Ji et al. prepared 5 vol.% chromium(Cr)/Al_2O_3 nanocomposites through a hot pressing technique and found that grain size of the Al_2O_3 was significantly reduced from 3.6 to 0.68 μm by adding Cr, as indicated in Figure 2.14 [45]. Meanwhile, compared to a pure Al_2O_3 sample which had strength and fracture toughness of around 475 MPa and 3.6 MPa $m^{1/2}$, the

5 vol.% Cr/ Al_2O_3 nanocomposite sintered at 1450℃ had strength and fracture toughness of around 736 MPa and 4 MPa $m^{1/2}$ respectively. The substantial increase in strength was attributed to the refined microstructure resulting from the addition of Cr. However, crack bridging and crack deflection induced by Cr were not observed (Figure 2.15) and the fracture mode transformation from intergranular failure for pure Al_2O_3 to transgranular fracture for the nanocomposites was considered responsible for the slight increase in fracture toughness.

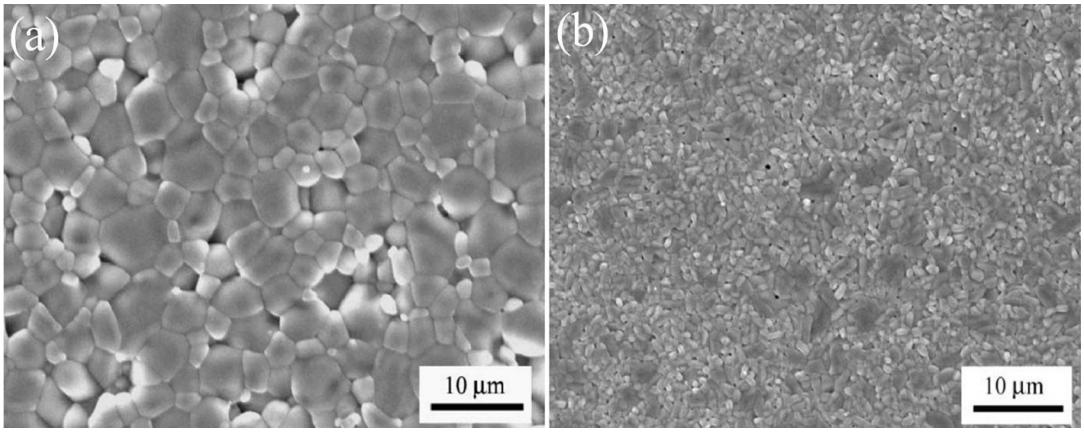

Figure 2.14. SEM images of thermally etched surfaces of pure Al_2O_3 (a) sintered at 1400 ˚C and Cr/ Al_2O_3 nanocomposite (b) sintered at 1450 ˚C.

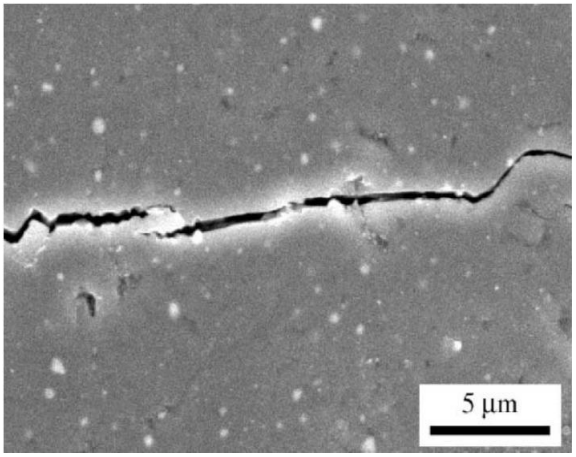

Figure 2.15. A SEM image of an indentation crack in the Cr/ Al_2O_3 nanocomposite

Chen et al. used the pressureless sintering method and fabricated Ni/Al_2O_3 nanocomposites [46]. Their results showed that microstructure of the Al_2O_3 was considerably refined with the addition of 5vol% Ni, as shown in Figure 2.16. The strength and toughness of Ni/Al_2O_3 are around 526Mpa and 4.2 $MPa{\cdot}m^{1/2}$, which were significantly higher than 390Mpa and 3.6 $MPa{\cdot}m^{1/2}$ for the monolithic Al_2O_3. Similarly, the refinement in the Al_2O_3 microstructure by the Ni particles is the reason for the enhancement of the strength. Nevertheless, unlike nano sized Cr (75 nm) which is too small to bridge the crack, Ni nanoparticles (118nm) can play the bridging role on the crack path (Figure 2.17).

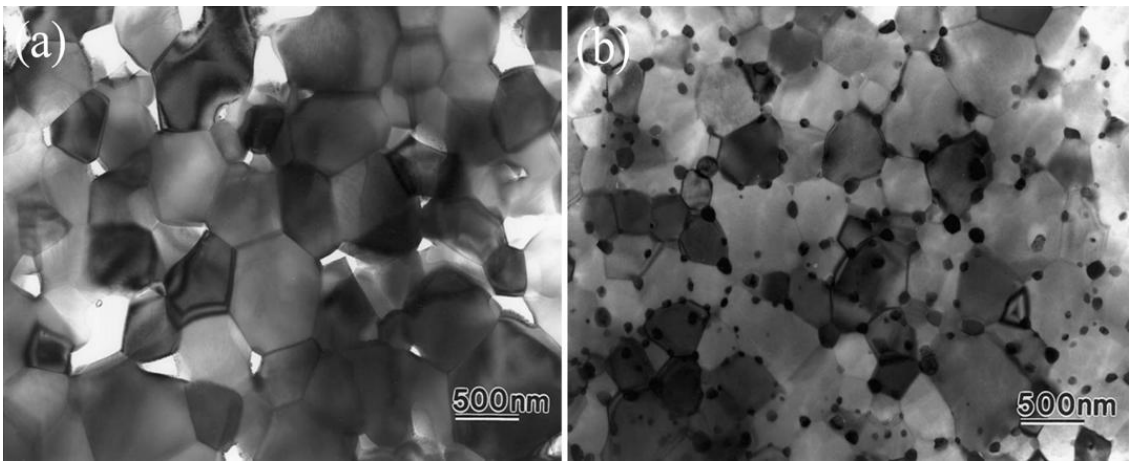

Figure 2.16. TEM images of sintered Al_2O_3 (a) and Ni/Al_2O_3 nanocomposite (b).

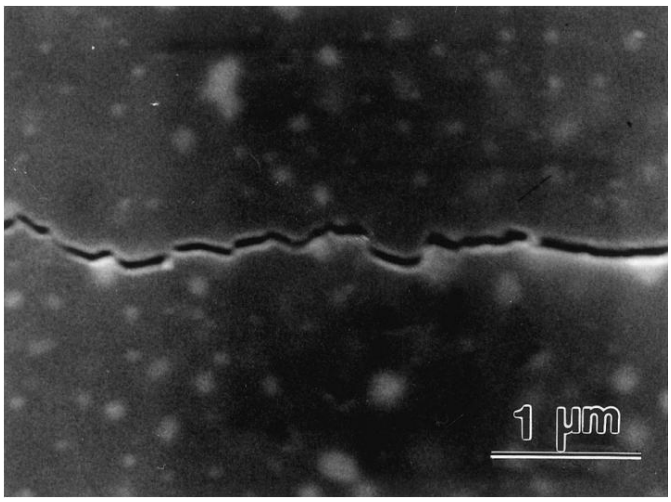

Figure 2.17. A SEM image of an indentation crack in the sintered Ni/Al_2O_3 nanocomposites.

The ductile metal nanoparticles are very effective in toughening ceramics. However, the introduction of metal particles usually causes a dramatic decrease in hardness. In order to produce strong, tough and hard ceramic materials, ceramic nanoparticles are employed as nano fillers to fabricate ceramic composites. Chae et al. ball milled SiC nanoparticles with Al_2O_3 powders and fabricated SiC/Al_2O_3 composites using SPS technique [47]. The 20% SiC/Al_2O_3 was reported to have fracture toughness of 3.62 MPa·$m^{1/2}$ and flexural strength of 812Mpa which were higher than 2.95 MPa·$m^{1/2}$ and flexural strength of 663Mpa for the pure monolithic Al_2O_3. The increase in fracture toughness was attributed to the change of fracture mode (Figure 2.18), particle bridging and stress-induced micro cracking (Figure 2.19).

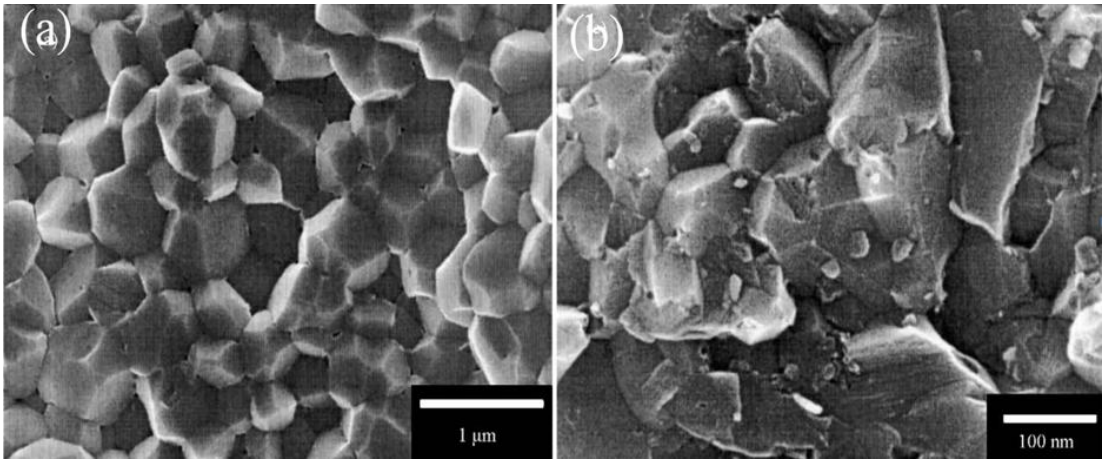

Figure 2.18. SEM images of the fractured surface of pure Al_2O_3 (a) and 20%SiC/Al_2O_3 nanocomposite (b) sintered at 1200 and 1400˚C respectively.

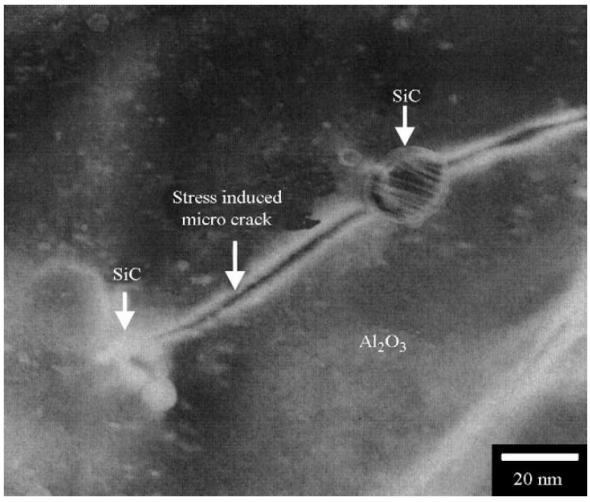

Figure 2.19. A TEM image of crack shielding and stress-induced micro cracking around a secondary particle in the SiC/Al_2O_3 nanocomposite.

There are three popular models proposed to explain the strengthening and toughening mechanisms of the nanocomposites reinforced by nanoparticles. They are grain boundary strengthening mechanism, c-mechanism where the critical flaw size is reduced and K-mechanism where the fracture toughness is increased [48].

Ohji et al. proposed a particle-bridge mechanism, where nano particles play a bridging role resulting in the increase in fracture toughness [49]. It is suggested that toughening mechanisms such as crack deflection and crack bowing are correlated with the differences of the thermo elastic properties between ceramic matrix and nano particles. In addition, no appreciable toughening effects are observed when large dispersed particles are used. Levin et al. used the Selsing equation to describe the residual stresses around the nanoparticles and explain the reinforcing mechanisms for the nanocomposites [50, 51]. They found that nano-sized particles could simultaneously result in the improvement in strength as well as the fracture toughness and the transformation of fracture mode was due to the ceramic matrix weakening and grain boundary strengthening. Levin et al. presented a model to explain the strengthening and toughening mechanism of SiC/Al_2O_3 nanocomposites [50]. It was implied that grain boundaries were strengthened because of compressive radial stress while tensile stress contributed to improvement in strength and fracture toughness. The proposed three models can account for the reinforcing mechanisms in ceramic nanocomposite materials. However none of them can explain all of the characteristics in the nanocomposites [48].

Due to the different thermal expansion coefficient between the matrix and the dispersed nanoparticles, highly localized residual stresses are likely to be generated around the particles. To shed light on the role of residual stress, Awaji et al. employed a simple model that was composed of a spherical particle in a concentric matrix sphere (Figure 2.20) to analyze the residual stress [48, 52]. It can be seen that the residual stress reduces dramatically with the distance from the boundary.

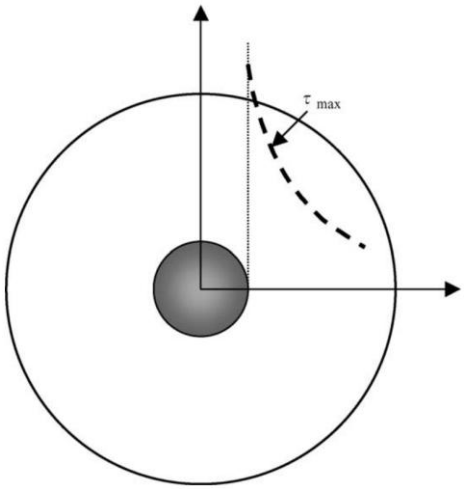

Figure 2.20. A model of intra-type nanostructure. Tmax is the maximum shear stress.

Lagerlof et al. investigated the correlations between temperature and slips in a single Al_2O_3 and the following relationships were concluded [53]:

$$Ln\,\tau_{cb} = Ln\tau_0 - 0.0052T \qquad (2\text{-}1)$$

$$Ln\,\tau_{cp} = Ln\tau_0 - 0.0026T \qquad (2\text{-}2)$$

Where τ_{cb} and τ_{cp} represent the critical resolved shear stresses for basal and prism slip planes. T is temperature and τ_0 equals 109 and 9 GPa for basal and prism plane slips. It is suggested that residual stresses around nanoparticles can merely generate such small defects as dislocations in vicinal areas around the nanoparticles (Figure 2.21a). However, dislocation movements could occur at high a temperature, which implies that an annealing process can help redistribute the dislocations within the matrix grains (Figure 2.21b).

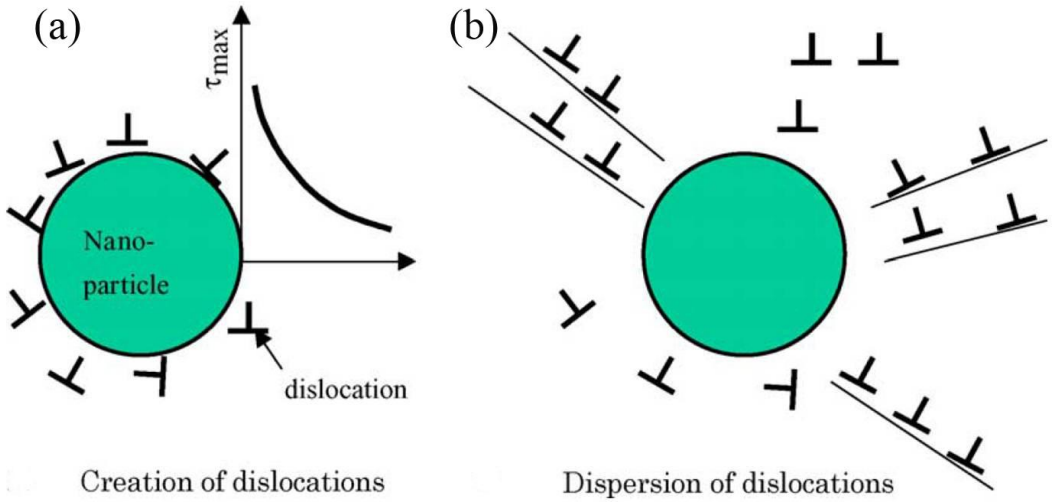

Figure 2.21. Dislocations after sintering (a) and after annealing (b).

Crack extension resistance in polycrystalline ceramics with R-curve behaviour is expressed as the following equation [48]:

$$K_R(\Delta a) = K_i + \Delta K_R(\Delta a) \qquad (2\text{-}3)$$

where $K_R(\Delta a)$ represents the fracture toughness of the material exhibiting R-curve behaviour, K_i is the intrinsic fracture toughness and $\Delta K_R(\Delta a)$ is the extrinsic increase in the fracture toughness after a certain extension from the initial crack tip, Δa. A schematic illustration expressing the toughening mechanisms in nanocomposites is shown in Figure 2.22. K_i indicates the energy required to create the damaged frontal process zone (FPZ), which means in order to improve the intrinsic fracture toughness, fracture energy needs to be increased.

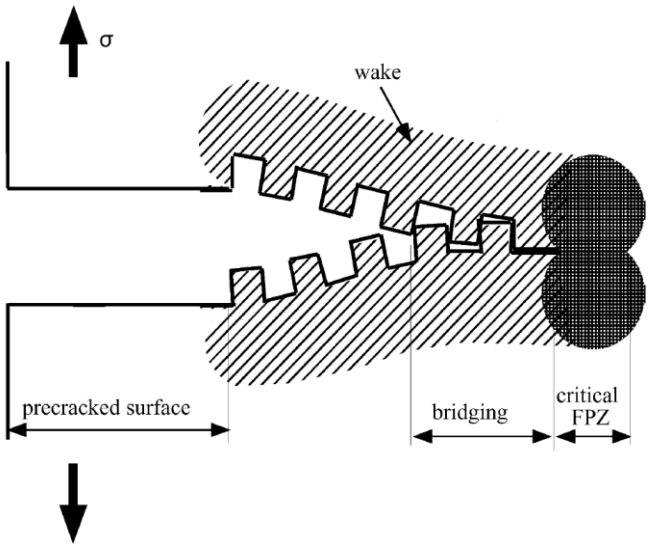

Figure 2.22. A schematic illustration of FPZ and bridging in ceramics with R-curve behaviour.

Meanwhile, ΔK_R suggests fracture toughness can also be increased by a crack bridging toughening mechanism in a process zone wake [52]. Figure 2.23 shows schematic illustrations of a particle dispersion toughening mechanism in SiC/Al_2O_3 nanocomposite materials [48]. Subgrain boundaries and dislocation networks are generated in areas around SiC nano particles and dislocations are dispersed in the matrix (Figure 2.23a). It is expected that when the tip of the crack propagates and meets the dislocations (Figure 2.23b), nucleation of nano cracks is likely to occur, which releases the stress in the FPZ and enhances the intrinsic fracture toughness.

Due to the anisotropic thermal expansion, different elastic modulus along the crystal axes and crystallographic misorientation across the grain boundaries, there will be residual tensile stresses remaining in the matrix grains and grain boundaries of the sintered alumina. Therefore, it is conceivable that cracks are created by the effects of both residual tensile stress

and processing defects and the length of the crack is equivalent to the grain size of the materials. It is well known that the strength of the materials is dominated by the weakest cracks generated along the grain boundaries and the smaller defect size results in higher strength of the materials. The dislocations generated within the matrix are therefore expected to release the residual stresses and reduce the defect size along the grain boundaries resulting in improved strength of nanocomposites.

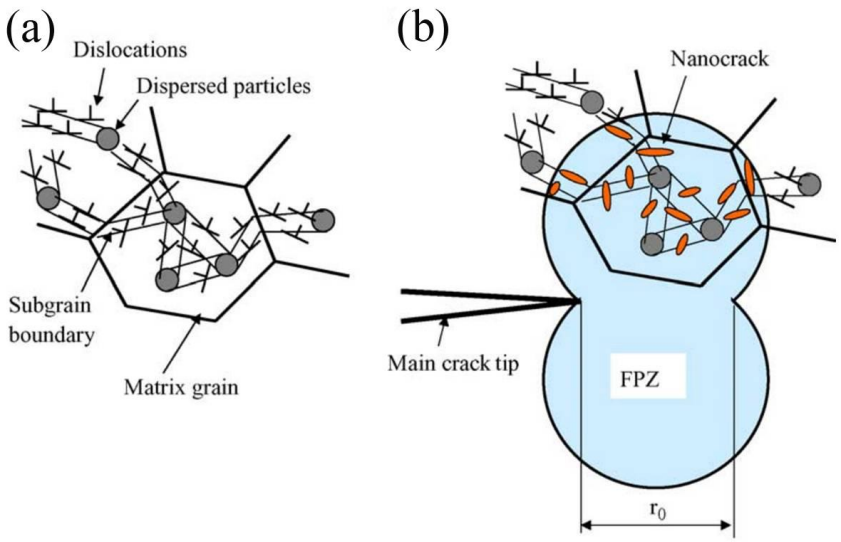

Figure 2.23. Schematic illustrations of the toughening mechanism in nanocomposites. (a) Nanostructure of the ceramic composites after annealing. (b) Creation of FPZ.

2.4.2 Phase transformation toughening

Phase transformation toughening was first discovered by Garvie et al and opened a new research area for the scientific and engineering communities [43]. Particularly in the case of ZrO_2 ceramics, toughness can be considerably improved by carefully controlling the

metastable phase in microstructures. Pure ZrO_2 exhibits the following phase transitions with the temperature (Figure 2.24) [54]. Usually under the influence of the external stress causing

$$m\text{-}ZrO_2 \underset{950\ ^\circ C}{\overset{1170\ ^\circ C}{\rightleftharpoons}} t\text{-}ZrO_2 \overset{2370\ ^\circ C}{\rightleftharpoons} c\text{-}ZrO_2 \overset{2680\ ^\circ C}{\rightleftharpoons} liquid$$

Figure 2.24. Phase transformation of ZrO_2 with temperature

the propagation of the cracks, ZrO_2 can undergo phase transformation from metastable tetragonal to stable monoclinic structure, which is accompanied by volume expansion and a shear strain [24, 55, 56]. The stress generated during phase transformation causes the disintegration of the ZrO_2 ceramics at room temperature. Dopants are therefore usually added to stabilize the tetragonal or cubic phase in sintered specimens [57]. Transformation toughening can take place when t-ZrO_2 transforms to m-ZrO_2 in close vicinity to a propagating crack where a tensile stress field is generated [40]. The phase transformation can introduce a net compressive stress in the process zone around the propagating crack tip (Figure 2.25) [58]. This can in part offset the external stress, hindering the progress of the cracks and increasing the toughness.

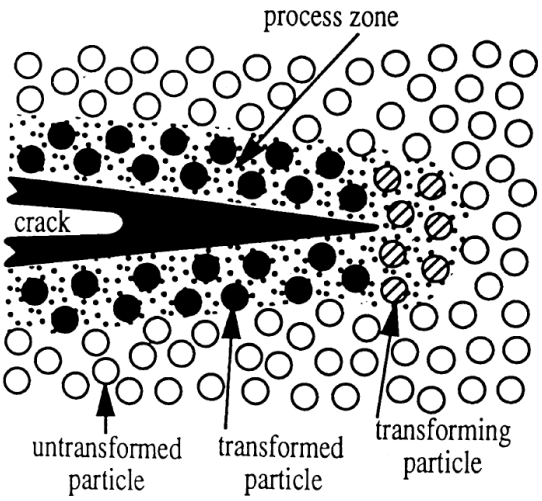

Figure 2.25. A schematic illustration of stress-induced transformation toughening

During the last two decades, with various techniques such as SEM, XRD, neutron powder diffraction and AFM a great effort was made to get a deep understanding of martensitic transformation [59-66]. In particular, attention was given to ZrO_2 composites to investigate the effects of phase transformation on the fracture toughness of the composites. Dongxu et al. evaluated mechanical reliability of the ZTA composites for dental applications and found that the mechanical properties of ZTA increased with the content of the 3Y-TZP [67]. In addition, ZTA composites with the addition of 30vol% 3Y-TZP exhibited around 80% increase in fracture toughness and 100% increase in flexural strength respectively, in comparison with the pure Al_2O_3. Significant grain refinement was observed in nanocomposites by adding ZrO_2 in Al_2O_3, as shown in Figure 2.26. Transformation toughening, micro cracking and crack deflection were considered the toughening mechanisms for the enhancement in fracture toughness while the causes of the improved strength were thought to be the grain refinement and transformation toughening.

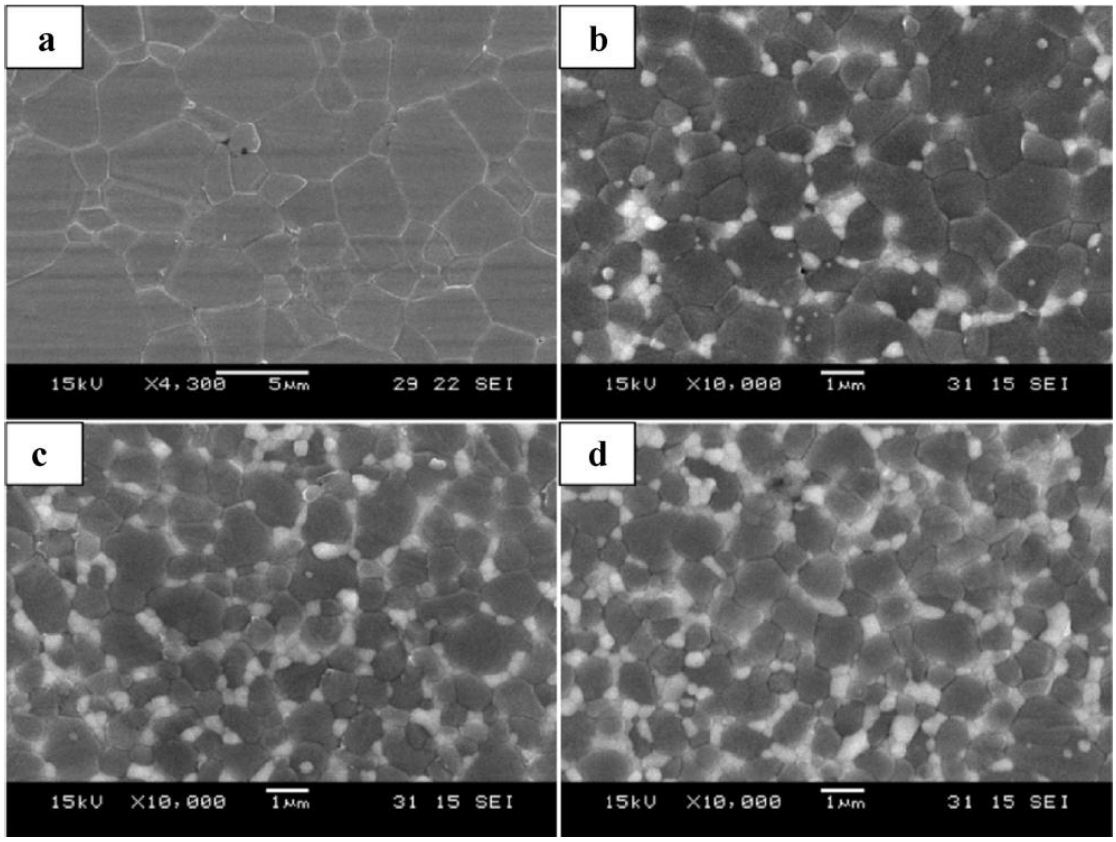

Figure 2.26. SEM images of ZTA composites sintered at 1600 ˚C for 2 hours. (a) Al_2O_3, (b) Al_2O_3+10% ZrO_2, (c) Al_2O_3+20% ZrO_2 and (d) Al_2O_3+30% ZrO_2.

X.W. Huang et al. used a liquid sintering method and fabricated ZTA composites [68]. It was found that mechanical properties of the ZTA were increased with the addition of ZrO_2 and when 50 vol% ZrO_2 was added, almost 169% and 34% increase in strength and toughness were obtained for ZTA respectively. The dramatic increase in strength was attributed to the significant grain refinement while the phase transformation toughening was considered the main toughening mechanism. Alfredo et al. used a conventional sintering method and fabricated Al_2O_3/ZrO_2 nanocomposites with the addition of 2.5wt% Al_2O_3 whiskers[69]. The results showed that fracture toughness of the nanocomposites was increased 62% over the pure Al_2O_3 and the crack defection toughening mechanism was more efficient in the ceramic samples with the Al_2O_3 whiskers than in pure Al_2O_3. In particular, phase transformation

toughening from Al_2O_3 whiskers made an important contribution to the fracture toughness improvement. Ma et al. prepared the ZTA composites and investigated the effect of the content of ZrO_2 on the densification, microstructure and transformation behaviour of the composites [70]. It was reported that when the ZTA composites had 20% ZrO_2, micro crack was the main toughening mechanism whereas when the 15% ZrO_2 was added, a stress-induced phase transformation toughening mechanism was predominant. Bikramjit et al. fabricated ZrO_2- Al_2O_3 composites using the hot pressing technique and studied how to tailor the toughness of the composites by tuning the ZrO_2 matrix composition [71]. The results indicated that the fracture toughness of ZrO_2-Al_2O_3 composites could be tailored from 5 to 10 $MPa{\cdot}m^{1/2}$ by adjusting the yttria (Y_2O_3) content in ZrO_2 and the addition of Al_2O_3 resulted in tensile residual stress in the ZrO_2 matrix, improving the fracture toughness by enhancing the phase transformation of ZrO_2. It should be noted that to enable the transformation from tetragonal to monilic phase under certain stress, there is a critical size for ZrO_2 particles. A number of studies were carried out to determine the critical size [72-74]. It is suggested that the critical size is in the range from 4.5~8 μm. Outside this range, no appreciable phase transformation toughening mechanism would be observed in composites containing ZrO_2 particles.*

2.4.3 Multilayer toughening

In 1990, when Clegg et al. reported a simple way to make tough ceramics, people have been inspired to prepare ceramics with laminated structures [75]. Primarily there are two laminate designs for improving the mechanical properties of ceramics. On one hand, laminated structures designed with weak interfaces can produce enhanced fracture energy by interface

delamination [76-83]. The fracture of the first layer is usually followed by crack propagation along the weak interface, preventing the ceramics from catastrophic failure. A typical example was made by Clegg [84]. He fabricated SiC multilayer ceramics with graphite interlayers. The load-deflection curve of the materials is shown in Figure 2.27. It was found that the failure of one layer of SiC did not suggest the complete failure of the materials. Compared to the pure SiC monolithic sample which had an apparent fracture toughness of 3.6 $MPa \cdot m^{1/2}$, multilayer ceramics presented a remarkably high fracture toughness of 17.7 $MPa \cdot m^{1/2}$ and an almost 390% increase had been achieved. The dramatic increase in toughness was associated with the long crack wake formed during the bending test (Figure 2.28), which dissipates quite an amount of energy.

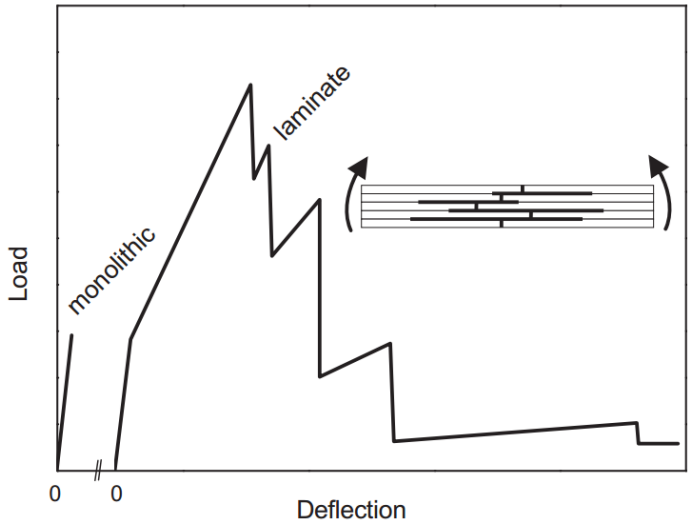

Figure 2.27. Typical load deflection diagram of a layered structure with weak interfaces. The steps show the failure of individual layers and the crack propagation along the interface. A schematic side view of a broken specimen showing crack deflection into the weak layers is shown in the inset. The failure of a monolithic is also shown for comparison.

On the other hand, a laminated structure with strong interface can exhibit crack growth resistance (R-curve) behaviour by carefully controlling the microstructure. Such a toughening mechanism is associated with residual stress in the layers. Orlovskaya et al. made an attempt and fabricated the silicon nitride (Si_3N_4) based laminates using a rolling and hot pressing technique [85]. The results showed that the apparent fracture toughness of Si_3N_4/ Si_3N_4 could be improved by introducing TiN particles and a maximum fracture toughness of 8.5 $MPa \cdot m^{1/2}$ was obtained for Si_3N_4/Si_3N_4-20wt%TiN, almost 50% higher than that for Si_3N_4/Si_3N_4. Meanwhile, it was implied that compressive stress in the layers resulted in the deflection and bifurcation of the crack, which considerably enhanced the fracture toughness (Figure 2.29a and b) while tensile stresses caused the formation of fracture steps leading to the decrease in mechanical properties (Figure 2.29c and d).

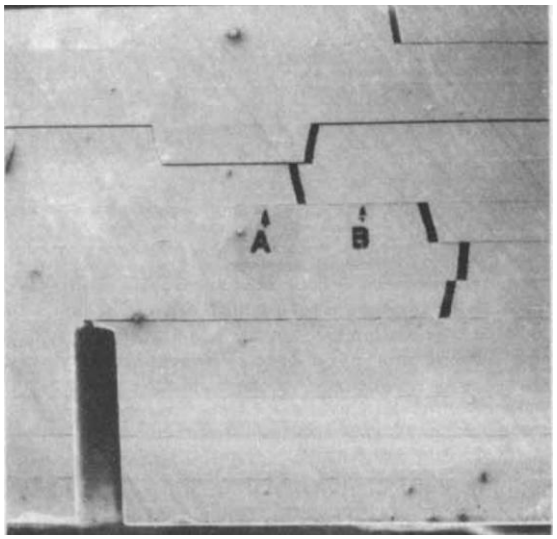

Figure 2.28. An optical image showing the path of a crack across a laminated sample containing a notch.

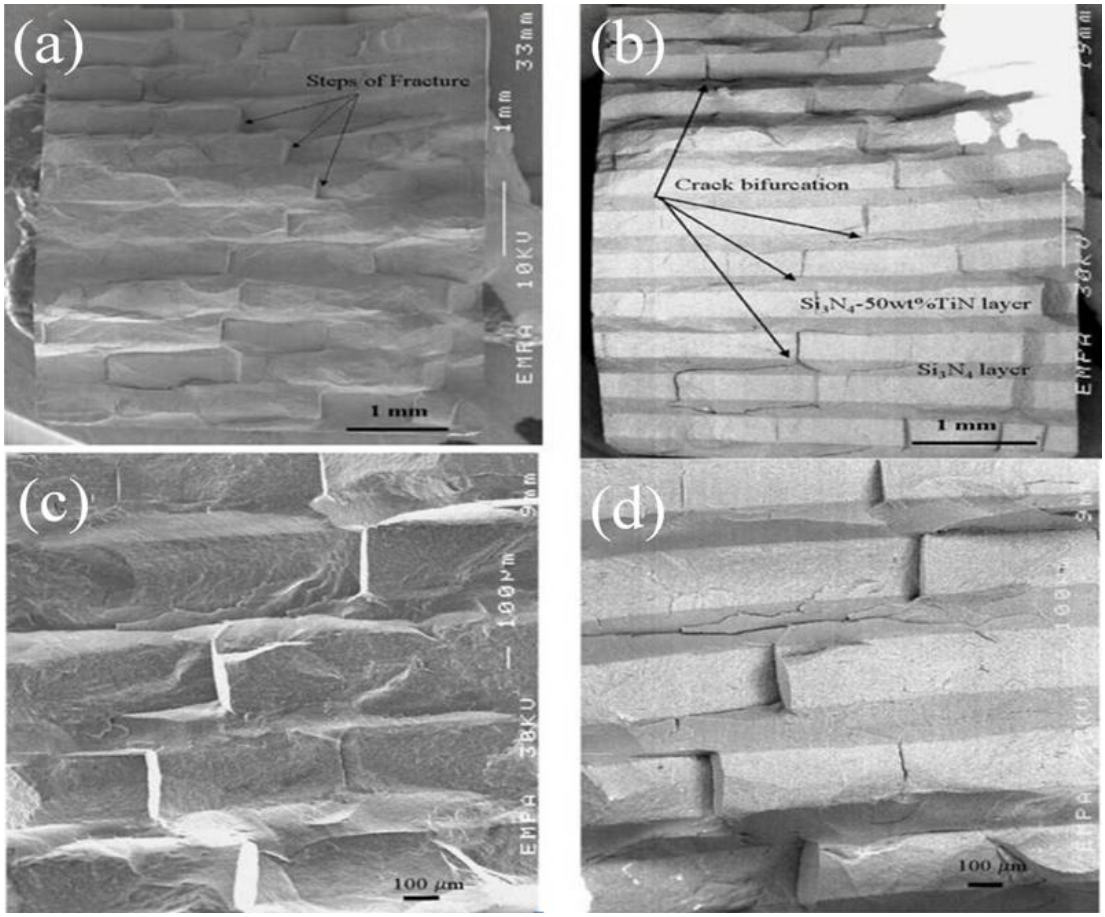

Figure 2.29. Fracture surface of Si_3N_4/ Si_3N_4-50% wt.%TiN composite. (a) and (c) are SEM images. (b) and (d) are backscattered images.

Xinghong et al. employed tape casting and hot pressing techniques to fabricate laminated ZrB_2-SiC ceramics [86]. It was found that the maximum apparent fracture toughness of the laminated ZrB_2-SiC ceramics was 10.4 $MPa \cdot m^{1/2}$, which was much higher than that of monolithic ZrB_2-SiC ceramics. Crack deflection was observed in the laminated ceramics (Figure 2.30). The crack would propagate through the tensile layers when the crack tips were in the tensile layers (Figure 2.30 b) while crack deflection would take place when the crack tips were in the compressive layers (Figure 2.30c). This suggested that residual compressive stresses could enhance the crack growth resistance and make the contribution to the fracture toughness. Similar results on laminated ZrB_2–SiC ceramics were reported by Peng et al. [87]. Flexural strength and fracture toughness of around 960 MPa and 8.8 $MPa \cdot m^{1/2}$ were obtained

for the laminated ceramics and were significantly higher than 517 Mpa and 5.6 MPa·$m^{1/2}$ for the monolithic ZrB_2–SiC.

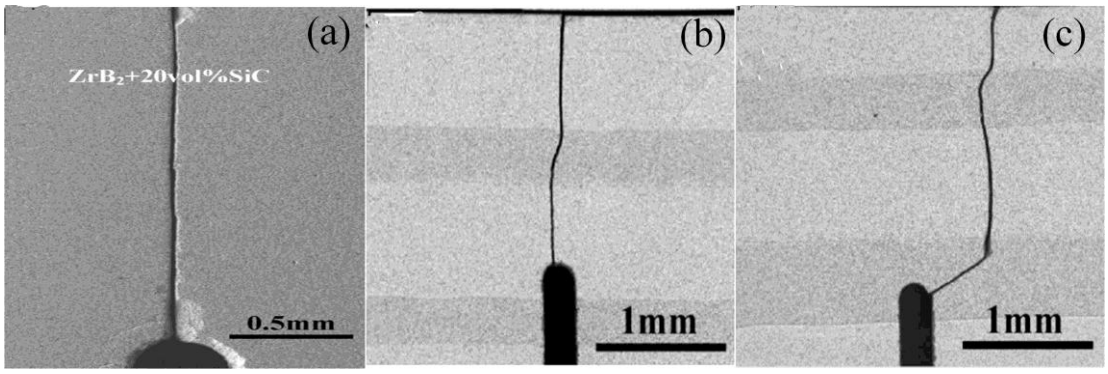

Figure 2.30. SEM images of the monolithic (a) and laminated (b and c) ceramic specimens after bending tests.

2.4.4 Fibre toughening

Over the last two decades, numerous reports have shown that fracture toughness of ceramics can be remarkably improved with the incorporation of fibres. When a macroscopic crack propagates and meets the fibres in a ceramic matrix, crack propagation would be arrested due to the bridging and pull-out toughening mechanisms in the crack wake. Guiming et al. used a hot pressing technique and fabricated short carbon fibre reinforced TiC composites [88]. It was found that short fibres were well dispersed in the TiC matrix (Figure 2.31) and the mechanical properties of the TiC ceramic matrix were significantly improved by adding carbon fibres. An almost 70% increase in fracture toughness, 25 % in flexural strength and 100% in high temperature strength were achieved for the composites. Three toughening mechanisms of crack bridging, fibre pullout and crack deflection were responsible for the dramatic increase in fracture toughness. Schematic illustrations of the toughening mechanisms are shown in Figure 2.32.

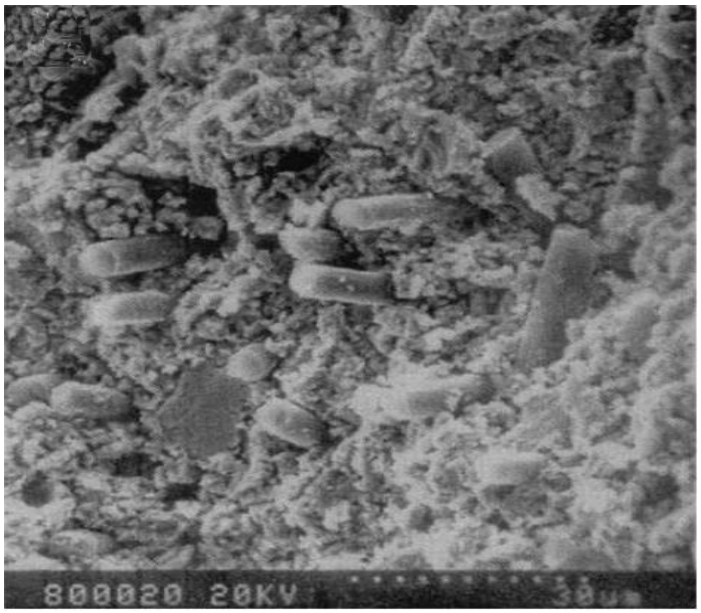

Figure 2.31. A SEM image of fracture surface of the carbon fibre reinforced TiC composites.

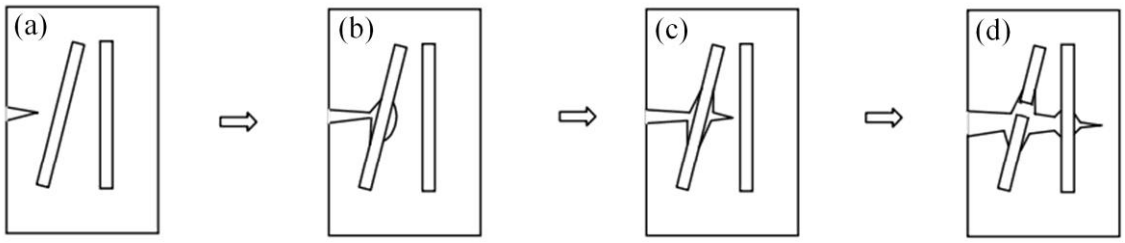

Figure 2.32. Fracture behaviour of carbon fibre/Ti ceramic composites. (a) A crack initiates in the ceramic matrx, (b) A crack meets with a fibre and debonding occurs between matrix and fibre, (c) Crack bridging and (d) Pullout and bridging of the fibres.

Junlei et al. studied the mechanical properties of short carbon fibre reinforced carbon/TiB_2 (C_{sf}/C/TiB_2) composites [89]. The results showed that a fracture toughness of 3.61 MPa·$m^{1/2}$ was obtained for C_{sf}/C/TiB_2 and was 40% higher than that of C/TiB_2 composites. Sciti et al. prepared the SiC fibres with ZrB_2 powders and sintered the powder mixtures [90]. It was reported that the addition of SiC fibres could allow fracture toughness to be increased from 3-

4 $MPa \cdot m^{1/2}$ for pure SiC ceramic to 5-6.2 $MPa \cdot m^{1/2}$. In addition, the oxidation stability of fibre reinforced composites was comparable to that of SiC particles at very high temperature. Ostertag produced Al_2O_3 matrix composites reinforced with SiC fibres using the pressure slip casting method and 30% higher toughness of Al_2O_3 matrix was obtained [91]. Hansson et al. sintered the SiC whisker reinforced Al_2O_3 composites and found a 100% increase in fracture toughness of the composites over the pure alumina samples [92].

2.4.5 Toughening in CNT/ceramic composites

Since the report on CNTs made by Iijima, CNT has drawn tremendous attention due to its excellent mechanical and electrical properties and a great effort has been put into fabricating CNT-reinforced ceramics with desired properties. A number of studies were reported. Yamamoto et al. used a precursor method and a spark plasma sintering technique to fabricate the CNT/Al_2O_3 composites [93]. It was reported that highly homogeneous CNTs were achieved in the Al_2O_3 matrix (Figure 2.33a) and a 25% increase in fracture toughness as well as a 27% increase in flexural strength were achieved for the composites. Toughening mechanisms such as pullout and crack bridging were observed and considered for the improvements in mechanical properties (Figure 2.33).

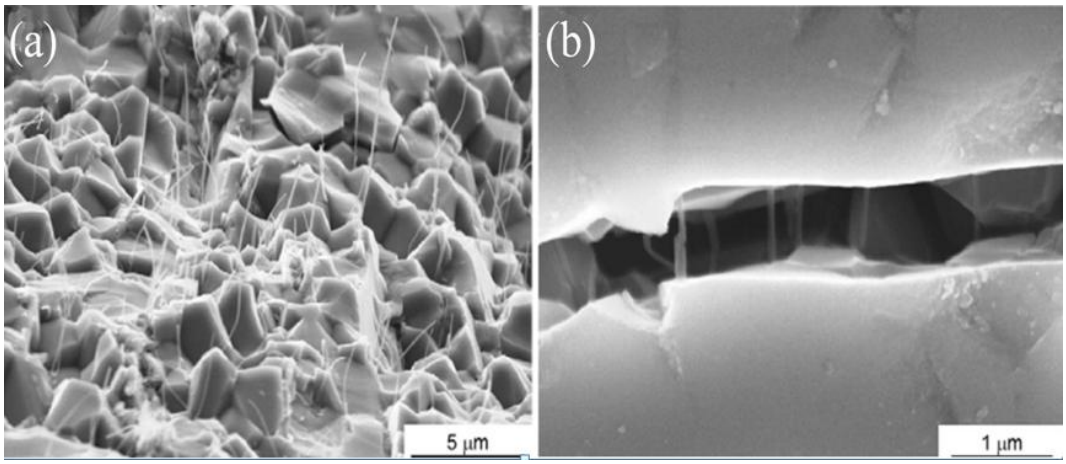

Figure 2.33. SEM images of fracture surfaces of the CNT/Al_2O_3 composites.

Ahmad et al. used a hot pressing technique to fabricate the CNT-reinforced Al_2O_3 composites and investigated the mechanical properties of the composites [94]. The results showed fracture toughness, hardness and flexural strength of the nanocomposites were increased by 94%, 13% and 6.4% respectively. It was suggested that toughening mechanism were affected by homogenous dispersion of the CNTs within the matrix and adequate densification would reduce the grain size of the ceramic matrix (Figure 2.34), causing formation of appropriate

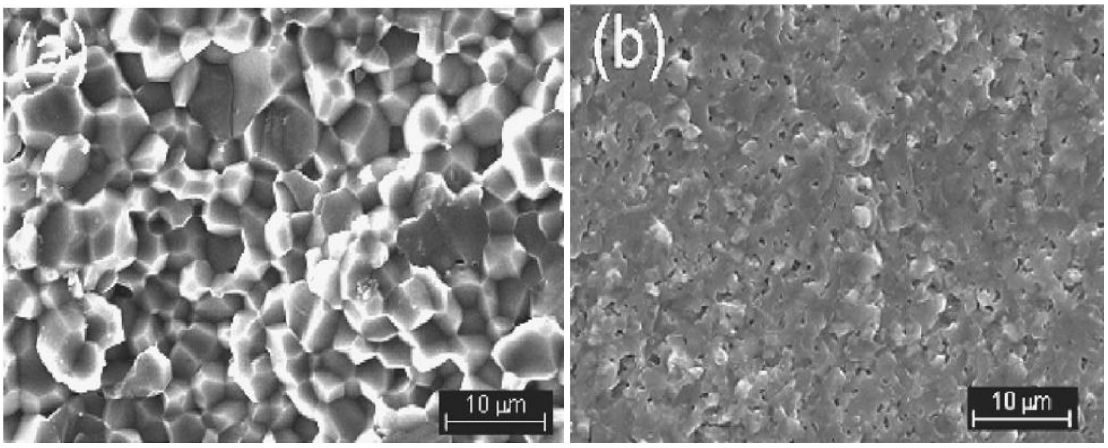

Figure 2.34. SEM images of fracture surfaces for monolithic Al_2O_3 (a) Al_2O_3–4vol% CNT nanocomposites (b).

CNT/matrix interfacial bonding. Bocanegra-Bernal et al. studied the effects of CNTs on the properties of ZTA composites and reported a 44% increase in fracture toughness over the pure ZTA [95]. Shi C et al. produced CNT/Al_2O_3 composites using a pressureless sintering method in a reducing atmosphere and an approximate 35% increase in fracture toughness was achieved for the composites [96].

2.4.6 Controversial fracture toughness evaluated using the indentation technique.

Although numerous reports have shown CNT can contribute to the improvement in fracture toughness, the effectiveness of CNTs on the mechanical proprieties of the ceramic composite materials is still a controversial topic. The argument started when Zhan et al. reported a dramatic increase of the indentation fracture toughness (from 3.3 to 9.7 $MPa \cdot m^{1/2}$) in CNT/ Al_2O_3 composites [97]. When Wang et al. used the SEVNB method to examine the fracture toughness of the same composites and reported a negligible increase in the fracture toughness [98], the reliability of the fracture toughness of CNT-reinforced ceramic composites using the indentation technique became controversial. It was found CNT/Al_2O_3 and graphite/Al_2O_3 composites were highly resistant to contact damage and no crack would likely be formed during the indentation test, as shown in Figure 2.35. Due to this fact, it is suggested that when it comes to the evaluation technique for the fracture toughness of the ceramic composites, techniques such as SEVNB or SENB are more preferable than the indentation technique [99]. However, many research communities still use this method to measure the toughness of the ceramics [100-104]. This may be because of a lack of a fast and effective alternative. The results obtained by the indentation method can only be used for comparison purposes and should not be used to determine the true fracture toughness as it would overestimate the value.

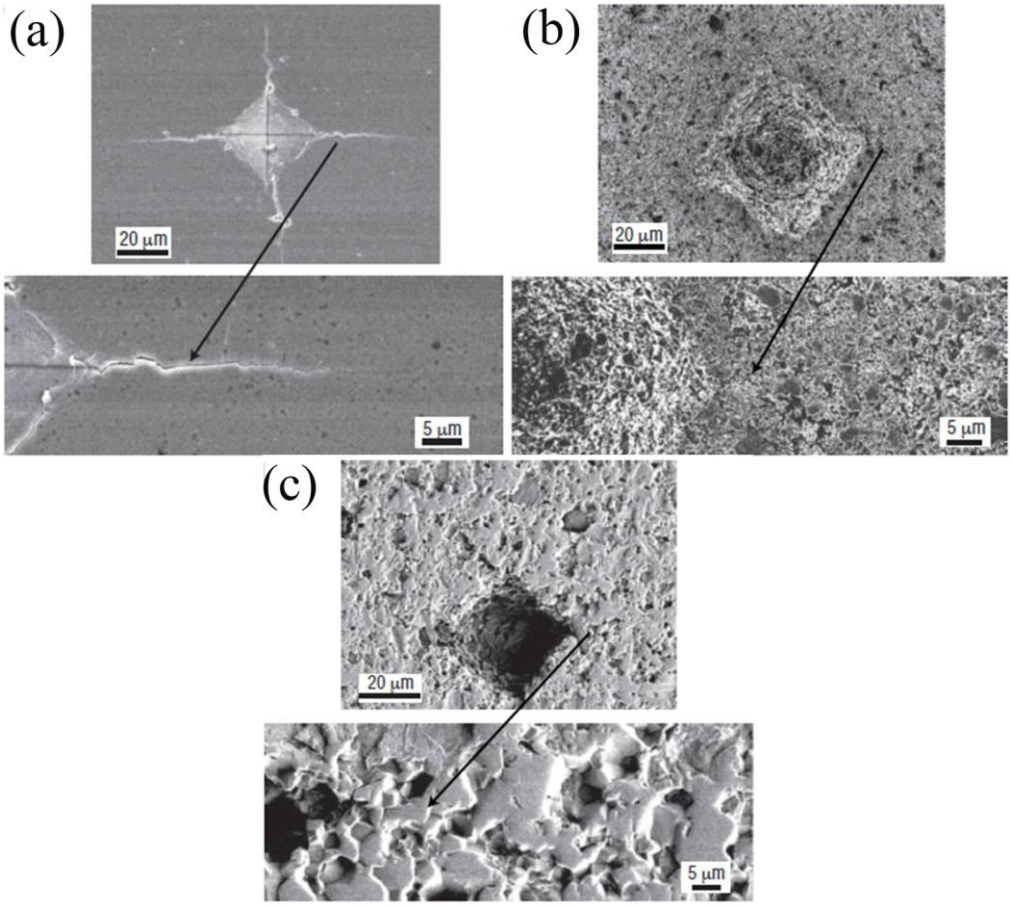

Figure 2.35. SEM images of the Vicker indentation sites. (a) dense Al_2O_3, showing radial cracks. (b) and (c) are CNT/Al_2O_3 and graphite/Al_2O_3 composites, showing no evidence of radial cracks.

2.4.7 Toughening in graphene/ceramic composites

Graphene has inspired the research community to make use of its excellent mechanical and electrical properties in a range of potential applications. In particular, it opens up opportunities for the improvements in strength and toughness of ceramic structural materials. When it comes to research of ceramic composites, multilayer graphene rather than monolayer graphene is often chosen as the reinforcement. This may be due to the fact that multilayer graphene is easier to mass produce using chemical methods. Multilayer graphene is usually

referred to in the literature as GPLs, graphene nanosheets (GNS), or graphene nanoplatelets (GNPs), which are formed by several layers of graphene with a thickness of up to approximately100 nm [4].

The first report using GPLs as reinforcing additives in Si_3N_4 matrix came from Luke et al. who investigated the effects of GPLs on the mechanical properties of the sintered Si_3N_4 matrix [104]. Their results showed that homogenous dispersion of GPLs within the ceramic matrix was obtained using an aqueous colloidal processing method. Fracture toughness of 6.6 MPa $m^{1/2}$ for the composite with 1.5 wt% of GPLs was achieved and was 136% higher than that for the monolithic Si_3N_4. Typical toughening mechanisms such as pullout, crack bridging and crack deflection are observed (Figure 2.36 and 2.37). It is important to notice that the crack deflection in three dimensions was suggested as making a great contribution to the remarkably high toughness of the sintered ceramics (Figure 2.37).

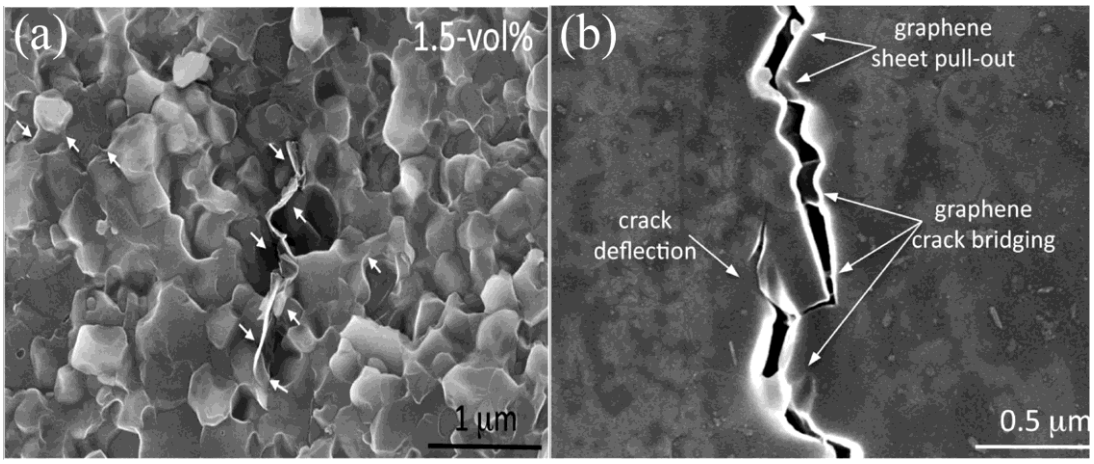

Figure 2.36. SEM images of the fracture surface of the GPL/Si_3N_4 composite (a) and an indentation crack (b).

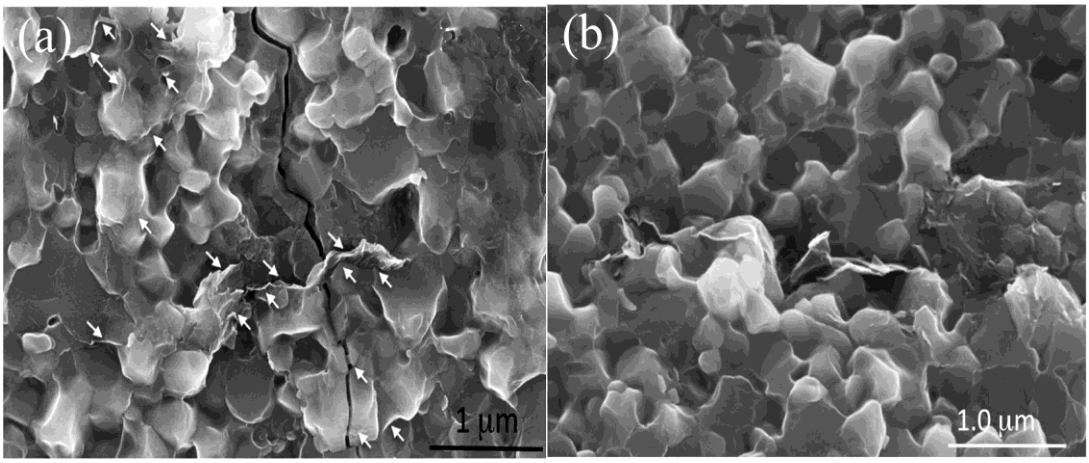

Figure 2.37. SEM images of the fracture surface of the GPL/Si_3N_4 composite, showing crack propagates and climbs over the graphene sheets, implying three dimensional toughening mechanism.

Wang et al. used SPS to prepare a GPL/Al_2O_3 composite and a 53% increase in fracture toughness was obtained with the addition of 2 wt% of GPLs [105]. Ján Dusza et al. prepared GPL-reinforced Si_3N_4 composites containing 1 wt% GPLs using HIP and reported an increase of about 44% in fracture toughness over the pure Si_3N_4 [28]. Jian Liu et al. employed the SPS to fabricate GPL/ZTA composites with the addition of 0.81 vol % GPLs and found an increase of nearly 40% in fracture toughness [4]. A summary of indentation fracture toughness of the composites reinforced with CNT or GPL is given in Table 2.2

Table 2.2. A summary of the fracture toughness of composites reinforced with CNTs or GPLs

Matrix materials	Processing methods	Reinforcements	Fracture toughness improvement (%)	Reference
Al_2O_3	SPS	CNT	194	[97]
Silica	SPS	CNT	158	[106]
Barium aluminosilicate glass	Hot pressing	CNT	143	[107]
Barium titanate	SPS	CNT	143	[108]
Al_2O_3	Hot pressing	CNT	103	[109]
Si_3N_4	HIP	GPL	135	[110]
Zirconium diboride	SPS	GPL	93	[111]
Si_3N_4	HIP	GPL	53	[112]
Hydroxyapatite	SPS	GPL	83	[113]

2.5 Sintering techniques

Sintering is the process of forming materials and components from powders under the action of thermal energy. Generally the sintering approaches can be divided into two categories: solid state sintering and liquid phase sintering. Solid sintering takes place when powder compacts are consolidated in a solid state during the sintering process while liquid phase sintering occurs when a liquid phase is formed during processing.

2.5.1 Conventional sintering

Conventional pressureless sintering to date is still the most attractive sintering method to produce ceramic parts since it is a simple and economical way to realize mass production of products. Heating of powder compacts is commonly achieved with electrical resistance furnaces which can attain temperatures as high as 2500 ˚C. Various types of electrical

furnaces are available commercially for specific purposes. Figure 2.38 shows typical furnaces available for conventional sintering. The box furnace is usually used for sintering in air while a tube furnace is frequently employed when a certain reducing atmosphere is desired. Although conventional sintering is widely used in industry, the lengthy time the sintering process takes and the high sintering temperature needed make it less desirable when efficiency is considered. In this sense, quite a few techniques such as SPS, HIP and field sintering have emerged in recent years.

Figure 2.38. Images of conventional furnaces. (a) is box furnace and (b) is tube furnace.

2.5.2 SPS

SPS as an innovative sintering technology has received more and more attention from scientific and industrial communities. SPS bears the capabilities to introduce rapid heating rates and high pressures, which can realize the sintering process at a relatively lower sintering

temperature and in a much shorter time. It has been used to process various materials, such as nanostructured materials, composite materials and gradient materials [114]. The SPS process was first developed by a Japanese company, Sumitomo Coal Mining Co. Ltd. in 1990 and is the most extensively used innovative sintering technology. A typical SPS was shown in Figure 2.39. In recent years FCT Systeme GmbH in Europe developed a similar process with a marketable level. In the current market both companies in Japan and Europe can basically produce high quality SPS equipment to meet the general requirement for scientific research and industrial applications.

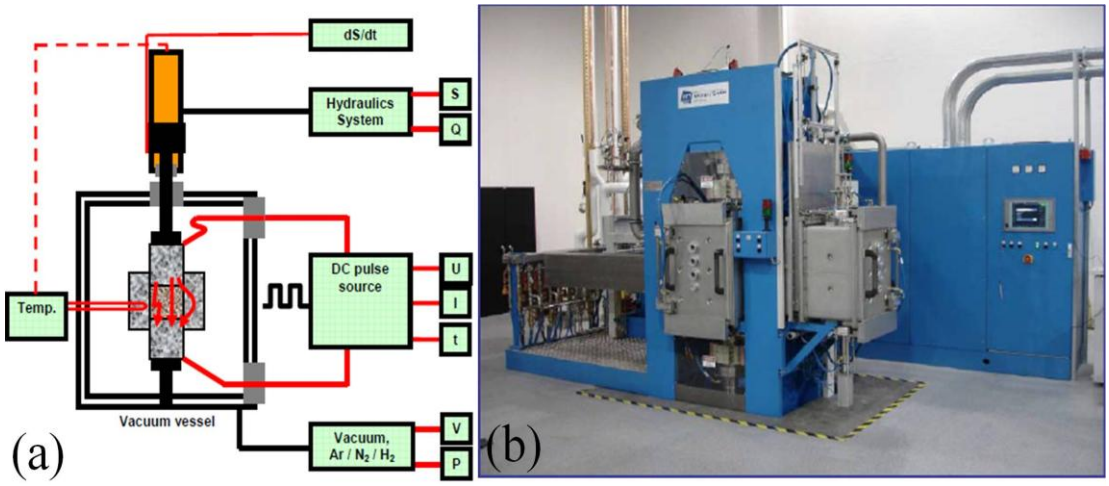

Figure 2.39. A schematic illustration of SPS (a) and an image of SPS (b).

The SPS process can be considered as a modified type of hot pressing process where pulsed electric current runs through the graphite die and the specimen (if conductive). The specimen is therefore heated by the joule heat from the specimen itself and from the heat transferred from the pressing die. This technique makes it possible to attain the temperature of 2000˚C at a heating rate of up to 1000˚C/min. Although various reports have been made to reveal the sintering mechanism of SPS, so far no convincing evidence is confirmed to unravel the microscopic mechanism of the sintering process. The debate goes on between the plasma

formation and electro migration supporters [115-117]. Evidence of these two phenomena is hard to find. Makino et al. sintered an alumina sample using SPS and found out that a major part of the electric current (1000A) was injected by the machine while a minor part of the current (100mA) ran through the ceramic sample [117]. A similar experiment was carried out by Tomino et al. and it was reported that no current passing through the ceramic sample was detected, indicating the absence of discharges in the dense insulators [118]. Munir et al. suggested that the formation of plasma or discharge might have a close link with contact surface areas of the powder particles and plasmas or discharges between particles were likely to be generated at the beginning of sintering for conductive powders [119]. It has been implied that in the application of pulsed direct current several factors may cause spark plasma, spark impact, Joule heating and electric field assisted diffusion, contributing to the densification of the powders [120].

Sintering parameters such as heating rates, pressure and pulse sequence are very important in the densification process. Shen et al. investigated the effects of heating rates on the density of Al_2O_3 samples and found that heating rates below 350 ˚C /min could produce dense samples but high heating rate yielded porous ceramics [121]. It is widely accepted that the imposition of pressure can help remove the pores and increase the density of green compacts, which promotes the mass transferring process. Usually the higher the pressure during the sintering process, the higher the density of the sintered sample will be achieved. An example of ZrO_2 produced by SPS is shown in Figure 2.40 [121]. Shen et al. studied the pulse effect on the sintering of Al_2O_3 samples and reported that the properties of Al_2O_3 were independent of the pulse [121].

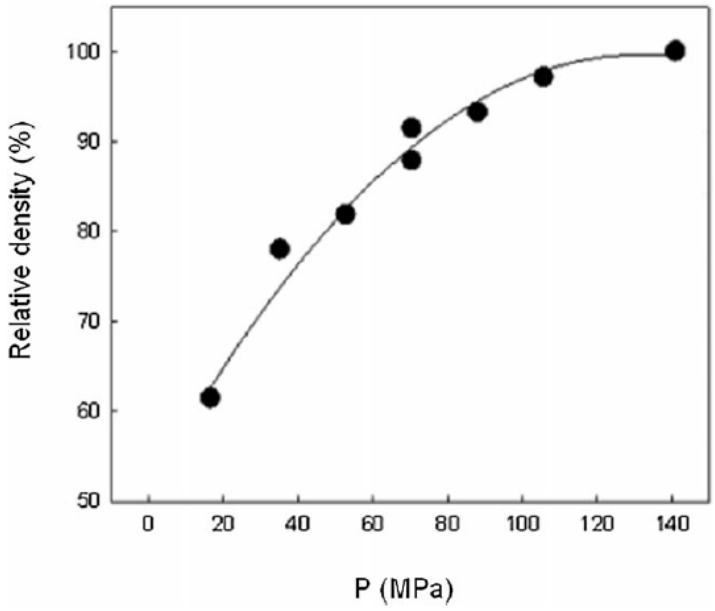

Figure 2.40. Relative density of ZrO_2 produced by SPS as a function of pressure.

SPS is a cost effective sintering process. The sintering time to consolidate the ceramic composites by SPS is just around ten percent of that by the traditional sintering process [122] and the sintering temperature of SPS to achieve full density is about 150-200 [123] or 250-300 ˚C [124] lower than that of the hot pressing technique. Meanwhile, SPS can also well control grain growth of the sintered sample. Lee et al. sintered TiO_2 using SPS and found that the grain size of around 200 nm was obtained [125]. This grain size was smaller than that achieved by microwave sintering (300nm) and conventional sintering (1-2 μm) [126].

2.5.3 HIP

Sintering with an external pressure is often referred to as pressure sintering. This technique is rather important to fabricate densified ceramic samples, which are difficult to consolidate

using traditional sintering. HIP (Figure 2.41) is one of the widely used pressure sintering technologies. In the process powders are tightly enclosed in a glass or a metal container which is evacuated and placed in a pressure vessel. Alternatively, samples can be preconsolidated using traditional sintering and subsequently HIP is used to further increase the density of the sample. During the sintering process, the required pressure within the chamber is achieved by introducing pressurizing gas through a compressor and when the required pressure is obtained, the metal container will collapse and then the isostatic pressure is transmitted to the sample.

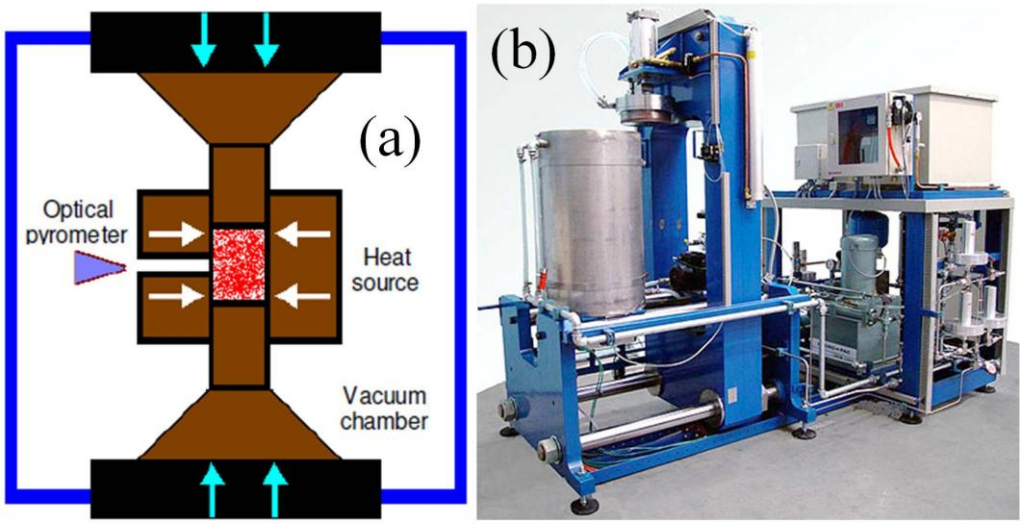

Figure 2.41. A schematic illustration of HIP (a) and an image of HIP (b).

2.5.4 SLS

SLS is a powder based additive manufacturing technique to produce three dimensional complex shaped parts [127]. A schematic illustration of this process is shown in Figure 2.42. The main feature of this technique is that the part is made in a layer by layer way with a

computer aided design model and each layer is consolidated into the part by fusing small particles of polymer, metal or ceramic into a mass of the desired three dimensional shapes. Various components with intricate shapes were produced by direct or indirect SLS (Figure 2.43) [127, 128] .

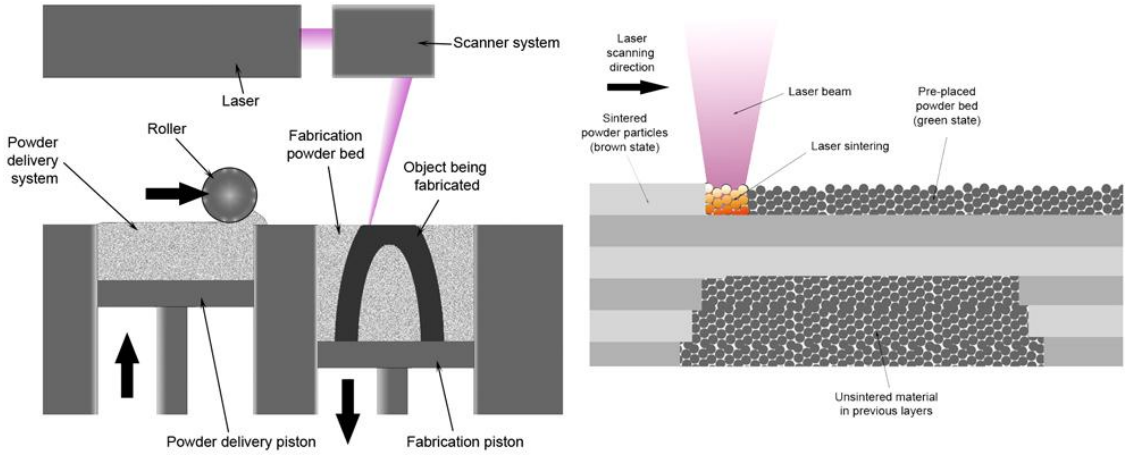

Figure 2.42. A schematic illustration of SLS process

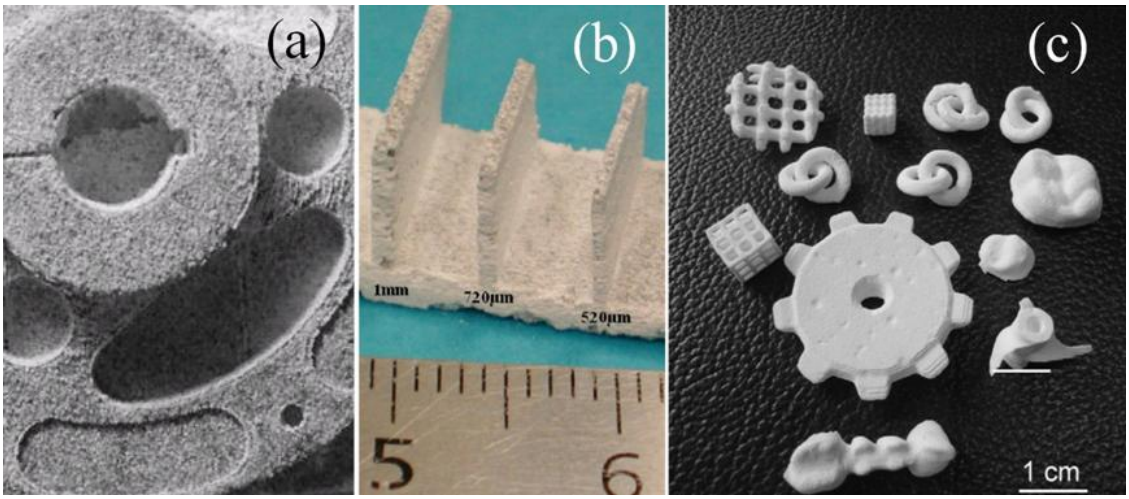

Figure 2.43. Images of components produced by SLS. (a) is a part of a turbine blade. (b) and (c) are ceramic parts.

2.5.5 Self-propagating high-temperature synthesis plus quick pressing (SHS/QP)

In recent years, Fu et al. proposed a novel sintering approach of SHS/QP to fabricate ceramic materials [129, 130]. A schematic representation of the process is shown in Figure 2.44. In this technique, green samples are sintered by heat from combustion synthesis or SHS. In the experimental process, the green sample is placed in an alumina crucible loaded in combustion reactants. The whole reaction system is put in a steel die and heat from combustion synthesis is generated to sinter the samples. In the meantime, a large external pressure can be imposed when the sintering temperature is achieved.

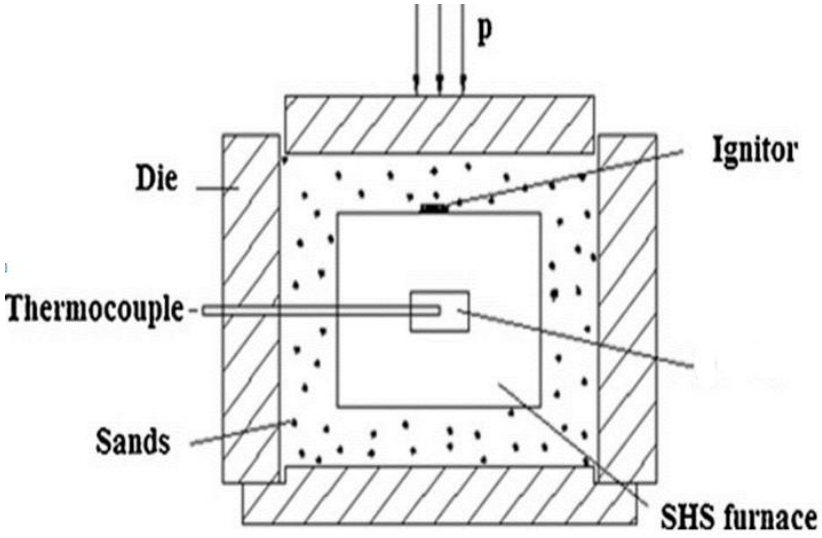

Figure 2.44. A schematic representation of SHS experiment process

2.5.6 Microwave sintering

For the past several decades, microwave sintering has attracted growing interest among researchers [131]. Microwave sintering is fundamentally different from traditional sintering.

As shown in Figure 2.45, for traditional sintering electrical resistance furnaces are commonly used and lead to conductive and convective heating phenomena whereas for microwave sintering, heat is generated internally because of the coupling between microwaves and the atoms, ions and molecules of the materials [132]. Numerous reports have shown that the processing temperature by microwave sintering is lower than that by traditional sintering and finer microstructures and improved properties can be achieved using microwave sintering [133-135]. For example, Ritzhaupt-Kleissl et al. sintered Al_2O_3 ceramics using both methods and found that grain size of the Al_2O_3 was one order of magnitude finer when it was sintered in a microwave furnace at 1550˚C [136]. Such a grain size is normally achieved at 1620˚C for 2 hours in a traditional furnace. Although microwave sintering has shown some advantages, to control the sintering process is difficult since local heating can be seriously affected by the shape of the ceramic specimen. Temperature gradient is usually developed within the ceramics and it is therefore difficult to achieve sufficiently uniform heating.

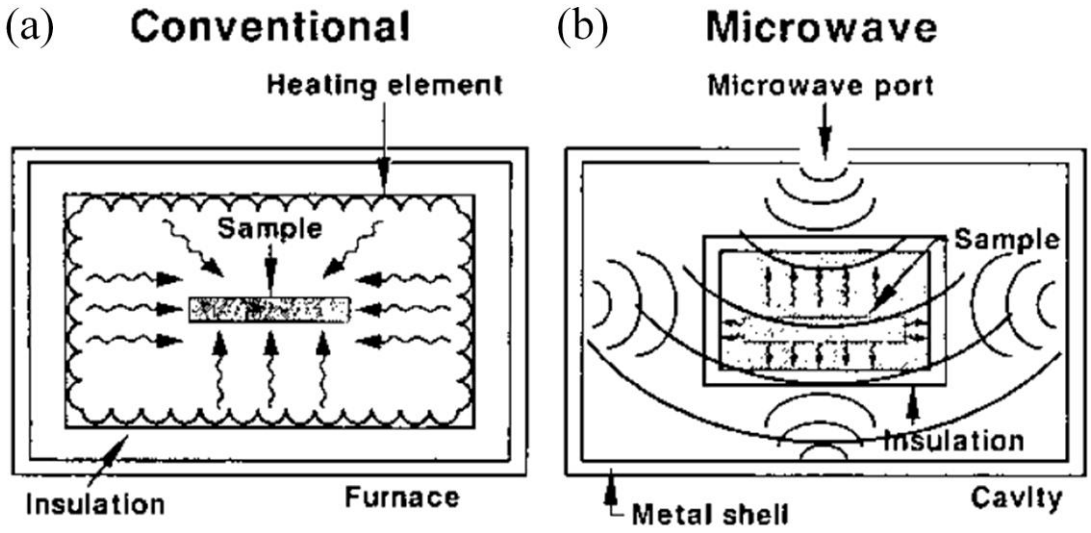

Figure 2.45. Heating patterns in conventional (a) and microwave (b) furnaces.

A summary of mechanical properties of the ceramics prepared using different methods is given in Table 2.3.

Table 2.3. A summary of the mechanical properties of ceramics

Materials	Processing methods	Sintering temperature (℃)	Sintering time	Flexural strength (MPa)	Fracture toughness (Mpa $m^{1/2}$)
Al_2O_3 [137]	Hot pressing	1700	30 mins	457	5.17
Al_2O_3 [138]	Pressureless sintering	1700	2 hrs	—	2.7
Al_2O_3 [139]	SPS	1350	5 mins	—	2.8
Al_2O_3 [139]	SPS	1150	5 mins	—	2.8
Al_2O_3 [121]	SPS	1300	3 mins	—	3.2
Al_2O_3 [140]	SPS	1150	5 mins	435	3.2
Al_2O_3 [95]	Pressureless sintering	1520	1 hrs	—	3.34
Al_2O_3 [121]	SPS	1250	3 mins	—	3.6
Al_2O_3 [121]	SPS	1450	3 mins	—	3.8
Al_2O_3 [141]	Hot pressing	1635	1 hrs	280	3.8
ZTA [95]	Pressureless sintering	1520	1 hrs	—	3.32
ZTA [142]	Pressureless sintering	1500	2 hrs	763	4.1
ZTA [143]	HIP	1475	1 hrs	—	4.2
ZTA [144]	SPS	1400	8 mins	1000	5.25
ZTA [145]	Pressureless sintering	1500	2 hrs	603	6.3
ZTA [67]	Pressureless sintering	1600	2 hrs	1000	8.9
4 vol%CNT/Al_2O_3 [94]	Hot pressing	1600	1 hrs	375	4.25
1 vol%CNT/Al_2O_3 [96]	Pressureless sintering	1600	2 hrs	543	4.1
1 vol%CNT/Al_2O_3 [93]	SPS	1500	10 min	689	5.9
12vol%CNT/Al_2O_3[146]	SPS	1500	1 hrs	314	5.55
10vol%CNT/Al_2O_3[147]	SPS	1150	3 mins	—	6.4
2wt%GPL/Al_2O_3 [105]	SPS	1300	3 mins	—	5.21
0.8vol%GPL/Al_2O_3[139]	SPS	1350	5 mins	—	3.8
0.01wt%CNT/ZTA [95]	Pressureless sintering	1520	1 hrs	—	4.68
0.1wt%CNT/ZTA [148]	SPS	1520	5 mins	—	5.5

2.6 Composite coatings for corrosion protection

Metallic materials such as steels possess excellent strength and ductility and are widely used in many industrial applications. However, they suffer poor corrosion resistance due to their thermodynamic instability when exposed to the environment. To solve this problem applying a coating on the surface of metals has become very popular since potentially it is a cost-effective way to realize mass production.

2.6.1 Electroplating deposition

Electroplating is a chemical process that employs electrical current to reduce dissolved metal cations so that a coating can be formed on certain electrodes. A schematic illustration of the electroplating process is shown in Figure 2.46. Electroplating has many advantages such as

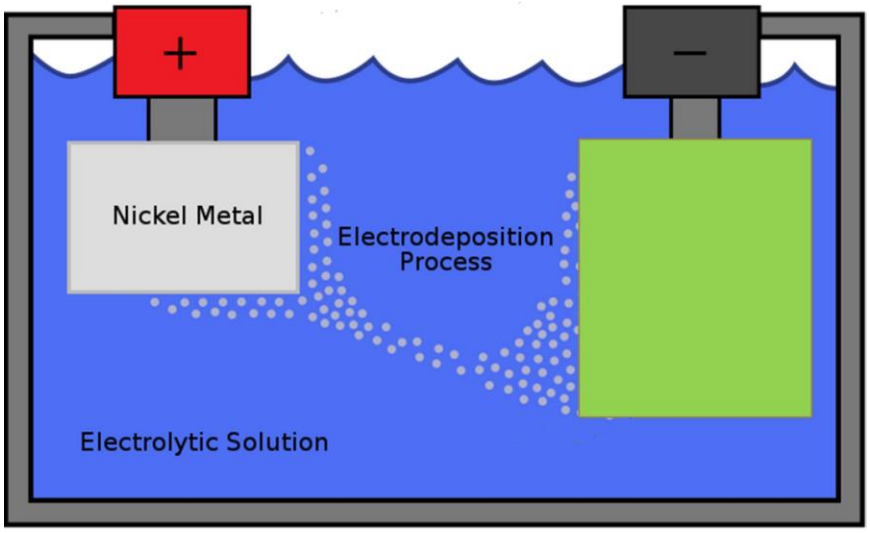

Figure 2.46. A schematic illustration of the electroplating deposition.

simple operation, low cost and high production rates. Using this method various composite coatings have been prepared onto the surface of the metals for improving corrosion and wear resistances.

Baghery et al. fabricated TiO_2/Ni nanocomposite coatings and investigated the effects of TiO_2 particles on the corrosion and wear properties of the coatings [149]. It was found that the addition of TiO_2 particles significantly improved the wear and corrosion resistant properties of the composite coatings and a higher content of TiO_2 particles resulted in better wear property. Benea et al. compared the corrosion and wear properties of pure Ni and SiC/Ni composite coatings[150]. The results showed that better wear and corrosion resistances were achieved by introducing SiC particles into the Ni matrix. Pompei et al. electrodeposited BN/Ni composites from a sulphamate bath containing dispersed nitride particles and reported higher hardness and improved wear resistance than the pure Ni coating [151]. Allaharam et al. employed a pulse and direct current electroplating method to prepare the Al_2O_3 nano particle reinforced Cu composite coatings [152]. It was shown that the mechanical properties of the composite coatings were much more superior to those of bare Cu coatings and the high content of nano Al_2O_3 caused the enhanced properties of the coatings. Zhu et al. fabricated the TiN/Ni composite films using the electroplating method and reported that smaller grain size and improved corrosion resistance of the Ni coatings were obtained by incorporating TiN particles [153]. Lekka et al. co-electrodeposited SiC nano particles in the Ni matrix and achieved a higher hardness and a better abrasion resistance. [154].

2.6.2 Electropheric deposition (EPD)

EPD has been widely used to produce various coatings on metallic substrates [155-157]. It bears the advantages of a short processing time, simple apparatus required and little restriction on the shape of the substrate [158]. A schematic illustration of the deposition process is shown in Figure 2.47. The main feature of this process is that colloidal particles are

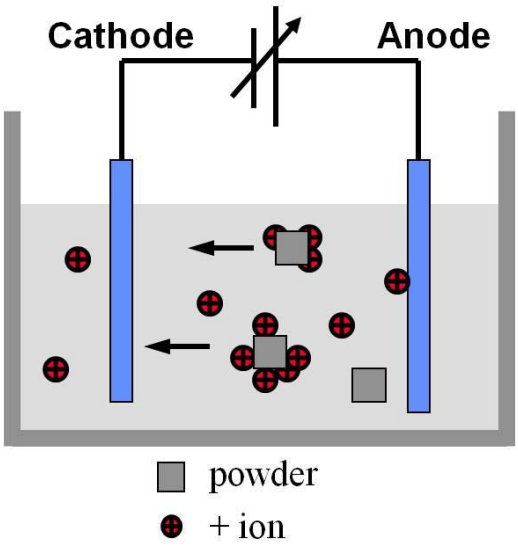

Figure 2.47. A schematic illustration of the electropheric deposition

first charged and dispersed in the liquid medium. Deposition commences when colloidal particles migrate under an electric field. EPD differs from electroplating in that particles of any composition rather than just ions can be deposited. Various composite coatings containing non-conductive particles have been prepared using this method. Corni et al. fabricated Al_2O_3/Polyether ether ketone composite coatings on the stainless steel and investigated the effects of Al_2O_3 content on the mechanical and corrosion properties [158]. It was found that a small amount of Al_2O_3 particles was enough to improve the mechanical properties and the composites' coatings showed considerably improved corrosion resistance

compared to bare stainless steel. Wang et al. produced diamond/borosilicate glass composite coatings using EPD and reported that a glass layer on diamond could protect it from oxidization and bond the diamond particles together [159]. Askaria et al. fabricated $Al_2O_3/SiC/ZrO_2$ graded materials by EPD and found that compared to Al_2O_3/ZrO_2 materials, $Al_2O_3/SiC/ZrO_2$ graded materials showed improved mechanical properties [160] .

2.6.3 Electroless deposition

Since it was developed in 1946 by Brenner and Riddell, the electroless plating technique has become a popular way to prepare various coatings for many applications. Electroless plating is an autocatalytic process where chemical compounds in the solution are oxidized so that metallic ions can be reduced to form the coatings [161]. A schematic illustration of electroless deposition process is shown in Figure 2.48. In the process, metallic cations receive

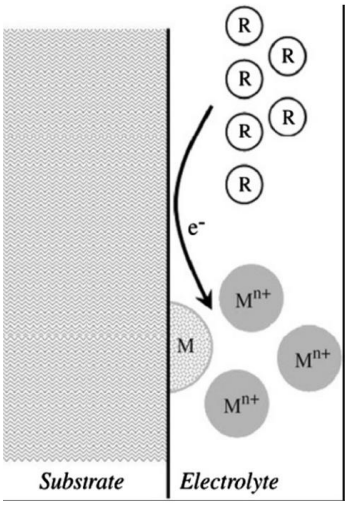

Figure 2.48. A schematic illustration of electroless deposition with reducing agent R as the source of electrons

electrons from the surface of a metallic substrate and are reduced during deposition while the reductant is oxidized by delivering electrons.

2.7 Potential applications of graphene based materials

2.7.1 Field effect transistors

Transistors are very important devices in the semiconductor industry and are the fundamental building blocks for various electronic devices, such as microprocessors and flash memories. Due to its excellent electrical and mechanical properties, graphene is considered to be a potential alternative for producing high performance transistors. The major limit for graphene is zero-gap behaviour, which does not allow graphene to be used in logic applications where frequent on/off switching is required. Various methods have been carried out to open the band gap of graphene. It was reported that by fabricating graphene in nanoribbons or quantum dots, the band structure of the graphene could be modified [162, 163] . Meanwhile, the band gap of graphene can be opened by biasing bi-layer graphene [18]. Figure 2.49 shows schematic illustrations of the graphene-based field effect transistors. It contains a gate, a graphene channel connecting source and drain electrodes and a dielectric barrier layer separating the gate from the channel [18].

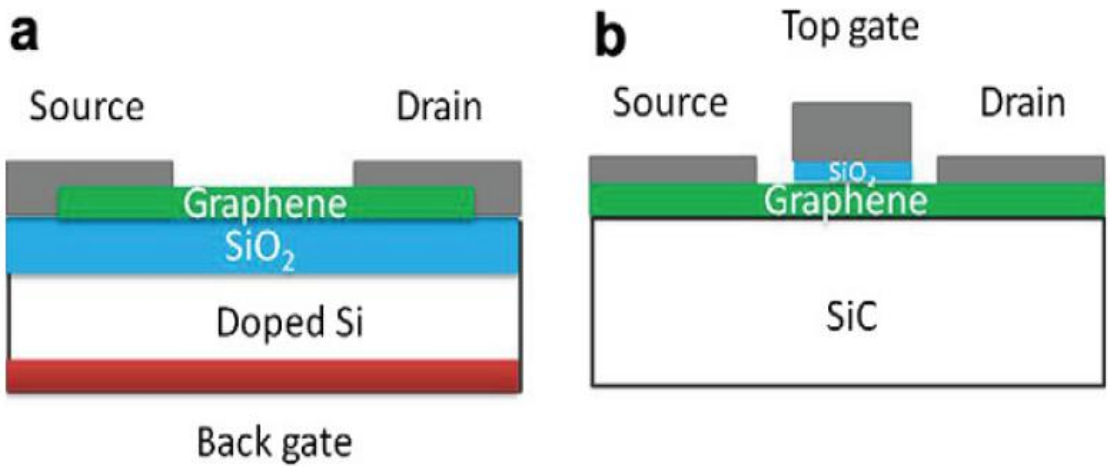

Figure 2.49. Schematic illustrations of back gated (a) and top gated (b) graphene field effect devices.

2.7.2 Graphene thin film as transparent electrodes

Becerril et al. prepared reduced graphene oxide (RGO) film and examined the correlation of thickness of the film and the degree of reduction with the transmittance and conductivity [164]. Their results are shown in Figure 2.50. It can be seen that the transmittance decreases with the increase of the thickness of the film and the conductivity of the film decreases with the increase of the transmittance. It is suggested that high quality transparent and conductive RGO thin film can be obtained by optimizing the film thickness and reduction process.

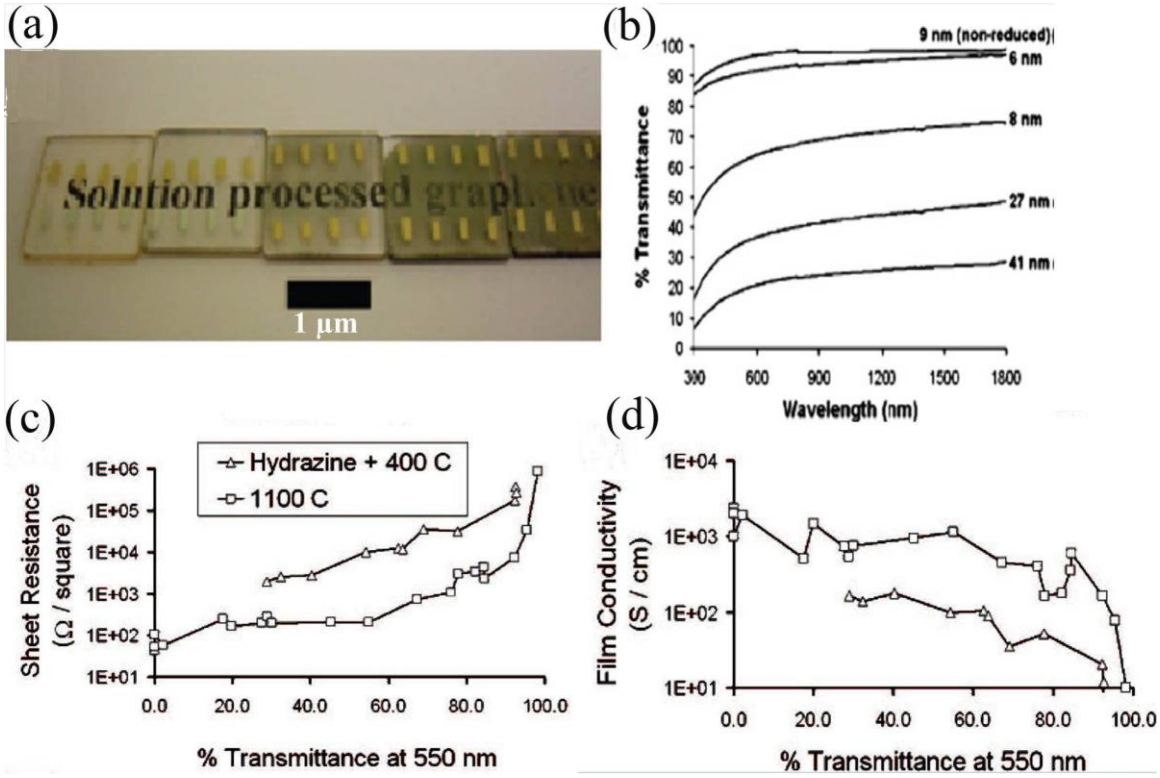

Figure 2.50. Optical and electrical properties of GO and RGO films on quartz. (a) Images of a GO (leftmost) and four RGO films with increasing thickness. (b) Optical transmittance of the films in (a) with the film thickness indicated. (c) Sheet resistance of the films prepared using two different methods as a function of optical transmittance at 550 nm light. (d) Film conductivity as a function of transmittance for films shown in (c).

Table 2.3 shows recent developments on optical and electrical properties of graphene-based thin films. RGO thin film bears the merits of good transparency, conductivity and flexibility and it is considered to be a promising alternative as an electrode material to replace the ITO, which is expensive and lacks mechanical flexibility.

Table 2.4. Properties of graphene-based transparent electrodes.

Materials	Reduction	Fabrication method	Film thickness	Sheet resistance (Ω/square)	Wave length (nm)	Transmittance (%)	References
RGO	Hydrazine solution/ annealing	Spray coating	1nm	20M	600-1000	96	[165]
RGO	Hydrazine vapour/ annealing	Vacuum filtration	3nm	0.16M	550	90	[25]
RGO	Hydrazine vapor	Langmuir-Blodgett	1-3nm	8K	1000	83	[166]
RGO	Hydrazine vapour/ annealing	Spin coating	1 µm	100-1000	400-1800	80	[164]
RGO	Acetylene-assisted thermal	Spin coating	1.1 µm	1425	500	70	[167]
RGO	Thionyl chloride treatment	Vacuum filtration	10 µm	40K	300-900	64	[168]
RGO	Hydrazine solution/ annealing	Spin coating	5 µm	240	UV visible	86	[169]
RGO	Hydrazine solution/ annealing	Spin coating	5-8 µm	0.4-19K	1000	60-80	[170]
RGO	Vacuum annealing	Spin coating	7 µm	0.8K	550	82	[171]

2.7.3 Solar cell

RGO transparent electrodes can be used for producing solar cell electrodes. Various studies indicate GO and RGO can be employed as active materials and hole transport layers. Wang et al. fabricated RGO film and used it as an anode for dye-sensitized solar cells, as shown in Figure 2.51 [172]. The lower short-circuit current in the RGO electrode may be associated with the lower transmittance of the materials, series of resistance of the device and space charge limited conduction.

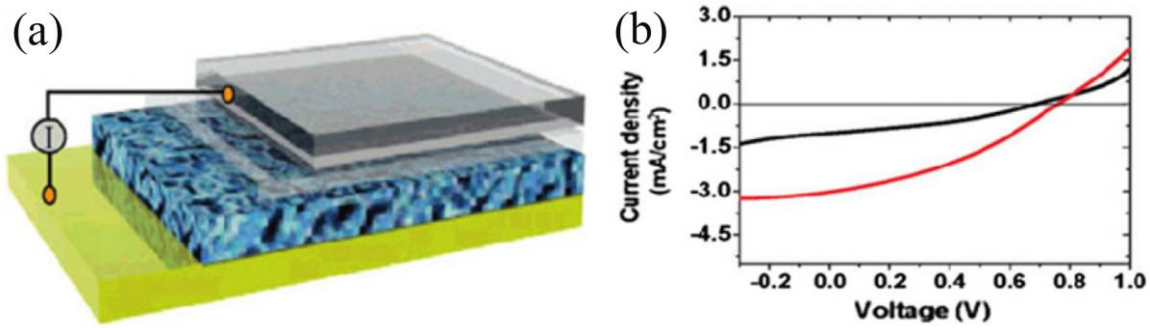

Figure 2.51. Schematic of the dye-sensitized solar cell (a) and variation of current density with the voltage (b). The four layers from bottom to top in (a) are gold, dye-sensitized heterojunction, compact titanium oxide, and graphene film. Black and red lines in (b) indicate graphene-based cell and fluorine doped tin oxide (FTO)-based cell respectively.

Poly(3,4-ethylene dioxythiophene):poly(styrene sulfonate) (PEDOT: PSS) is the most common hole transport layer in polymer solar cells. However, this combination causes the corrosion of ITO at high temperatures, leading to degradation of the device's performance. In order to overcome this disadvantage, ITO/GO/ poly(3-hexylthiophene) (P3HT): phenyl-C61-butyric acid methyl ester (PCBM)/aluminum (Al) configuration (Figure 2.52a) was designed to increase the efficiency of the holes [173]. It is suggested that the GO films with a thickness of 2 nm can lead to better efficiency of the device than those with thicknesses higher than 4 nm, due to their lower transmittance and the increased serial resistance brought by the film. Meanwhile, graphene/ P3HT was also used as the active layer in polymer photovoltaic cells (Figure 2.52b) to increase the device efficiency. It is reported that the addition of 10 wt% of graphene can significantly enhance the device performance and a maximum power conversion efficiency of 1.1% can be achieved. Table 2.4 summarizes the photovoltaic properties of the solar cells using RGO as active materials and electrodes.

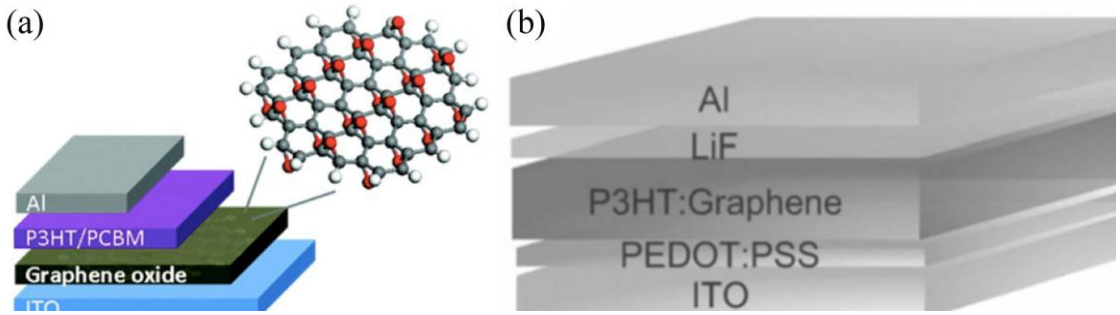

Figure 2.52. Schematic illustrations of the photovoltaic device structures. (a) ITO/GO/P3HT:PCBM/A and (b) ITO/PEDOT:PSS/P3HT:Graphene/LiF/Al.

Table 2.5. Photovoltaic properties of solar cells containing RGO.

Active materials	Electrode materials	Deposition	Thickness (nm)	Power conversion efficiency (%)	Reference
P3HT:PCBM	RGO/PET	Spin coating	16	0.78	[174]
TiO_2 film (RGO/TiO_2 composite interlayer)	FTO	Spin coating	15	5.26	[22]
P3HT:graphene/ PEDOT:PSS	Al:LiF/ ITO	Spin coating	100	1.1	[175]
PEDOT:PSS/P3HT/ zinc oxide nanorods	Au/RGO	Spin coating	5–13	0.31	[170]
TiO_2/dye/spiroOMeTAD	Au/RGO	Dip coating	10	0.84	[172]

2.7.4 Electrochemical sensors and biosensors

RGO is considered to have high potential to be used for electrochemical and biological sensors because functional groups on the edge of RGO are rather sensitive to chemical and biological change. The sensitivity of the gas sensors is largely dependent on the charge carrier transfer on the surface between GO and RGO since adsorption of gases such as NO_2, NH_3 and H_2O on the surface would cause appreciable change in charge concentration [176,

177]. For example, GO exhibits no response to NO_2 while the RGO is very sensitive to NO_2 and usually would present p-type transitory behaviour [18]. A summary of recent reports over RGO-based sensors are given in Table 2.5 [18].

Table 2.6. RGO based chemical sensors and biosensors

Active material	Reduction method	Sensor type	Analyte	Measurement	Detection limits	References
RGO	Thermal	Gas	NO_2	I vs.t	100ppm	[23]
RGO+Pd	Chemical	Gas	H_2	R vs.t	N/A	[178]
RGO	Thermal	Molecular	HCN	G vs.t	ppb	[176]
RGO	Chemical	Gas	NO_2	R vs.t	ppm	[177]
RGO	thermal	Gas	NO_2	I vs.t	ppm	[179]

2.7.5 Graphene composite for energy storage.

Graphene bears the merits of high electrical conductivity, large surface to volume ratio, good flexibility and chemical stability and is considered a good candidate to build composites with metal or metal oxide nanoparticles for energy storage applications. The introduction of graphene in lithium ion batteries (LIBs) can significantly enhance the properties of the batteries since graphene can accommodate the volume expansion or contraction of nanoparticles during the charge and discharge process [18]. Wang et al. synthesized the manganese oxide (Mn_3O_4)/RGO hybrid materials and used them as an anode for LIBs [26]. It was found that uniform distribution of nano particles on graphene significantly enhanced the capacity at varied current densities (Figure 2.53). Shubin Yang et al. used a co-assembly method to fabricate graphene encapsulated cobalt oxide (Co_3O_4) for anode materials of LIBs and they found that remarkable reversible capacity and excellent cycle performance were

achieved [180]. Some recent works using metal oxides/graphene composites as electrode materials for LIBs are summarized in Table 2.6 [18].

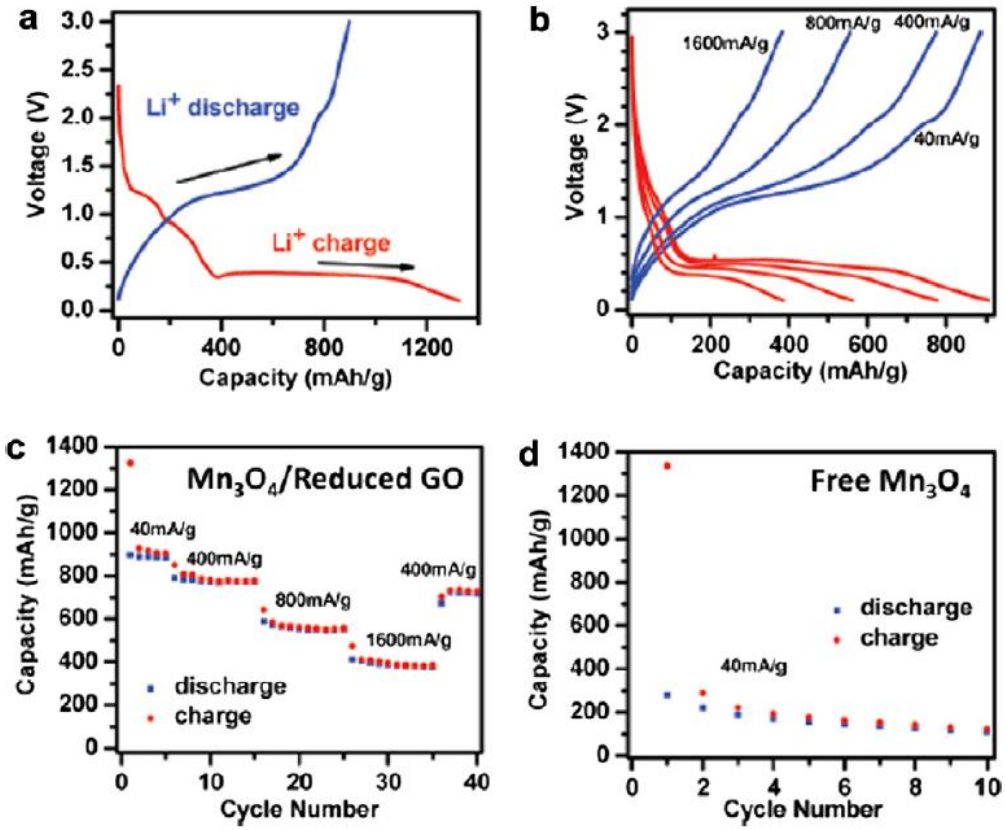

Figure 2.53. Electrochemical properties of a half-cell composed of Mn_3O_4/RGO and Li. (a) Charge and discharge curves of Mn_3O_4/RGO at a current density of 40 mA/g. (b) Charge and discharge curves of Mn_3O_4/RGO at various current densities. (c) Capacity retention of Mn_3O_4/RGO at various current densities. (d) Capacity retention of Mn_3O_4 at a current density of 40 mA/g.

Table 2.7. Performances of graphene based lithium ion battery materials

Materials	Energy density (mA h/g)	Current density (mA/g)	Cycles	references
Graphene/ Co_3O_4	1000-1100	74	130	[180]
Graphene/Co_3O_4	935	50	30	[181]
Graphene/Mn_3O_4	730-780	400	50	[26]
Graphene/Tin oxide (SnO_2)	625	10	10	[30]
Graphene/Fe_3O_4	1026	35	30	[31]
Graphene/TiO_2	160	-	100	[182]

On the other hand, graphene can be used as electrode materials for supercapacitors due to its very good electrical conductivity, high specific surface area, chemical and mechanical stability [183]. Ruoff et al. first used the chemically reduced graphene as electrodes for supercapacitors [184]. They found that specific capacitances of the supercapacitor were 135F/g in potassium hydroxide (KOH) electrolyte and 99F/g in organic electrolyte respectively. Meanwhile, it was suggested that agglomeration of graphene would considerably reduce the specific capacitance of the supercapacitors due to the Van der Waals attraction. To overcome this problem, nano sized metal oxides are introduced to separate the graphene. For example, Wu et al. prepared a MnO_2/graphene based capacitor and remarkable energy density of 30 Kw/kg and power density of 5 kW/kg were achieved [185]. A variety of graphene based super capacitors and their properties are given in Table 2.7. It can be seen that graphene based materials show excellent specific capacitance as well as power density and they can be a prominent candidate for supercapacitors.

Table 2.8. Properties of graphene based supercapacitors

Materials	Specific capacitance (F/g)	Energy density	Electrolyte	References
38.3wt% Ruthenium oxide (RuO_2)/graphene	570	20.1 Wh/kg at 100 mA/g, 10 kW/kg at 4.32 h/kg	----	[186]
Manganese dioxide (MnO_2)/graphene	216	---	1M Sodium sulfate	[187]
MnO2 nanowire/ graphene	117 31	--- 30.4 Wh/kg	sulfuric acid Sodium sulfate	[185]
polyaniline (PANI)/graphene	1046	-	6M KOH	[188]
Thermally reduced graphene	75 F/g	31.9 Wh/kg	N-butyl-N-methylpyrrolidimiumbi simide	[189]
Hydrazine reduced GO	205	28 Wh/kg 10 Wh/kg	KOH	[190]

Recently, research attention has been given to polymer/graphene composite materials which exhibit better flexibility and superior capacitance compared to other carbon based polymer capacitors. Jun Yan et al. synthesized graphene nanosheet/PANI composites using in situ polymerization and the obtained composites have a specific capacitance of 1046 F/g at a scan rate of 1 mV/s [191]. Wang et al. fabricated graphene/PANI composite paper (Figure 2.54) for the application of a flexible electrode via in situ anodic electropolymerization [188]. It was found that the tensile strength of 12.6 Mpa and a large electrochemical capacitance of 233 F/g were achieved, which enabled this electrode to outperform many current carbon based flexible electrodes.

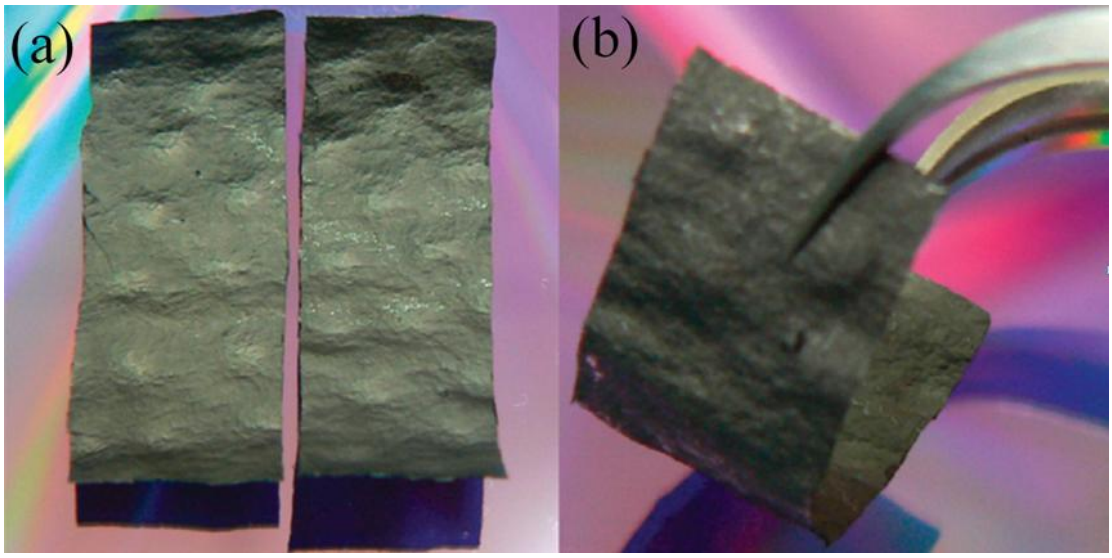

Figure 2.54. Images of graphene papers.

2.8 Summary

The review of the structure, mechanical and functional properties of graphene are presented in Section 2.2, which shows graphene's potentiality as a reinforcement filler to increase certain matrix materials' strength, thermal and electrical conductivities.

Various approaches of producing graphene or GPLs are reviewed in Section 2.3. The main advantages, disadvantages and comments on each approach are reported. In particular, for mass producing large and high quality monolayer graphene, CVD is more preferable while for fabricating GPLs in large quantities, chemical conversion from graphite to graphene is more suitable.

Toughening mechanisms in ceramics and ceramic composites are introduced in Section 2.4, in which particle dispersion toughening, phase transformation toughening, multilayer toughening and fibre toughening mechanisms are discussed. Particularly, fracture toughness of ceramic composites reinforced with CNTs and GPLs are presented. The techniques for measuring fracture toughness are discussed and it is suggested that SEVNB and SENB methods are better than the indentation method for examining the true value of the fracture toughness of composites containing CNTs and GPLs.

A variety of sintering techniques and related equipment are outlined in Section 2.5. The advantages and disadvantages of each technique are reported. Especially SPS can simultaneously introduce a high pressure and a heating rate which can realize the condensation process of ceramic composites at a low sintering temperature and in a very short sintering time.

Fabrication techniques of composite coatings for corrosion resistance are reviewed in Section 2.6, in which electroplating deposition, electropheric deposition and electroless deposition are discussed. Their differences are presented and each deposition technique can be chosen for coating specific materials in light of their characteristics.

Potential applications of graphene are reviewed in Section 2.7. The good flexibility and excellent thermal and electrical conductivities make it a very suitable candidate for transparent electrodes, sensors and energy storage.

The reported work in this chapter has a considerable influence on the direction of the research in this PhD thesis and the author's future work. This chapter introduces sintering techniques for producing GPL/ceramic composites in Chapters 3, 4 and 5. On the other hand, the coating technologies presented in this chapter give useful information for fabricating GPL/Ni composite coatings in Chapter 6. The review of the potential applications of graphene introduced in this chapter would help the author pursue new research areas in the future.

Chapter 3: SPS and characterization of GPL/ZTA composites

3.1 Introduction

This chapter presents SPS and characterization of ZTA composites with the addition of GPLs. The effects of sintering temperature on the densification and mechanical properties of the GPL-reinforced ZTA composites are investigated. The aim of the research in this chapter is to find the optimum sintering temperature for producing GPL/ZTA composites with improved fracture toughness. To begin with, experiments of the fabrication process are introduced in section 3.2, in which processing parameters for preparing GPL/ZTA composites using SPS and characterization techniques of the composites are presented. Afterwards, characterization results of GPL/ZTA composites and discussion are presented in section 3.3. In particular, Raman spectra of the pristine GPL and GPLs in the composites are introduced in section 3.3.4. Mechanical properties of the GPL/ZTA composites are given in section 3.3.6 and toughening mechanisms induced by GPLs are discussed in sections 3.3.7 and 3.3.8. Finally, the chapter is summarized in section 3.4.

3.2 Experiments of the fabrication process

Generally the experiments in the research of this chapter consist of three parts, which are powder mixing, sintering of the prepared powder mixtures using SPS at different temperatures and characterization of the sintered bulk specimens.

3.2.1 Powders

In the research of this chapter, micro α-Al_2O_3 powders and GPLs were used for preparing the powder mixtures. The micro α-Al_2O_3 powders used in the research are obtained from Sigma–Aldrich, UK. The density and average particle size of the Al_2O_3 powders are 4 g cm^{-3} and 10 μm respectively. SEM images of the micro Al_2O_3 powders are shown in Figure 3.1.

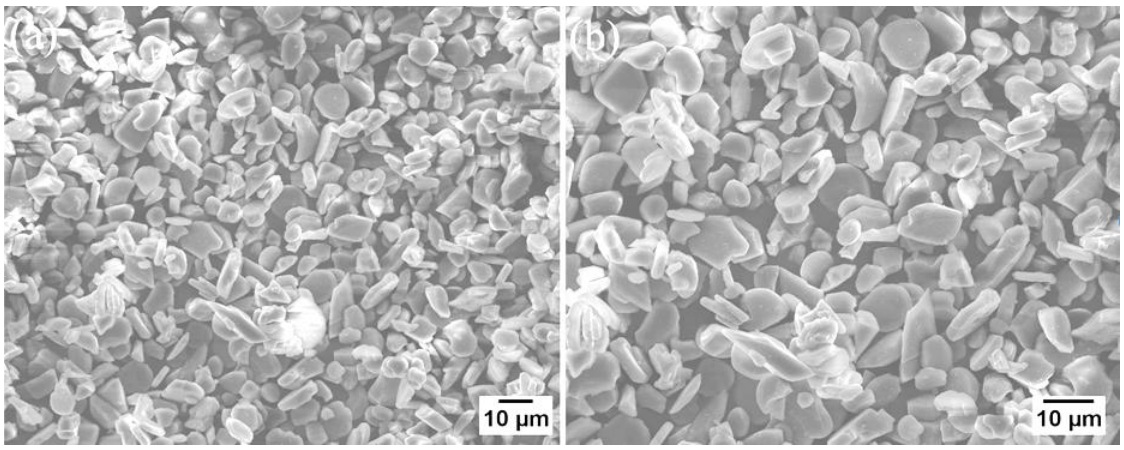

Figure 3.1. SEM images of the Al_2O_3 powders. (b) is a magnified image of (a).

GPLs were procured from Graphene Industries Ltd, Manchester, UK. SEM and AFM images of the GPLs are shown in Figure 3.2. For the AFM measurement, GPLs were firstly dispersed in ethanol and ultrasonicated for 10 min and then one droplet of the solution was placed on a silicon substrate. The sample was ready for the measurement when the ethanol was dried out.

The obtained GPLs are produced by rapid thermal expansion and subsequent exfoliation of graphite using sulphuric acid as a intercalating agent [192]. The thickness and diameter of the resultant GPLs are about 6-8 nm and 15-25 μm respectively. The purity of the GPLs is higher

than 95% and it contains approximately 4% oxygen which is in functional groups (carboxyl, hydroxyl, etc.) at the edges of the nanoplatelets.

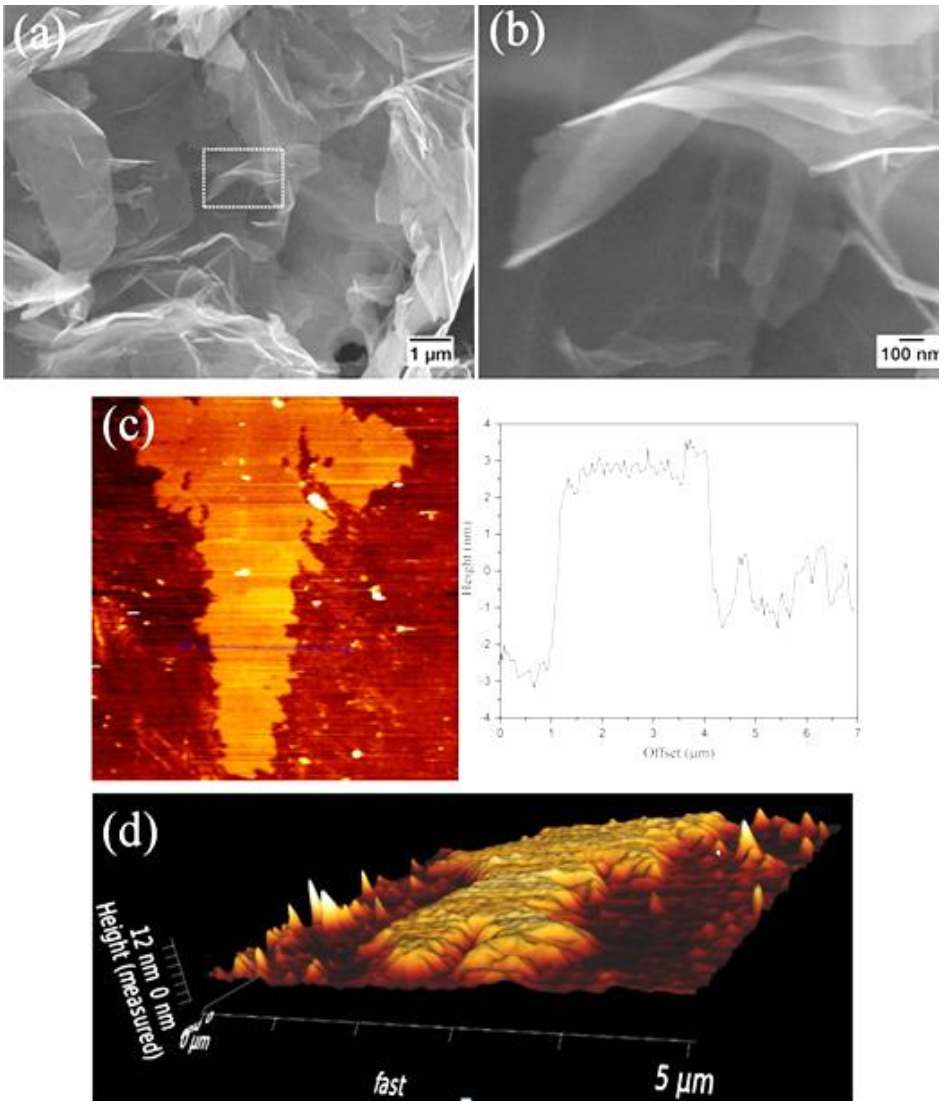

Figure 3.2. SEM (a-b) and AFM (c-d) images of GPLs. (b) is the magnified part of the square area in (a). (d) is the three dimensional topography image of GPL.

3.2.2 Composite powder preparation and sintering

Micro Al_2O_3 powder (20 g) was ball milled at 200 rpm in a planetary ball mill (PM 100, Retsch, UK) for 6 hours to produce a powder mixture of Al_2O_3 and ZrO_2, during which DMF was used as a solvent. The milling was carried out in a cylindrical ZrO_2 container using 3 mol % yttria (Y_2O_3) stabilized ZrO_2 balls (10 mm in diameter, density: 5.9 g cm^{-3}). To produce debris from the ZrO_2 balls, a high ball-to-powder weight ratio of 16 was selected for the ball milling process. The milled slurry mixture was dried at 90˚C in an oven for 3 days. The dried powder mixture was ground manually and sieved using a 140 mesh. To form the GPL–ZrO_2–Al_2O_3 powder mixture, GPLs (0.1 g) were first dispersed in DMF (100 ml) and sonicated for 1 hour. The same amount of Al_2O_3 powder (20g) was added then and the mixture was further sonicated for 10 minutes. This was followed by the same ball milling procedure used for producing the pure ZrO_2–Al_2O_3 powder mixture. SEM images of the powder mixtures after the ball milling process are shown in Figure 3.3. It can be seen that small GPLs separated from each other among a uniform dispersion of ceramic particles (Figure 3.3a) and a large GPL is decorated with ceramic particles (Figures 3.3b and c). Meanwhile, no serious agglomeration of GPLs is noticed, which suggests reasonably good dispersion of GPLs is achieved

.

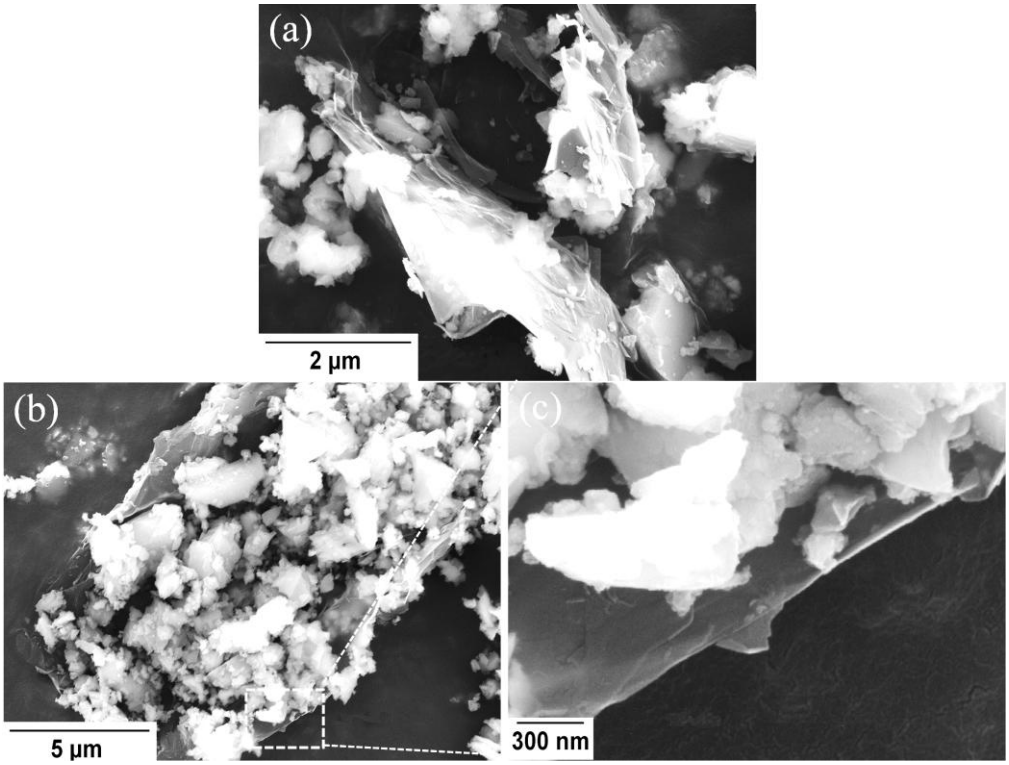

Figure 3.3. SEM images of powder mixtures. (a) SEM images of small GPLs. (b) low and (c) higher resolution SEM images of a large GPL.

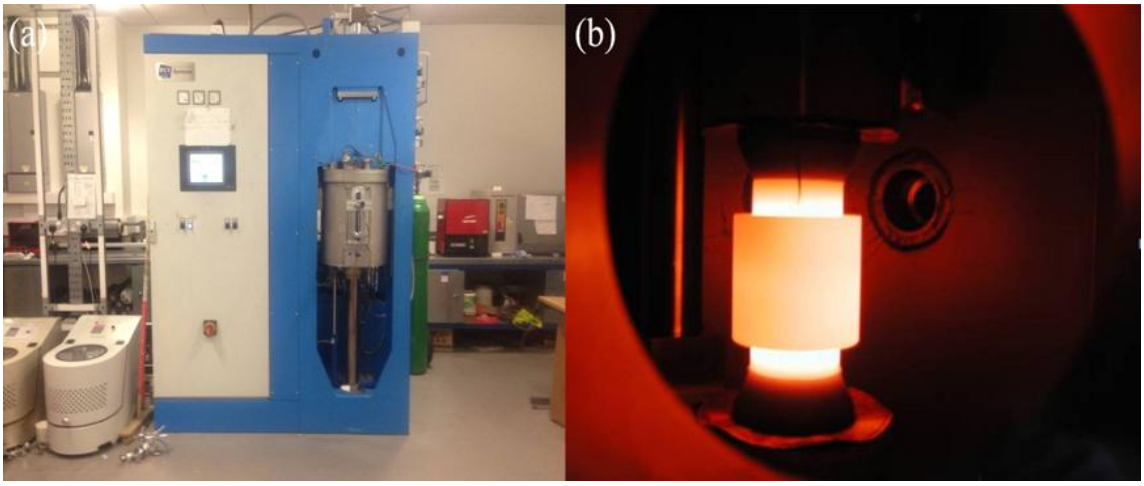

Figure 3.4. SPS facility by FCT Systeme, Germany. (a) SPS facility at Queen Mary, University of London, UK and (b) SPS at 1550˚C.

Bulk composites were sintered in a SPS furnace (Figure 3.4). The powder mixture of GPL–ZrO_2–Al_2O_3 was poured into a graphite die of 20 mm in diameter for producing ZTA

composites reinforced with GPLs. A sheet of graphitic paper was placed between the punch and the powder and between the die and the powder for easy removal of the sintered sample. The sintering process was conducted under a vacuum of 5 Pa. Sintering profiles are shown in Figure 3.5. A uniaxial pressure of 50MPa was applied throughout the sintering cycle. The process was started by raising the temperature to 400 ˚C using a preset heating program. Afterwards, the sintering temperature was increased to the range of 1450–1650 ˚C at a rate of 50 ˚C/min and a 3 minute soaking time was used during the sintering. For comparison purposes, pure ZTA was sintered at 1550 ˚C. The temperature was measured and controlled using an optical pyrometer. The punch speeds and displacements were recorded during SPS process and used to show the shrinkage rates and displacements of the sintered samples. Afterwards, the samples were ground and polished to 0.5μm using SiC paper and diamond suspension.

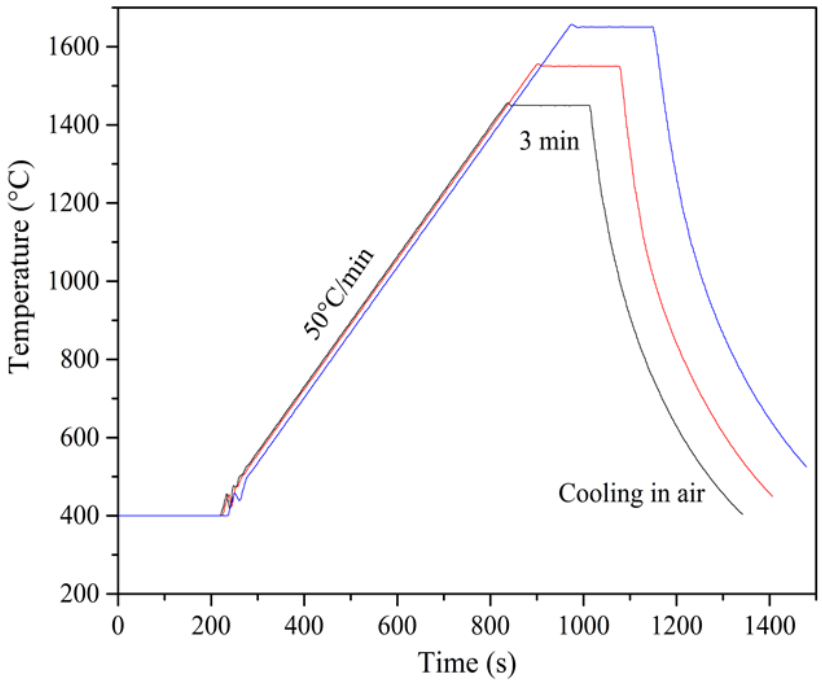

Figure 3.5. Sintering profiles for GPL/ZTA composites.

3.2.3 Material characterisations

3.2.3.1 Density measurement

Helium pycnometry (Micrometitics AccuPyc II 1340) was used to measure the densities of the powder mixtures. The obtained densities of the powder mixtures were employed to determine the content of ZrO_2. The Archimedes' method was used to evaluate the bulk densities of the sintered samples. The densities of the sintered samples are calculated using the following equation.

$$\frac{\rho_A}{\rho_w} = \frac{m_A}{m_A - m_w} \times 100\% \qquad (3.1)$$

Where ρ_A is the actual density of the sintered sample. ρ_w is the density of distilled water. m_A and m_w are the weight of the sintered sample measured in air and distilled water respectively.

3.2.3.2 X-ray fluorescence (XRF) analysis

The XRF spectrometer (Figure 3.6) is capable of determining the elemental composition of materials. Compared to other analytical techniques for element analysis, it bears an advantage that no hazardous chemicals are involved during the preparation of samples for the measurements. In this chapter, in order to determine the content of ZrO_2 in ZrO_2/Al_2O_3 and $GPL/ZrO_2/Al_2O_3$ powder mixtures, XRF tests were carried out and the contents of oxides in the powder mixtures were analyzed. For XRF analysis 0.5 g powder mixtures were mixed

with 0.1 g wax using a mortar and pestle. Afterwards, the powder mixtures were pressed to form pellets with a diameter of 13 mm. A mask of 8 mm was used for the measurement in which a spectrometer applying an X-ray tube with up to 170 mA current at full 4 kW power was utilized.

Figure 3.6. An image of XRF Spectrometer

3.2.3.3 X-Ray diffraction (XRD) analysis

XRD patterns of different phases within the ceramic materials were obtained by using Cu K-α (Wavelength λ=1.54178 Å) radiation with a Bruker D8 Advance Diffractometer (Figure 3.7) located at the Science City Advanced Materials II Laboratory in the University of Birmingham. XRD scans were performed within the 2θ range of 10-80˚ with step size 0.02 and step time of 0.6 s. The phases were determined by comparing the obtained results with standard patterns.

Figure 3.7. An image of the Bruker D8 Advance Diffractometer

3.2.3.4 SEM observation

An environment SEM (XL30 ESEM-FEG) was used to observe the fractured surfaces of the sintered samples and a SEM (JOEL 7000F, 20 kV) was used to characterize the ceramic powders and polished surfaces of the samples. SEI imaging mode was used for all the specimens and before the SEM examination specimens were coated with a thin layer of platinum or gold. An operating voltage between 10-20kv was used.

3.2.3.5 Raman study

A Raman microscope (Renishaw InVia Reflex) located at the Science City Advanced Materials II Laboratory in the University of Birmingham is shown in Figure 3.8 and was used to characterize the pristine GPL and GPLs in the sintered samples with the 532 nm laser

wavelength excitation. A laser power of 10 mW and a detector with 4 cm^{-1} spectral resolution were utilized and to avoid causing damage to the GPLs, only 10% laser energy was focused on the GPLs.

Figure 3.8. An image of the Raman Microscope

3.2.3.6 Micro hardness measurement

Hardness is a property of materials, showing the resistance to plastic deformation under a constant compression load. For micro hardness, measurement is performed on a microscopic scale. Before the hardness measurement, the sintered sample was ground and polished to 0.5 µm using SiC papers and diamond suspension. Vickers hardness tests were carried out using 5 kg force in the Buhler Metallographic Laboratory UK and the hardness value was determined based on the equation 3.2. A schematic illustration of a Vickers' indent is shown in Figure 3.9. Crack length was measured with the help of an optical microscope and SEM. The indentation fracture toughness was derived from equation (3.3) [95].

$$H = 1.8544\frac{P}{d^2} \qquad (3.2)$$

Where H is hardness, P is indentation load and d is the average length of indentation diagonals.

$$k_c = 0.0752 \frac{P}{C^{3/2}} \qquad (3.3)$$

Where k_c is the indentation fracture toughness and C is the half of the mean radial crack length.

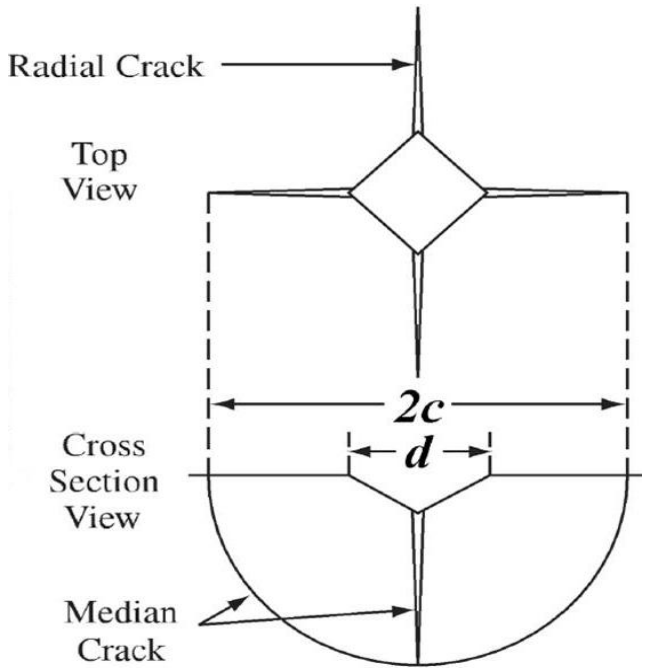

Figure 3.9. A schematic illustration of the typical Vickers' indent.

3.2.3.7 Fracture toughness measurement

An Instron mechanical tester (Figure 3.10) in the Science City Advanced Materials II Laboratory at the University of Birmingham was used to determine the fracture toughness of

the ceramic composites. The SENB method was used to measure the fracture toughness of the sintered samples. For the measurement, specimens of 2 mm (width) ×2.5mm (thickness) ×13mm (length) were machined. Notches of 0.5mm in depth and 0.2mm in width were cut at the centre of the test specimens. A span length of 10 mm and crosshead speed of 0.05mm min^{-1} were applied in the toughness tests. Three bars were tested for each material.

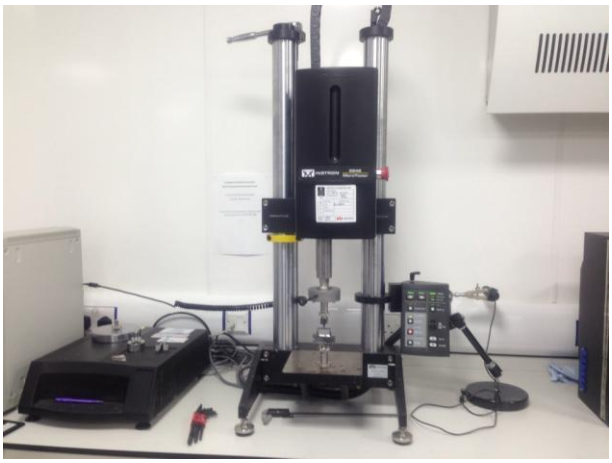

Figure 3.10. An image of the Instron mechanical tester

The configuration shown in Figure 3.11 was used for all specimens. The fracture toughness of the specimens was determined from the failure load and the geometry of the test piece using equations 3.4-3.6 [193].

$$K_{1c} = \sigma_f \sqrt{c} \times Y \quad (3.4)$$

$$\sigma_f = \frac{3PL}{2BW^2} \quad (3.5)$$

$$Y = 1.93 - 3.07\frac{c}{w} + 14.53\left(\frac{c}{w}\right)^2 - 25.07\left(\frac{c}{w}\right)^3 + 25.8\left(\frac{c}{w}\right)^4 \quad (3.6)$$

in which σ_f is the fracture strength, c is the depth of the notch, Y is the shape factor, P is the critical load and L, B and W are the span, width and depth of the specimen, respectively.

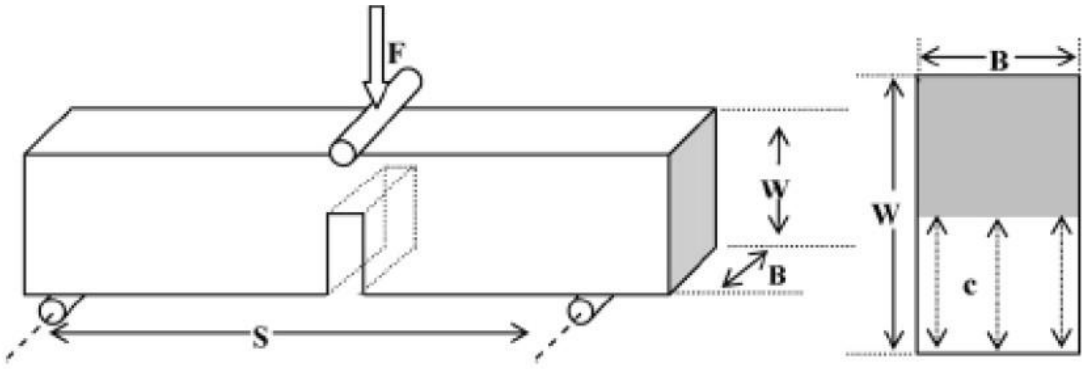

Figure 3.11. A schematic illustration of the SENB test.

3.3 Results and discussion

3.3.1 Selection of dispersants

The selection of proper solvents for dispersing GPLs is very important since the mechanical properties of the sintered ceramic composites are largely dependent on the dispersion of the GPLs, which determines the thickness of the GPLs and GPLs' distribution in the ceramic matrix. Research has shown that Hansen solubility parameters including δd (dispersion cohesion parameter), δp (polarity cohesion parameter) and δh (hydrogen bonding cohesion parameter) can be used to evaluate the dispersibility of carbon fillers in organic solvents [194]. It is suggested that a higher value of δp + δh are favourable for producing homogeneous dispersion of GPLs, while high δd seems more useful to achieve good dispersion of CNTs.Figure 3.12 compares colloidal dispersion stability of GPLs in ethanol,

DMF and N-Methyl-2-pyrrolidone (NMP). It can be seen that after one week GPLs are still very stable in DMF and NMP, while GPLs in ethanol agglomerate and settle swiftly after 2 hours. Such results indicate that good dispersion of GPLs can be obtained using DMF and NMP.

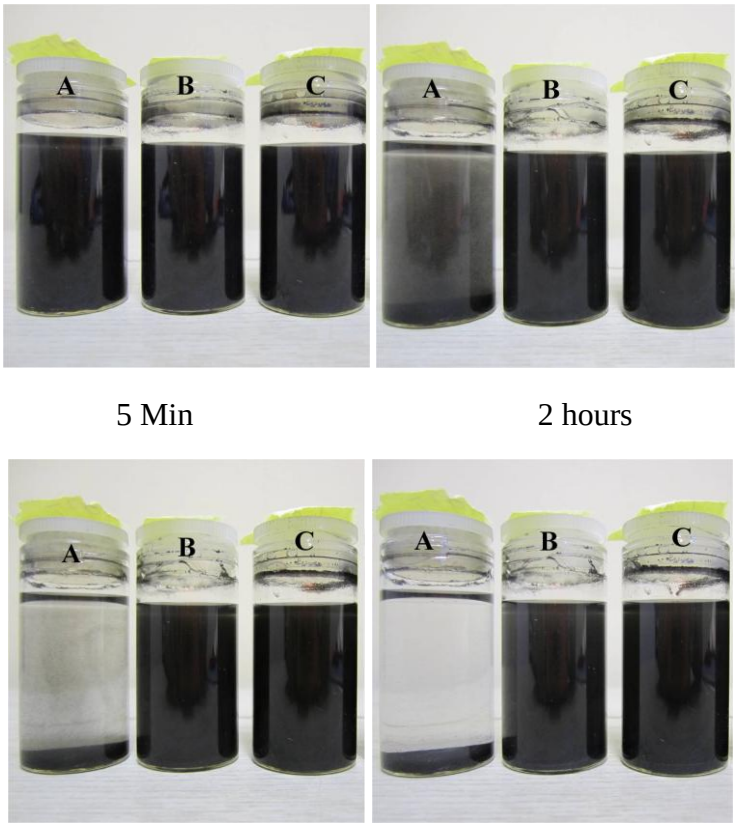

Figure 3.12. Comparison of colloidal dispersion stability of GPLs in different solvents after 1 hour ultrasonication. (A), (B) and (C) indicate dispersion of GPLs in ethanol, DMF and NMP. The concentration for all cases is 0.008 g/ml.

3.3.2 Densities of the powder mixtures

The densities of the powder mixtures measured using the pycnometer are shown in Figure 3.13. The results show that the density of the ZTA powder mixture is slightly higher than that of the GPL/ZTA powder mixture. Since the weight ratio of GPL powder to Al_2O_3 (0g/20g for pure ZTA and 0.1g/20g for GPL/ZTA) is known, the theoretical density and composition of the powder mixtures can be calculated according to rule of mixture using densities of 4, 5.9, 5.01 and 2.1 g m^{-3} for Al_2O_3, ZrO_2, Y_2O_3 and GPL. The composition of the powder mixtures is given in Table 3.1.

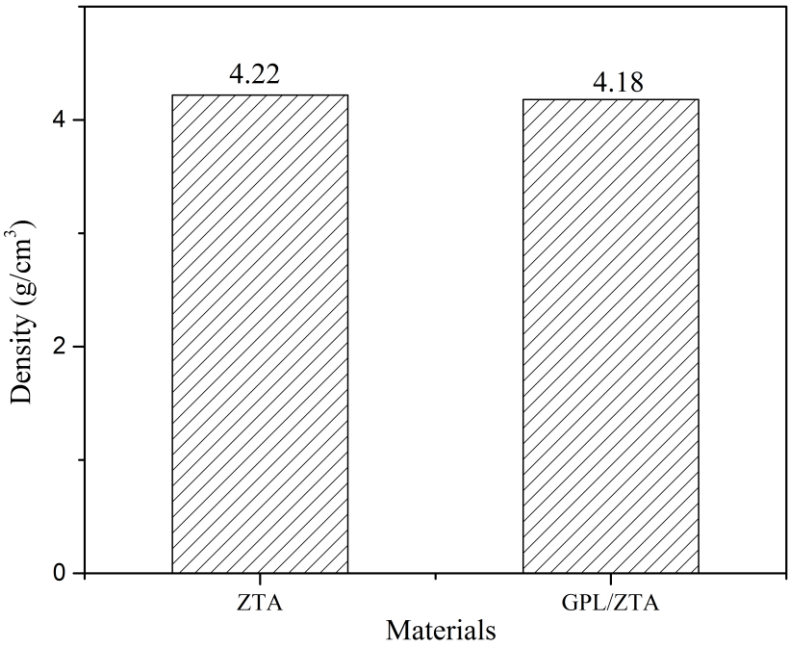

Figure 3.13. Densities of the powder mixtures

Table 3.1. Composition of the powder mixtures.

Powder mixtures	Al_2O_3 (vol%)	ZrO_2 (vol%)	Y_2O_3 (vol%)	GPL (vol%)
ZTA	88.43	10.89	0.68	0
GPL/ZTA	88.7	9.8	0.61	0.89

To further confirm the content of the ZrO_2, XRF was used to determine the composition of the powder mixtures. The results are shown in Table 3.2. Theoretical density and volume percentage of each material therefore can be calculated based on the XRF results and are given in Table 3.3. It can be noticed that ZrO_2 contents determined by XRF are slightly higher than those calculated from the true densities (4.22 g m^{-3} for Pure ZTA and 4.18 g m^{-3} for GPL/ZTA) measured by Helium pycnometry. The different densities obtained using gas pycnometry may be the result of considerable adsorption on the GPLs, which is suggested in the CNTs/glass powder mixtures and leads to inaccurate results [195]. Therefore the content of ZrO_2 determined by XRF is used in this research.

Table 3.2. Content of the oxides in the powder mixtures

Samples	Al_2O_3 (wt%)	ZrO_2 (wt%)	Y_2O_3 (wt%)	Others (wt%)
Pure ZTA	80.02	18.3	0.915	0.765
GPL/ZTA	80.34	17.8	0.864	0.996

Table 3.3. Theoretical density and composition of the powder mixtures

Samples	Theoretical density (g m^{-3})	Al_2O_3 (vol%)	ZrO_2 (vol%)	Y_2O_3 (vol%)	GPL (vol%)
Pure ZTA	4.26	85.90	13.31	0.79	0
GPL/ZTA	4.24	85.60	12.87	0.72	0.81

3.3.3 SPS behaviours of the GPL/ZTA composites

In order to get a better understanding of the sintering process, the temperature and displacement profiles are plotted in Figure 3.14. Taking Figure 3.14c as an example, the sintering process can be divided into three stages. The first stage (I) is within the temperature range from 400 to approximately 1200 ˚C. Particle rearrangement and packing are expected to occur during this stage due to the applied pressure and the relatively low temperature. Meanwhile, sintering necks are usually formed and slight shrinkage of the compact would be observed [196].

The second stage (II) is within the temperature range between approximately 1200˚C and 1600˚C. At this stage, the temperature is high enough for the grain boundary and volume diffusion processes to take place, which cause dramatic shrinkage with the formation of interconnected pores.

The third stage (III) is within the temperature range from approximately 1600 to 1650˚C. At this stage, isolated pores are normally formed at grain boundaries and triple junctions. The pores can shrink by the flux of vacancies from pores to the compact surfaces primarily through grain boundary diffusion [197]. However, abnormal grain growth and pore coarsening would likely happen in this stage resulting in degradation of the mechanical properties of the ceramics.

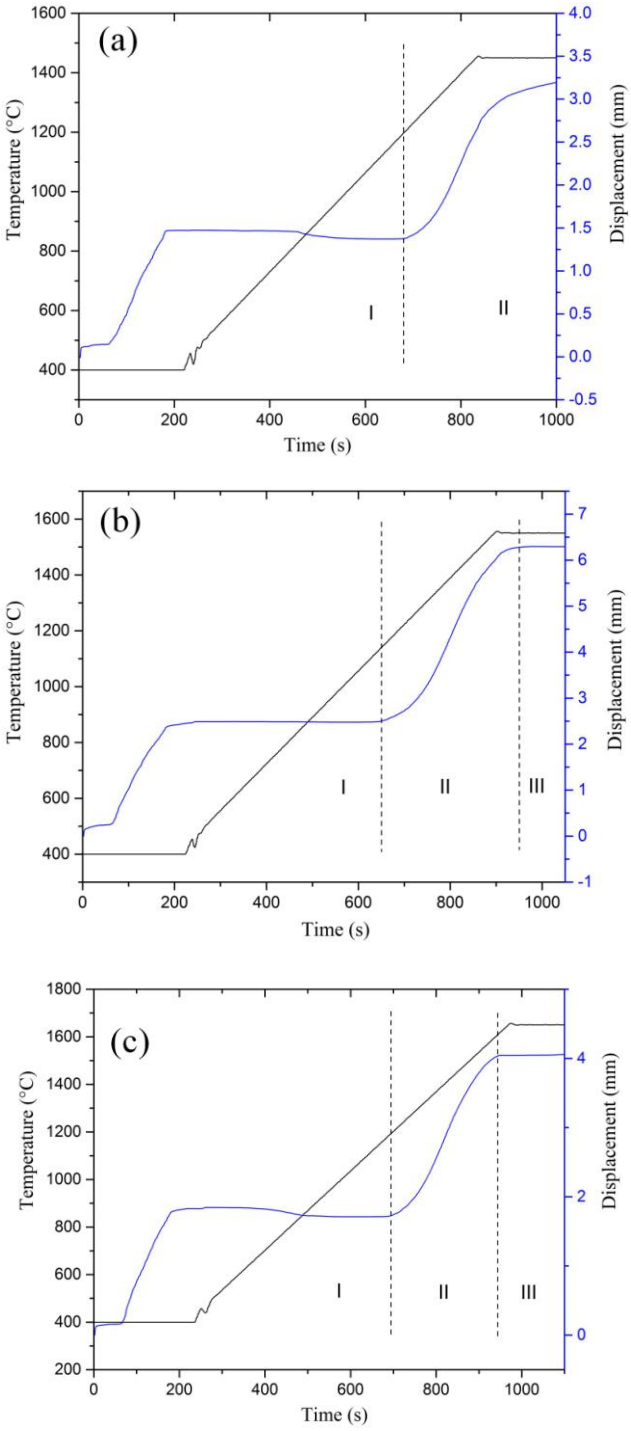

Figure 3.14. Temperature and displacement profiles of the sintered samples. (a), (b) and (c) are for samples sintered at 1450, 1550 and 1650 ˚C respectively.

It is evident that the displacement profiles under different sintering temperatures exhibit nearly the same first sintering stages, but differ in the second sintering stages which initiate at

around 1200 ˚C. Figures 3.14a and b show the second sintering stages still progress when sintering temperatures (1450 and 1550˚C) are reached, while Figure 3.14c exhibits the end of the second sintering stage before the sintering temperature (1650˚C) is attained. It is expected that after the sintering temperature is reached severe shrinkage and volume diffusion would still occur (Figure 3.14 a), or modest shrinkage and volume diffusion will possibly take place (Figure 3.14 b), or displacement varies little and surface diffusion is likely to dominate the soaking process (Figure 3.14c). Due to a long time surface diffusion leading to dramatic grain growth of the ceramic grains and degrading the mechanical properties of the ceramic materials, the optimum sintering temperature for consolidating the GPL/ZTA ceramic composite is believed to be lower than 1650 ˚C. To provide further insight into the sintering behaviour, the variation of the shrinkage rate with the temperature is plotted in Figure 3.15. It can be observed that maximum shrinkage rate is obtained for GPL/ZTA ceramic composite sintered at 1550˚C, implying that at this temperature the highest density of the GPL/ZTA ceramic composite can be reached.

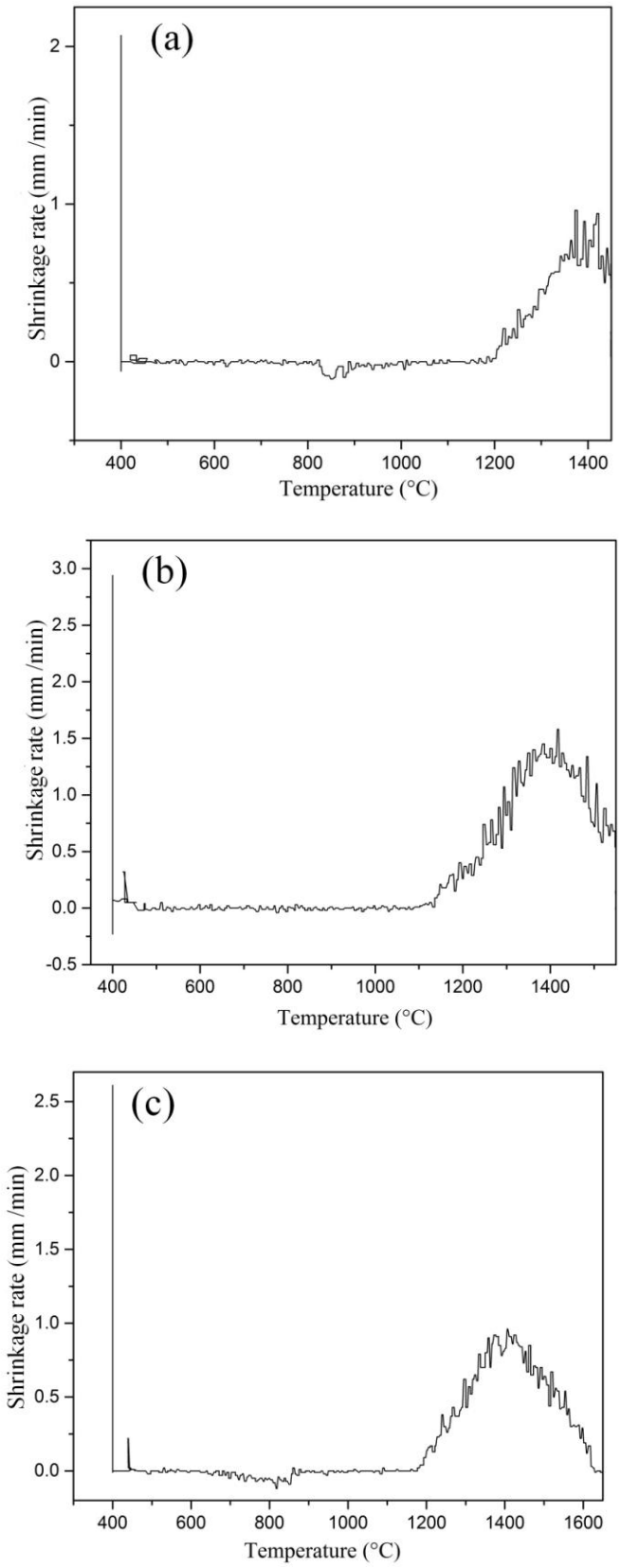

Figure 3.15. Variation of shrinkage rate with heating temperature. (a), (b) and (c) are for samples sintered at 1450, 1550 and 1650 ˚C respectively.

3.3.4 XRD patterns of the sintered samples

The phase composition of the ceramic composites was determined by XRD and the results are shown in Figure 3.16. It can be seen that all of the patterns consist of Al_2O_3 and ZrO_2. In addition, relative intensities of Al_2O_3 and ZrO_2 peaks are nearly the same in all of the XRD patterns, which indirectly demonstrates all the samples contain approximately the same amount of ZrO_2.

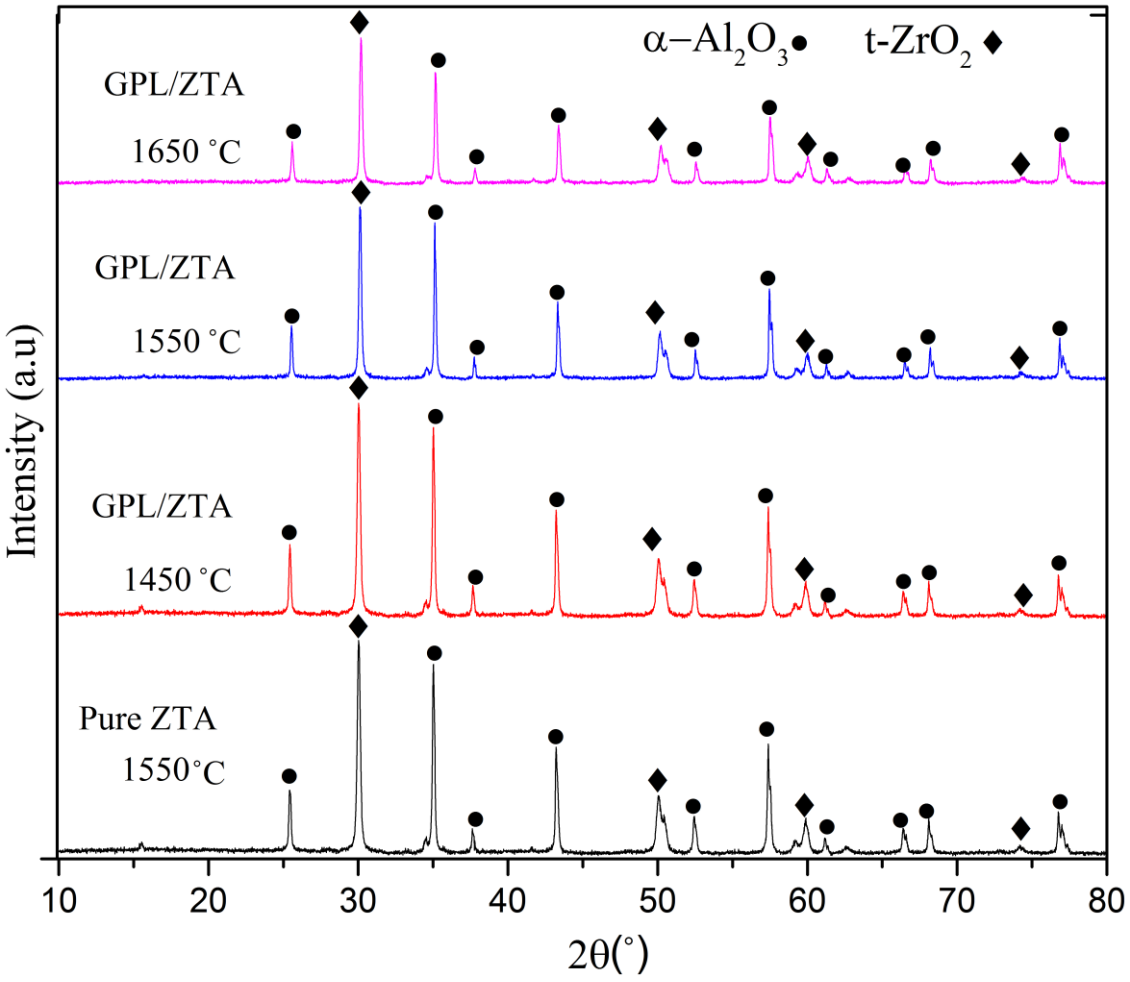

Figure 3.16. XRD patterns of ZTA and GPL/ZTA ceramic composites.

3.3.4 Raman spectra of GPLs in the sintered GPL/ZTA composites.

Figure 3.17 compares the Raman spectra of the pristine GPL and the GPLs in the sintered ceramic composites. It is evident that the GPLs in the sintered GPL/ZTA ceramic composites exhibit much higher intensities of G peaks than the pristine GPL and the intensities of the 2D peaks are much lower than those of the G peaks in the sintered ceramic composites.

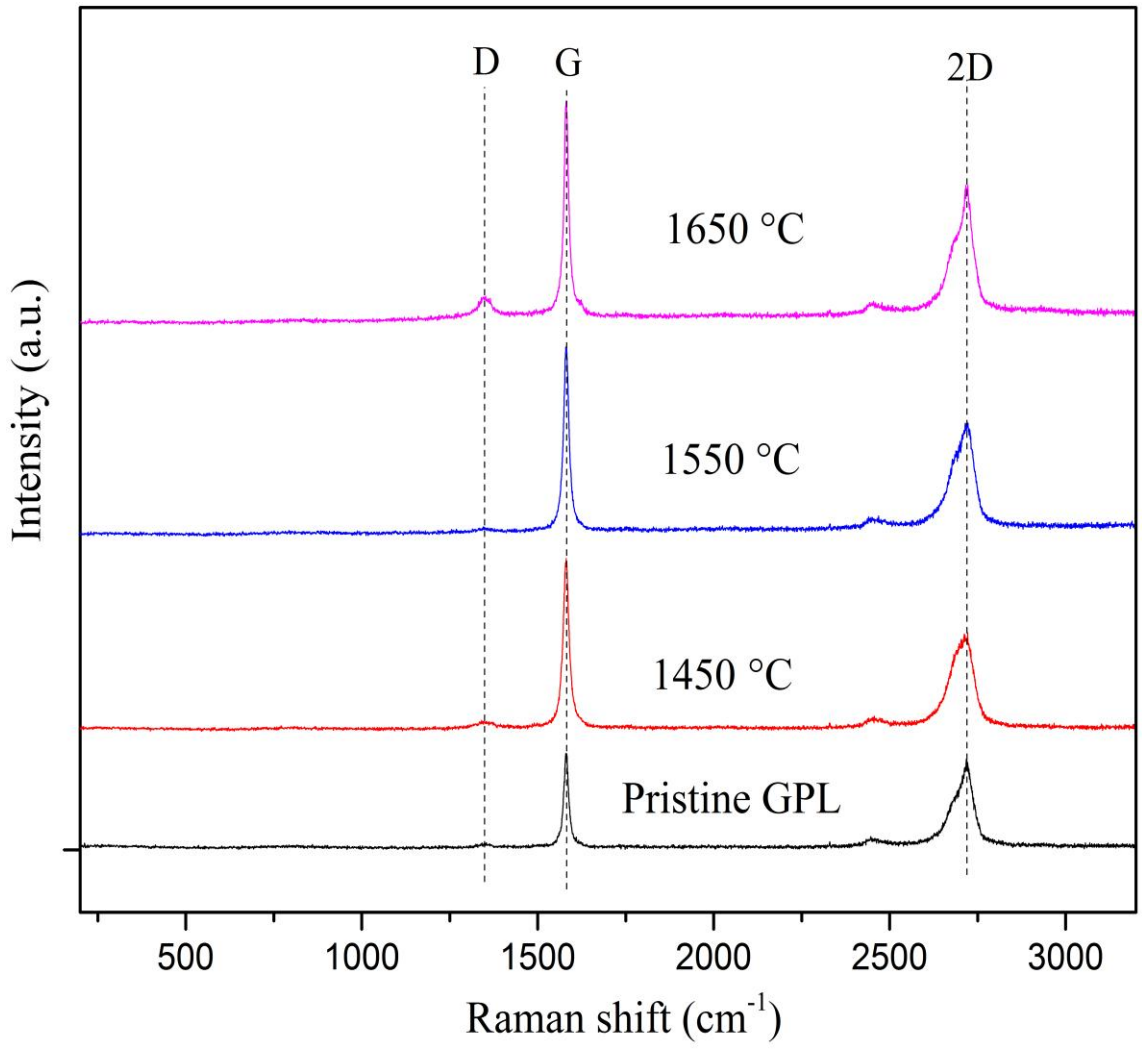

Figure 3.17. Raman spectra of the pristine GPL and the GPLs in the composites

To provide further analysis Raman parameters are summarized in Table 3.4. The ratio of intensities of D to G peaks (I_D/I_G) is usually used to quantify the density of defects in graphitic carbon materials [111]. It can be observed that the defect density of the pristine GPL is same as that of the GPLs in ceramic composites sintered at 1450 and 1550 ℃ while significantly higher defect density is obtained for samples sintered at 1650 ℃. This indicates that higher sintering temperature can introduce more defect density, probably by enhancing the interaction of GPLs with the ZTA ceramic matrix. Previous studies suggest that the ratio between intensities of the 2D and G peaks (I_{2D}/I_G) can be used to evaluate the graphene structure and usually I_{2D}/I_G decreases with the increasing number of graphene layers [113].

Table 3.4. Raman parameters of the pristine GPL and the GPLs in the composites.

Materials	Sintering Temperature (˚C)	I_D/I_G	FWHM (G)	ν (G)	FWHM (2D)	ν (2D)	I_{2D}/I_G
Pristine GPL	----	0.07	12	1581	64	2719	0.94
GPL in GPL/ZTA	1450	0.07	17	1580	75	2720	0.57
GPL in GPL/ZTA	1550	0.07	16	1580	68	2720	0.61
GPL in GPL/ZTA	1650	0.15	16	1580	65	2722	0.63

It is noted that I_{2D}/I_G of GPL in sintered ceramic composites is lower than that of the pristine GPL suggesting graphene layers in GPL increase during the ball milling process. In addition, I_{2D}/I_G for the GPL-reinforced composites increases with the increasing sintering temperature, which indicates thinning of the GPL occurs at high sintering temperatures and higher temperatures tend to enable the formation of thinner GPLs. This is supported by the decreasing full width at half maximum (FWHM) of 2D bands for the GPLs in the ceramic composites with the increasing sintering temperature. Meanwhile, it is also noticed that the position of the G band of GPLs in the composites shifts to a lower wave number in

comparison with that of the pristine GPL and the position of the 2D bands shifts to a higher wave number. The shifting of the G and 2D bands can be attributed to the thermal stress incurred due to the different contraction of the GPL and the ZTA ceramic matrix.

3.3.5 Microstructures of the 'as-prepared' samples

Figure 3.18 shows the SEM images of the fracture surfaces of the samples with and without GPLs. Usually a pure Al_2O_3 sample indicates an intergranular fracture mode. However, as can be seen from Figure 3.18a, ZTA composite presents a mixture of intergranular and transgranular fracture modes and ZrO_2 particles are either embedded within the Al_2O_3 or distributed at the boundary between Al_2O_3 particles. The change in fracture mode is a clear indication of enhanced grain boundary induced by the introduction of ZrO_2 particles. In comparison with the ZTA samples, GPL-reinforced ZTA composites present a decreasing fraction of the transgranular mode. Such a fracture mode suggests the bonding strength between GPLs and the matrix is less strong than that between ZrO_2 and Al_2O_3, and less than the strength of the Al_2O_3 grains.

Figure 3.19 shows the SEM images of the thermally etched samples sintered at 1550˚C. It can be observed that pure ZTA exhibits many elongated grains while GPL/ZTA composite presents more spherical grains. This indicates that the introduction of GPLs helps hinder the growth of elongated grains and causes the formation of a more homogenous microstructure.

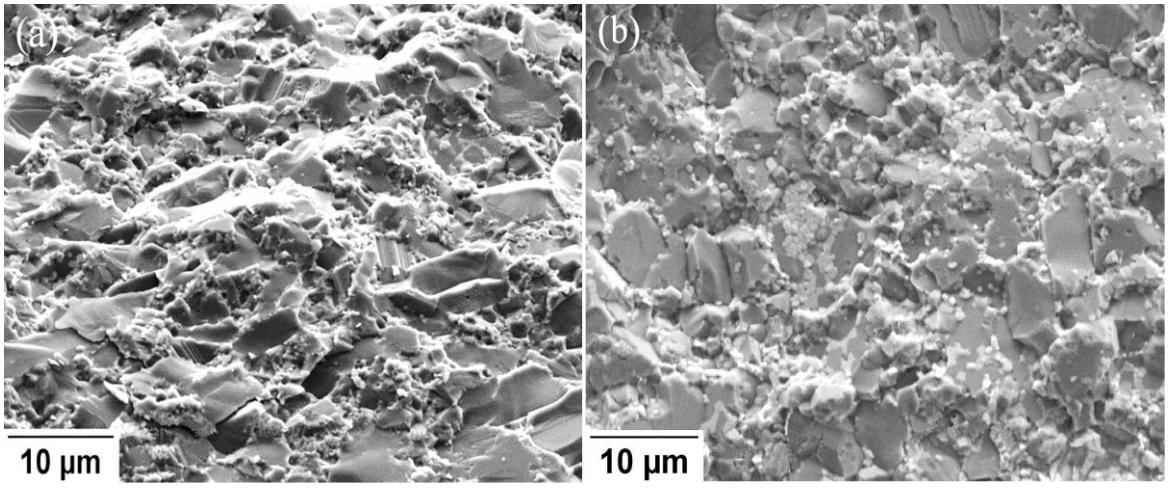

Figure 3.18. SEM images of fracture surfaces of the samples sintered at 1550˚C (a) is the sample without GPLs and (b) is with GPLs.

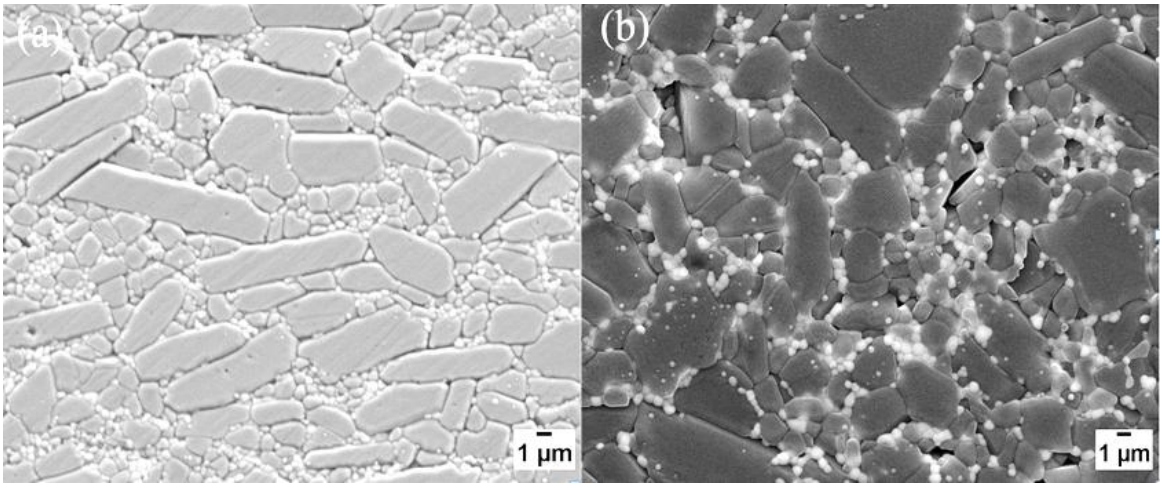

Figure 3.19. SEM images of the thermally etched surfaces. (a) pure ZTA (b) GPL/ZTA composites.

Figure 3.20 shows the SEM images of the fracture surfaces of the sample sintered at 1650˚C. From the highly magnified images, it can be seen that many GPLs are well distributed in the ceramic matrix, indicating a result of good dispersion of GPLs.

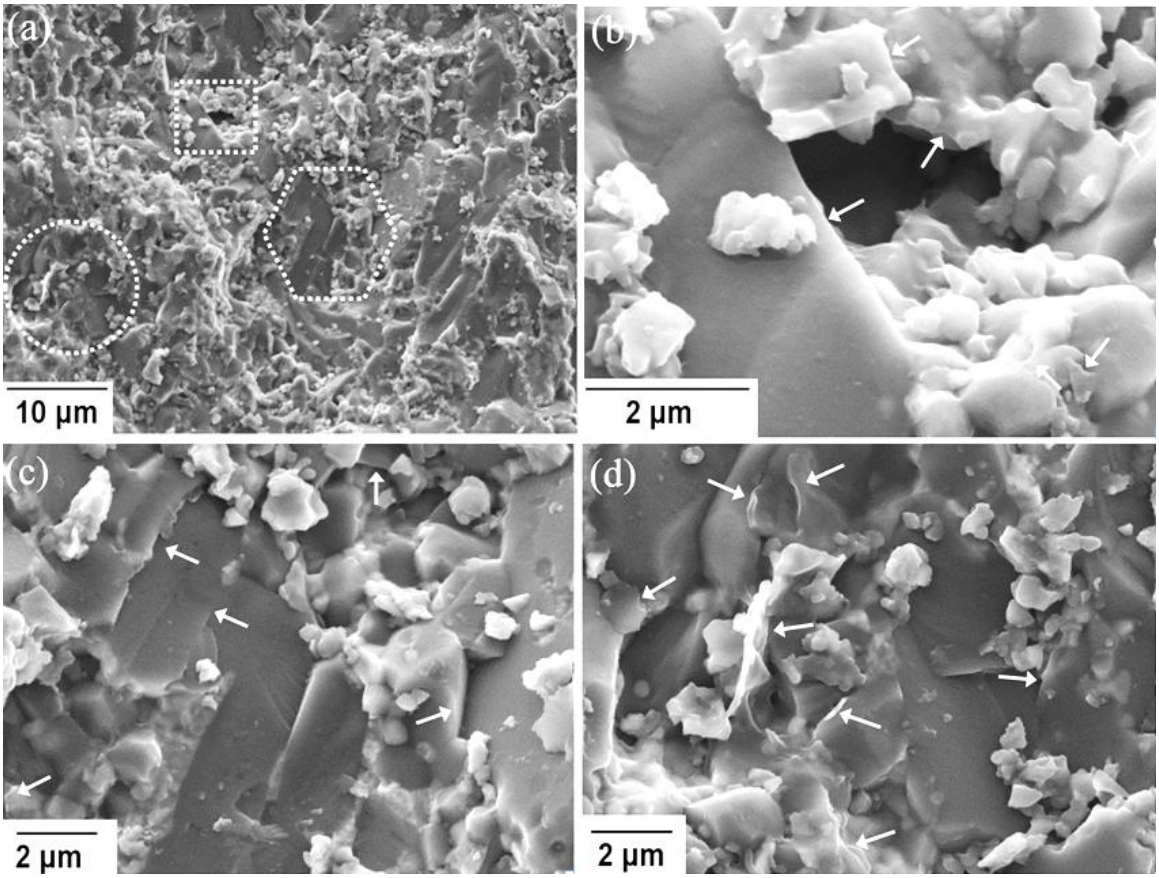

Figure 3.20. SEM images of fracture surfaces for GPL-reinforced ZTA composite sintered at 1650˚C, (b), (c) and (d) are the magnified parts of square, hexagonal and circular areas in (a). The white arrows point at GPLs.

3.3.6 Mechanical properties of the sintered samples

Relative densities of the sintered samples are shown in Figure 3.21. It can be seen that all of the samples nearly achieve full density during the sintering process. Meanwhile, it is noted that at the same sintering temperature, composites with GPLs have relatively lower densities than pure ZTA, which implies that the introduction of GPLs hinders the densification process.

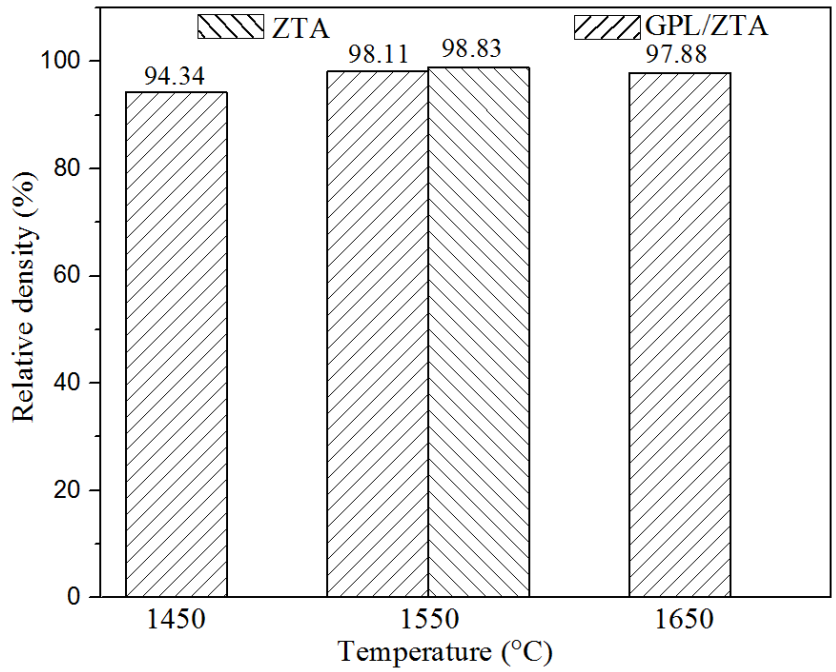

Figure 3.21. Relative densities of the sintered ZTA and GPL/ZTA composites

Figure 3.22 shows hardness of the sintered samples. It can be observed that the hardness of GPL/ZTA samples increases when the sintering temperature is increased to 1550 ˚C and decreases with the temperature further increased to 1650˚C. As expected, a pure ZTA sample sintered at 1550˚C has greater hardness than the GPL/ZTA sample because of its higher relative density. The fracture toughness of GPL/ZTA ceramic composites and pure ZTA is plotted in Figure 3.23. It can be seen that the introduction of GPLs considerably improves the fracture toughness of the ZTA ceramic matrix. Similar to hardness, fracture toughness increases with the temperature but decreases with the further increase of the temperature. The maximum fracture toughness of 9.05MPam$^{1/2}$ is achieved for the samples sintered at 1550˚C and approximately 40% increase in fracture toughness has been obtained. Such an increase is comparable to CNT-reinforced ceramics [198, 105, 199, 93, 200]. As can be seen from Table 3.3, the contents of ZrO_2 and Y_2O_3 vary little in ZTA and GPL/ZTA ceramic composites,

therefore it is believed that the improvement of fracture toughness can be attributed to the addition of GPLs.

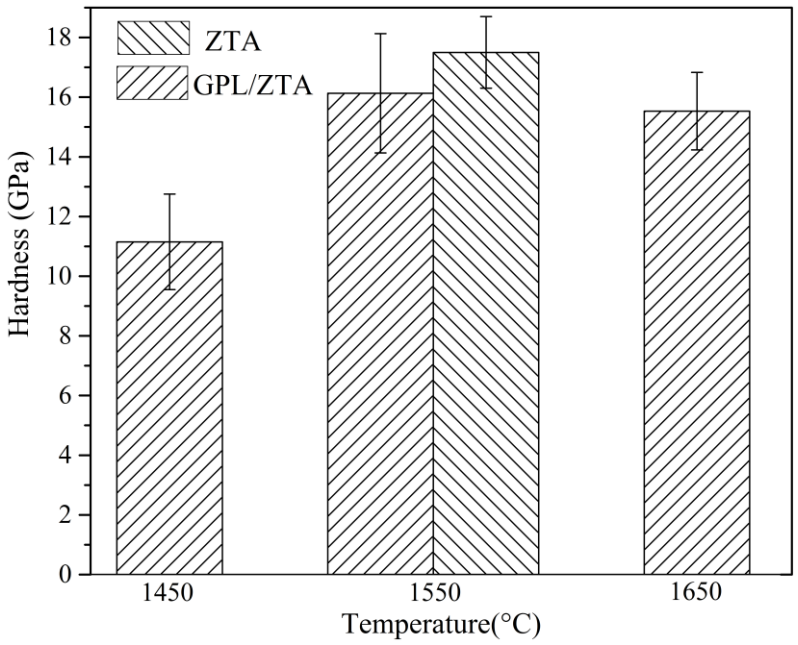

Figure 3.22. Hardness of the sintered ZTA and GPL/ZTA composites.

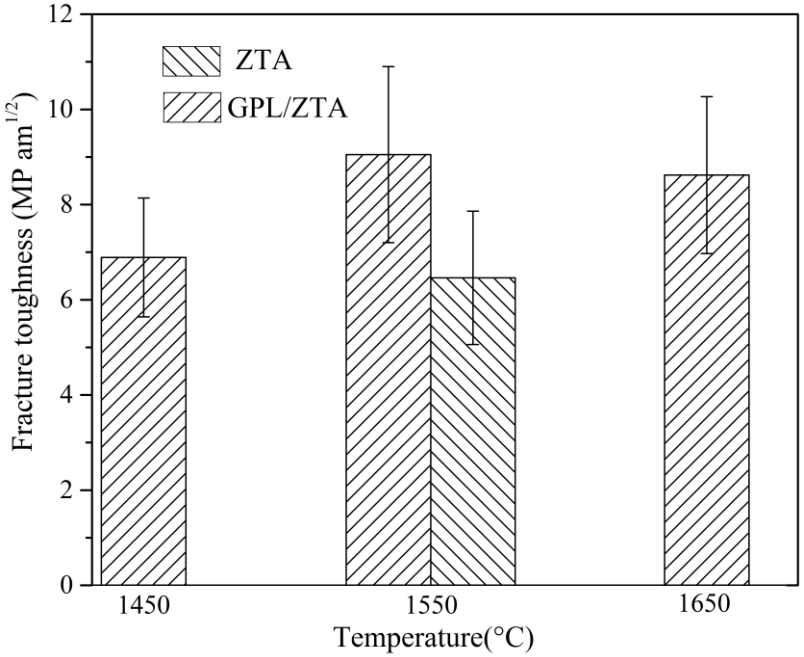

Figure 3.23. Fracture toughness of the sintered ZTA and GPL/ZTA composites.

3.3.7 Toughening mechanisms in the GPL/ZTA ceramic composites

Toughening mechanisms such as pull-out, crack bridging and crack deflection are observed in the GPL/ZTA composites. As can be seen from Figure 3.24, a very thin layer of graphene sheet seems strongly anchored within the ceramic matrix (Figure 3.24a and b) and a large interface area between the GPL and ceramic matrix is created during the consolidation process (Figure 3.24c).

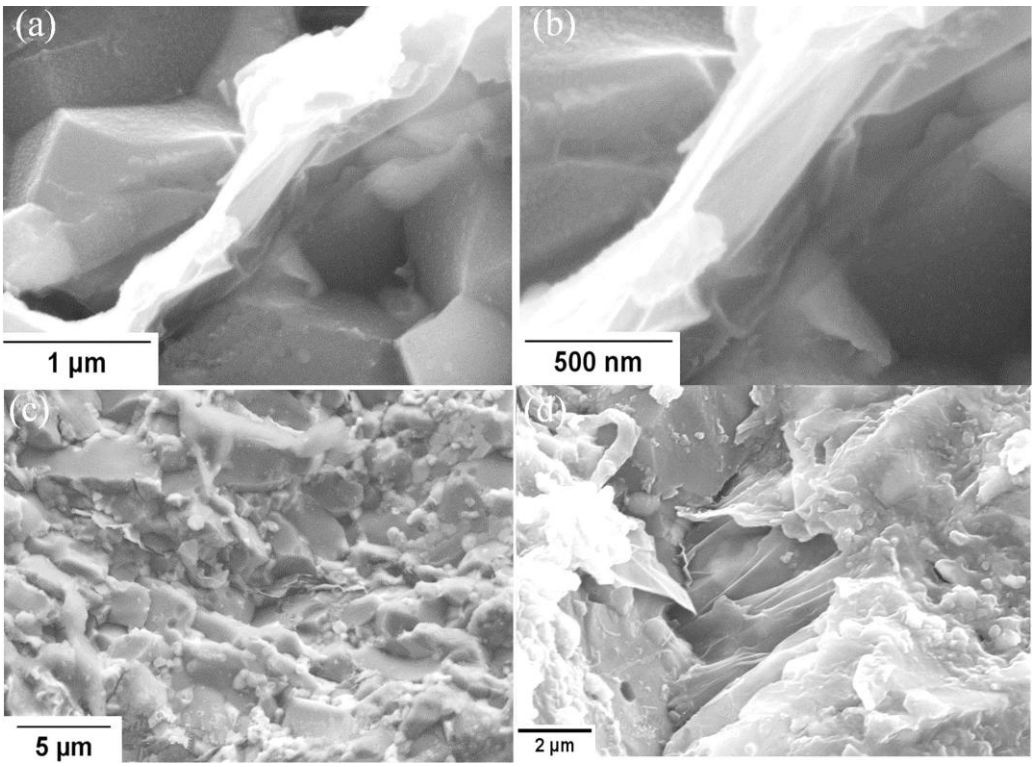

Figure 3.24. SEM images of fracture surfaces of GPL/ ZTA composite sintered at 1650˚C.

It is suggested that interfacial friction generated at the interface would make it difficult for the pull-out process to proceed, which would significantly improve the fracture toughness of the ceramic matrix. In addition, the more contact area formed between GPLs and ceramic matrix, the more difficult it would be to pull out graphene sheets. Meanwhile, it is observed

that ceramic matrix grains are bridged by a number of graphene sheets (Figure 3.24d), which serve a function to prevent the development of cracks.

On the other hand, a crack deflection toughening mechanism is noticed and shown in Figure 3.25. It can be seen that a crack is stopped when meeting with a large GPL and deflects in-plane (Figure 3.25a). It is expected that a tortuous crack path is likely to be created and would help release the stress because of the crack deflection. Another example of crack deflection is shown in Figure 3.25c, in which a few layers of graphene drape over the fracture surface, indicating that GPLs direct the fracture along its surface.

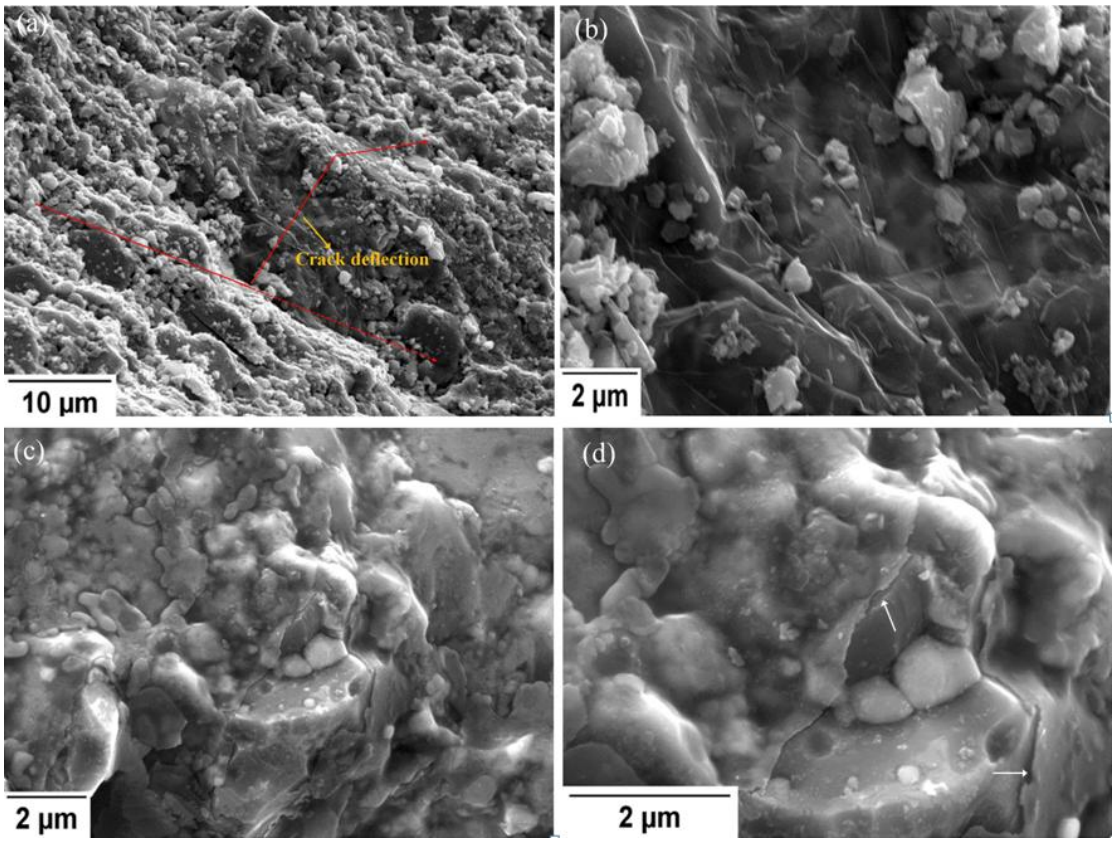

Figure 3.25. SEM images of fracture surfaces of GPL/ZTA composite sintered at 1450˚C (a-b) and 1650˚C (c-d). (b) is the magnified GPL in (a). (d) shows the magnified GPL in (c). The solid and dashed lines in (a) indicate the crack paths with or without GPL. White arrows point at GPLs.

3.3.8 Indentation fracture toughness of the pure ZTA and GPL/ZTA composites

Indentation fracture toughness of the pure ZTA and GPL/ZTA sintered at 1550 ˚C was compared and shown in Figure 3.26. It can be observed that the indentation fracture toughness of the ceramic matrix is significantly improved by adding the GPLs and nearly a 30% increase in fracture toughness is achieved for GPL/ZTA ceramic composites. To reveal the indentation toughening mechanisms, cracks stemming from the indents are characterized using SEM. As shown in Figure 3.27, pull-out, crack bridging and crack deflection toughening mechanisms are observed and are believed to seriously prevent the progress of the cracks. It should be noted that the indentation fracture toughens is much smaller than that obtained using the SENB method. Based on the fracture toughness shown in Table 2.3, it is expected that in this chapter the K_{IC} of ZTA composites determined by the SENB is likely to

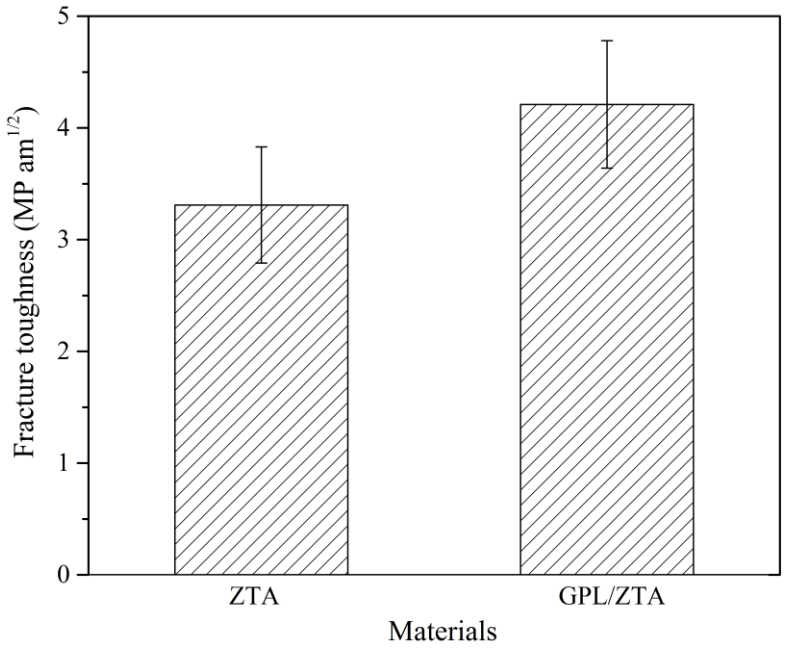

Figure 3.26. Indentation fracture toughness of the pure ZTA and GPL/ZTA ceramic composites.

be overestimated. This might be associated with the sizes of the test specimens and notches as it is reported that a small specimen and a wide notch tend to result in a high fracture toughness [193, 201].

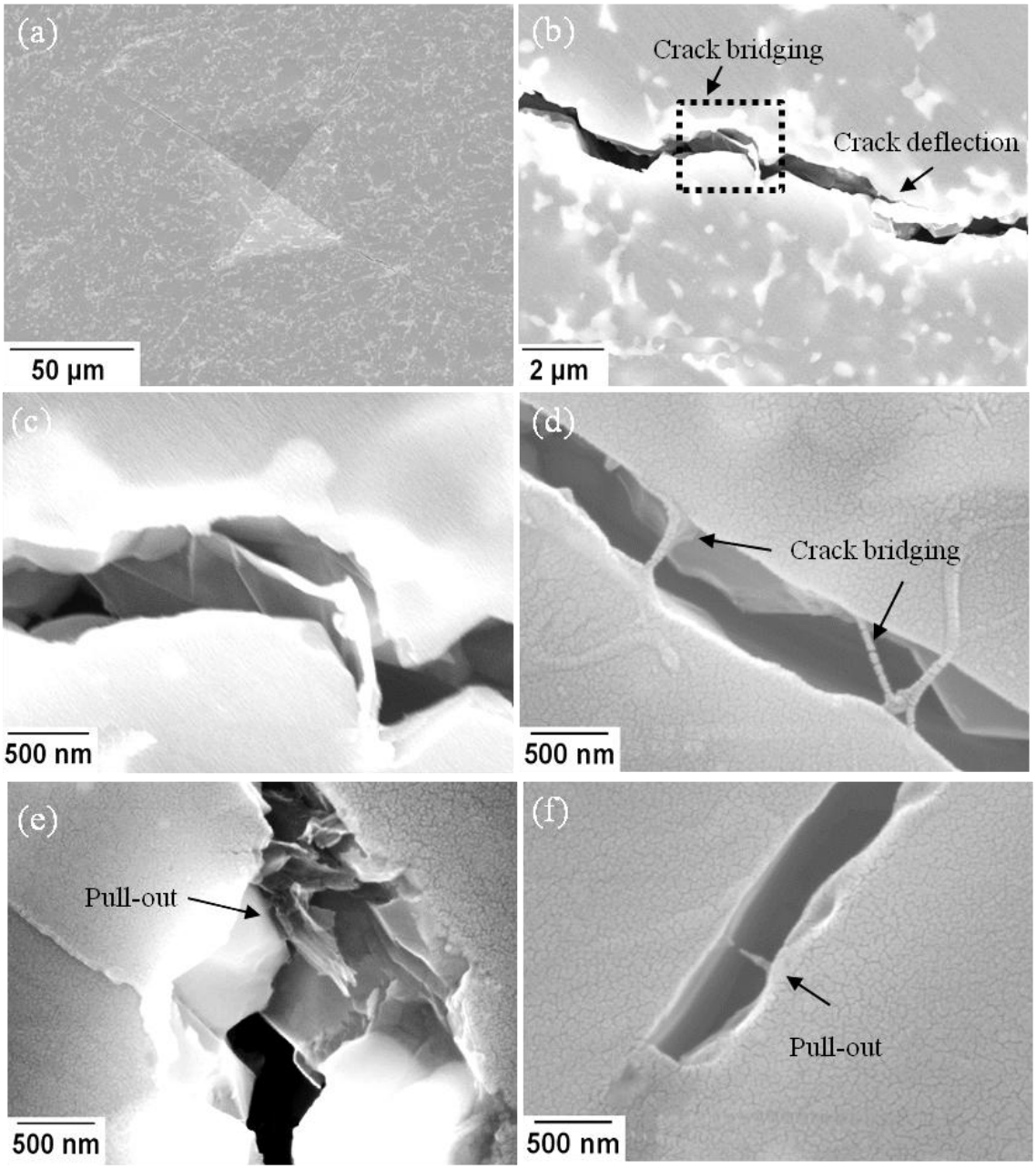

Figure 3.27. SEM images of a micro hardness indent (a) and radial cracks (b-f). (c) is magnified part of the square area in (b).

In Walker's research [19], GPL-reinforced Si_3N_4 composites produced a 135% increase in toughness over the monolith. Such a high increase in toughness is attributed to a variety of toughening mechanisms, including crack deflection in three dimensions. In this work, the three-dimensional toughness mechanism has not been observed. The difference in the observed results may be explained as follows: in a fibre-reinforced ceramic, the high strength of the reinforcing fibres is critical because once a matrix crack is initiated and extended, load is transferred from the matrix to the fibres in the wake of the crack. If the interface is weak enough for the matrix crack to be deflected along the interface, the fibre remains intact and the composite can be tough. If the interface is too strong, the matrix crack penetrates through the fibre and the composite is brittle like a monolithic ceramic[202].

Similar to a fibre-reinforced composite, there can be three ways a crack propagates in a GPL-reinforced ceramic composite, i.e. singly deflected crack, doubly deflected crack and penetrating crack across the reinforcing platelets, as shown in Figure 3.28. However, the crack propagating behaviour can be different with the introduction of GPLs. Due to the high strength and large specific surface area of GPLs, when the bonding between GPLs and the matrix is strong, the crack may cross it to form a three dimensional path instead of penetrating the GPLs (Figure 3.28d), as indicated by the red line in Figure 3.28f. It is expected that composite ceramics of a nano grain matrix can be tougher than those of a micro grain matrix at the same density, as they provide more contact areas with the GPL. Therefore, three dimensional cracks are more likely to be observed in the composite ceramics of nano grains whereas deflection in-plane is prone to take place in ceramics of micro grains.

In the research of this chapter, it is found that fracture propagation is resisted by bridging, pull-out and two dimensional deflection of GPLs. Considering the increased contact area and

large GPLs which provide a lengthy deflection path, the contribution to toughness brought by GPLs can be much greater than that by nano fibres.

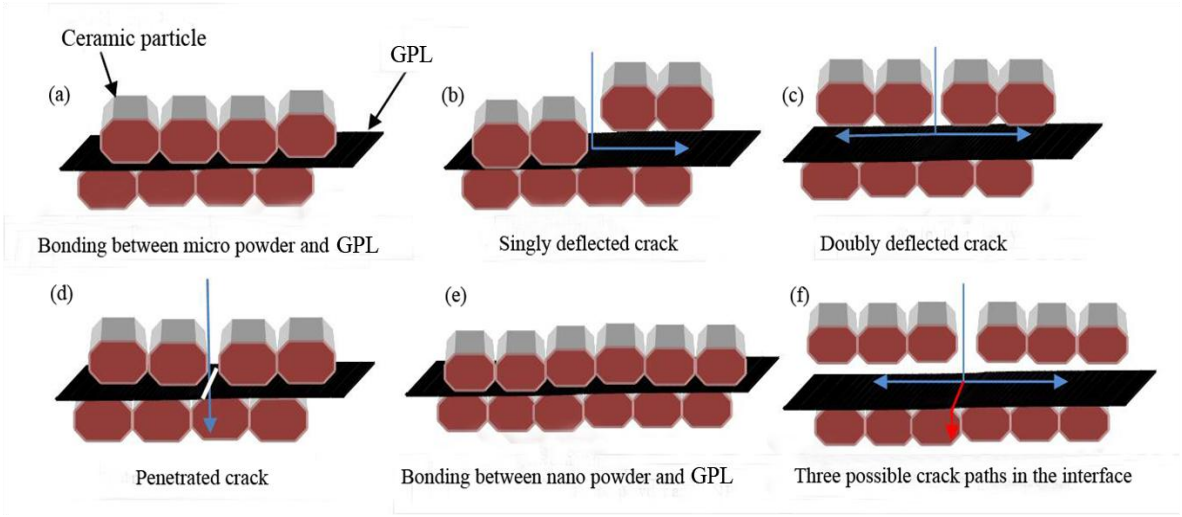

Figure 3.28. Schematic illustrations of toughening mechanisms in GPL-reinforced ceramic composites with micro and nano scale ceramic matrices.

3.4 Summary

In this chapter, research on preparation and characterisation of GPL/ZTA ceramic composites was carried out. The results of the research can be summarized as follows:

1. DMF has shown to be a very effective dispersant to achieve a good dispersion of GPLs, as suggested by the wide distribution of GPLs in the ZTA matrix.

2. Higher sintering temperatures tend to introduce more defect density in GPLs and result in the formation of thinner GPLs, probably by enhancing the interaction of GPLs with the ZTA matrix.

3. The optimum sintering temperature for consolidating GPL/ZTA composites is 1550 ˚C as the largest shrinkage rate and highest density are obtained at this temperature.

4. Hardness of GPL/ZTA is lower than that of pure ZTA. The fracture toughness of the ZTA matrix is significantly improved by adding 0.81 vol% GPLs. The maximum fracture toughness of the GPL/ ZTA composites determined by a SENB method is 40% higher than that of the pure ZTA while indentation fracture toughness of GPL/ZTA composites is 30% higher than that of the pure ZTA.

5. Pull-out of GPLs, crack bridging and crack deflection have been observed and believed as the causes of increased fracture toughness.

The presented research shows GPLs as nanofillers have potential to considerably improve the fracture toughness of ceramic composites and lead to a variety of light and strong ceramics to suit engineering applications.

Chapter 4: SPS and characterization of GPL/Al_2O_3 and GPL-SiC/Al_2O_3 composites

4.1 Introduction

This chapter presents SPS and characterization of Al_2O_3 based composites with the addition of nano fillers. GPL-reinforced Al_2O_3 composites and GPL/SiC-reinforced Al_2O_3 composites were prepared respectively and their microstructures and mechanical properties were studied. The aim of the research is to find the optimum content of the nano fillers for improving the mechanical properties of the Al_2O_3 matrix material. To begin with, experiments of the fabrication process and related characterization techniques are introduced in Section 4.2. Afterwards, results and discussion are presented in Section 4.3. In particular, GPL-reinforced Al_2O_3 composites prepared using SPS are introduced in Section 4.3.1, where their microstructures and mechanical properties are presented and the optimum content of the GPLs is found by comparing the mechanical properties of the GPL/Al_2O_3 composites with different additions of GPLs. Additionally, in Section 4.3.2 the Al_2O_3 composites reinforced with GPLs and SiC nanoparticles sintered using SPS are introduced. The microstructures and mechanical properties of the GPL-SiC/Al_2O_3 composites are presented. The effects of dual fillers on the microstructure and mechanical properties of the Al_2O_3 composites are discussed. Finally, the chapter is summarized in Section 4.4.

4.2 Experiments of fabrication process

The experiments in the research of this chapter are similar as those described in section 3.2 in Chapter 3. The major difference is that the powder mixtures of GPL/Al_2O_3 and GPL-SiC/ Al_2O_3 are prepared by ball milling processes with a low ball-to-powder ratio and contamination from the grinding balls is avoided.

4.2.1 Powders

In the research of this chapter, α-Al_2O_3 nanopowders, β-SiC nanoparticles and GPLs were used for the preparation of GPL/Al_2O_3 and GPL-SiC/Al_2O_3 powder mixtures. α-Al_2O_3 powders (99.85%, 150 nm, Inframat Advanced Materials, Farmington, CT, USA) and β-SiC nanoparticles (99.85%, 40nm, Shang Hai Chaoweinami, Ltd) were employed in this study. SEM images of the Al_2O_3 and SiC nanoparticles are shown in Figure 4.1. The detailed information of the GPLs is given in section 3.2.1 in Chapter 3.

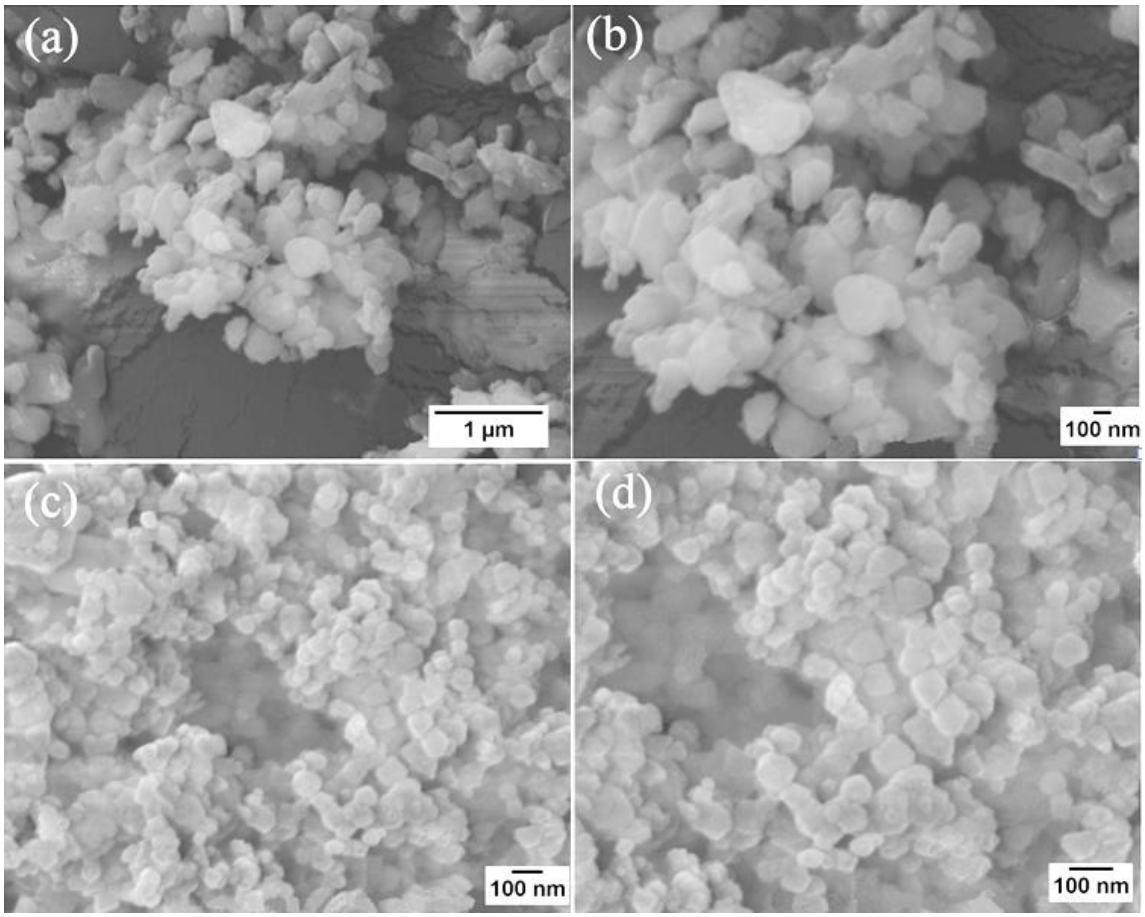

Figure 4.1. SEM images of Al_2O_3 (a-b) and SiC (c-d) powders. (b) and (d) are the magnified images of (c) and (d).

4.2.2 Composite powder preparation and sintering

GPL/Al_2O_3 and GPL-SiC/Al_2O_3 ceramic nanocomposites were prepared in the research of this chapter. The fabrication processes for the two types of ceramic composites are nearly the same and can be divided into two stages. The first stage is to prepare the powder mixtures. They were prepared by mixing the Al_2O_3 powders with nano fillers which are treated with ultrasonication in DMF. The mixing was carried out at 100 rpm in a planetary ball mill (PM 100, Retsch, UK) for 2 hours. A grinding jar of zirconia (ZrO_2) and ZrO_2 balls with diameters of 10 mm were used during the ball milling process. In order to avoid contamination from the

grinding balls, a small ball-to-powder weight ratio of 2 was selected for the milling process. Afterwards, the milled slurry mixture was dried and sieved. A brief summary of the powder preparation process is given in Figure 4.2. SEM images of the powder mixtures are shown in Figure 4.3.

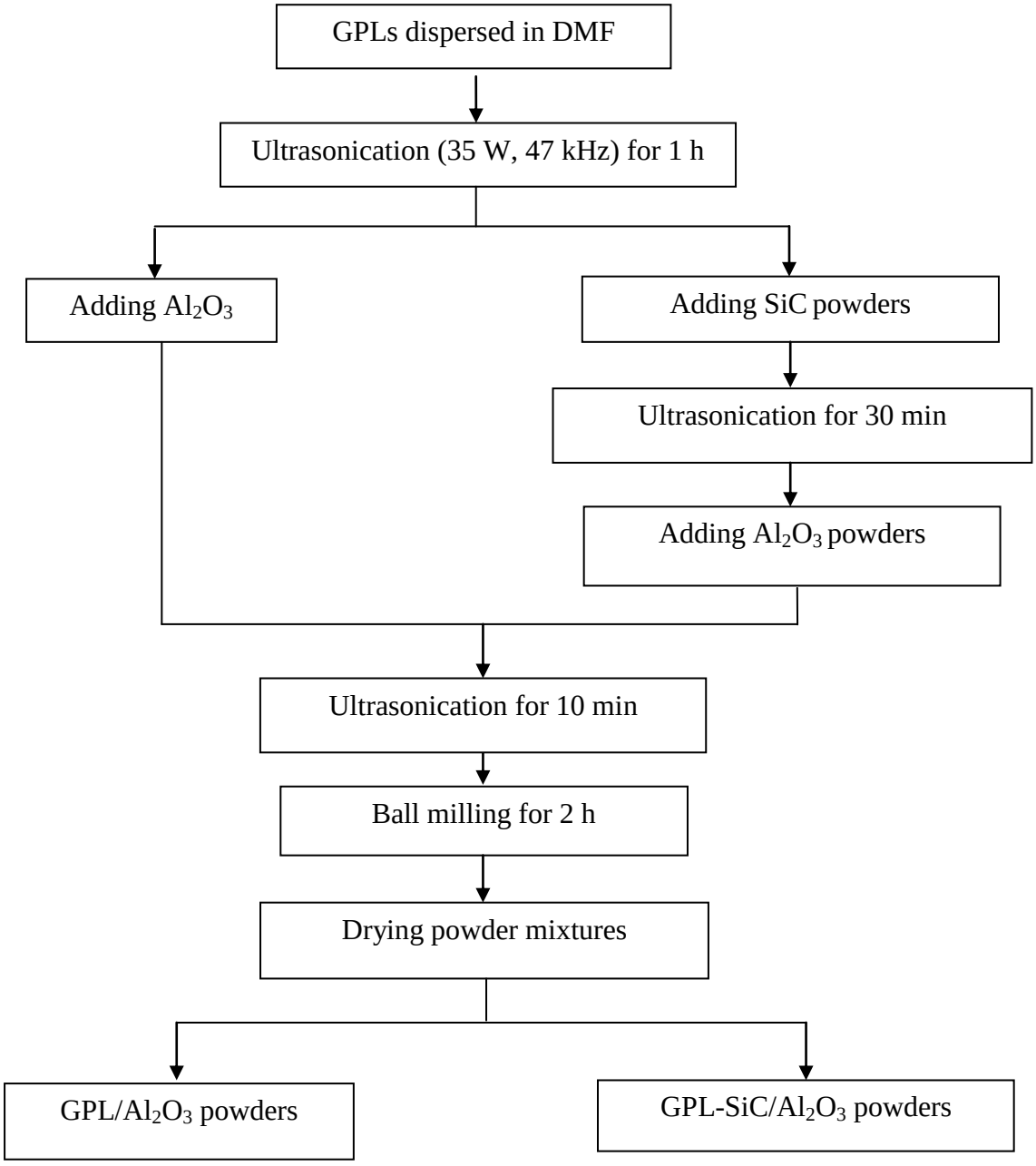

Figure 4.2. The flow chart of the preparation of the powder mixtures

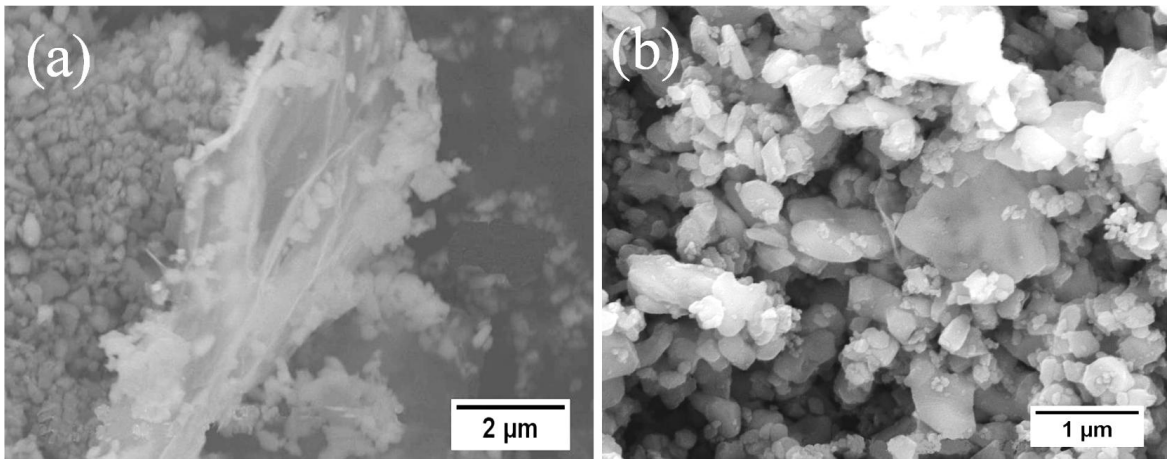

Figure 4.3. SEM images of the GPL/Al_2O_3 (a) and GPL-SiC/Al_2O_3 (b) powder mixtures.

The second stage is to consolidate the powder mixtures using a SPS furnace. Based on previous reports [203, 121], sintering temperatures of 1500-1650 ˚C and a heating rate of 50 min/˚C were selected to achieve the densification process. For comparison purposes, pure Al_2O_3 ceramic was sintered.

4.2.3 Material Characterizations

Equipment and characterization techniques such as SEM, Raman spectroscopy and the density measurement method introduced in Chapter 3 were also employed in the research of this chapter. In particular, the SEM was used to examine the polished surfaces of the samples and grain size of each material was determined with the aid of the ImageJ software (UTSHCSA, USA) by taking at least 200 readings. Meanwhile, in the research a SEVNB method was used to measure the fracture toughness of the sintered samples and three-point bending tests were employed to obtain flexural strength of the sintered samples.

4.2.3.1 Bending tests

To obtain the flexural strength and fracture toughness of the sintered samples, three-point bending tests were carried out on an Instron 6025 using a load cell of 1KN. For the flexural strength tests the configuration shown in Figure 4.4a was used and specimens of 1.5 × 2 × 25 mm were machined according to ASTM C1161-02c. The span length and crosshead speed for the strength tests were 20 mm and 0.05 mm min^{-1}. To avoid stress concentration, all the edges and corners of the specimens were chamfered using SiC grinding paper. Equation 4.1 was used to determine the flexural strength of the specimens [1].

$$S = \frac{3PL}{2BW^2} \qquad (4.1)$$

Where S is the flexural strength, P is the maximum loading, L is the length of the support span and B and W are the width and thickness of the specimen respectively.

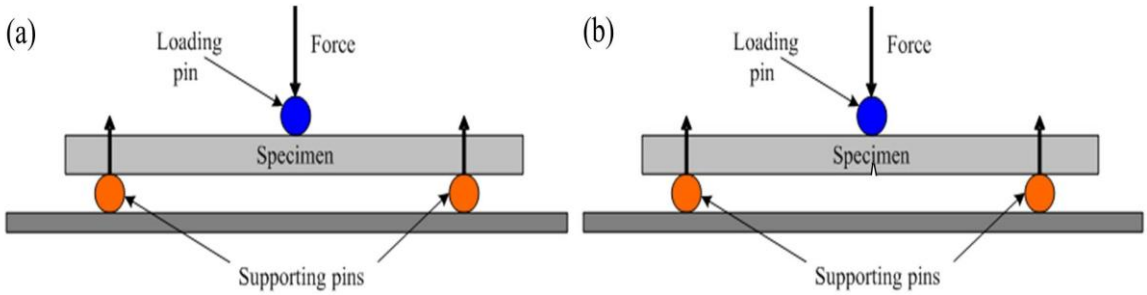

Figure 4.4. Schematic illustrations of three-point bending configurations for the measurements of the flexural strength (a) and fracture toughness (b).

The SEVNB method was used to measure the fracture toughness of the sintered samples at room temperature. Test specimens of 3 × 4 × 36 mm were machined for the measurement in

accordance with international standard (ISO 23146). Notches at the centre of the test specimens were cut by a diamond wheel and further sharpened using a razor blade with the aid of diamond paste up to 1 μm. The ratio between the notch depth and specimen thickness was approximately 0.25-0.5 for the sintered composites. As shown in Figure 4.4b, the notch within the specimen should be aligned with the imposed force in order to obtain valid results. A span length of 30 mm and crosshead speed of 0.05 mm/min were applied in the toughness tests. Five samples were tested for each material. The toughness was determined based on equation 4.2 [1].

$$K_{Ic} = \frac{P}{B\sqrt{W}} \cdot \frac{L}{W} \cdot \frac{3\sqrt{a/W}}{2} \cdot Y \qquad (4.2)$$

Where K_{Ic} is the fracture toughness, P is the fracture load, B is the width of the specimen, W is the depth of the specimen, L is the support span, a is the V notch depth and Y is the stress intensity shape factor, which is described as the following relation:

$$Y = 1.964 - 2.837\frac{a}{W} + 13.7714(\frac{a}{W})^2 - 23250(\frac{a}{W})^3 + 24109(\frac{a}{W})^4 \qquad (4.3)$$

4.2.3.2 Micro hardness measurement

For the Vickers hardness test, the sintered sample was ground and polished and a load of 1kg was introduced onto the surface of the sample for a duration of 10 seconds with a diamond indenter. Vickers hardness was determined using the equation (3.2) described in Chapter 3.At least five measurements were carried out for each sample.

4.3 Results and discussion

4.3.1 GPL-reinforced Al_2O_3 ceramic nanocomposites

4.3.1.1 Sintering behaviours of the samples during SPS

Temperature and displacement profiles for samples sintered at 1500 ˚C were plotted in Figure 4.5. It can be seen that when the temperature is below 1400 ˚C, pure Al_2O_3 shows slightly higher displacement than the GPL/Al_2O_3 composite, which suggests that the addition of GPLs in Al_2O_3 impedes the densification process of the ceramics. As discussed in section 3.3 in Chapter 3, the sintering profiles can be generally divided into three stages: I - particle rearrangement and partial sintering of the particles in which sintering necks are unusually formed; II - violent volume and boundary diffusion, in which formation of interconnected pores occurs; III - removal of the formed pores through diffusional creep. Clearly the second stage, where considerable shrinkage takes place, plays a dominant role during the densification process.

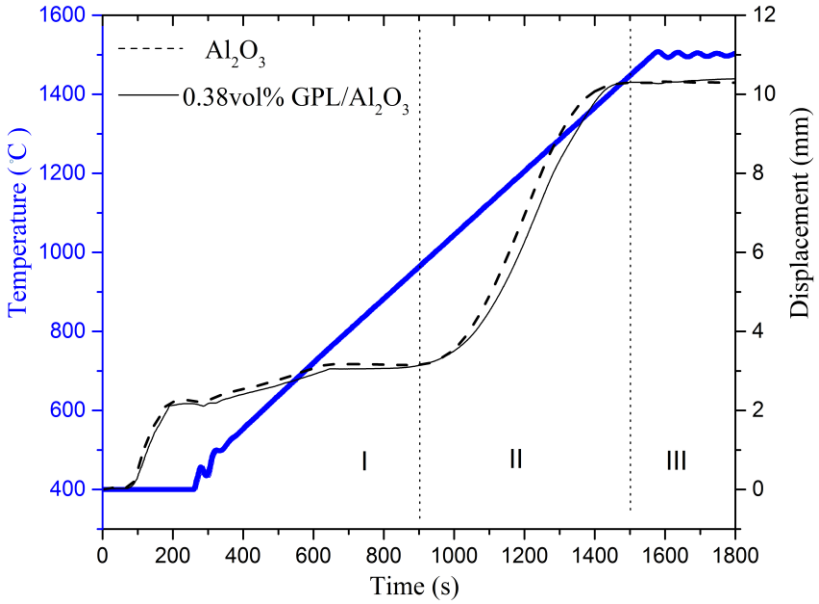

Figure 4.5. Temperature and displacement profiles for the pure Al_2O_3 and 0.38 vol% GPL/Al_2O_3 composite.

To get a further insight of the second stage, variation of shrinkage rate with the temperature is plotted in Figure 4.6. Three distinctive periods can be noticed in this stage. The first period shows the increasing trend of the shrinkage rate within the temperature range between 950 and 1230 ˚C, where the shrinkage rate for the pure Al_2O_3 sample is higher than that for the GPL/Al_2O_3 composite. The second period exhibits a decreasing trend of the shrinkage rate within the temperature range of between 1230 to 1300˚C, in which shrinkage rates for both pure Al_2O_3 and GPL/Al_2O_3 samples are nearly the same. The third period presents a decreasing trend of the shrinkage rate as in the second period. However, the shrinkage rate of the GPL/Al_2O_3 composite is higher than that of the pure Al_2O_3 sample. It is expected that in the first stage, more sintering necks are formed in the pure Al_2O_3 sample than in the GPL/Al_2O_3 composite due to the addition of GPLs. The densification process through either volume or grain boundary diffusion therefore proceeds faster in the pure Al_2O_3 sample (period 1). With the progress of the sintering process, more sintering necks will be formed in

the GPL/Al_2O_3 composite and densification process is thus expected to proceed in a faster way in the GPL/Al_2O_3 composite than in pure Al_2O_3 at the later sintering period. Consequently, the shrinkage rate of GPL/Al_2O_3 composite will be higher than that of the pure Al_2O_3 sample with the further sintering process (period 3). The different densification behaviours of the pure Al_2O_3 sample and the GPL/Al_2O_3 composite, further support the argument that the introduction of GPLs causes inhibition of the densification process.

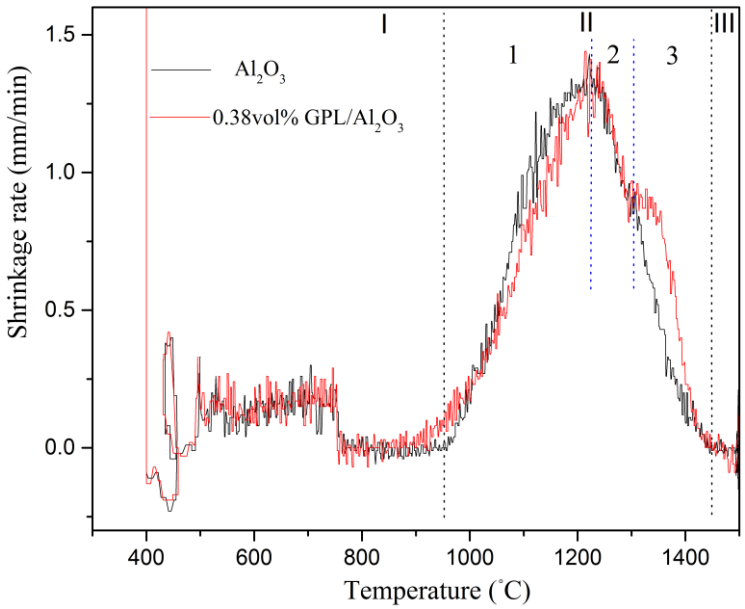

Figure 4.6. Profiles of shrinkage rates for the pure Al_2O_3 and 0.38vol% GPL/Al_2O_3 composite.

4.3.1.2 Microstructures of the ceramic composites

Sintered ceramic samples were fractured and their microstructures were examined. Figure 4.7 shows the SEM images of the fracture surfaces of the sintered samples. It can be seen that the GPLs are well distributed in the ceramic matrix. From the fracture surfaces, which present a mainly intergranular fracture mode, debonded GPLs pulled out from the ceramic matrix can be observed [1]. In addition, in comparison to the pure Al_2O_3 sample where large and uneven

grains are observed, GPL/Al_2O_3 composites exhibit more uniform microstructures. Meanwhile, as shown in Figure 4.7b-e, GPLs tend to be distributed between ceramic grain boundaries and prevent the migration of the grain boundaries, resulting in the refinement of the microstructures.

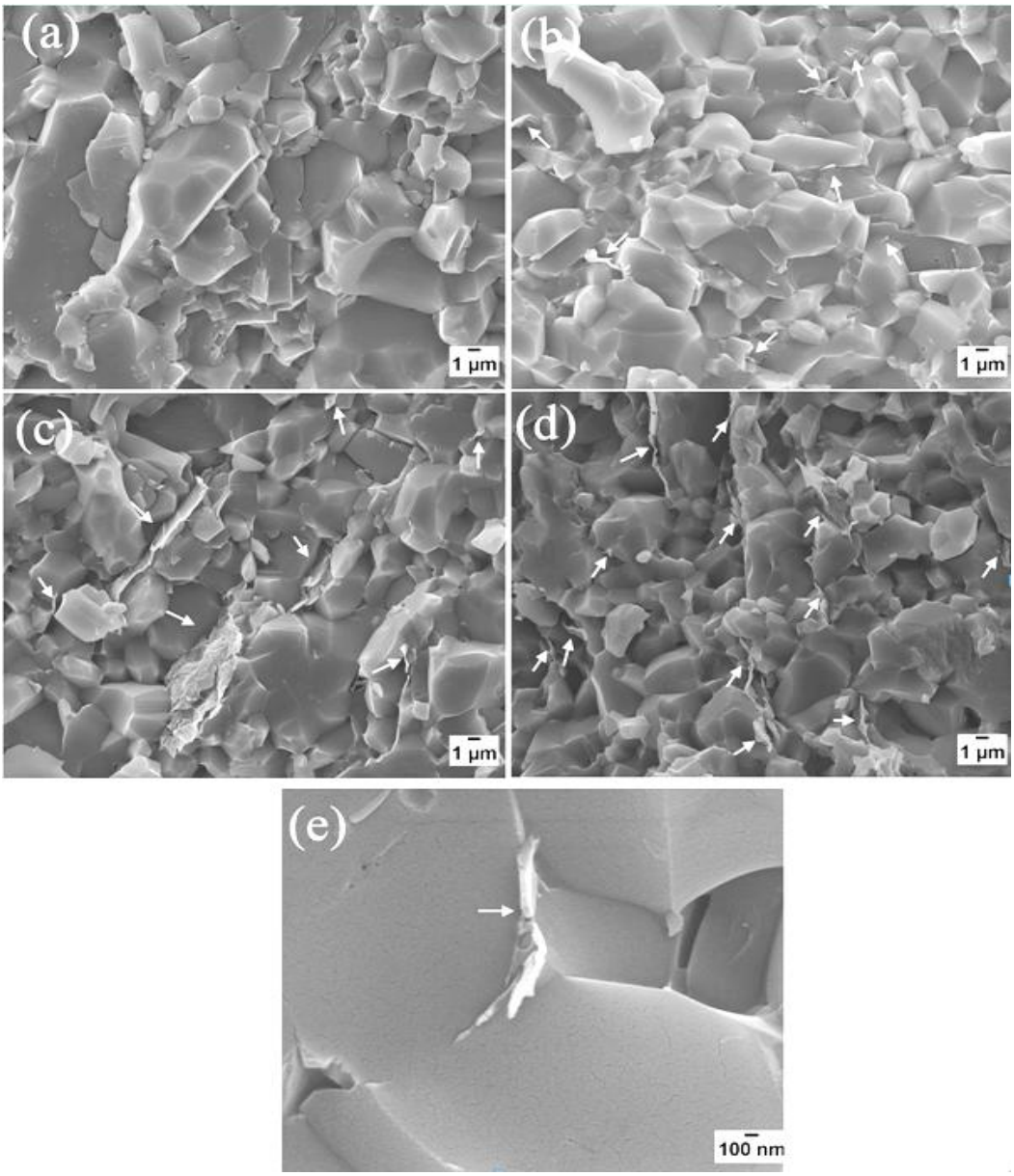

Figure 4.7. SEM images of fracture surfaces of the pure Al_2O_3 samples (a), 0.38 vol% GPL/Al_2O_3 composite (b), 0.76 vol% GPL/Al_2O_3 composite (c) and 1.33 vol% GPL/Al_2O_3 composite (d). The arrows point at GPLs. (e) A high magnification SEM image showing the pinning effect of GPLs in the grain boundaries.

4.3.1.3 Mechanical properties of sintered samples

Table 4.1 gives the densities of the sintered samples. It can be seen that all of the samples are nearly fully densified and the addition of GPLs results in a slight decrease in the relative density.

Table 4.1. Densities of the sintered samples.

Materials	Al_2O_3	0.38 vol% GPL/ Al_2O_3	0.76 vol % GPL/ Al_2O_3	1.33 vol% GPL/ Al_2O_3
Sintering temperature	1500˚C	1500˚C	1550˚C	1550˚C
Sintering time	3 min	3 min	3 min	3 min
Relative density	100±0.55	99.58±0.33	99.92±0.35	99.87±0.48

The hardness of the ceramics was examined and the results are given in Figure 4.8. As expected, the introduction of the GPLs causes the lower degree of hardness of the ceramic composites. Especially the addition of 1.33vol% GPLs results in approximately 10% decrease in hardness for the GPL-reinforced Al_2O_3 composites. Such a decrease can be explained by the relatively lower density of the GPL/Al_2O_3 composites and the lower degree of hardness of the added GPLs.

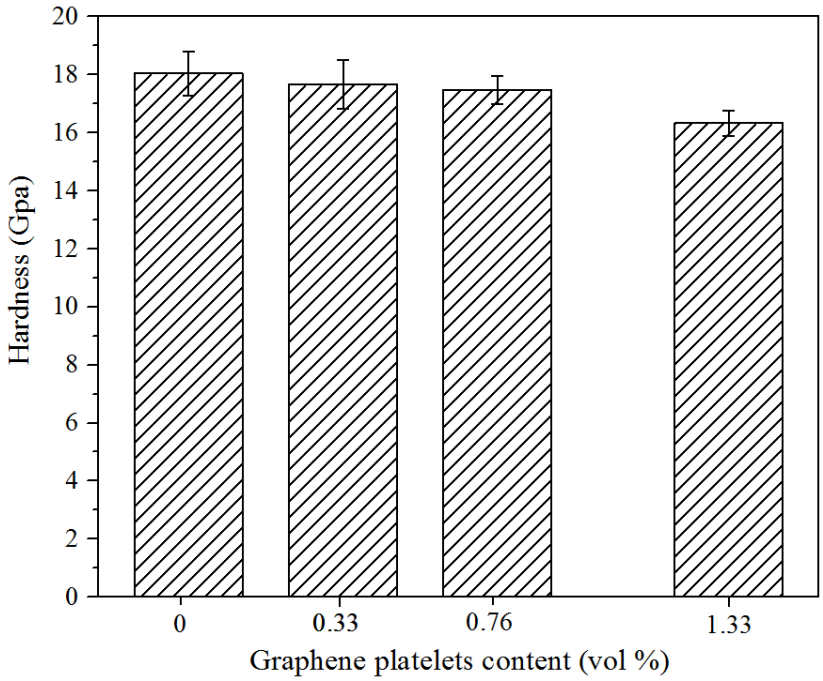

Figure 4.8. Hardness of the GPL/Al_2O_3 composites as a function of GPLs content.

Flexural strength and fracture toughness of the ceramic composites were evaluated using a three-point method and are shown in Figure 4.9 and 4.10. It is noticed that flexural strength and fracture toughness are significantly improved with the minor addition of GPLs. Both the flexural strength and fracture toughness decrease with the further increase of the GPLs. The maximum flexural strength and fracture toughness are obtained by adding 0.38 vol% GPLs, reaching 523±30 MPa and 4.49±0.33 MPa $m^{1/2}$ respectively. Compared to the pure Al_2O_3 sample, approximately a 31% and a 27% increase in flexural strength and fracture toughness have been achieved respectively.

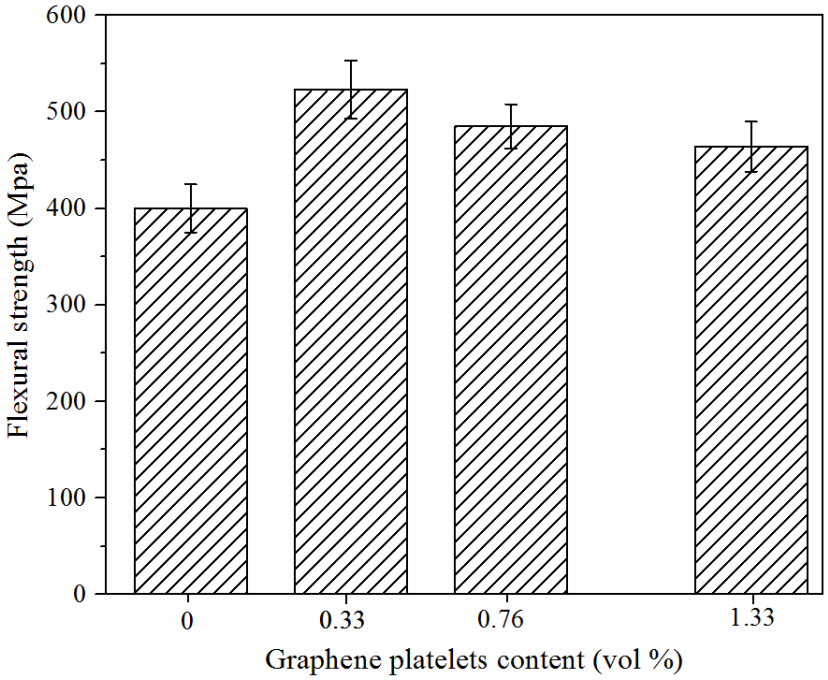

Figure 4.9. Flexural strength of the GPL/Al_2O_3 composites as a function of GPLs content.

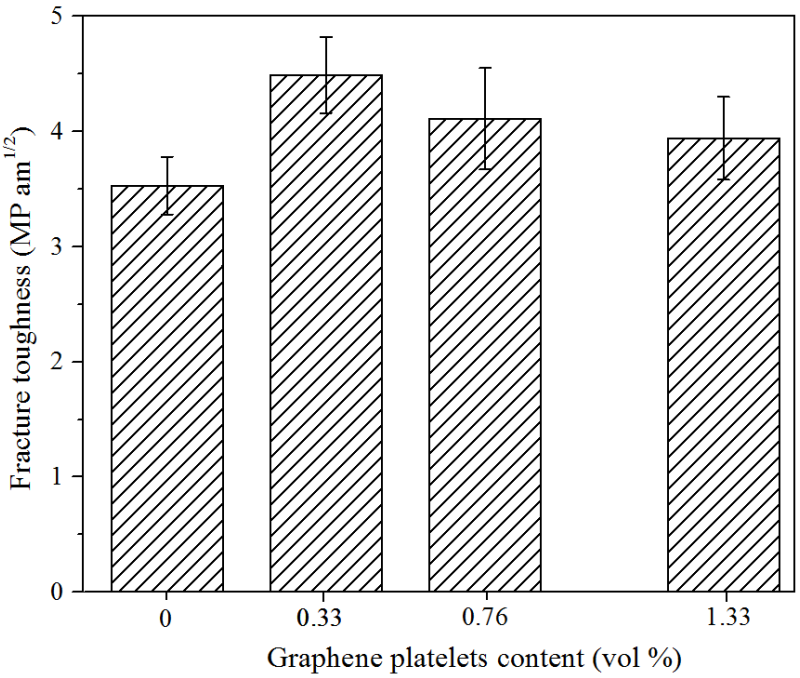

Figure 4.10. Fracture toughness of the GPL/Al_2O_3 composites as a function of GPLs content.

It should be noted that the radii of the notch is a very vital factor for obtaining a valid fracture toughness. It is suggested that a larger size of the notch results in higher value of the fracture toughness and radii of the notch below 10 μm is recommended [204]. In the research, a radii of a notch between 10-20 μm, close to the recommended value is used. Figure 4.11 shows SEM images of a notch before the bending test (Figure 4.11 a-b) and optical images of a notch after the bending test (Figure 4.11 c-d).

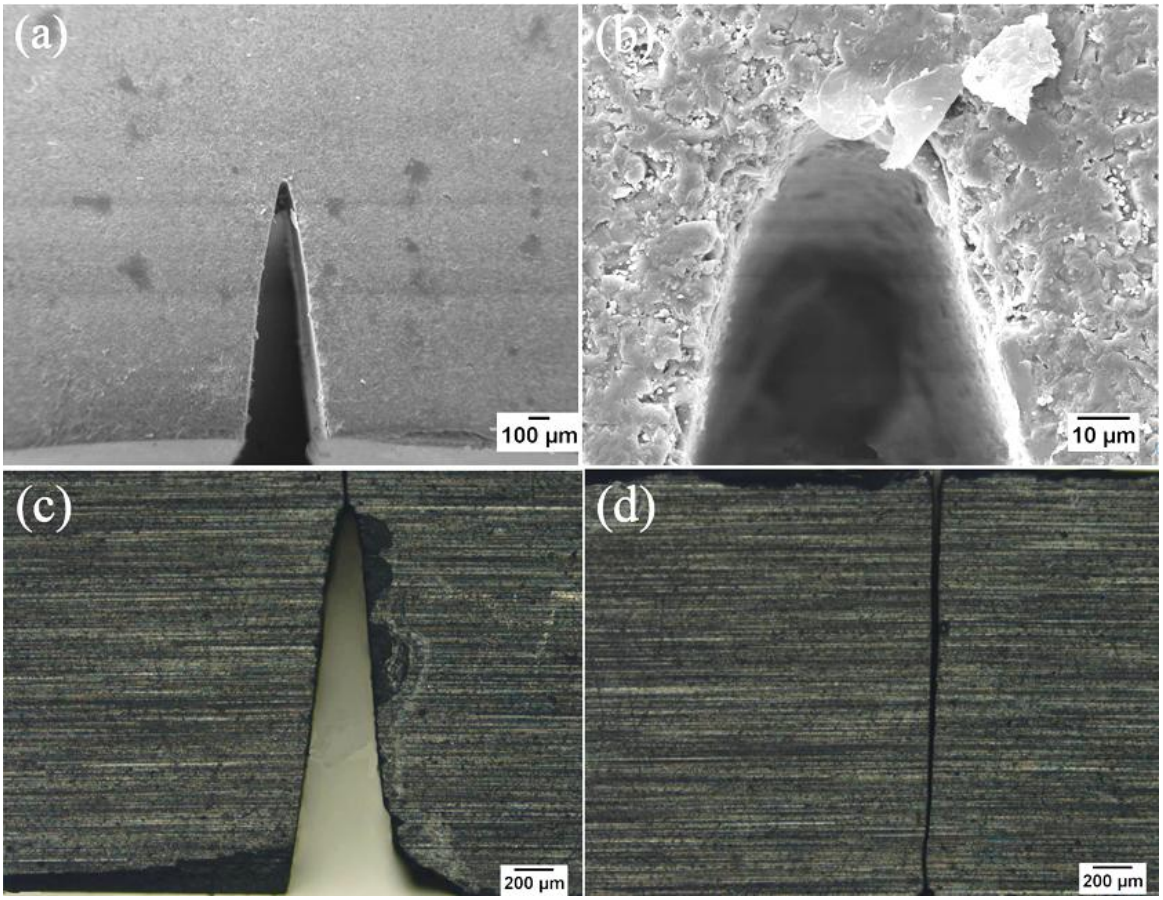

Figure 4.11. SEM images and optical images of notches before (a-b) and after (c-d) the bending test.

4.3.1.4 Effects of GPLs in the GPL/Al_2O_3 composites

As with the GPL/ZTA ceramic composites, toughening mechanisms such as pull-out and crack deflection are observed on the fracture surfaces of the Al_2O_3 ceramic composites reinforced with GPLs. Figure 4.12 shows a large GPL runs along the grain boundary and forms a large area of interface (Figure 4.12 a) and small graphene sheets are securely anchored within the grain boundaries of the matrix microstructure (Figure 4.12b and 4.12c) [1, 4]. It is expected that when the consolidation proceeds during the sintering, GPLs conform with the force applied by their neighbouring matrix grains and are bent and embedded between the grains. Such close contact between the matrix grains and GPLs enables the platelets to anchor at and bind with the matrix grains, which results in an increased contact area. Fracture toughness of the ceramics is therefore believed to be greatly improved due to the interfacial friction in the interface between the graphene sheet and ceramic matrix and the energy to pull out a graphene sheet is expected to be much greater than to pull out a nano fibre or CNT. In addition, it is found that GPLs deflect cracks, just as do fibres in ceramics. As shown in Figure 4.12 e and f, when a crack propagates and meets with a GPL, it is arrested and deflected in-plane. Clearly such a crack deflection mechanism would create a more tortuous path which is believed to help release stress and increase the fracture toughness.

Usually the reinforcing efficiency of the nanoscale fillers in ceramics is mainly determined by the following factors: (1) the intrinsic mechanical properties of the filler material, (2) the efficiency of load transfer at the interface of matrix and filler, and (3) the dispersion level of the nanoscale fillers in the ceramic matrix. In the GPL-reinforced Al_2O_3 composites, GPLs with high Young's modulus and a large specific area are well dispersed in the ceramic matrix. They are either distributed in the grain boundary (Figure 4.12 a, b and c) helping transfer the

load from the ceramic matrix, or embedded within the grains (Figure 4.12 d) reinforcing the ceramic matrix, which significantly improves the flexural strength of the composites [1].

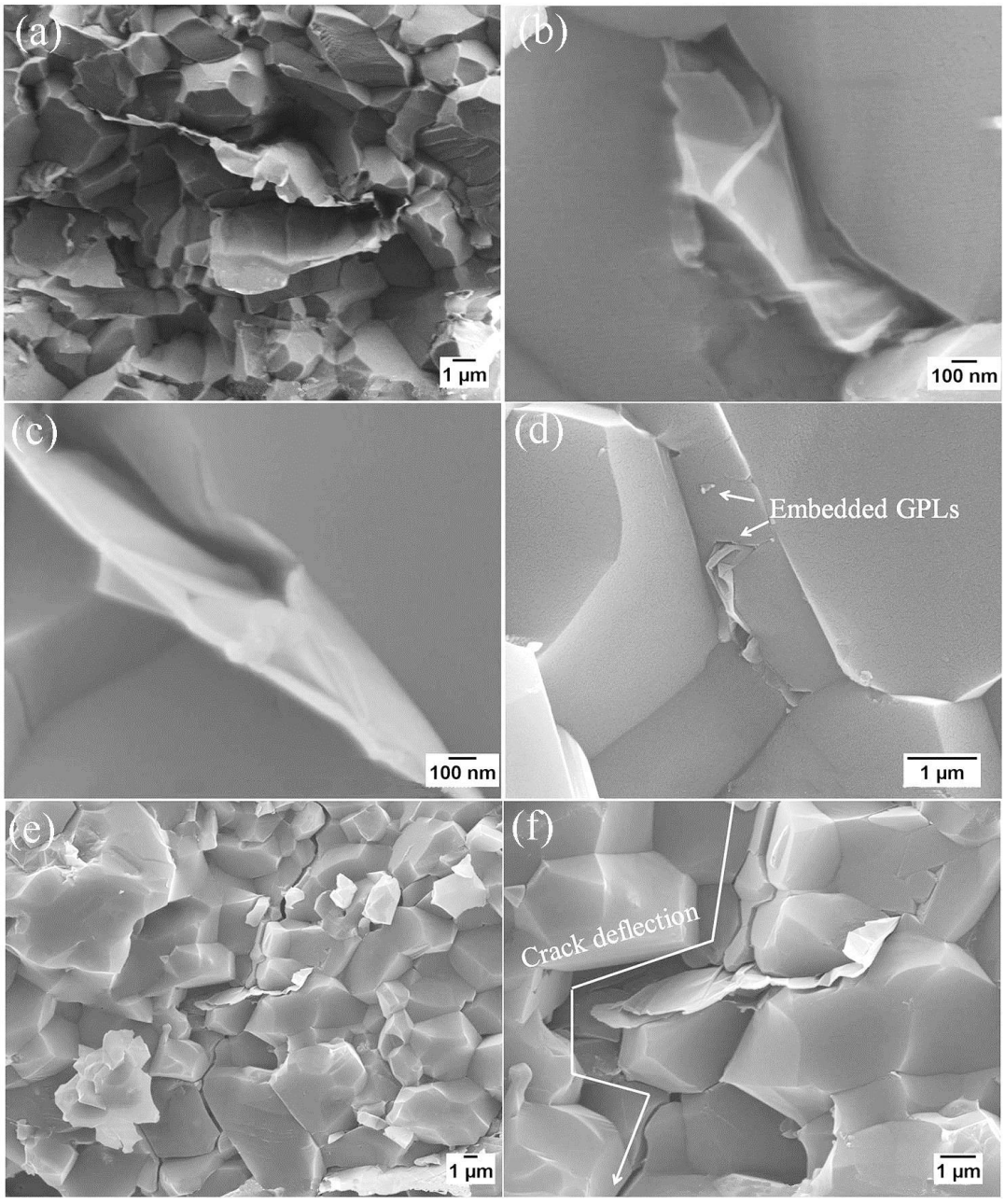

Figure 4.12. SEM images of fracture surfaces of GPL-reinforced Al_2O_3 composites showing the toughening and reinforcing mechanisms.

4.3.1.5 Porosity induced by GPLs in the GPL/Al_2O_3 composites

Although nearly fully densified samples are obtained, some elongated pores are observed, as shown in Figure 4.13. Similar results have been reported in CNT-reinforcing metal oxide composites and GPL/Si_3N_4 ceramic composites [28, 109, 205]. As GPLs tend to be distributed in the grain boundaries of the ceramic matrix, pores are likely to be formed when a good bonding between GPLs and the ceramic matrix are not formed, which make it difficult to accommodate different shrinkages in the interface between GPLs and the ceramic matrix during a cooling process. In addition, these pores are believed to be the origins of the fractures and weaken the strength of the ceramic composites, which explains the fact that excessive addition of GPLs leads to less strong composites. An optimum percentage of GPLs in the GPL–reinforced ceramic composites can result in the maximum flexural strength.

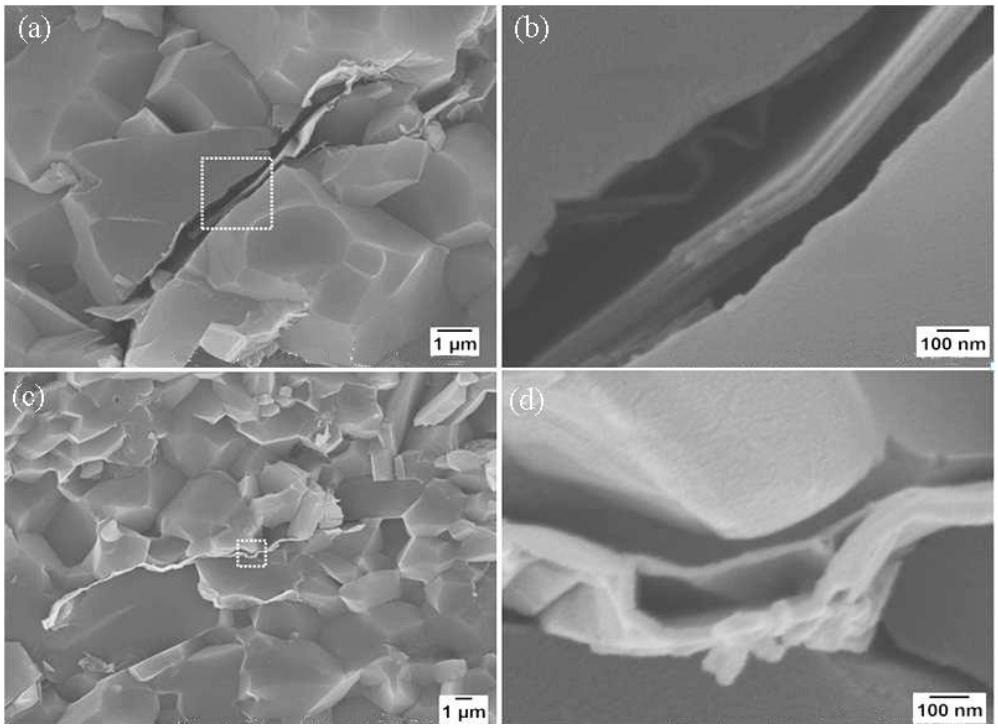

Figure 4.13. SEM images of fracture surfaces of GPL-reinforced Al_2O_3 composites showing the pores and aggregates of GPLs. (b) and (d) are the magnified part of white square areas in (a) and (c).

Although the GPLs shown in Figure 4.7 are well dispersed in the ceramic matrix, overlapping of GPLs is observed in Figure 4.13. The single platelets used in the research are 6-8 nm thick, whereas the overlapped platelets are 20-110 nm thick, which indicates moderate agglomeration of GPLs occurs in the fabrication process. The presence of aggregates is believed to drastically affect the mechanical properties of composite materials, as in comparison with thin GPLs, thick GPLs would induce more pores in the interface between the GPLs and the ceramic matrix because of the degraded flexibility of the thick GPLs. These pores undermine the role of the crack deflection toughening mechanism for they result in a decreased contact area between the ceramic matrix and GPLs, as well as initiate cracks along which stress is released in a less effective way. Meanwhile, when GPLs act in a pull-out role, the pores weaken the interfacial friction in the interface between the ceramic matrix and the GPLs. Therefore aggregates would degrade the strengthening as well as toughening effects of the GPLs and cause detrimental effects to the mechanical properties of the composites[1].

Obviously the dispersion level of nanostructures in a matrix is one of the key factors in defining the mechanical properties of the composites. It is necessary to achieve complete as possible dispersion of the GPLs to obtain ceramic composites with excellent mechanical properties[1].

4.3.2 Al_2O_3 composites reinforced with GPLs and SiC nanoparticles.

In section 4.3.1 it has been concluded that the GPL/Al_2O_3 composite with maximum fracture toughness and flexural strength was produced by adding 0.38 vol% GPLs in the Al_2O_3 matrix. However, the introduction of GPLs inevitably reduces the hardness of the ceramics. To

overcome this problem, a ternary system comprised of Al_2O_3, GPL and SiC nanoparticles was designed to produce hard as well as tough ceramic composites. SiC particles as nano fillers can serve two functions. On one hand, the hardness of SiC is higher than that of the Al_2O_3 matrix and the introduction of SiC would increase the hardness of the Al_2O_3 matrix material. On the other hand, it has been reported that the fracture toughness of the Al_2O_3 matrix can be improved by adding nano particles [48]. Therefore, it is expected that the addition of SiC to the Al_2O_3 matrix may contribute the improvement in mechanical properties of the GPL/Al_2O_3 composites.

4.3.2.1 Raman spectra of the GPLs in the powder mixtures and sintered samples

Figure 4.14 shows Raman spectra of the pristine GPL and the GPLs in the powder mixtures after ball milling. The D, G and 2D bands are observed in all of the Raman spectra and show the typical features of thick graphene sheets [17].

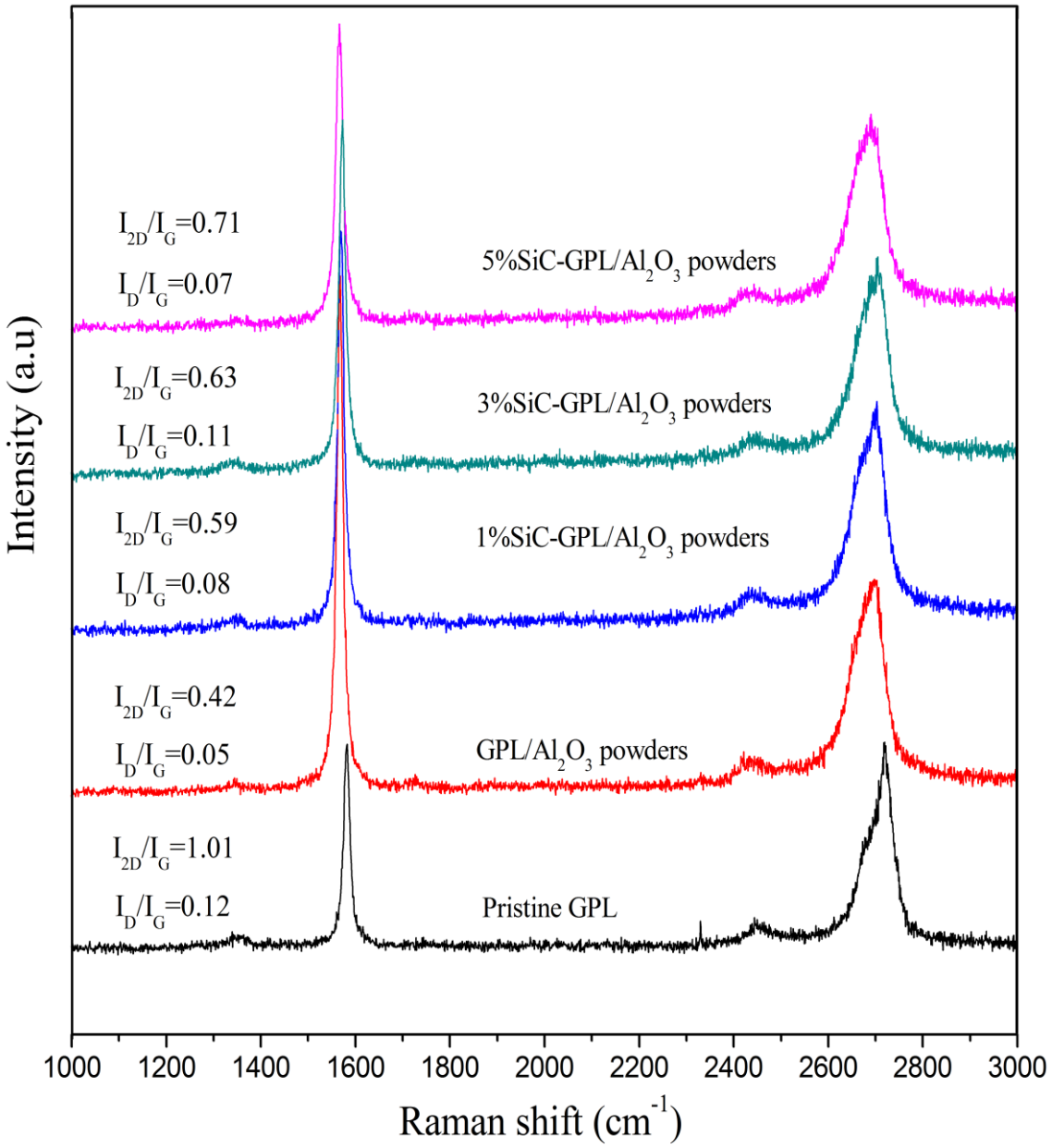

Figure 4.14. Raman spectra of the pristine GPL and GPLs in the composites

Raman parameters were compiled into Table 4.2 to get detailed information of the structure of GPLs. It is evident after ball milling I_D/I_G values of the GPLs decrease, implying fewer defects remain in the GPL in the composites than in the pristine GPL. On the other hand, compared to the pristine GPLs, GPLs in the composites show significant higher G peaks

which indicates more carbon atoms are detected and agglomeration of GPLs occurs to form thick GPLs during ball milling processes.

Table 4.2. Raman parameters of the pristine GPL and the GPLs in powder mixtures.

Materials	I_D/I_G	I_{2D}/I_G	FWHM (G)	ν (G)	FWHM (2D)	ν (2D)
Pristine GPLs	0.12	1.01	15	1583	53	2719
0.38% GPL/Al_2O_3 powders	0.11	0.42	16	1572	85	2702
1% SiC-GPL/Al_2O_3 powders	0.08	0.59	15	1570	80	2699
3% SiC-GPL /Al_2O_3 powders	0.05	0.63	16	1568	79	2702
5% SiC-GPL /Al_2O_3 powders	0.07	0.71	18	1566	79	2688

It is also noted I_{2D}/I_G of GPLs in powder mixtures is lower than that of the pristine GPL, which again proves that stacking of graphene sheets takes place during the ball milling process. Meanwhile, powder mixtures containing SiC nanoparticles present higher I_{2D}/I_G of GPLs as compared to the GPL/Al_2O_3 powder mixture, which indicates the introduction of SiC impedes the agglomeration of GPLs. In addition, I_{2D}/I_G increases with the increasing percentage of SiC nanoparticles, suggesting a higher percentage of SiC can help the formation of relatively thinner GPLs. This is further supported by smaller FWHM of 2D bands for the composites with a higher percentage of SiC. Meanwhile, it is noticed that G and 2D bands for the GPLs in the composites shift to a lower wavelength. This might be due to the different defect population of GPLs and the different number of graphene layers [111].

Figure 4.15 compares the Raman spectra of GPLs in the GPL-SiC/ Al_2O_3 powder mixtures and the sintered sample and the corresponding Raman parameters are shown in Table 4.3. It can be observed that the I_D/I_G is higher for the sintered samples and G peaks remain nearly

unchanged. The increase in I_D/I_G after sintering can be attributed to the interfacial reaction between the GPLs and the ceramic matrix at a higher sintering temperature and pressure.

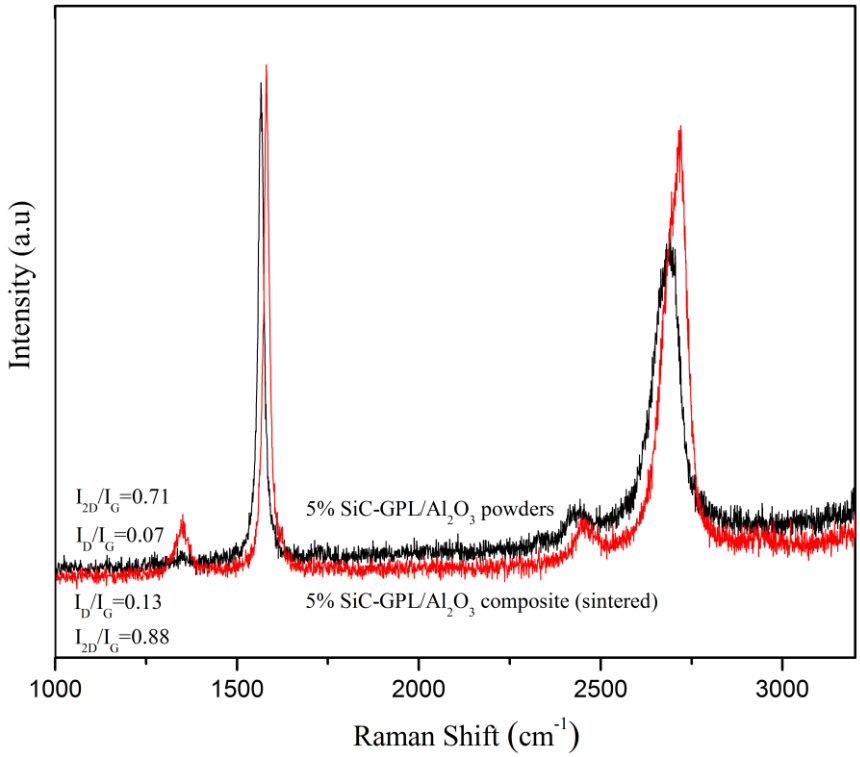

Figure 4.15. Raman spectra of the GPLs in the GPL-SiC/Al_2O_3 powder mixture and the sintered composite.

Table 4.3. Raman parameters of the pristine GPL and the GPLs in the sintered sample.

Materials	I_D/I_G	I_{2D}/I_G	FWHM (G)	ν (G)	FWHM (2D)	ν (2D)
5% SiC-GPL/ Al_2O_3 powders	0.07	0.71	18	1566	79	2688
5% SiC-GPL/ Al_2O_3 bulk sample	0.13	0.88	27	1581	72	2720

Meanwhile, an appreciable sharper and higher 2D peak is noticed for GPLs after sintering, which suggests the formation of thinner GPLs. This is further confirmed by higher I_{2D}/I_G of GPLs in the sintered sample. Similar results are observed in GPL/Si_3N_4 and GPL/ZrB_2 ceramic composites [104, 111]. It is inferred that the interfacial reaction between GPLs and the ceramic matrix during the SPS process may consume layers of graphene sheets resulting

in thinning of the multilayer GPLs into few-layer GPLs. Moreover, G and 2D bands of the GPLs in the sintered composites shift slightly to higher wave number. As mentioned in Chapter 3, the shifting of both bands may be attributed to the thermal residual stresses due to the difference between thermal expansion coefficients of GPLs and the Al_2O_3 ceramic matrix.

4.3.2.2 Microstructures of the sintered GPL-SiC/Al_2O_3 composites

Fracture surfaces of the sintered GPL-SiC/Al_2O_3 composites were examined and compared with those of the pure Al_2O_3 and GPL/Al_2O_3 composites. As can be seen from Figure 4.16, GPLs appear to be distributed homogeneously in the Al_2O_3 matrix in all ceramic composites. In addition, ceramic composites reinforced with GPLs and SiC nanoparticles exhibit more uniform and finer microstructures as compared to the pure Al_2O_3 and GPL/Al_2O_3 composites. Meanwhile, the average grain sizes of the ceramic matrices decrease with the increasing percentage of SiC nanoparticles. The reduction in the grain sizes can be attributed to grain pinning by GPLs and SiC nanoparticles.

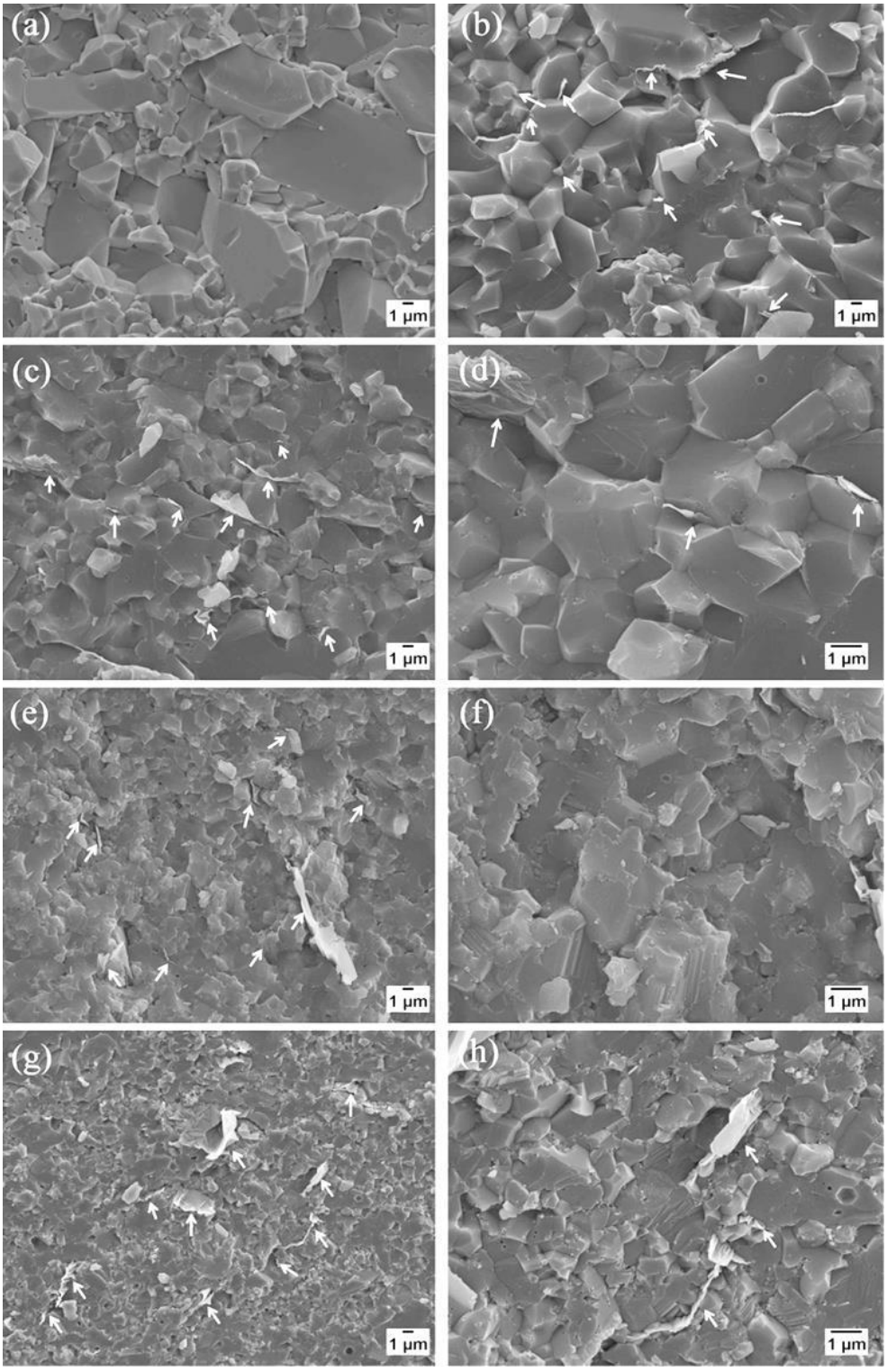

Figure 4.16. SEM images of fracture surfaces of the sintered pure Al_2O_3 (a), GPL/Al_2O_3 composite (b), 1vol% SiC-GPL/Al_2O_3 composite (c), 3vol% SiC-GPL/Al_2O_3 composite (e) and 5vol% SiC-GPL/Al_2O_3 (g) composite. (d), (f) and (h) are the magnified images of (c), (e) and (g) respectively. White arrows indicate the GPLs.

4.3.2.3 Grain sizes and mechanical properties of the sintered Al_2O_3 composites

The pure Al_2O_3 and ceramic composites were polished and thermally etched at 1400 ˚C in an argon atmosphere in a tube furnace. Grain sizes are shown in Figure 4.17 and SEM images of the polished surfaces of the samples are shown in Figure 4.18. It is obvious that the introduction of the GPL and SiC results in a significant reduction of the grain size of the Al_2O_3 matrix. In addition, grain sizes of the Al_2O_3 matrix decrease with the increasing percentage of the SiC nanoparticles.

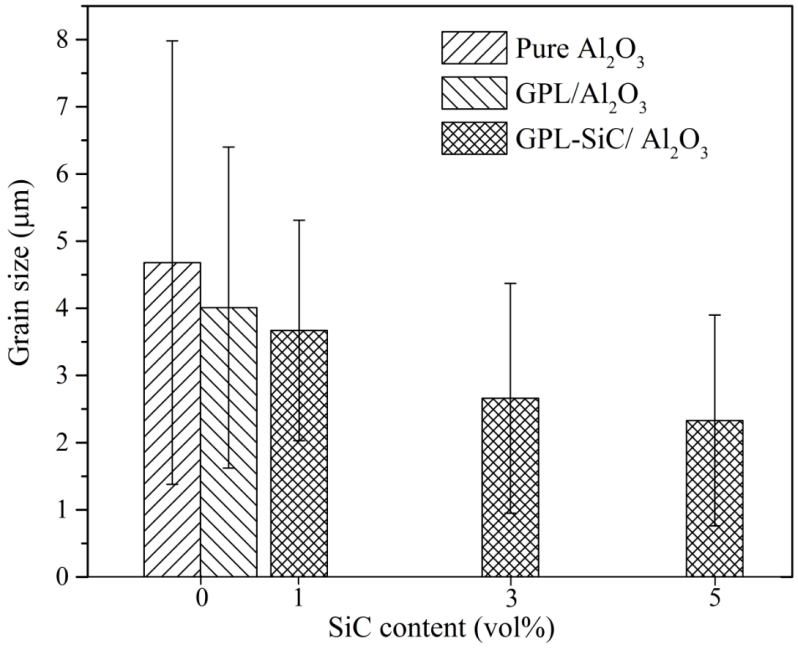

Figure 4.17. Grain sizes of the pure Al_2O_3 and GPL-SiC/Al_2O_3 composites as a function of SiC content.

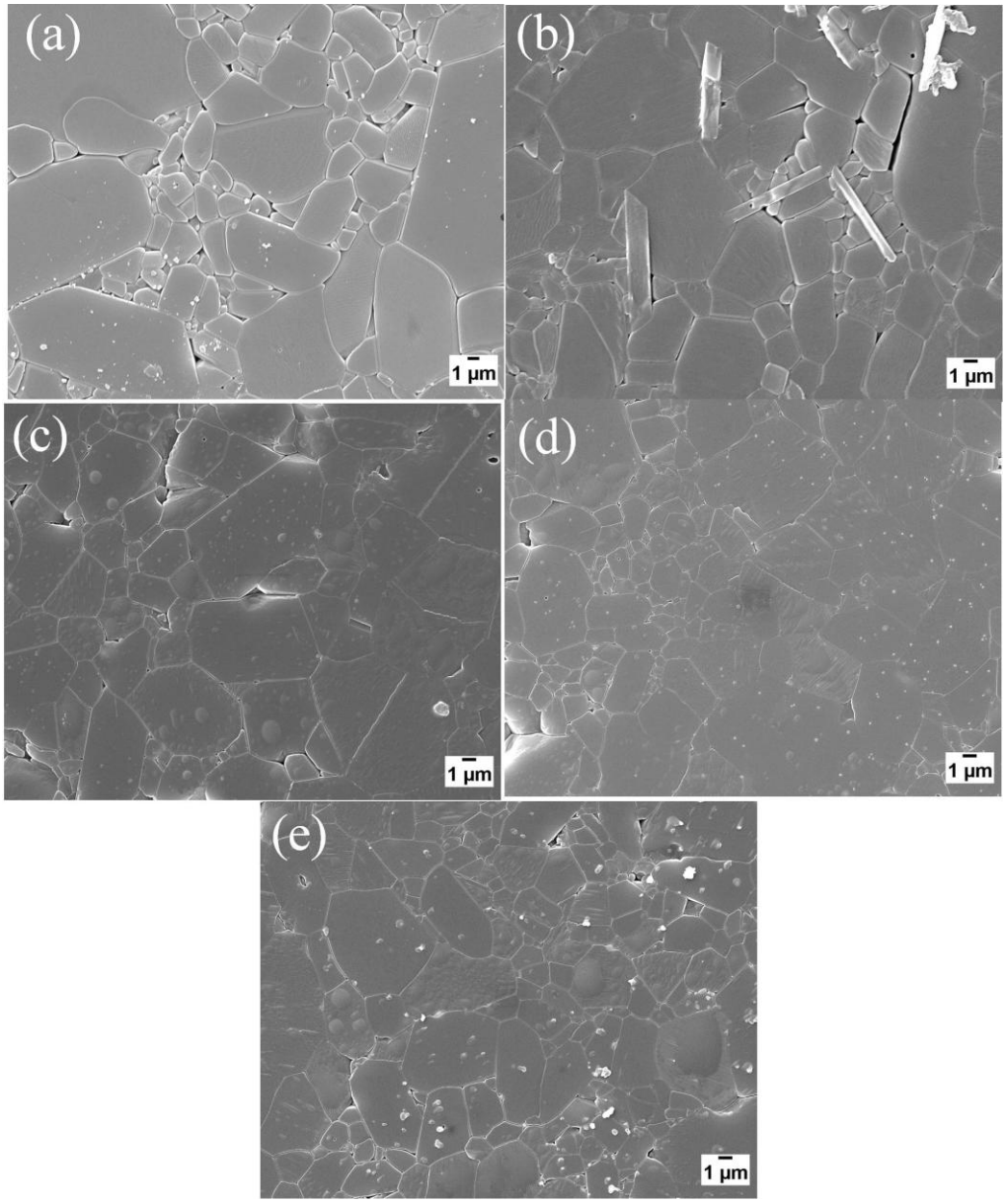

Figure 4.18. SEM images of fractured surfaces of the sintered pure Al_2O_3 (a), GPL/Al_2O_3 composite (b), 1vol% SiC-GPL/Al_2O_3 composite (c), 3vol% SiC-GPL/Al_2O_3 composite (d) and 5vol% SiC-GPL/Al_2O_3 composite (e).

Densities of the GPL-SiC/Al_2O_3 composites sintered at 1500 ˚C are presented in Figure 4.19. It can be seen that the densities of the SiC-GPL/Al_2O_3 composites are relatively smaller than those of pure Al_2O_3 and GPL/Al_2O_3 composites shown in Table.4.1. This indicates that the introduction of the SiC nanoparticles hinder the densification process of the composites

during the sintering. In addition, densities of the composites decrease with the increasing percentage of the SiC nanoparticles. The variation of the densities suggests that to achieve a high density for GPL-SiC/Al_2O_3 composites with a high percentage of SiC nanoparticles, a higher sintering temperature may be required.

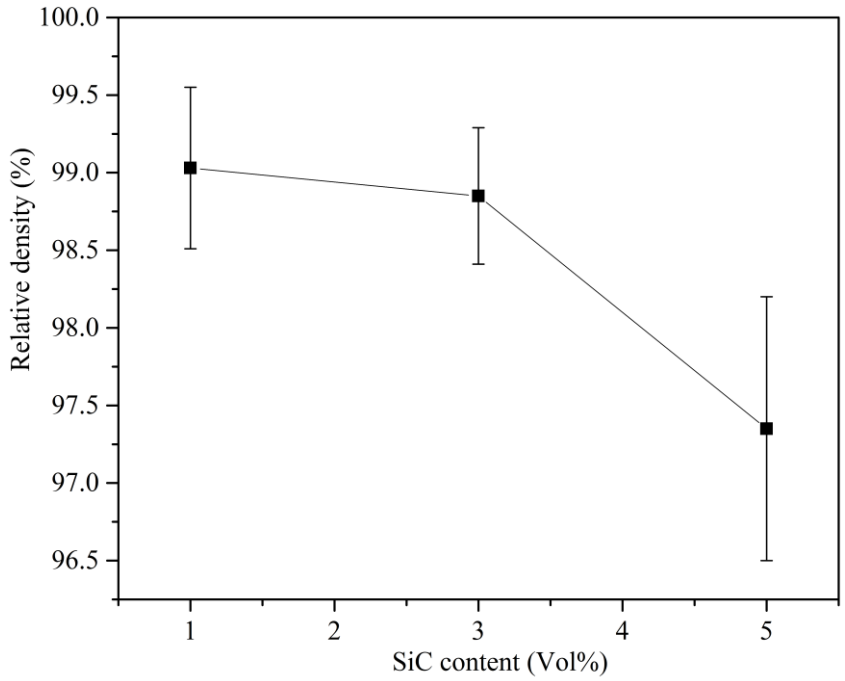

Figure 4.19. Densities of the GPL-SiC/Al_2O_3 composites as a function of SiC content.

Hardness of the sintered GPL-SiC/Al_2O_3 composites is given in Figure 4.20. It is evident that the hardness of GPL-SiC/Al_2O_3 composites is higher than that of the pure Al_2O_3 and GPL/Al_2O_3 composites shown in Figure 4.8. It reaches the maximum at 3% SiC and decreases slightly at 5% SiC. Approximately a 36 % increase in hardness of Al_2O_3 matrix is achieved by introducing SiC nanoparticles. The improved hardness can be attributed to the addition of hard secondary SiC particles and the refined microstructures. Meanwhile, it should be noted that the residual porosity in the Al_2O_3 composites with a high percentage of

SiC has adverse effect on hardness, which may compromise the improvement brought by the SiC.

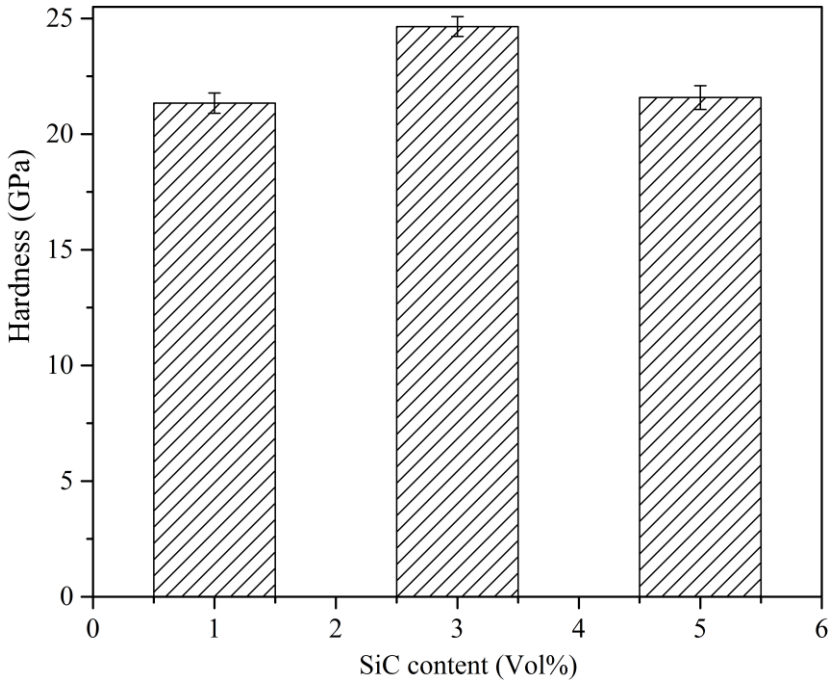

Figure 4.20. Hardness of the GPL-SiC/Al_2O_3 composites as a function of SiC content.

Flexural strength and fracture toughness of the GPL-SiC/Al_2O_3 composites obtained using the bending method are shown in Figure 4.21 and Figure 4.22. It can be seen that flexural strength shows a considerable increase at 1 vol% SiC and decrease at 3% SiC. Further increase in SiC leads to an increase in flexural strength again. An approximately 43% increase in flexural strength was achieved by adding 0.38 vol% GPL and 1 vol% SiC. The variation in flexural strength can be explained by the double effects of grain size and residual porosity. The smaller grain size results in better flexural strength while porosity causes lower fracture energy due to the stress concentration around the pores.

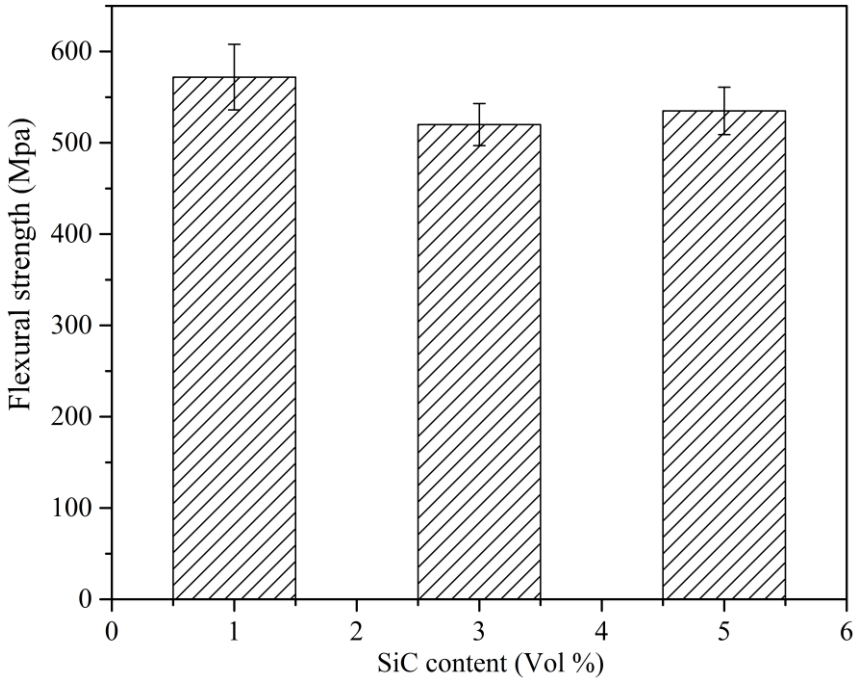

Figure 4.21. Flexural strength of the GPL-SiC/Al_2O_3 composites as a function of SiC content.

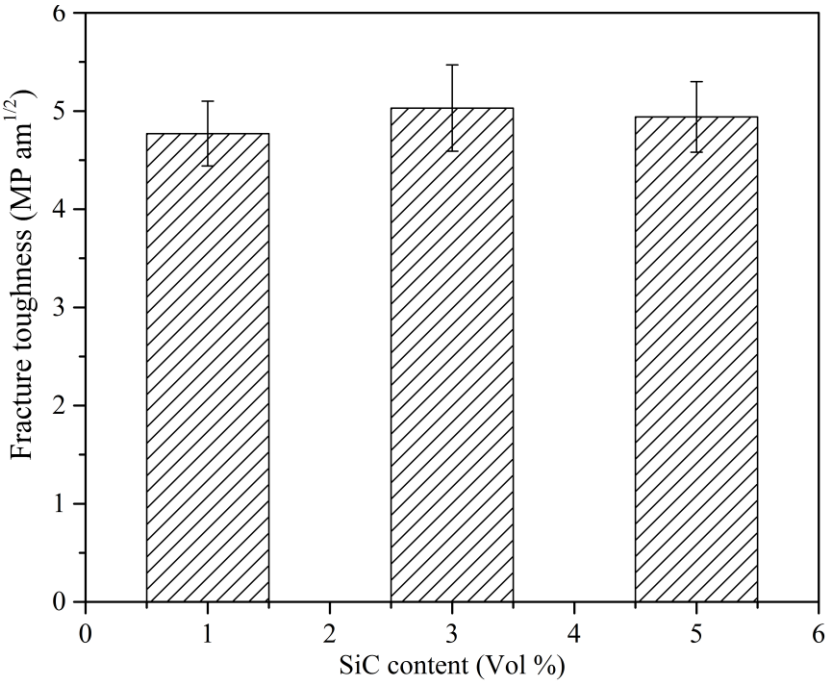

Figure 4.22. Fracture toughness of the GPL-SiC/Al_2O_3 composites as a function of SiC content.

Fracture toughness shows a substantial increase with a minor addition of SiC and varies little with the further increase of SiC. In comparison with the pure Al_2O_3 samples, composites reinforced with dual fillers show an approximately 47.51% increase in fracture toughness. Similar toughening mechanisms, such as pull-out, crack deflection and bridging observed in GPL/Al_2O_3 composites are also noticed in GPL-SiC/Al_2O_3 composites (Figure 4.23).

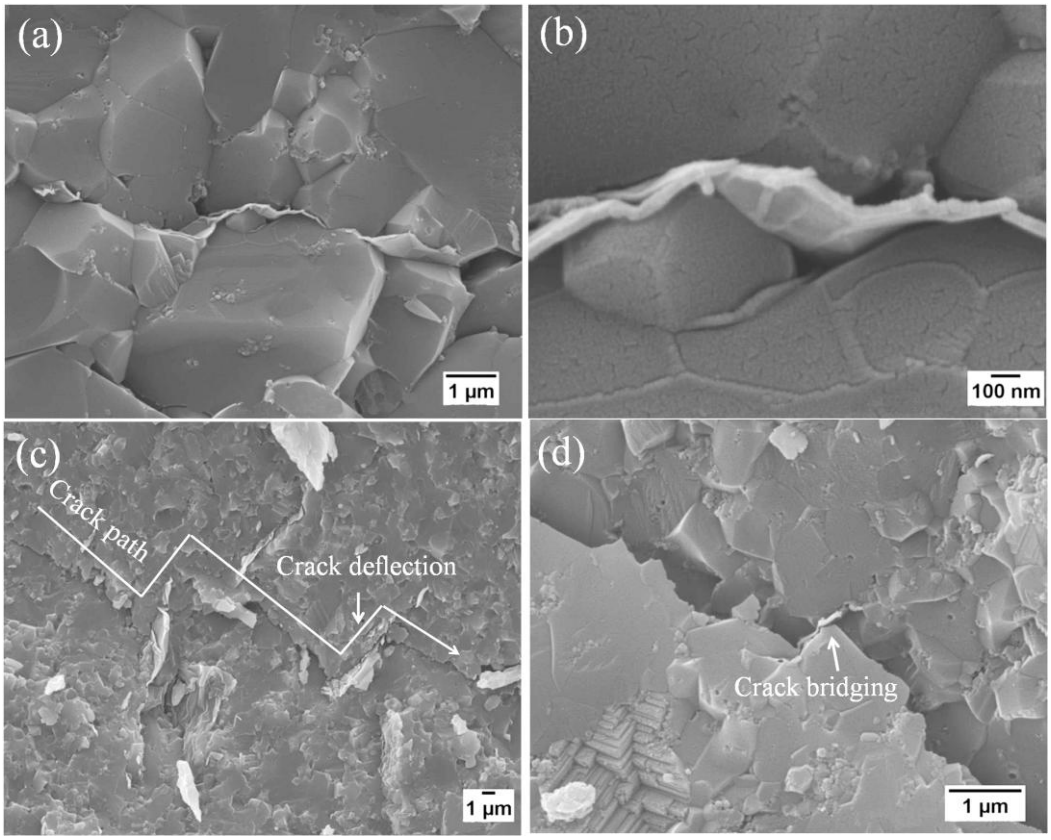

Figure 4.23. SEM images of fracture surfaces of the GPL-SiC/Al_2O_3 composites.

4.3.2.4 Dispersion of SiC nanoparticles and its effects in the composites

Figure 4.24 shows the SEM images of polished and fracture surfaces of the sintered samples. It can be seen that most of the SiC particles are well dispersed while some clusters are found

in the composites. These SiC particles are located not only in the grain boundaries (Figure 4.24 c and d) or triple-grain junctions, but also inside the grains (Figure 4.24 a and b).

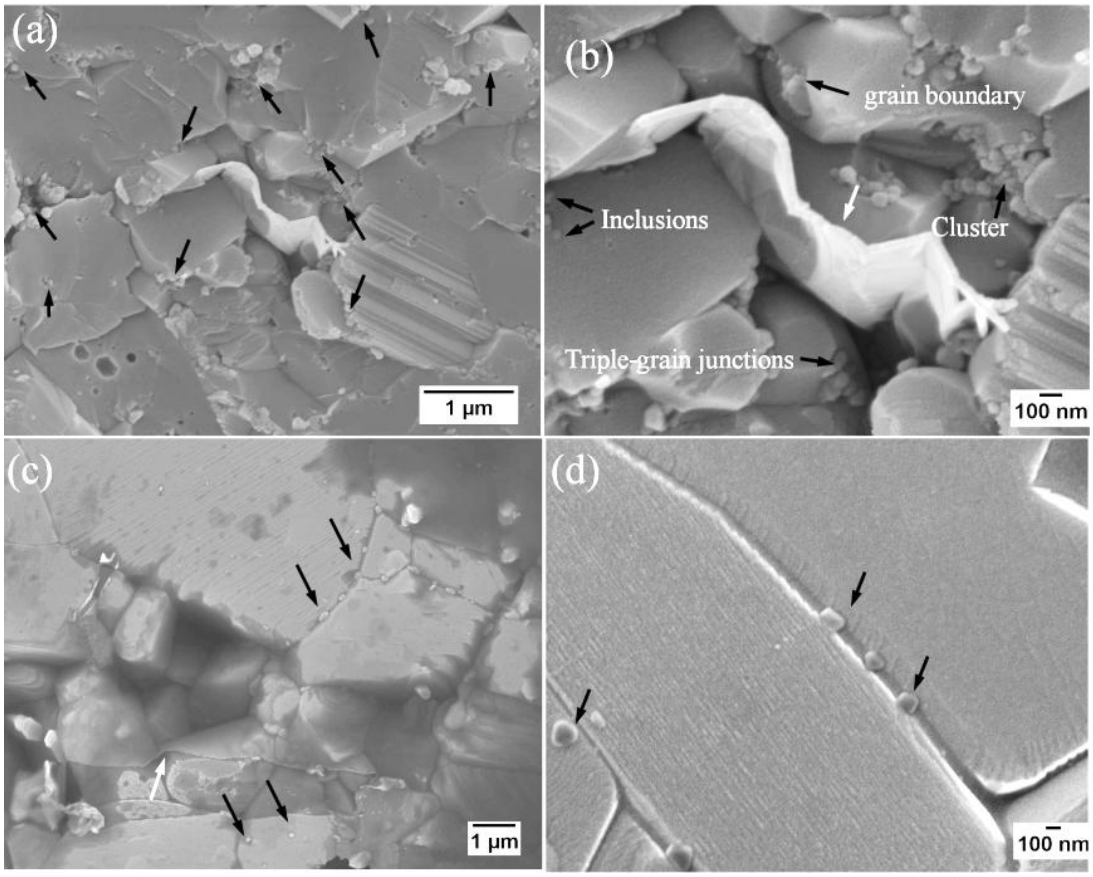

Figure 4.24. SEM images of fracture surfaces (a-b) and polished surfaces (c-d) of GPL-SiC/Al_2O_3 composites. White and black arrows indicate GPLs and SiC nanoparticles respectively.

It is suggested that when the grain boundary reaches a particle, the total free energy of a segment of boundary reduces by the product of the cross-sectional area of the particle and the specific boundary free energy [206]. A breakaway stress will then have to be applied in order to release the boundary from the pinning particle. Clearly smaller particles provide less effective pinning force than larger ones and they are more likely to become inclusions in the ceramic matrix, since the decrease of the boundary energy is small and boundaries can easily break away from them. Conversely, larger particles tend to remain at grain boundaries

because they significantly decrease the boundary energy and require larger breakaway stresses [207, 208].

On the other hand, incorporation of SiC nanoparticles is expected to enhance the toughening effect of GPLs, since more contact areas are formed between the GPLs and the ceramic matrix during the consolidation process due to the significant grain refinement. High energy is therefore expected to pull a GPL out of the fine microstructures. In addition, SiC nanoparticles, either distributed in grain boundaries or embedded in the ceramic matrix, can create dislocations to release the tensile stress along the grain boundaries and generate compressive stress to strengthen the grain boundaries (Figure 4.25), which results in strong bonding between GPLs and the ceramic matrix. Such a bonding enables GPLs to effectively

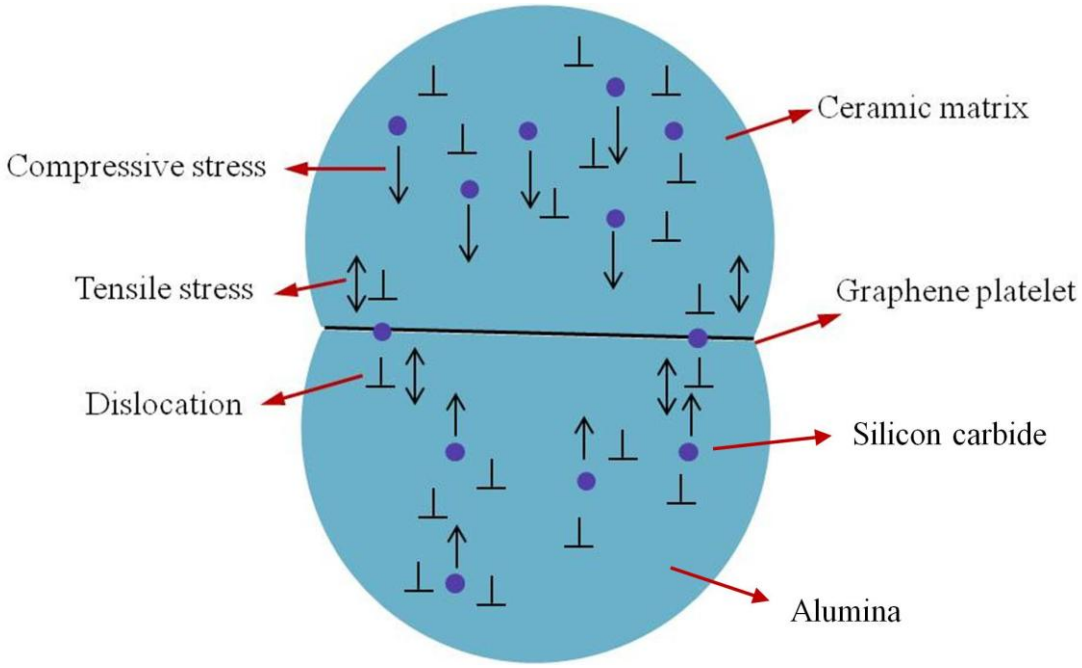

Figure 4.25 A schematic illustration of the strengthened grain boundaries induced by SiC nanopartilces.

transfer load from the ceramic matrix and leads to the improvement of flexural strength. As discussed in section 4.3.1.5, densification process plays a vital role in forming a good bonding between GPLs and the ceramic matrix. Lower densities of the samples imply load transfer from the ceramic matrix to GPLs is ineffective and the residue porosity could even be a source of cracks, which causes the decrease of the flexural strength. In addition, the residue porosity can result in the decrease of the fracture toughness by decreasing the contact area between GPLs and the ceramic matrix. This may explain why Al_2O_3 ceramic composites with smaller grain size show lower fracture toughness.

4.4 Summary

This chapter reports on a study of the preparation and characterisation of GPL/Al_2O_3 and GPL-SiC/Al_2O_3 ceramic composites. Pure Al_2O_3, GPL/Al_2O_3 and GPL-SiC/Al_2O_3 ceramic composites were sintered using SPS. Microstructures of the sintered samples were examined by SEM. Flexural strength and fracture toughness were determined by bending tests. Vickers hardness was obtained using a hardness tester. Raman spectra of the GPLs in the powder mixtures and sintered samples were obtained to show the structural integrities of the GPLs. Mechanical properties of the pure Al_2O_3, GPL/Al_2O_3 and GPL-SiC/Al_2O_3 ceramic composites were compared to find out the optimum content of the nano fillers. The results of the research can be summarized as follows:

1. Pure Al_2O_3, GPL/Al_2O_3 and GPL-SiC/Al_2O_3 ceramic composites are nearly fully densified during the SPS process. The additions of GPLs and SiC nanoparticles cause a slight decrease in relative densities. The microstructures of the composites show that the nano

fillers are well distributed in the Al_2O_3 matrix and grain sizes of the Al_2O_3 matrix are considerably reduced by adding GPLs and SiC nanoparticles. In addition, the higher the percentage of the nano fillers, the more refined the matrix microstructures.

2. The Raman spectra shows that moderate agglomeration of GPLs takes place during the ball milling process and the addition of SiC nanoparticles prevents the formation of GPL aggregates. Additionally, it is implied that the a higher percentage of SiC nanoparticles results in thinner GPLs after ball milling.

3. The flexural strength and fracture toughness of Al_2O_3 matrix are significantly improved by adding GPLs. The addition of only 0.38 vol% GPLs to Al_2O_3 matrix results in 30.75% and 27.20% simultaneous increases in flexural strength (523 ± 30 MPa) and fracture toughness (4.49 ± 0.33 MPa $m^{1/2}$), respectively. However, the addition of GPLs causes a slight decrease in the hardness of the composites.

4. The addition of GPLs and SiC nanoparticles results in a further improvement in the mechanical properties of the Al_2O_3 matrix. Approximately, a 36 % increase in hardness, a 40% increase in flexural strength and a 50% increase in fracture toughness have been achieved by adding GPLs and SiC particles into Al_2O_3.

5. Toughening mechanisms such as pull-out, crack deflection and crack bridging are observed and are responsible for the significant improvement in the fracture toughness of the Al_2O_3 matrix.

The research shows the introduction of GPLs and SiC nanoparticles in the ceramic matrix can improve the mechanical properties of the ceramic matrix and it is likely that the ceramic composites, with additions of dual nano fillers, can be potentially used for many engineering applications in the future.

Chapter 5: Pressureless sintering and characterization of GPL/Al_2O_3 composites

5.1 Introduction

This chapter presents fabrication and characterization of Al_2O_3 composites reinforced with GPLs sintered in flowing inert gases. The research in this chapter aims to fabricate the GPL/Al_2O_3 composites through pressureless sintering and to investigate the effects of GPLs content on the mechanical properties of the GPL-reinforced Al_2O_3 composites. Firstly, experiments of the fabrication process and characterization techniques are introduced in section 5.2. Then, pressureless sintering and the mechanical properties of GPL/Al_2O_3 composites are presented in section 5.3. In particular, microstructures and densities of the GPL/Al_2O_3 composites sintered under various processing parameters are introduced in section 5.3.1, in which optimum sintering parameters are determined by comparing the morphologies of the GPLs and the densities of the composites. In section 5.3.2, the GPL/Al_2O_3 composites with different additions of GPLs sintered under the optimum processing parameters are introduced and their microstructures and mechanical properties are presented. Finally, this chapter is summarized in section 5.4.

5.2 Experiments of fabrication

The experiments in the research of this chapter are similar to those described in Chapter 3 and Chapter 4. The major difference is that pressureless sintering was used to consolidate the powder mixtures.

5.2.1 Powder mixture preparation

The powders of GPL and Al_2O_3 introduced in Chapter 4 are also employed in the research of this chapter. The powder mixtures' preparation process is similar to the process described in section 4.2.2. The appropriate amount of GPLs was ultrasonicated for one hour using NMP as the dispersant and ball milled with Al_2O_3 powders for two hours. The milled slurry was dried in an oven and sieved using a 140 mesh.

5.2.2 Formation of green compacts using CIP

A soft mould (Figure 5.1) was filled with the dried powders and subsequently underwent CIP using a hydraulic press (Figure 5.2) to form green compacts (Figure 5.3).

Figure 5.1. An image of the soft mould.

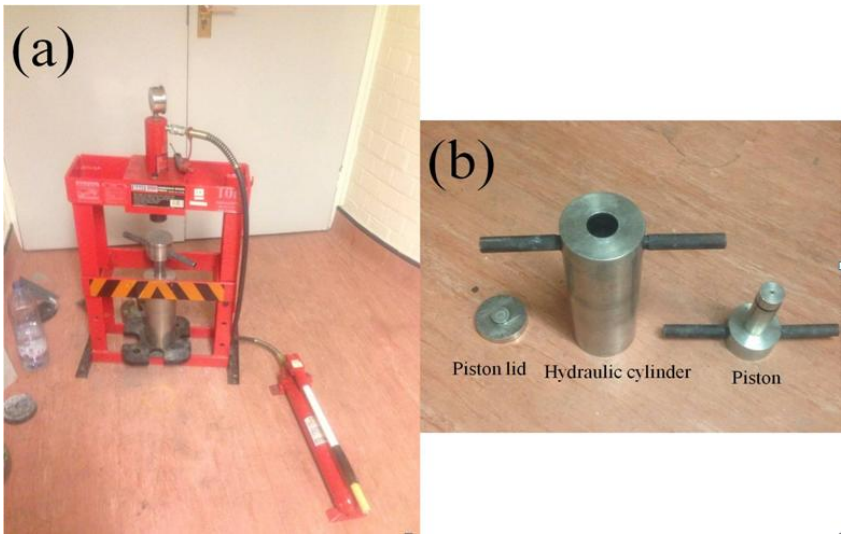

Figure 5.2. Images of the hydraulic press. (a) the hydraulic press and cylinder assembly (b) hydraulic cylinder.

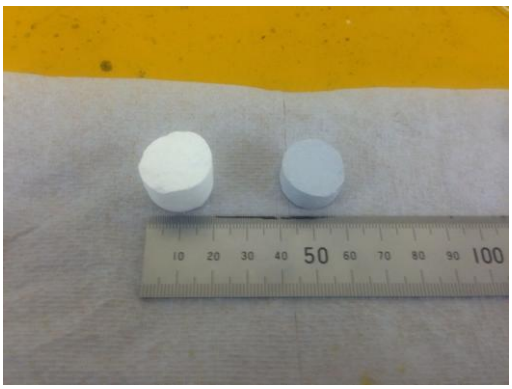

Figure 5.3. An image of the typical green compacts formed by CIP. White is the pure Al_2O_3 and blue is the GPL/Al_2O_3 sample.

5.2.3 Sintering of the GPL/Al_2O_3 composites with different content of GPLs

Green compacts were sintered under various processing parameters to determine which parameters were the optimum. A tube furnace (Figure 5.4) was used for the sintering experiments, in which nitrogen or forming gas was introduced during sintering to protect the GPLs within the powder compacts. The optimum processing parameters are obtained by comparing the morphologies of GPLs in the sintered composites and the densities of the sintered composites.

Figure 5.4. An image of the tube furnace for sintering.

Afterwards, green compacts with varied content of GPLs were sintered respectively under the determined optimum sintering parameters. Figure 5.5 shows an example of a sintered GPL/Al_2O_3 sample. Mechanical properties and microstructures of the sintered samples were characterized.

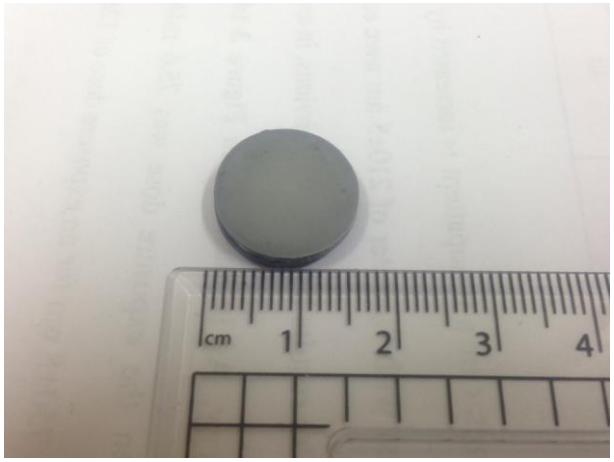

Figure 5.5. An image of a sintered sample.

5.2.4 Material characterizations

Equipment and characterization techniques such as SEM, Raman spectroscopy, XRD, hardness tester and the density measurement method used in Chapter 3 were also employed in the research of this chapter. The major differences are that four-point bending tests were used to measure the flexural strength and fracture toughness of the sintered samples and thermo gravimetric analysis (TGA) was carried out to examine the GPLs content within the sintered samples.

.

5.2.4.1 TGA of the GPL/Al_2O_3 powder mixtures

The sintered samples were crushed, milled and sieved using a 140 mesh to produce powder mixtures for TGA. TGA was performed using NETZSCH (STA 449C) and an image of the instrument for TGA is shown in Figure 5.6. For each test, the powder mixture of 100 mg was

placed in an Al_2O_3 crucible and examined in the temperature range between 200 and 800 ℃ in air.

Figure 5.6. An image of the instrument for TGA.

5.2.4.2 Bending tests

To obtain the flexural strength and fracture toughness of the sintered samples, four-point bending tests (Figure 5.7) were carried out on an Instron 6025. For the flexural strength test, the configuration shown in Figure 5.7b was used and specimens of 1.5 × 2× 13 mm were machined. The span length and crosshead speed for the strength tests were 10 mm and 0.05 mm min^{-1}. To avoid stress concentration, all the edges and corners of the specimens were chamfered using SiC grinding paper. Equation 5.1 was used to determine the flexural strength of the specimens.

$$S = \frac{3PL}{4BW^2} \qquad (5.1)$$

Where S is the flexural strength, P is the maximum loading, L is the length of the support span and B and W are width and thickness of the specimen respectively.

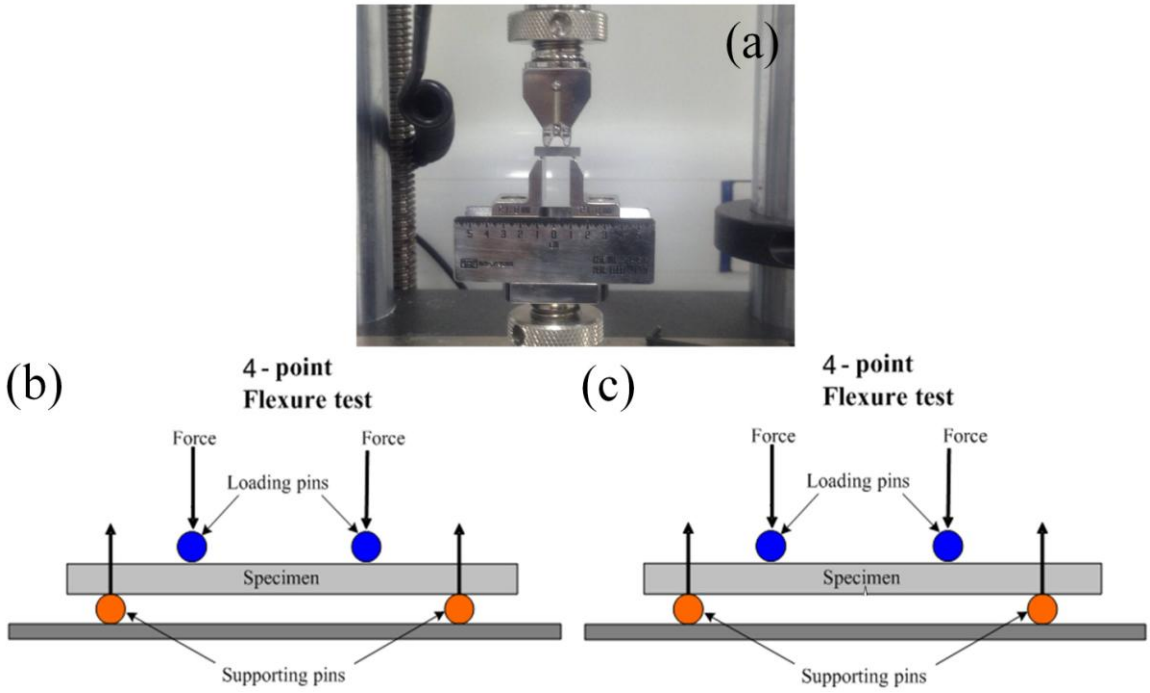

Figure 5.7. An image of four-point bending configuration (a) and schematic illustrations of four-point bending configurations for the measurements of flexural strength (b) and fracture toughness (c).

The SEVNB method was used to determine the fracture toughness of the sintered samples at room temperature. Test specimens of 2 × 3 × 15 mm were machined for the measurement. Notches at the centre of the test specimens were cut by a diamond wheel and further sharpened using a razor blade with the aid of diamond paste up to 1 μm. The ratio between the notch depth and specimen thickness was approximately 0.25. Inner and outer spans of 6 mm and 10 mm, as well as a crosshead speed of 0.05 mm/min, were applied in the toughness tests. The configuration shown in Figure 5.7c was used for the measurement. Three samples were tested for each material. The toughness was determined based on equation 5.2.

$$K_{Ic} = \frac{P}{B\sqrt{W}} \cdot \frac{L_1 - L_2}{W} \cdot \frac{3\sqrt{\alpha}}{2(1-\alpha)^{1.5}} \cdot Y \quad (5.2)$$

$$Y = 1.9887 - 1.326\alpha - \frac{\alpha(1-\alpha)(3.49 - 0.68\alpha + 1.35\alpha^2}{(1+\alpha)^2} \quad (5.3)$$

Where K_{Ic} is the fracture toughness, P is the bending force, B and W are the specimen depth and thickness, L_1 and L_2 are the outer span and inner span respectively and α is the V-notch depth.

5.3 Results and discussion

5.3.1 Microstructures and densities of the GPL/Al_2O_3 composites sintered under various processing parameters.

Various sintering temperatures and flowing rates of nitrogen or forming gas were studied to determine the optimum processing parameters for sintering the Al_2O_3 composites reinforced with GPLs. Figures 5.8 and 5.9 show fracture surfaces of the 0.45vo% GPL/Al_2O_3 composites sintered at 1200 and 1300 ℃ in a nitrogen atmosphere. It can be seen that GPLs present wire–like shape materials (Figure 5.8) at a lower flowing rate of 3L/min, implying GPLs were damaged during sintering process while large graphene sheets are observed and drape over the Al_2O_3 matrix grains (Figure 5.9) at a relatively higher flowing rate of 6 L/min, indicating GPLs are relatively better protected at a higher flowing rate of nitrogen.

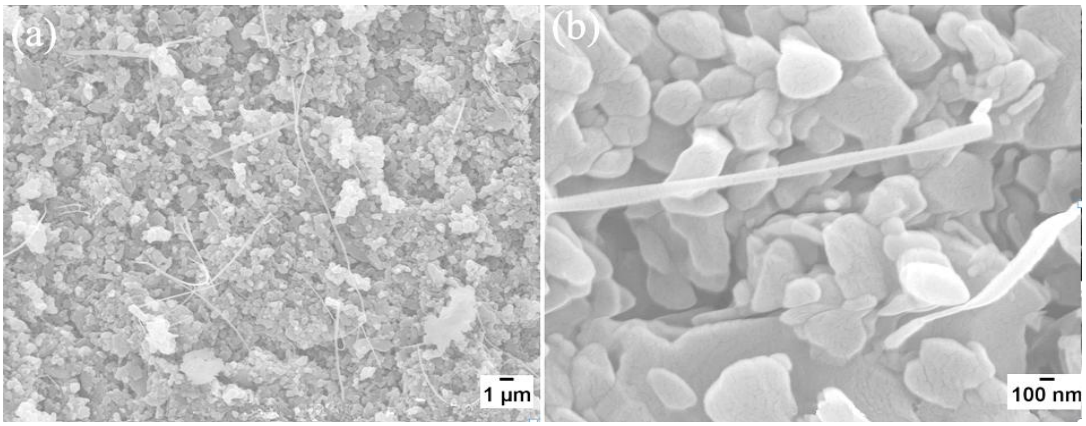

Figure 5.8. Fracture surfaces of the sintered GPL/Al_2O_3 composites processed under the following parameters: heating rate: 3 ℃/s; sintering temperature: 1200 ℃; sintering time: 2.5 hours; sintering atmosphere: nitrogen; flowing rate of nitrogen: 3L/min.

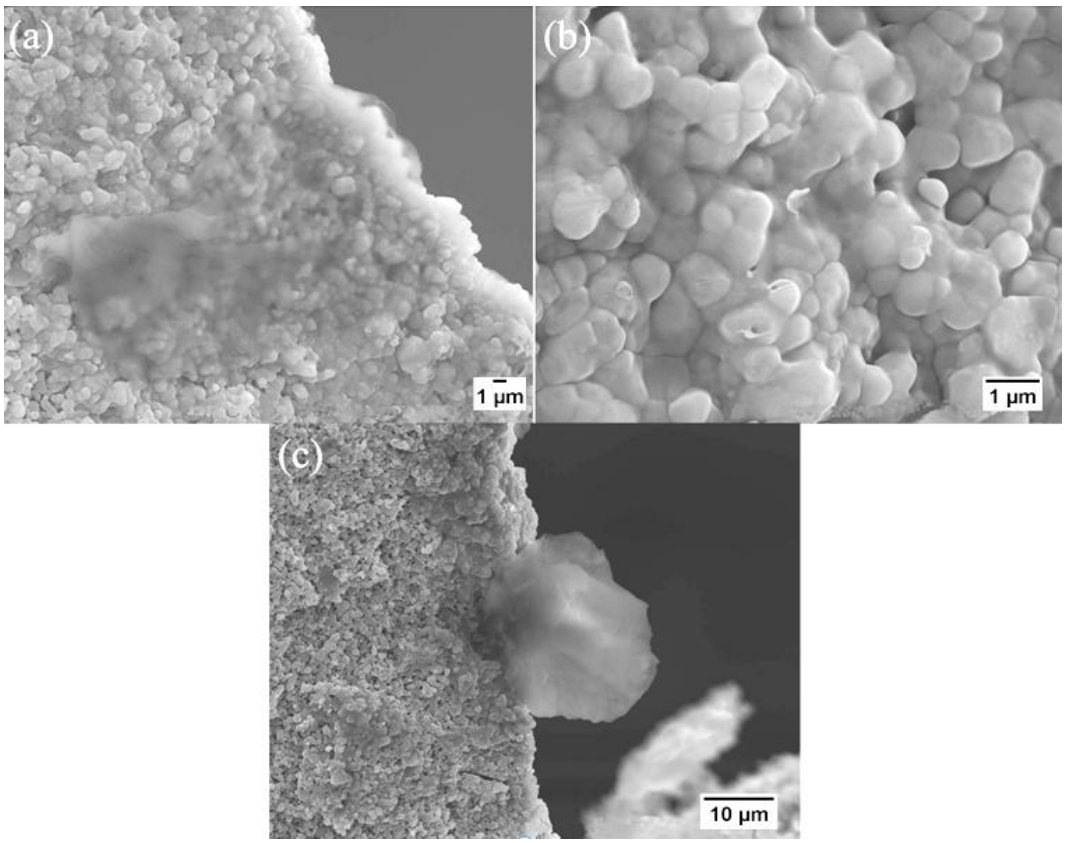

Figure 5.9. Fracture surfaces of the GPL/Al_2O_3 composites processed under the following parameters: heating rate: 5 ℃/s; sintering temperature: 1300 ℃; sintering time: 2.5 hours; sintering atmosphere: nitrogen; flowing rate of nitrogen: 6 L/min.

The damage to the GPLs can be attributed to the interaction of the residue oxygen within the tube and powder compacts with the GPLs during the sintering. The measured densities of the 0.45vo% GPL/Al_2O_3 composites sintered at 1200 and 1300 ℃ are 61% or 72% respectively and are too low for the composites to be used as engineering materials. It is expected that higher sintering temperaures are required to consolidate the composites.

Figures 5.10 and 5.11 show fracture and polished surfaces of the 0.45vo% GPL/Al_2O_3 composites sintered at 1400 ℃ in flowing nitrogen and forming gas. It is evident that the GPLs shown in Figure 5.10a become rope-like materials, indicating damaged structures while Figure 5.10b clearly shows GPL aggregates successfully survive the sintering process. In Figure 5.11, a very thin layer of graphene sheet running along the grain boundaries of the ceramic matrix is observed (Figure 5.11b), which is indicative of good protection of GPLs in the forming gas. This argument is further supported by GPLs noticed in the polished surface of the sintered samples (Figure 5.11d and f).

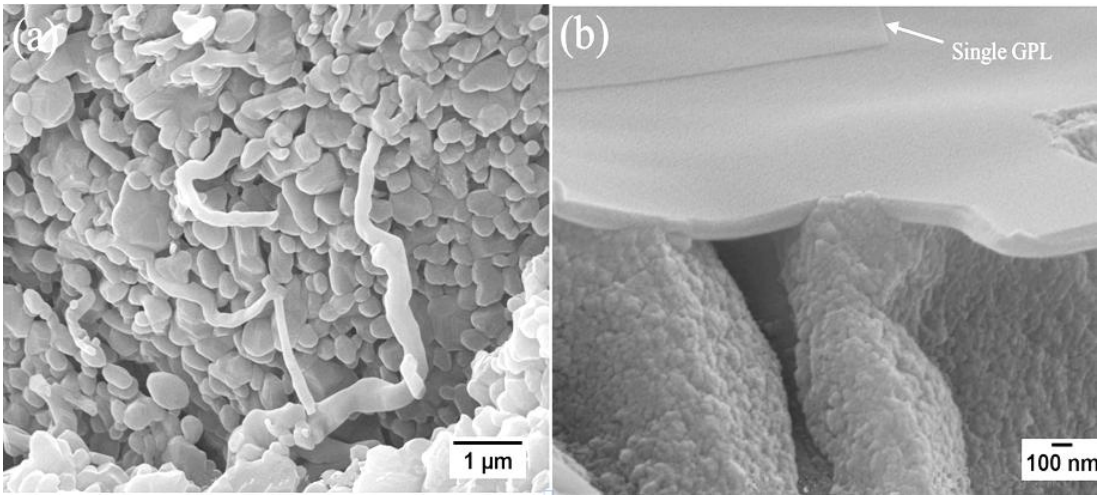

Figure 5.10. Fracture surfaces of the GPL/Al_2O_3 composites processed under the following parameters: heating rate: 5 ℃/s; sintering temperature: 1400 ℃; sintering time: 3 hours; sintering atmosphere: nitrogen; flowing rate of nitrogen: 6 L/min.

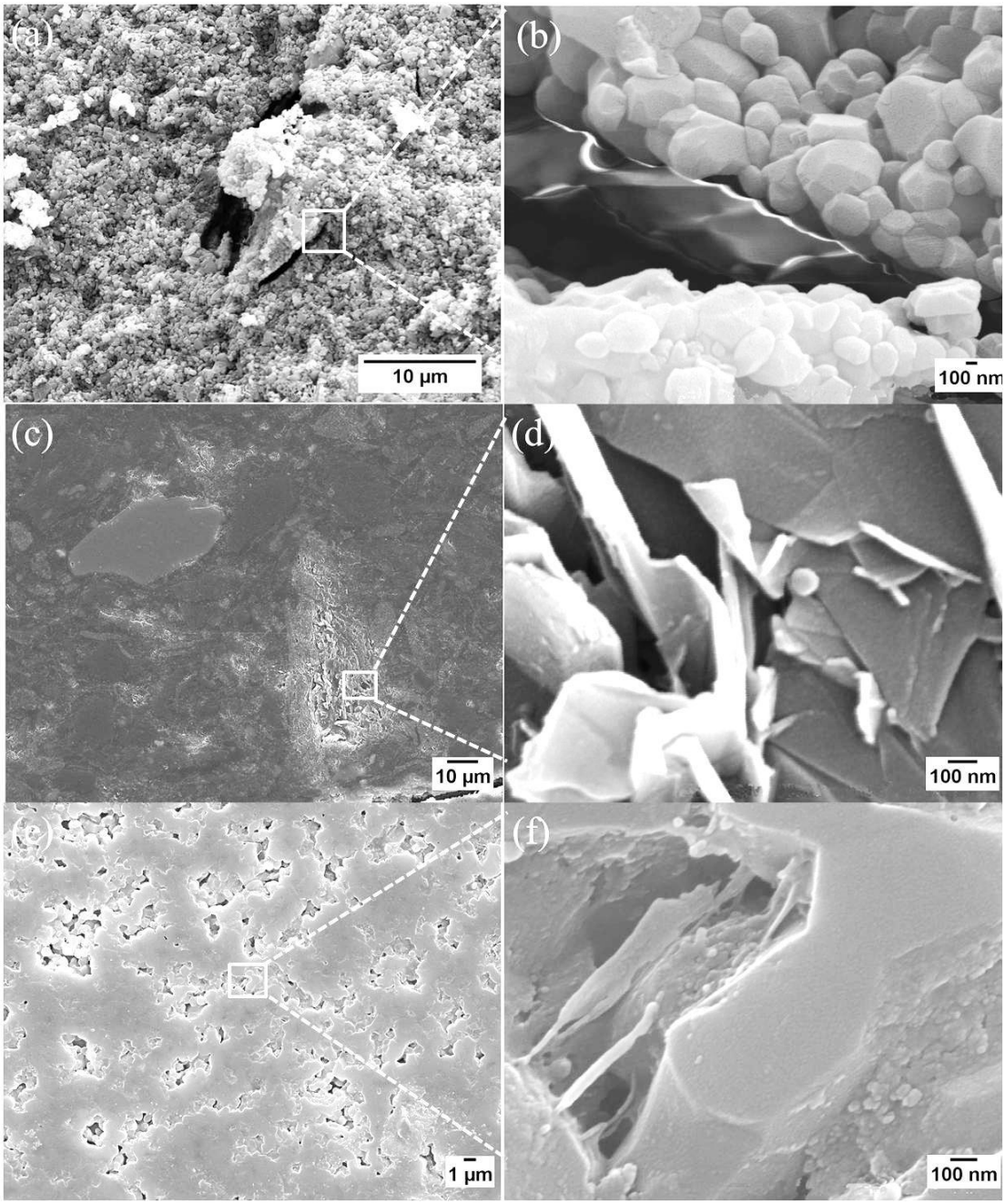

Figure 5.11. Fracture and polished surfaces of the GPL/Al_2O_3 composites processed under the following parameters: heating rate: 5 ℃/s; sintering temperature: 1400 ℃; sintering time: 3 hours; sintering atmosphere: forming gas; flowing rate of forming gas: 6 L/min.

Forming gas is a mixture of 95vol% nitrogen and 5vol% hydrogen. It is believed that GPLs are better protected in forming gas than in nitrogen gas, for the hydrogen in forming gas tends to react with the residue oxygen in the furnace. Densities of the GPL/Al_2O_3 composites

sintered at 1400 ℃ in nitrogen and forming gases are 78% and 83% respectively, which is still far from the desired value for dense microstructures.

Higher sintering temperatures of 1650 and 1770 ℃ and higher flowing rate of inert gases were then used to sinter the 0.45vol% GPL/Al_2O_3 composites. Their fracture surfaces are shown in Figures 5.12 and 5.13. It can be seen from Figure 5.12a and Figure 5.13a GPLs are well distributed in the Al_2O_3 matrix and indicate a good dispersion of GPLs during the ball milling process. In addition, Figure 5.12d and Figures 5.13 b and c reveal that thin GPLs survive the sintering process and are anchored within the Al_2O_3 matrix.

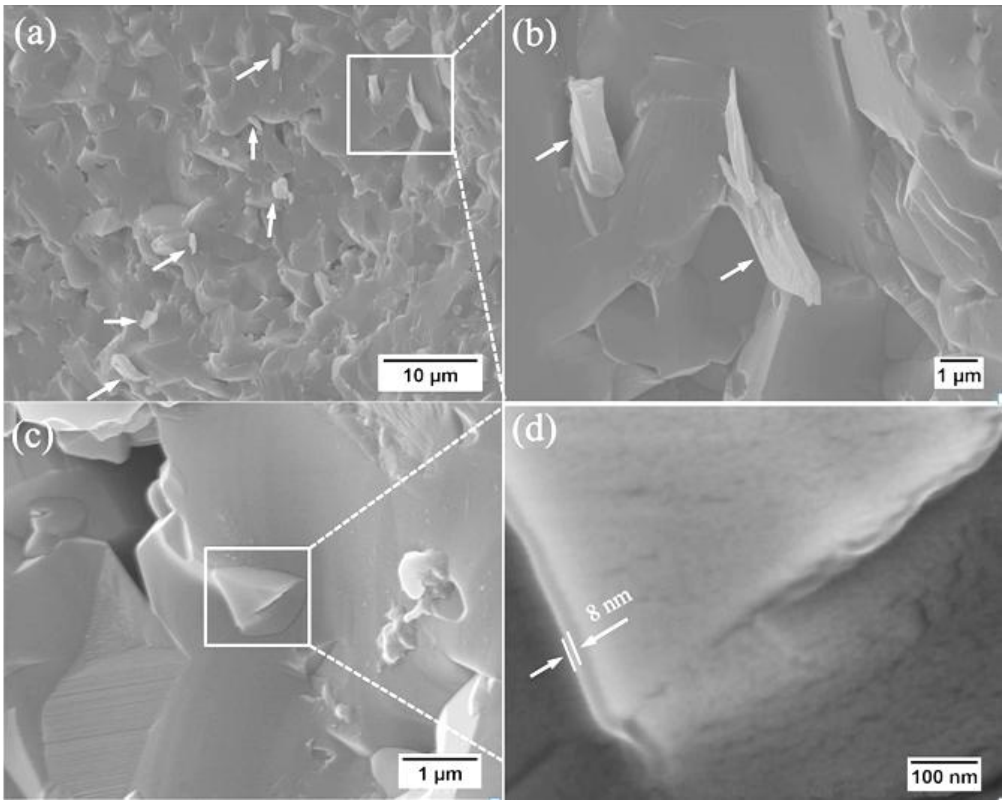

Figure 5.12. Fracture surfaces of the GPL/Al_2O_3 composites processed under the following parameters: heating rate: 5 ℃/s; sintering temperature: 1650 ℃; sintering time: 3 hours; sintering atmosphere: forming gas; flowing rate of forming gas: 8 L/min. White arrows indicate GPLs.

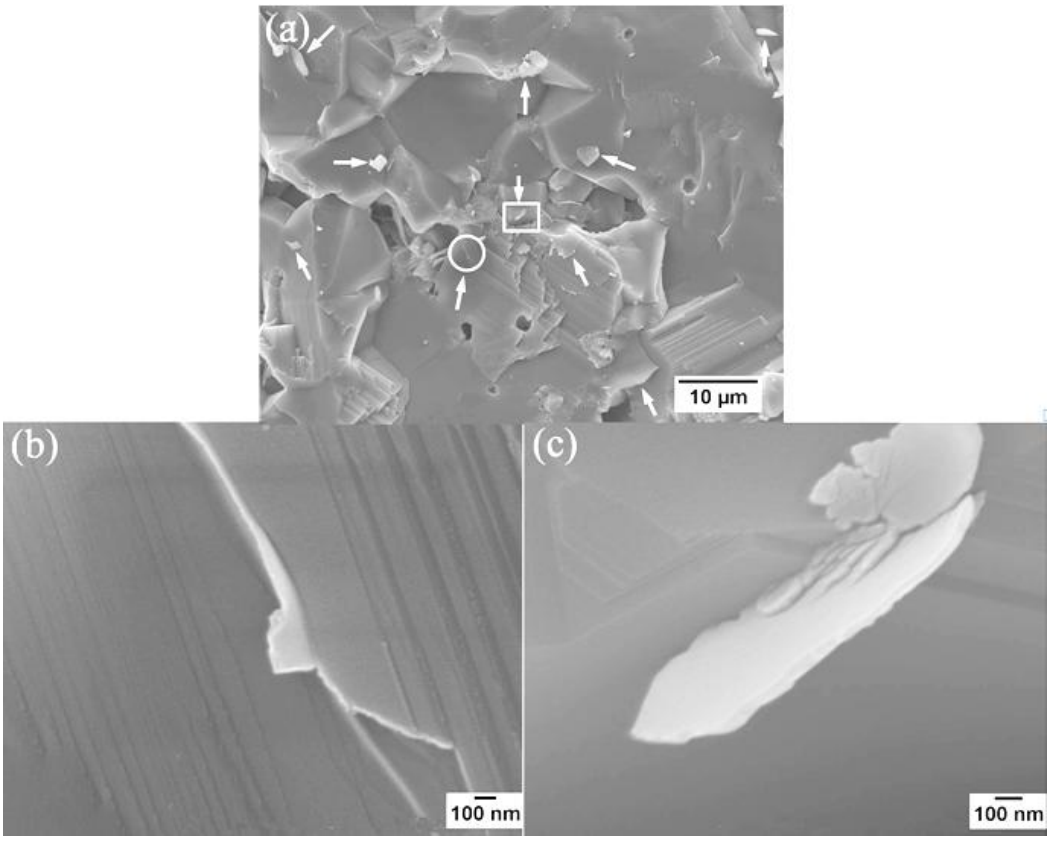

Figure 5.13. Fracture surfaces of the GPL/Al_2O_3 composites processed under the following parameters: heating rate: 5 ℃/s; sintering temperature: 1770 ℃; sintering time: 2.5 hours; sintering atmosphere: nitrogen gas; flowing rate of nitrogen gas: 8 L/min. (b) and (c) are the magnified circle and square areas in (a). White arrows indicate GPLs.

The measured relative densities for the GPL/Al_2O_3 composites sintered at 1650 and 1770 ℃ are 99 % and 99.5% respectively. The high relative densities imply that at these two sintering temperatures consolidation of the GPL/Al_2O_3 composites can be achieved. However, compared to the sample sintered at 1650 ℃, the sample sintered at 1770 ℃ is likely to suffer from significant grain growth, which would degrade the mechanical properties of the ceramic composites.

A summary of the densities of the sintered samples under different processing parameters are compiled into Table 5.1. It is believed that processing parameters (heating rate: 5 ℃/s; sintering temperature: 1650 ℃; sintering time: 3 hours; sintering atmosphere: forming gas; flowing rate of forming gas: 8 L/min) are the optimum parameters among the others because relatively well protected GPLs and a dense microstructure without considerable grain growth can be obtained after sintering.

Table 5.1. A summary of densities of the sintered samples under various processing parameters

Materials	Sintering temperature (℃)	Sintering time (hours)	Flowing Gas	Flowing rate (L/min)	Relative density (%)
GPL/Al_2O_3	1200	2.5	N_2	4	65%
GPL/Al_2O_3	1300	2.5	N_2	6	70
GPL/Al_2O_3	1400	3	N_2	6	78%
GPL/Al_2O_3	1400	3	N_2/H_2	8	80%
GPL/Al_2O_3	1650	3	N_2/H_2	8	99%
GPL/Al_2O_3	1770	2.5	N_2	8	99.5%

5.3.2 Effects of content of GPLs on the microstructures and mechanical properties of GPL/Al_2O_3 composites.

Green compacts with 0, 1.17, 1.85 and 2.75 vol% GPLs were sintered respectively under the optimum sintering parameters determined in section 5.3.1. Microstructures and mechanical properties of the sintered samples are characterized.

5.3.2.1 The GPLs content in the sintered GPL/Al_2O_3 composites.

The results of TGA tests are shown in Figure 5.14. It is found that the sintered GPL/Al_2O_3 composites contain 0.4, 0.69 and 0.79 wt% GPLs respectively and the corresponding volume percent of GPLs in the sintered composites are 0.75, 1.3 and 1.48 vol%. Approximately 35.9%, 29.73% and 46.19% GPLs in each composite were lost during the sintering process.

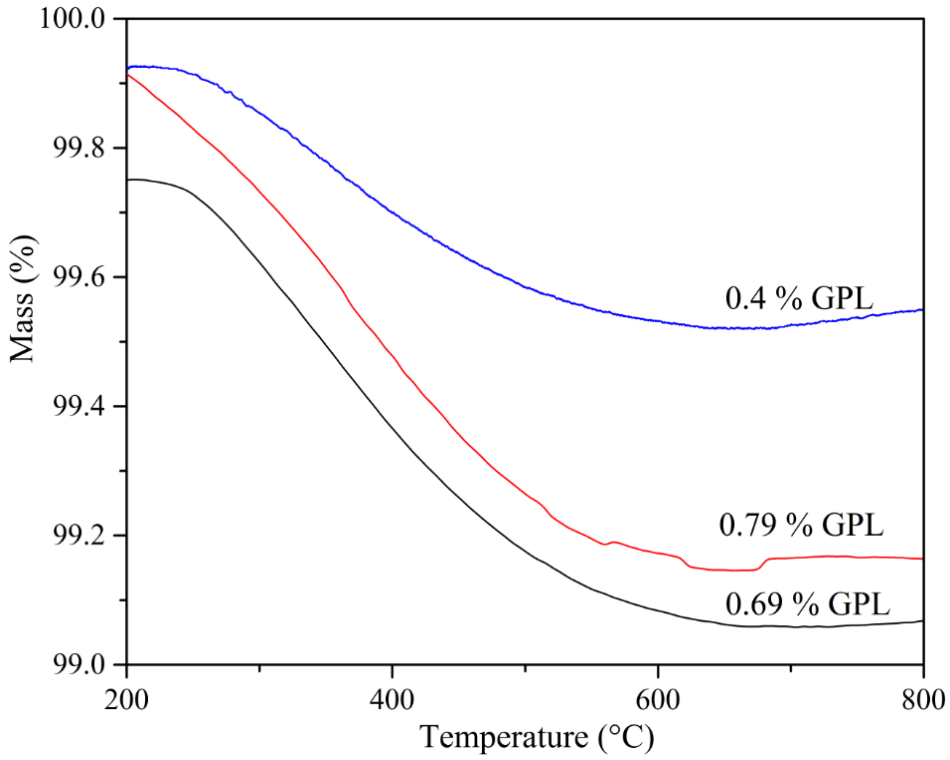

Figure 5.14. TGA for the sintered samples with different GPLs content.

5.3.2.2 Microstructures of the sintered samples

Fracture surfaces of the sintered samples are shown in Figure 5.15. It can be seen that the pure Al_2O_3 matrix exhibits an intergranular fracture mode while GPL-reinforced Al_2O_3 composites present both an intergranular and intragranular fracture modes. The fracture mode

is determined by strengths of the ceramic matrix and the boundaries between them. For the pure Al_2O_3, the strength of grain boundaries are weaker than the Al_2O_3 grains, which enables cracks easily to propogate along the grain boundaries while for GPL-reinforced Al_2O_3 composites, the observed fracture mode implies the strenghed grain boundaries and moderate improvement in fracture tougheness [52]. Meanwhile, it is noted that GPLs are well distributed in the Al_2O_3 matrices, indicating the good dispersion of GPLs during the ball milling process.

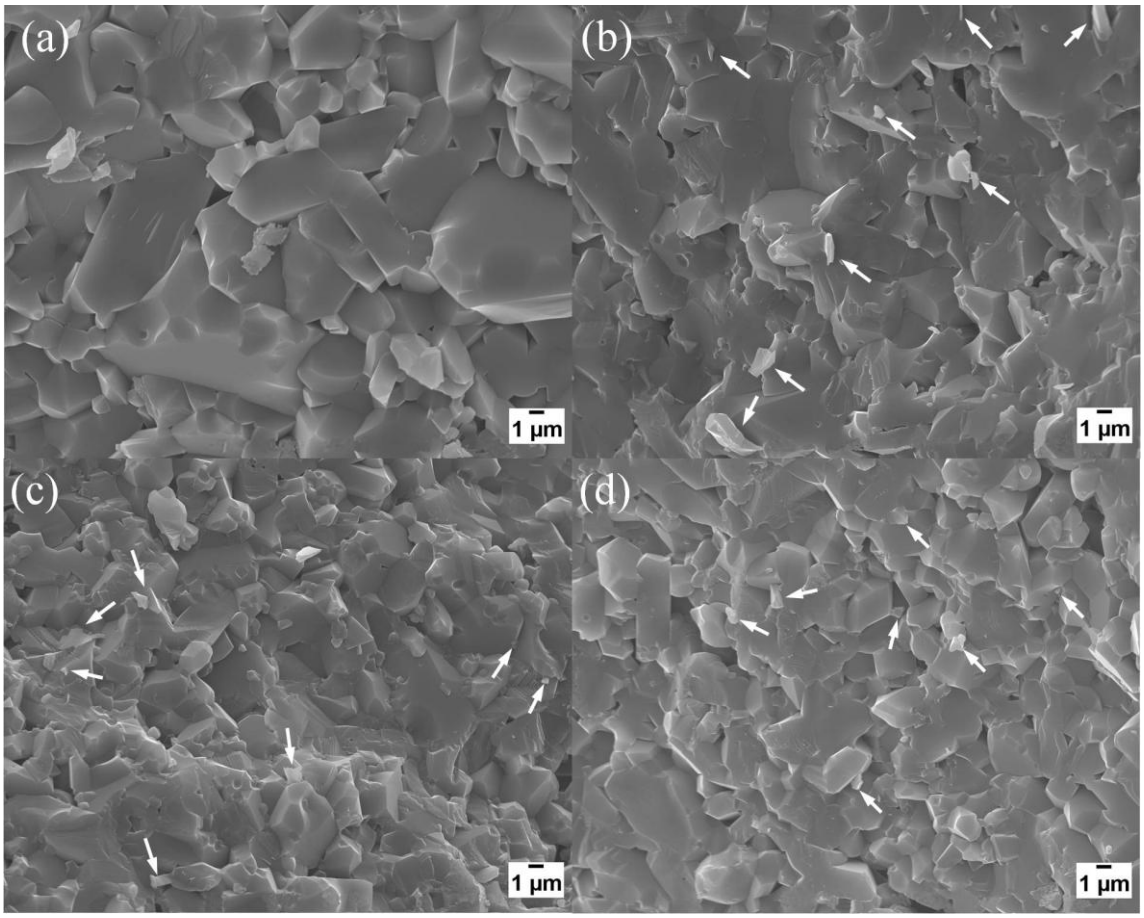

Figure 5.15. Fracture surfaces of the sintered samples. (a) Al_2O_3, (b) 0.75 vol% GPL/Al_2O_3, (c) 1.3 vol% GPL/Al_2O_3 and (d) 1.48 vol% GPL/Al_2O_3.

In addition, grain sizes of the Al_2O_3 matrices decrease with the increasing percentage of GPLs. The decrease in grain size is associated with the pinning effect of GPLs in the grain boundaries. To obtain the average grain sizes of the Al_2O_3 matrices, polished and thermally etched surfaces of the sintered samples are characterized using SEM. As shown in Figure 5.16, significant grain decrease is observed by adding the GPLs. With the increasing percentage of GPLs, Al_2O_3 matrices exhibit a more uniform and finer microstructure.

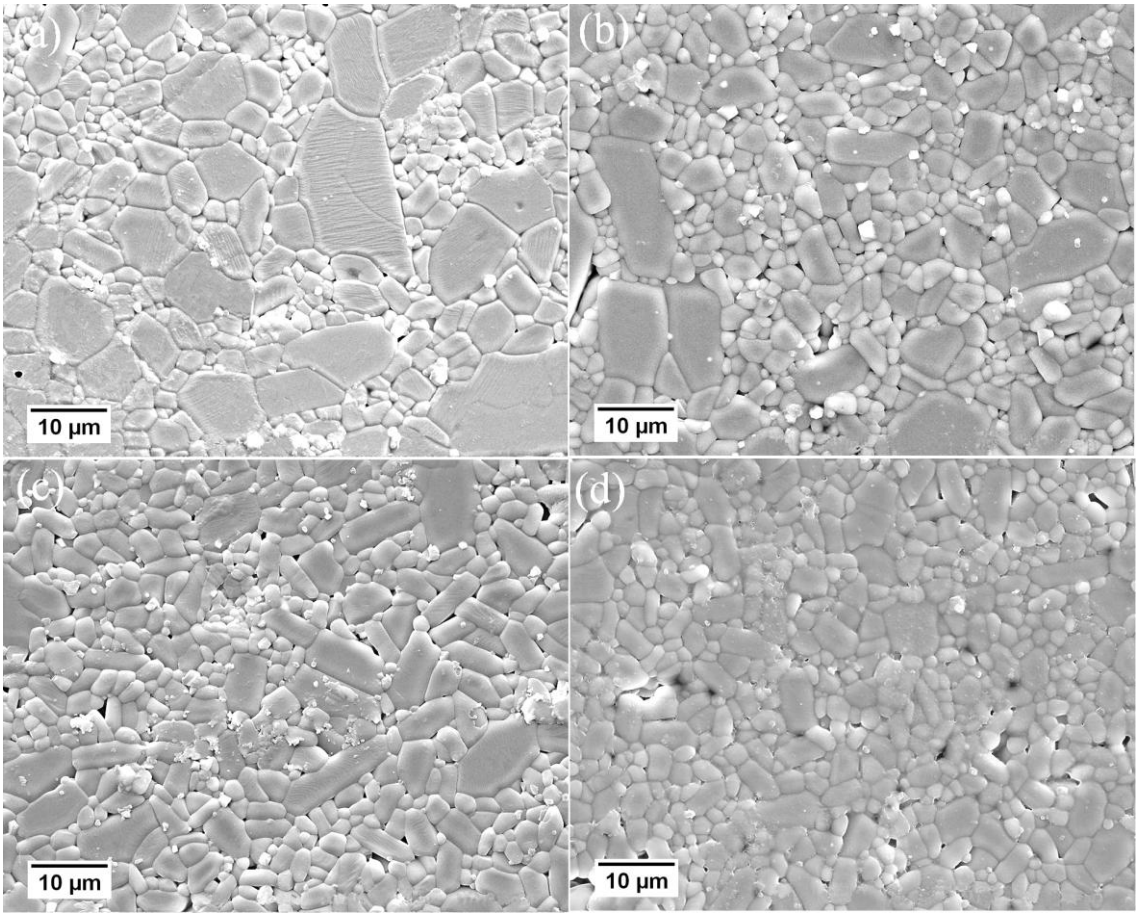

Figure 5.16. SEM images of the polished and thermally etched surfaces of the sintered samples. (a) Al_2O_3, (b) 0.75 vol% GPL/Al_2O_3, (c) 1.3 vol% GPL/Al_2O_3 and (d) 1.48 vol% GPL/Al_2O_3.

The grain sizes of the Al_2O_3 matrices are plotted in Figure 5.17. It can be seen that the grain sizes decrease from 4.31 to 2.87 µm with the increasing concentration of GPLs from 0 to 1.48

vol%. The significant refinement in the matrix microstructures is expected to contribute to the increase in both hardness and flexural strength.

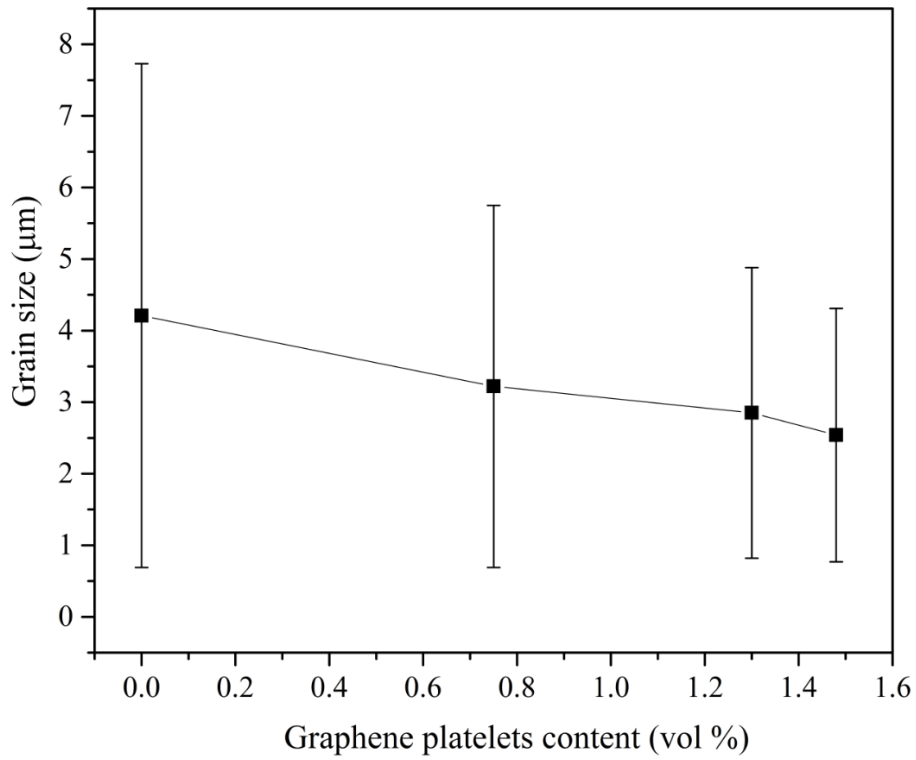

Figure 5.17. Grain sizes of Al_2O_3 matrices as a function of GPLs content.

5.3.2.3 Raman spectra of the pristine GPL and GPLs after ball milling and sintering.

Raman spectra of the pristine GPL and GPLs after the ball milling process are presented in Figure 5.18. It is very evident that D peaks of GPLs in powder mixtures show pronounced lower intensities than those of the pristine GPL.

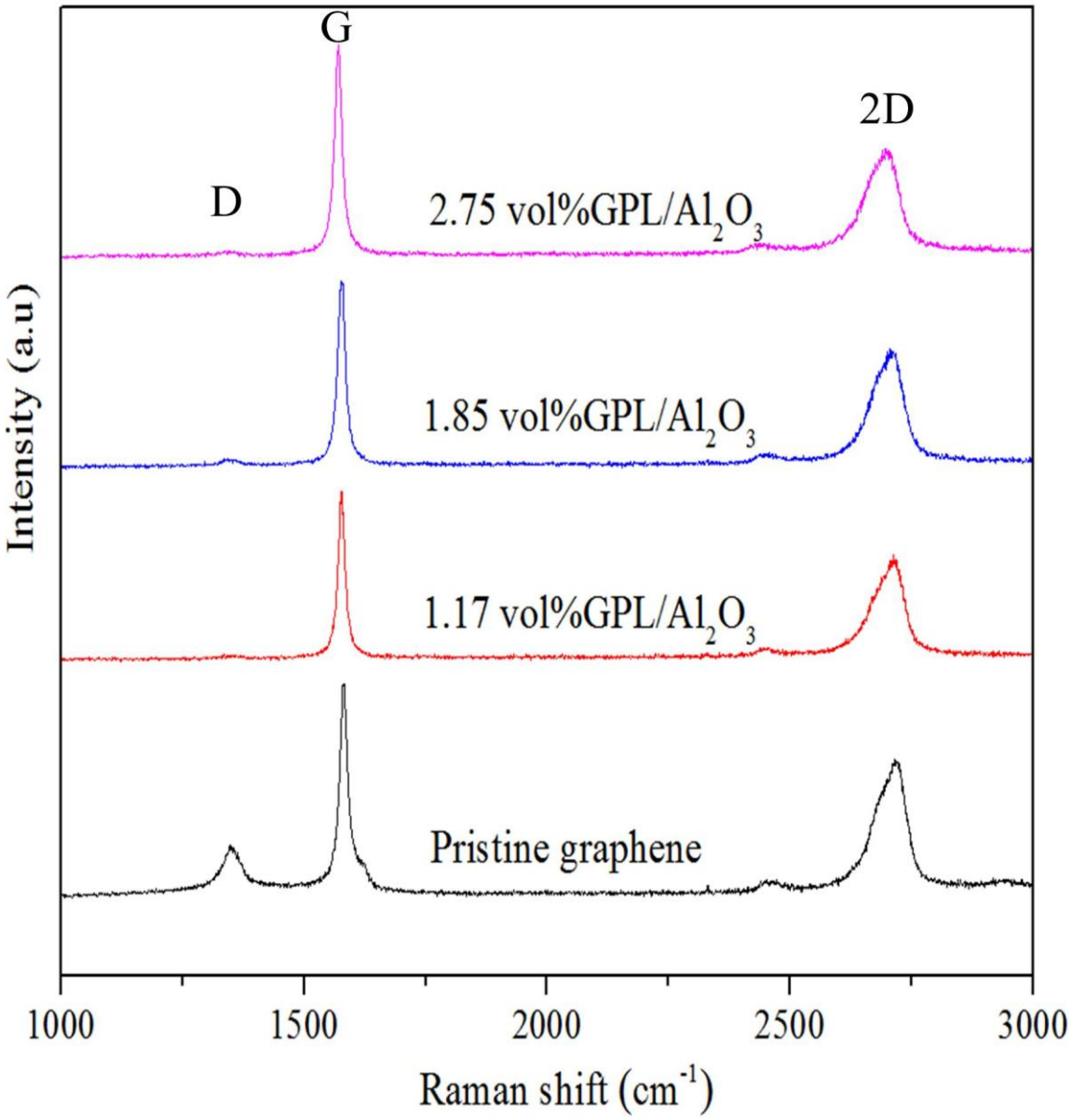

Figure 5.18. Raman spectra of the pristine GPL and GPLs in powder mixtures.

To gain further insight into the structures of GPLs Raman parameters are compiled in Table 5.2. It is noticed that GPLs in powder mixtures exhibit much lower I_D/I_G compared to the pristine GPLs, indicating decreased defects of the GPLs [111]. The result can be explained by the agglomeration of GPLs during ball milling, resulting in decreased number of edge defects. On the other hand, the I_{2D}/I_G of the GPLs in powder mixtures is lower than that of the pristine GPL which again indicates the occurrence of an agglomeration of GPLs. In addition, I_{2D}/I_G

decreases with the increasing percentage of GPLs, implying addition of a high percentage of GPLs is more prone to causing formation of GPL aggregates [113]. This argument can be further supported by the increasing FWHM of 2D bands with an increasing percentage of GPLs.

Table 5.2. Raman parameters of the pristine GPL and the GPLs in the powder mixtures

Materials	I_D/I_G	FWHM (G)	ν (G)	FWHM (2D)	ν (2D)	I_{2D}/I_G
Pristine GPL	0.26	18	1582	75	2714	0.65
1.17 vol% GPL/Al_2O_3	0.04	17	1577	75	2712	0.63
1.85 vol% GPL/Al_2O_3	0.06	18	1576	78	2704	0.63
2.75 vol% GPL/Al_2O_3	0.04	18	1571	85	2695	0.52

The Raman spectra of the pristine GPL and GPLs in the sintered samples are compared in Figure 5.19. It can be seen that GPLs in the sintered samples exhibit much higher spectrum backgrounds compared to the pristine GPL. The increased spectrum backgrounds can be attributed to interaction of GPLs with the Al_2O_3 during the sintering process. Meanwhile, it is evident that the after sintering GPLs show significantly higher graphitic defects (I_D/I_G) and the presence of D+G mode is observed in sintered samples. On the other hand, it is also noted that GPLs in the sintered samples show far weaker signitures of G and 2D bands in comparision with the pristine GPL, which implies that damage is induced during the sintering process [209]. The induced damages might be the result of hole doping caused by ambient oxygen molecules within the sintering tube and the interfacial reactions between the GPLs and ceramic matrix.

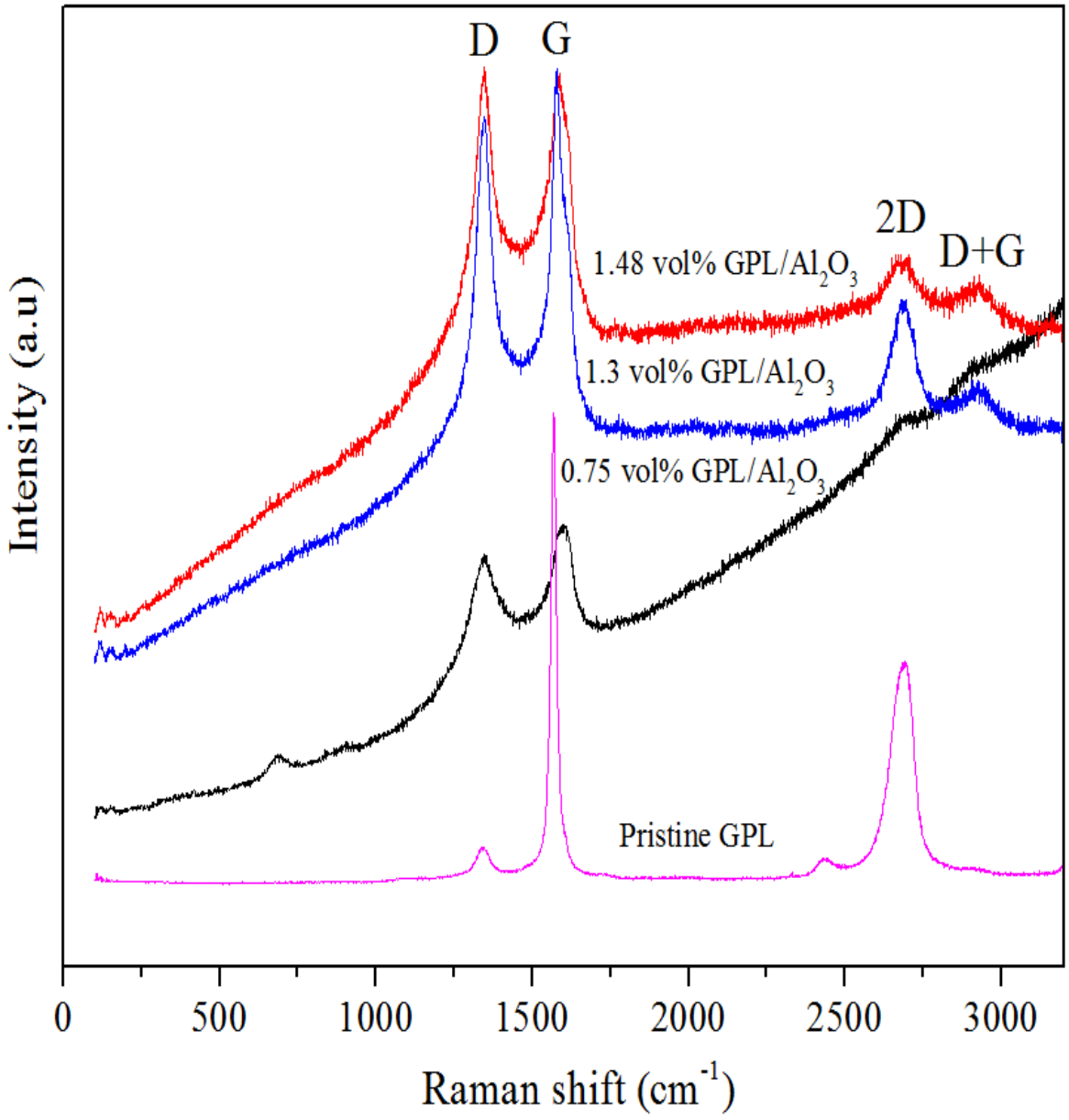

Figure 5.19. Raman spectra of the pristine GPL and GPLs after sintering.

5.3.2.4 XRD patterns of the pristine GPL and the sintered samples

XRD analysis of the pristine GPL, pure Al_2O_3 and GPL/Al_2O_3 composites were carried out and presented in Figure 5.20. It can be seen that the GPL exhibits the same XRD pattern as

the natural graphite and there is no sign of the presence of new phases in the composites. It is reported that aluminum oxycarbides are likely to be formed during a high temperature sintering process [210]. However, no such phases are observed in XRD patterns. The reason for this result might be related to the low addition of GPLs which makes it hard to trace the reaction products.

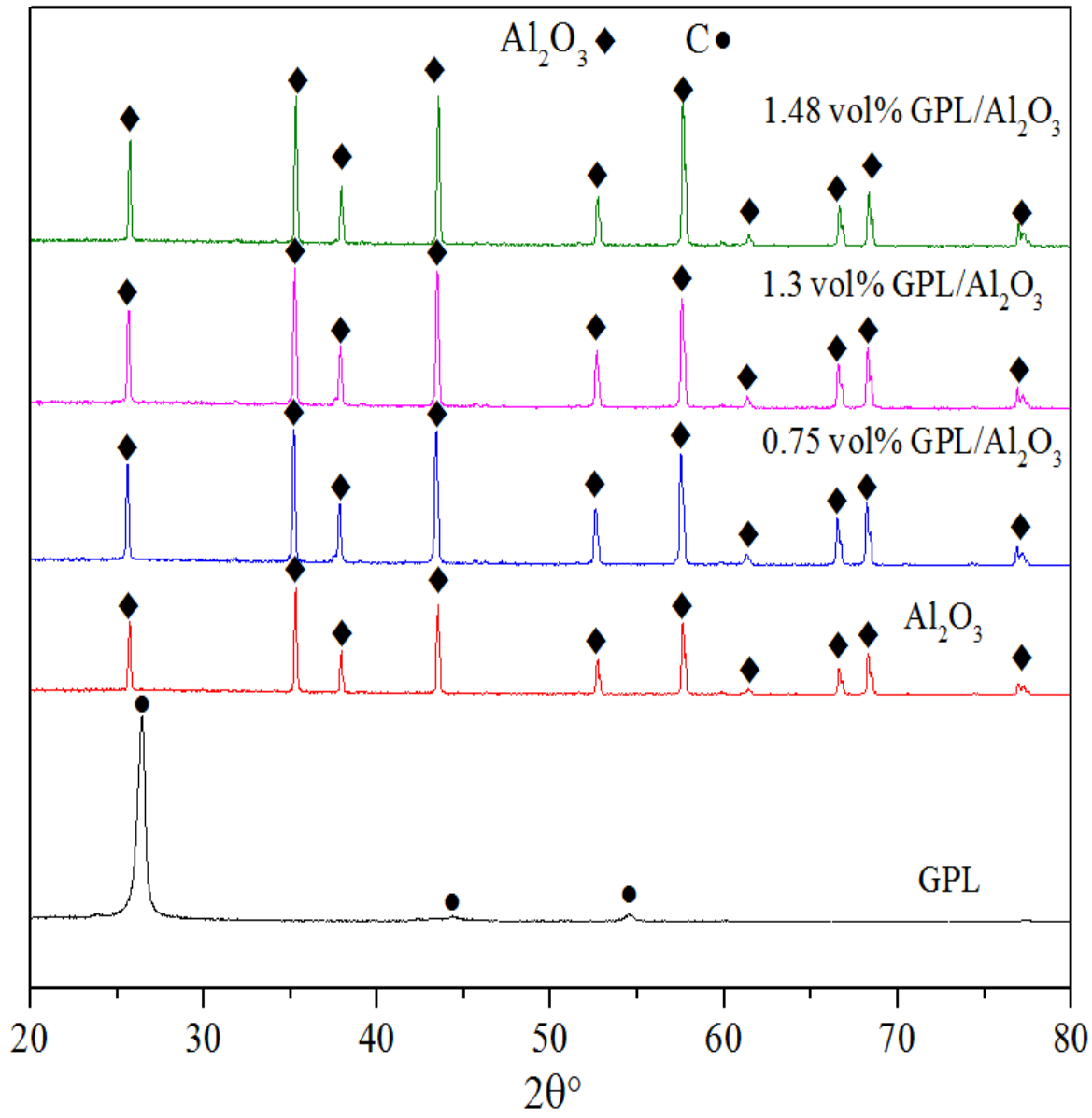

Figure 5.20. XRD pattens of the pristine GPL, pure Al_2O_3 and GPL/Al_2O_3 composites.

5.3.2.5 Mechanical properties of the pressureless sintered pure Al_2O_3 and GPL/Al_2O_3 composites

Figure 5.21 shows the densities of pure Al_2O_3 and GPL/Al_2O_3 composites. It can be seen that the pure Al_2O_3 has nearly been fully densified while the GPL-Al_2O_3 composites present relatively lower densities, which decrease from 98.2 to 95.6% with the increasing concentration of GPLs from 0.75 to 1.48 vol%. The result suggests that the addition of GPLs hinders the densifcation process of GPL/Al_2O_3 composites during pressureless sintering and a higher sintering temperature or longer sintering time, may be requried to obtain fully dense samples.

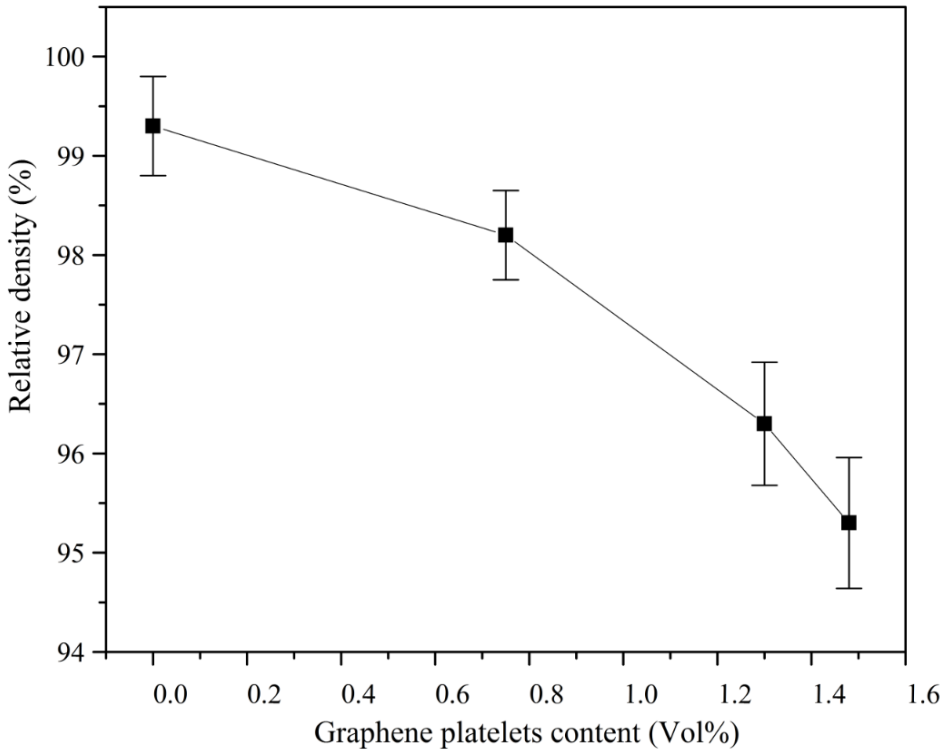

Figure 5.21. Densities of the GPL/Al_2O_3 samples as a function of GPLs content

Hardness of pure Al_2O_3 and GPL/Al_2O_3 composites are compared and plotted in Figure 5.22. It is noticed that the hardness decreases with an increasing percentage of GPLs. Usually density and grain size play the major roles in the degree of hardness. Higher density and smaller grain size would result in greater hardness. Although the decreased grain size brought by GPLs would contribute to the increase of hardness, the addition of GPLs causes the lower density of the composites and the decrease of hardness. This explains why GPL/Al_2O_3 composites with finer microstructure exhibit a lower degree of hardness.

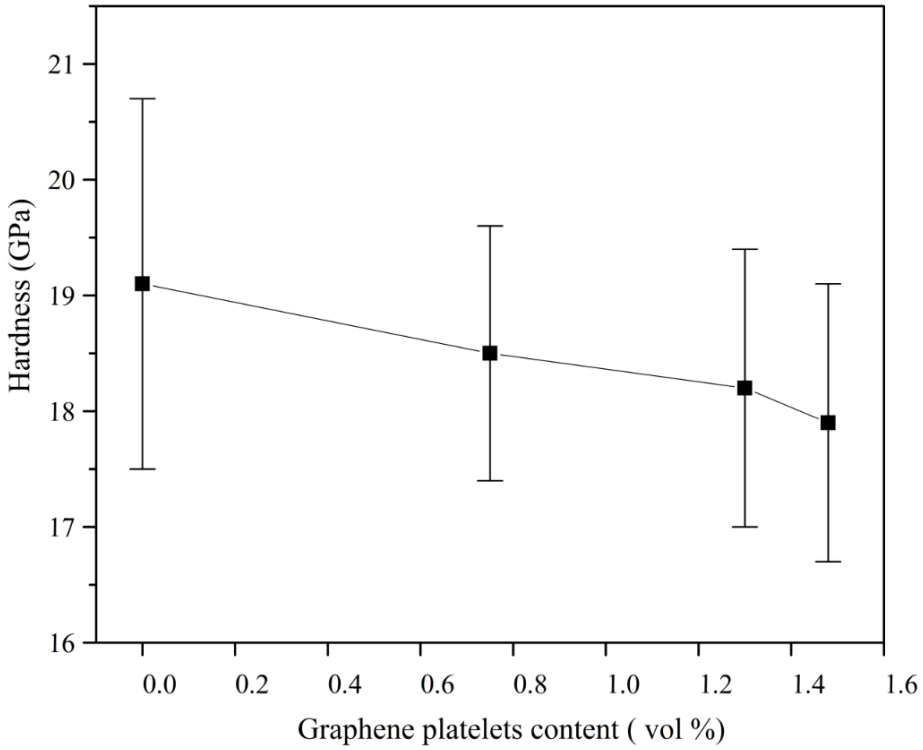

Figure 5.22. Hardness of the GPL/Al_2O_3 samples as a function of GPLs content.

Figure 5.23 presents flexural strength of the pure Al_2O_3 and GPL/Al_2O_3 composites. It can be observed that the flexural strength of the Al_2O_3 has been significantly improved by adding GPLs and it increases considerably with a minor addition of GPLs and decreases with the

further increase of GPLs. A maximum increase of approximately 60% in flexural strength was achieved by introducing 0.75 vol% GPLs. Similar to hardness, flexural strength is mainly affected by the grain size and residual porosity. The smaller grain size with reduced flaw size would result in better flexural strength while the presence of pores would allow cracks to be formed easily and cause the small fracture energy due to the stress concentration around the pores [203].

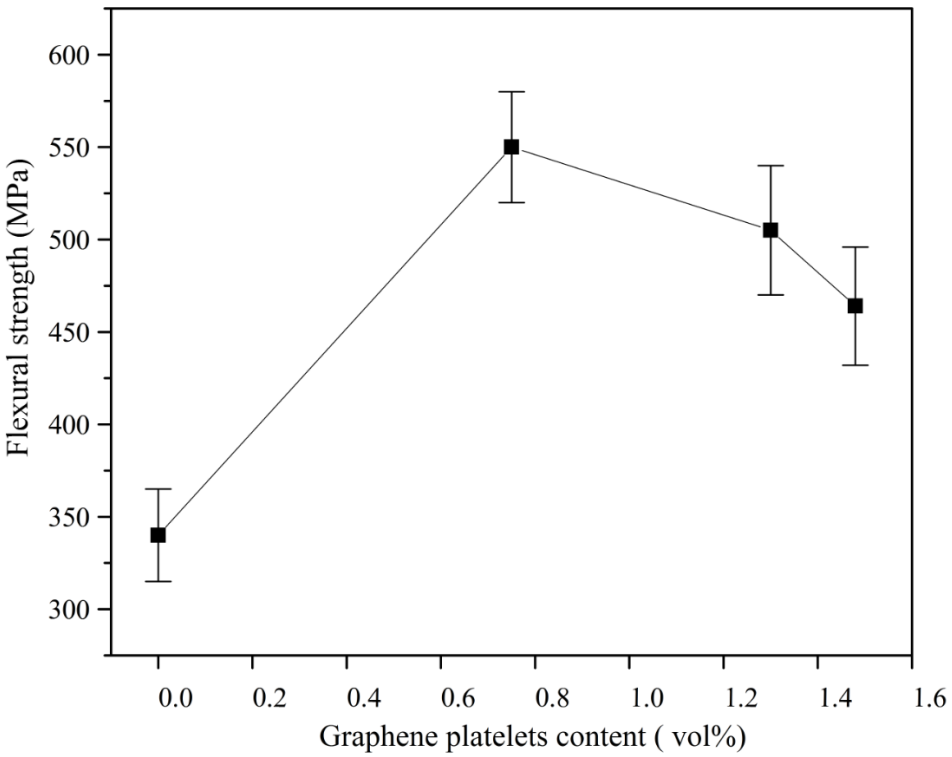

Figure 5.23. Flexural strength of the GPL/ Al_2O_3 samples as a function of GPLs content.

Fracture toughness of the sintered samples and the typical notch size of the specimen are shown in Figure 5.24 and Figure 5.25. It is noted that variation in fracture toughness exhibits the same trend as the flexural strength and all of the GPL/Al_2O_3 composites present improved fracture toughness in comparision with pure Al_2O_3. A significant increase in fracture toughness has been achieved by introducing 0.75vol% GPLs. A further increase of GPLs

leads to a decrease in fracture toughness. The obtained maxmium fracture toughness of the GPL/Al_2O_3 composites is appoximately 70% higher than that of pure Al_2O_3.

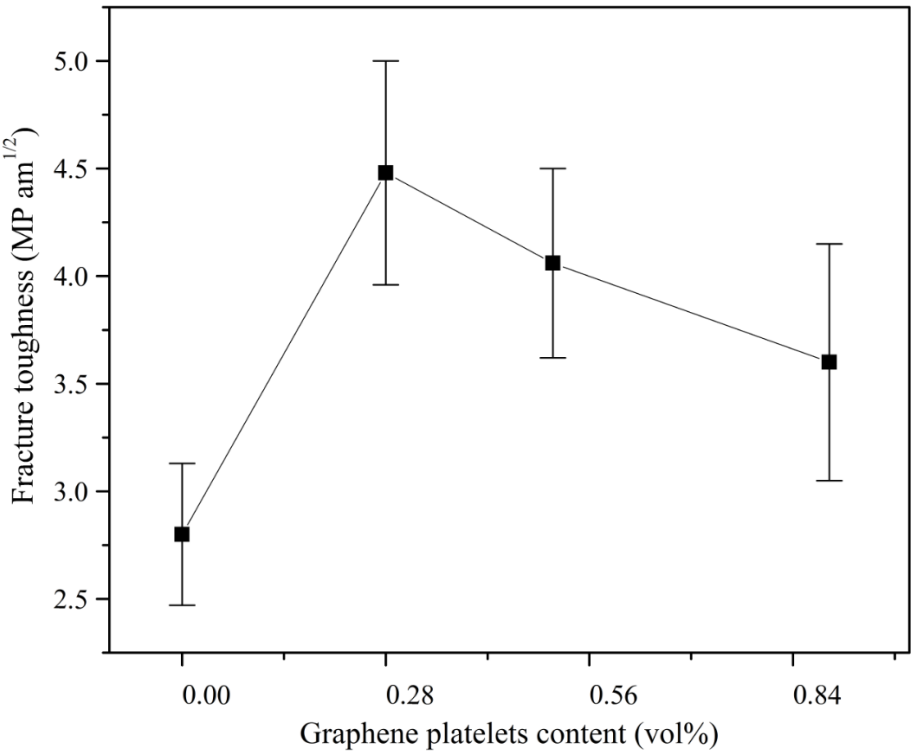

Figure 5.24. Fracture toughness of the GPL/Al_2O_3 samples as a function of GPLs content.

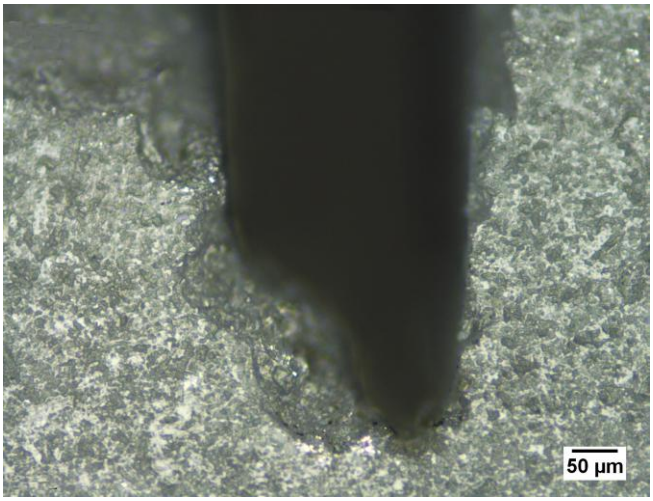

Figure 5.25. A SEM image of the typical notch tip.

5.3.2.6 Effects of GPLs on the mechanical properties of the GPL/Al_2O_3 composites

As mentioned in Chapter 3, the mechanical properties of the densifed GPL-reinforced Al_2O_3 are mainly dependent on the dispersion of GPL in the matrix and interaction between GPLs and the ceramic matrix. In the research of this chapter, well dispersed GPLs in the ceramic matrix are achieved, as shown in Figures 5.26 a, c and e. A good dispersion of GPLs in the ceramic matrix would contribute to the mechanical propreties in two ways. On one hand, the distribution of GPLs in the grain boundaries of the ceramic matrix prevents the migration of grain boundaries during the long time sintering process and causes the formation of a fine microstructure, which benefits the flexural strength and fracture toughness by decreasing the defect size of the ceramic matrix and increasing the contact areas between the GPLs and the ceramic matrix respectively. On the other hand, due to the GPLs' high Young's modulus, the embeded GPLs in the ceramic matrix (Figures 5.26 b, d and f) can reinforce the matrix, leading to improved flexural strength.

Meanwhile, due to the long time sintering process at the high temperature, GPLs securely anchored in the ceramic matrix and close interaction between GPLs and the ceramic matrix are observed (Figures 5.26 b and f). A good interaction between GPLs and the ceramic matrix would enable an efficient load transfer from the ceramic matrix to the GPLs, resulting in the improvement in flexural strength. Additionally, high energy is required to overcome the strong interfiacial friction at the interface between the ceramic matrix and the GPLs to pull out the GPLs, leading to the increase in fracture toughness. It should be noted that GPL aggregates (Figures 5.26 c) are observed and embeded in the ceramic matrix. It is believed that during propagation of cracks interlayer sliding in the GPL aggregates is likely to occur to help energy dissipation and thus contribute to the fracture toughness of the composites [211].

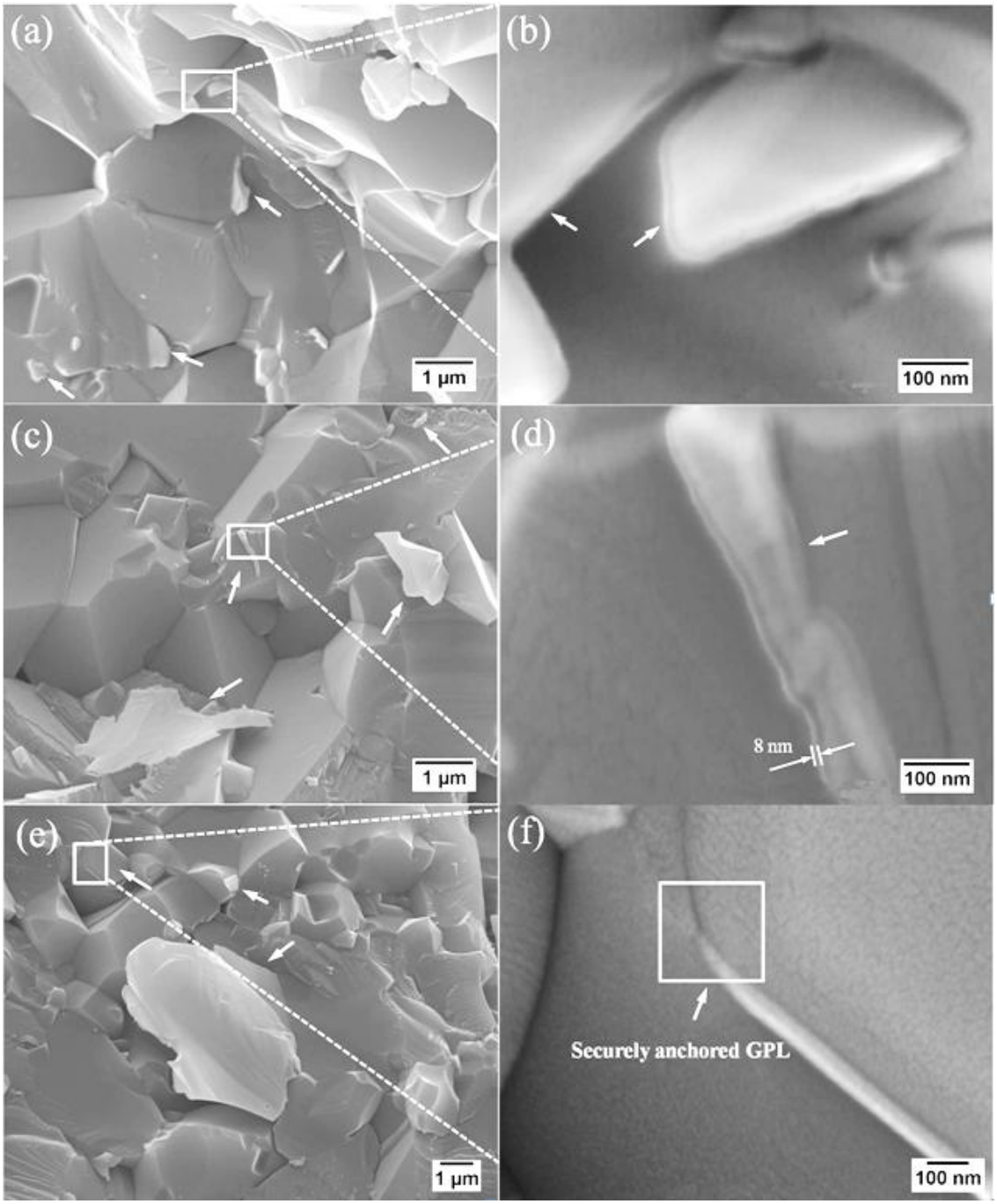

Figure 5.26. Fracture surfaces of GPL/Al_2O_3 composites

5.4 Summary

In this chapter, for the first time, pressureless sintering of GPL/Al_2O_3 composites is reported. GPL/Al_2O_3 composites were sintered in a coventional furnace and various characterization

techniques such as XRD, SEM and Raman spectroscopy were used to analyze the sintered composites. The obtained results can be summarized as follows:

1. The optimum processing parameters for pressureless sintering of the GPL/Al_2O_3 composites are: heating rate: 5 ℃/min, sintering temperature: 1650 ℃, sintering time: 3 hours, sintering atmosphere: forming gas and flowing rate: 8L/min.

2. GPL/Al_2O_3 composites containing 0, 0.75, 1.3 and 1.48 vol% GPLs were nearly fully densified under the optimum processing parameters and densities of the composites decrease with the increasing percentage of GPLs.

3. Grain sizes of Al_2O_3 ceramic matrix decrease from 4.31 to 2.87 μm with an increasing percentage of GPLs from 0 to 1.48 vol% GPLs.

4. Raman studies show moderate agglomeration of GPLs occurs during the ball milling process and a high percentage of GPLs is more prone to causing the formation of GPL aggregates. Meanwhile, a significant amount of defects are generated in the GPLs after sintering.

5. The mechanical properties of the Al_2O_3 matrix are significantly improved by adding GPLs. Hardness of the GPL/Al_2O_3 composites decreases with an increasing percentage of GPLs. Flexural strength and fracture toughness of GPL/Al_2O_3 composites increase with a minor addition of GPLs and then decrease with the further increase of GPLs. A maximum

increase of approximately 60% in flexural strength and 70% in fracture toughness are achieved by introducing 0.75vol% GPLs. The good dispersion of GPLs and the interaction between GPLs and the ceramic matrix are the main factors enhancing the mechanical properties.

Chapter 6: Electrodeposition and characterization of GPL/Ni composite coatings

6.1 Introduction

This chapter presents electrodeposition and characterization of GPL/Ni composite coatings. The research in this chapter aims to explore new composite coatings with the addition of GPLs for improved corrosion resistance. This chapter starts by introducing experiments of the fabrication process and characterization techniques in section 6.2. Afterwards, the characterization results of the pure Ni and GPL/Ni coatings are presented in section 6.3. In particular, Raman spectra of GPLs and XRD of the coatings are given in sections 6.3.2 and 6.3.3 respectively. The polarization curves and impedance spectra of the coatings and discussion concerning corrosion resistance are presented in section 6.3.4. Finally, this chapter is summarized in section 6.4.

6.2 Experiments of fabrication

6.2.1 Starting materials

GPLs are used in the fabrication of GPL/Ni composite coating. The detailed information of GPL can be found in section 3 in Chapter 3. The Ni electrolyte made of Ni (85-95 g/L), Ni chloride (8-12 g/L) and boric acid (25-35 g/L) was purchased from PMD Chemicals Ltd, UK.

A surfactant of sodium dodecyl sulphate (SDS) obtained from Sigma-Aldrich was added as a stabilizer.

6.2.2 Electrodeposition

A mild steel plate with dimension of 10 mm × 10 mm × 4 mm was mounted in a resin (Figure 6.1) and used as a cathode. An Ni plate was used as an anode. Electrodeposition was carried out to prepare the Ni and GPL/Ni coatings at a current density of 0.1 A/cm^2 using the corresponding Ni bath solution. The temperature of the bath solution was maintained at 45 ^oC and the pH of the bath solution was adjusted to 3-4. The deposition surface of the steel plate was ground using SiC paper and polished with diamond suspension. The pure Ni deposits were obtained from the Ni bath solution without GPLs. The composite coatings were prepared from the bath solution containing the 0.1g/L and 0.2 g/L GPLs and they are denoted as 1-GPL/Ni and 2-GPL/Ni respectively. Prior to the composite coating, the bath solution was stirred by mechanical mixer and high power ultrasonic equipment simultaneously for 1 hour. To achieve a good dispersion of GPLs, a surfactant of SDS was added as a stabilizer. The concentration of SDS was 0.2 g/L and 0.4 g/L in the Ni plating bath containing 0.1g/L and 0.2g/L GPLs respectively. The deposition time was adjusted to produce around 50 μm coatings thickness. After electrodeposition, samples were ultrasonicated in an acetone bath to remove loose GPLs from the surfaces of the coatings.

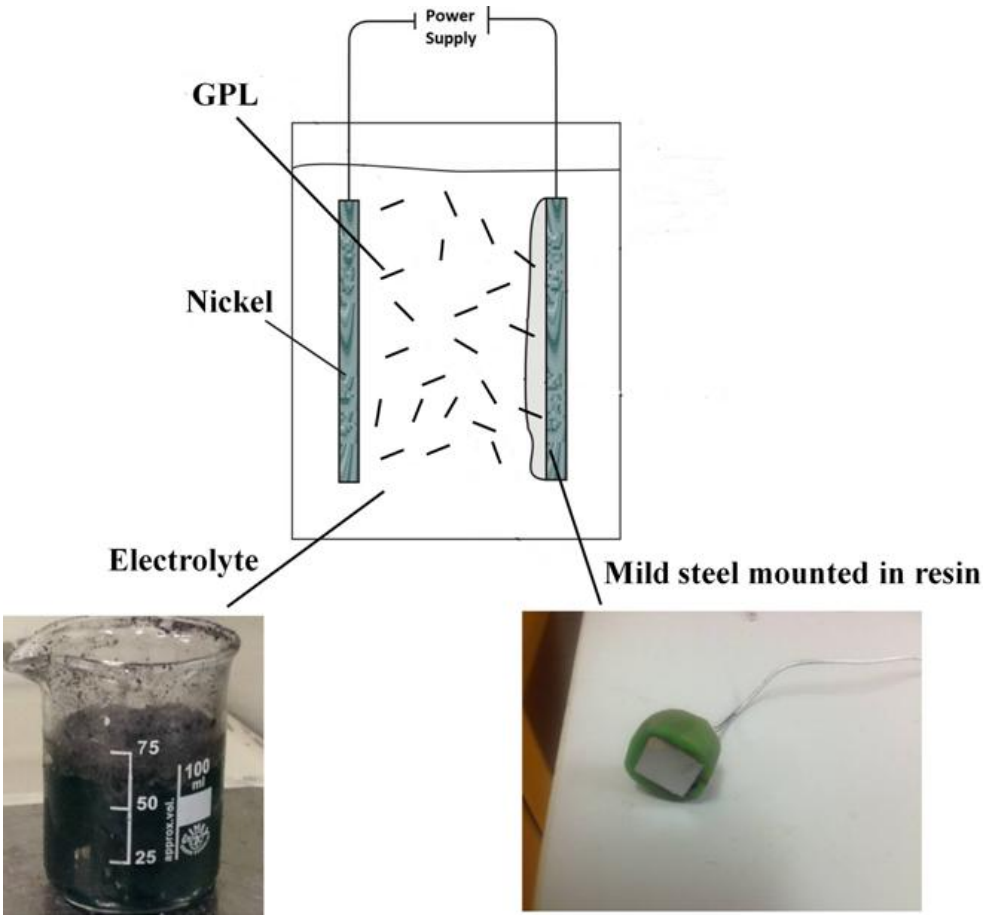

Figure 6.1. A schematic illustration of the electrodeposition process.

6.2.3 Material Characterizations

Equipment and characterization techniques such as the hardness tester, SEM, Raman spectroscopy and XRD and used in previous chapters were also employed in the research of this chapter. The major difference is an electrochemical analyzer was used to investigate the corrosion resistances of the electrodeposited coatings.

6.2.3.1 Electrochemical measurement

Polarization curves and impedances of the coatings were carried out using an electrochemical analyzer (ACM instrument, Gill AC, UK) (Figure 6.2) in a three-electrode cell (Figure 6.3) with a platinum plate as the counter electrode and a saturated calomel electrode as the reference electrode. The electrodeposited samples were used as the working electrode. Polarization curves of the specimens were measured in 3.5% sodium chloride (NaCl) solution at room temperature by a potential scanning rate of 1.0 mV/s. As for the impedance measurements, samples were immersed in NaCl solution for 1 hour to stabilize the open-circuit potential. Impedances were obtained in the frequency range of 0.01Hz-10 kHz.

Figure 6.2. An image of electrochemical analyzer.

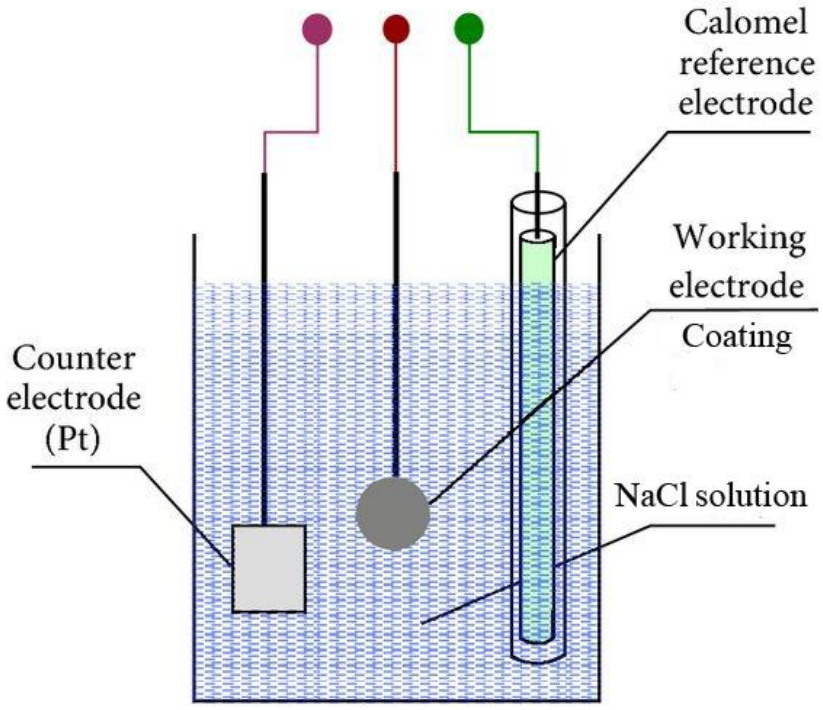

Figure 6.3. Schematic of three-electrode cell.

6.3 Results and discussion

6.3.1 Surface morphologies and microstructures of the coatings

Figure 6.4 shows the surface morphologies of the electrodeposited coatings. Carbon contents of the composite coatings prepared from plating baths containing 0.1g/L and 0.2/g/L GPLs are estimated to be 20.48 and 32.06 wt% respectively from the energy dispersive spectroscopy (EDS) mapping analysis (Figure 6.4c and e). It can be seen that pure Ni coating presents a flat surface and a uniform structure while there are bulges distributed on the surfaces of GPL/Ni composite coatings. Similar results are observed for CNT/Ni composite

coatings [212]. In addition, more and larger bulges are observed on the surface of composite coating prepared from a bath with a higher content of GPLs.

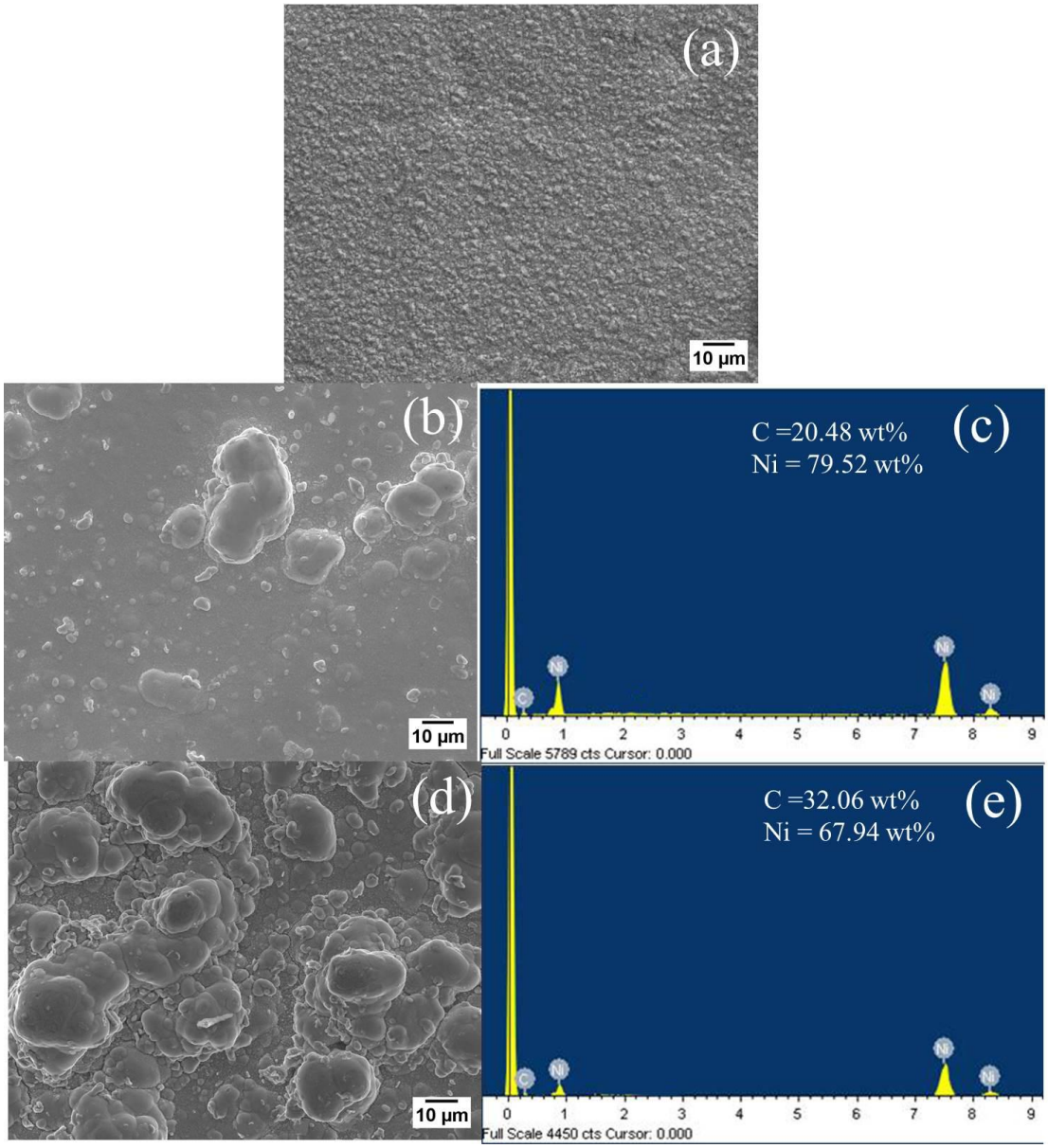

Figure 6.4. Surface morphologies and elemental composition of electrodeposited coatings. (a) pure nickel, (b) 1-GPL/Ni and (d) 2-GPL/Ni. (c) and (e) are the EDS results of the square areas in (b) and (d).

The difference between surface morphologies of the pure Ni and composite coatings can be related to the electrical property of the GPLs. Due to the fact that GPLs are very conductive fillers, cathode surfaces are inevitably increased by incorporating GPLs in the Ni matrix. During electrodeposition, electrons can transfer from the entrapped GPLs' surfaces to the Ni matrix and as a result, the Ni ions are reduced either on the surface of the cathode or GPLs' surfaces. In addition, since GPLs have a better conductivity than the Ni matrix, reduction rates of Ni ions on the surfaces of the GPLs would be higher than those on the surfaces of the Ni matrix. Therefore, Ni ions would be preferably deposited onto the GPLs and lead to the formation of some bulging parts on the surfaces of the final coatings. A schematic illustration of the deposition process of Ni and GPL/Ni is shown in Figure 6.5. This explanation for the deposition process is further supported by Figure 6.6, in which the GPLs observed either stick out from the Ni matrix (Figure 6.6 a and b) or are incorporated in the Ni matrix (Figure 6.6c), implying the Ni ions deposit onto the GPLs and gradually bury them into the Ni matrix. Another example is noticed in Figure 6.6 d and e, in which the EDS result indicates GPLs protruding from the Ni matrix are covered by Ni. On the other hand, uniformly distributed bulges can be found in Figure 6.4 and suggest good dispersion of GPLs in the Ni matrix.

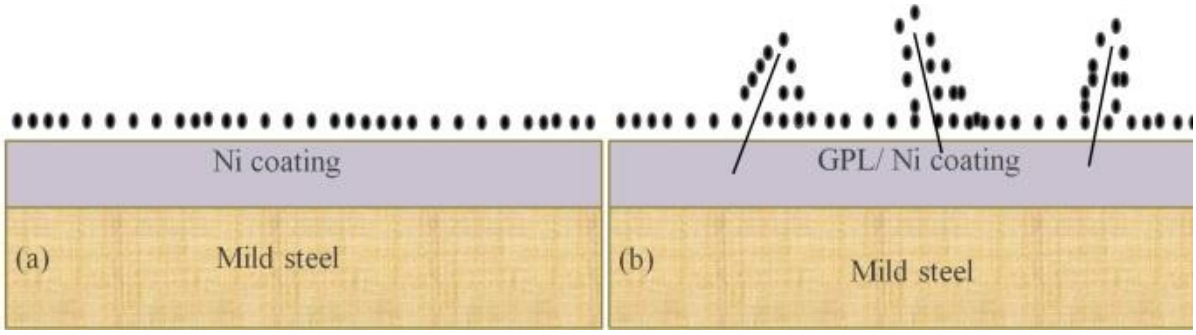

Figure 6.5. Schematic illustrations of the deposition process of Ni (a) and GPL/Ni (b) coatings.

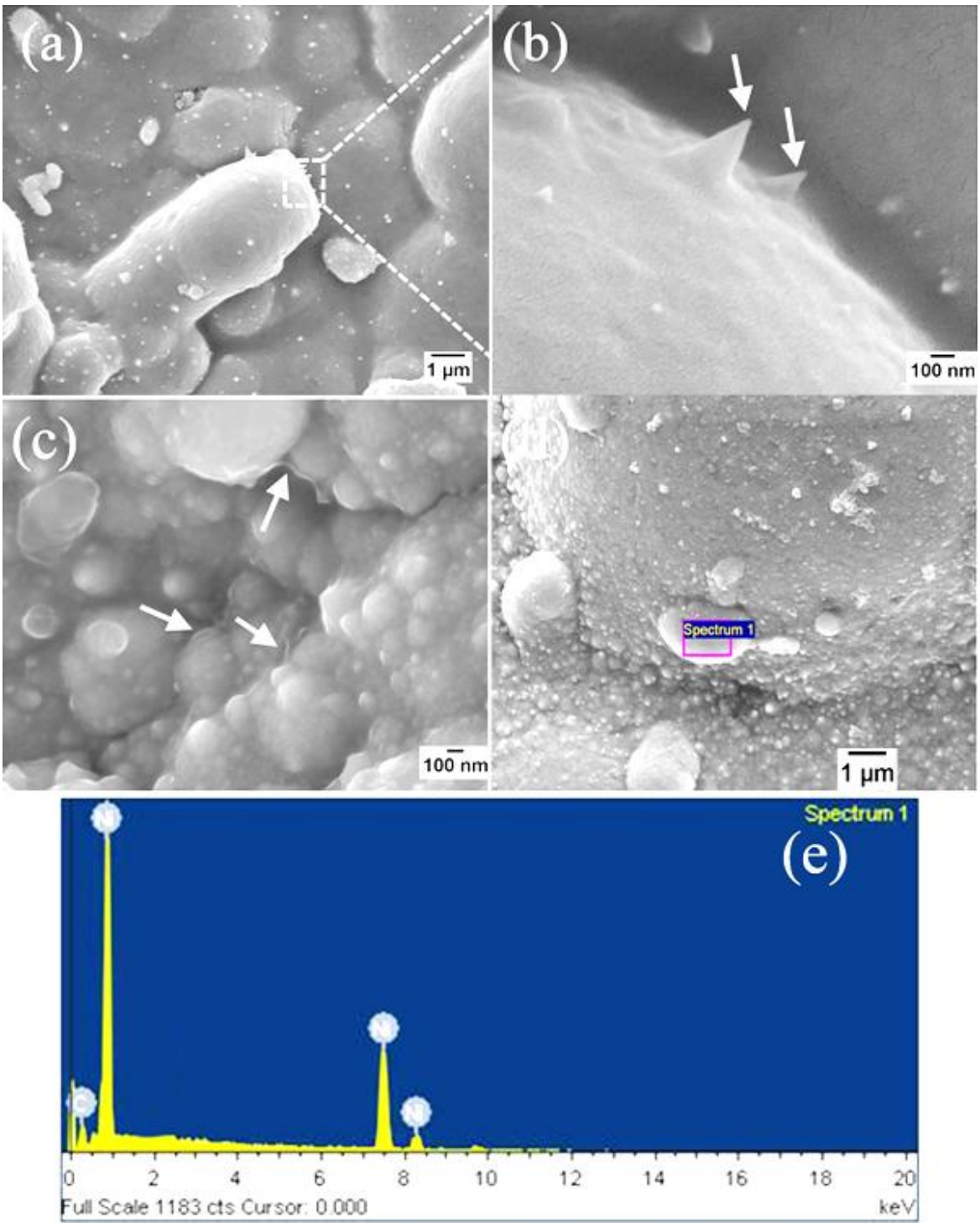

Figure 6.6. Surface morphologies (a-d) and elemental composition (e) of the electrodeposited GPL/Ni composite coatings. (e) is the EDS result of the square area in (d).

6.3.2 Raman spectra of the GPLs in the coatings

Raman spectra of the GPLs in the electrodeposited GPL/Ni coatings were recorded and compared to the Raman spectrum of the pristine GPL, as shown in Figure 6.7. It can be noticed that 2D bands of the GPLs in the GPL/Ni coatings show broader FWHM than the 2D band of the pristine GPL, suggesting the agglomeration of GPLs occurs during the electrodepositing process. In addition, the GPLs in the composite coatings with a higher content of GPLs show broader FWHMs of 2D bands than those with a lower content of GPLs, suggesting relatively thicker GPLs are formed when a bath solution with a higher content of GPLs is used.

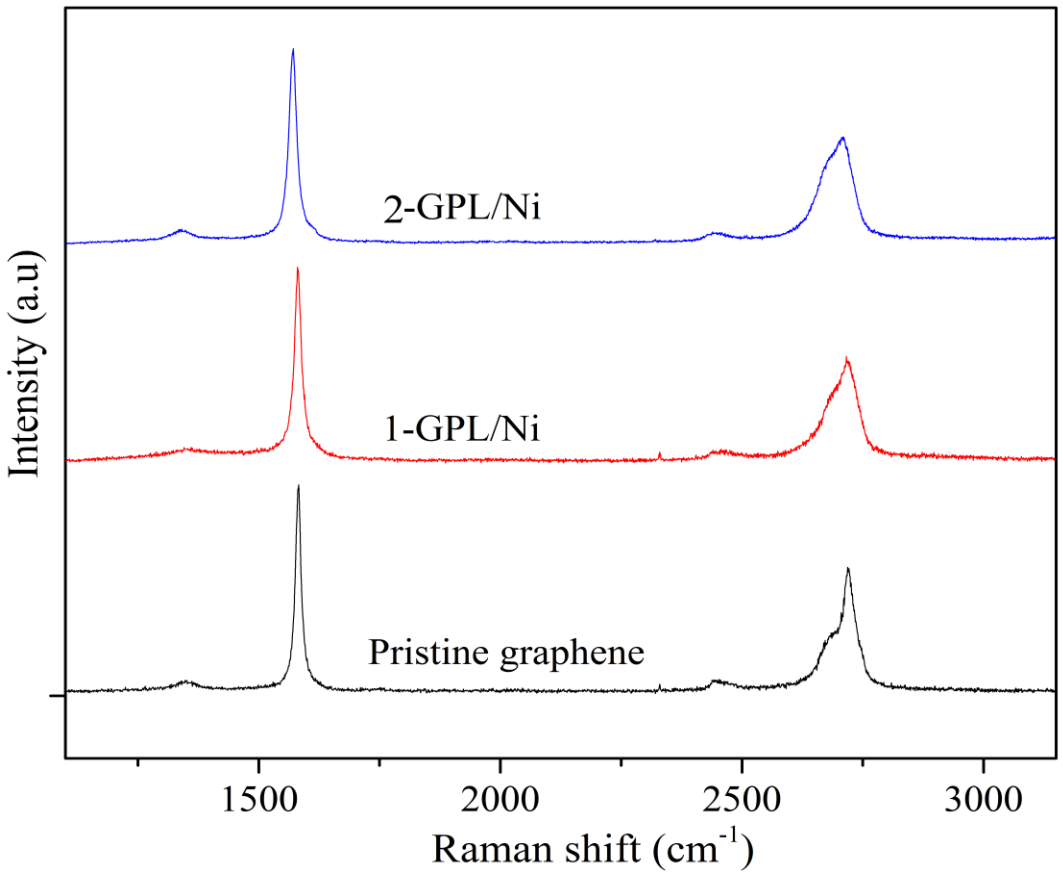

Figure 6.7. Raman spectra of the pristine GPL and the GPLs in the electrodeposited GPL/Ni.

Raman parameters of the pristine GPL and the GPLs in the composite coatings were compiled in Table 6.1. It can be seen that GPLs in the composite coatings present a higher value of I_D/I_G than the pristine GPL, indicating a higher amount of defects are formed during the electrodeposition process. Meanwhile, it is observed that G bands and 2D bands of the GPLs in the composite coatings shift to a lower frequency in comparison with those of the pristine GPL. The formation of higher defects and the position shift of G and 2 D bands may be associated with the interaction between GPLs and the Ni matrix. Meanwhile, it is noted that I_{2D}/I_G of GPLs in composite coatings exhibits a lower value than that of the pristine GPL, which further proves GPL aggregates are formed during the deposition process.

Table 6.1. Raman parameters of the pristine GPL and the GPLs in the composite coatings.

Materials	I_D/I_G	FWHM (G)	ν (G)	FWHM (2D)	ν (2D)	I_{2D}/I_G
Pristine GPL	0.073	14	1582	37	2723	0.6
GPL in1-GPL/Ni	0.093	19	1580	58	2716	0.55
GPL in 2-GPL/Ni	0.104	21	1571	64	2712	0.54

6.3.3 Grain sizes and texture coefficients of the electrodeposited coatings

Figure 6.8 shows XRD patterns of the electrodeposited pure and GPL/Ni composite coatings. It can be seen that the peak widths of the Ni in the GPL/Ni composite coatings are broader than the peak width of the pure Ni coating. This is attributed to the decrease in the grain size of the Ni matrix due to the introduction of GPLs.

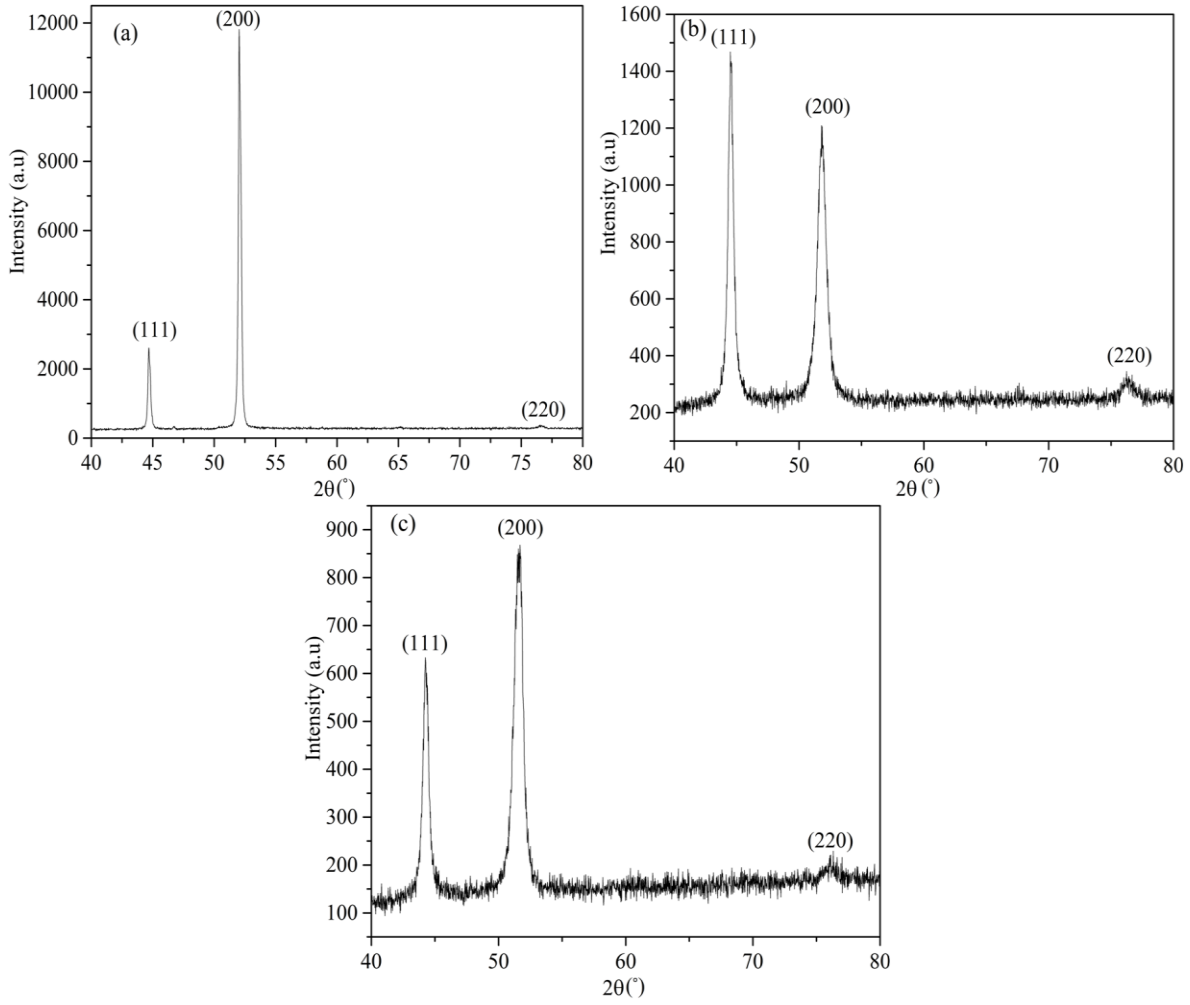

Figure 6.8. XRD patterns of pure Ni and GPL/Ni composite coatings. (a) pure Ni, (b) 1-GPL/Ni and (c) 2-GPL/Ni.

Huis et al. reported that in determining the mean cluster sizes, the results from XRD method and transmission electron microscopy (TEM) observations are very consistent [213]. So the average grain sizes of the composite coatings are calculated by the Scherrer's equation [214]:

$$Q = K\lambda/\beta cos\theta \qquad (6.1)$$

Where Q is the average crystallite size, K is the Scherrer constant, λ is the wave length, β is the FWHM and θ is the diffraction angle.

The grain sizes of the pure Ni and GPL/Ni composite coatings are shown in Figure 6.9. It can be seen that the GPL/Ni composite coatings show smaller grain sizes than the pure Ni coating and the higher percentage of GPLs causes a smaller grain size. It is expected that during the electrodeposition, GPLs incorporated in the Ni matrix enhance the nucleation sites and hinder the grain growth for the reduced Ni ions, which results in significant grain refinement.

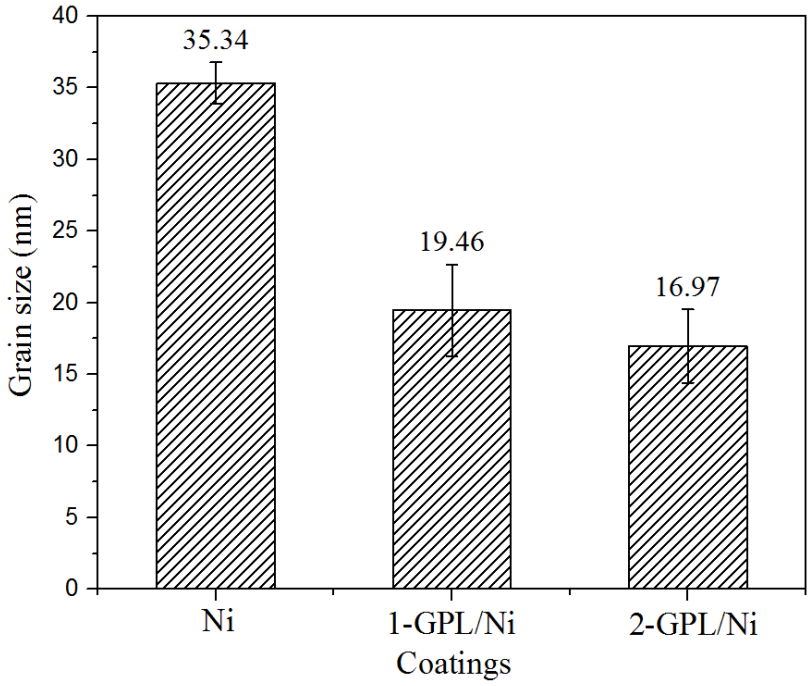

Figure 6.9. XRD patterns of the pure Ni and GPL/Ni coatings.

The preferred orientations of the Ni grain were estimated from the XRD according to the methodology developed by Berube and Esperance. The texture coefficient for each plane was calculated by using the following equation [215, 216]:

$$Tc_{(hkl)} = I_{(hkl)} / \sum I_{(hkl)} \times \sum I_{o(hkl)} / I_{o(hkl)} \times 100\% \qquad (6.2)$$

Where $I_{(hkl)}$ is the intensity of the reflection for the examined sample and $I_{o(hkl)}$ is the intensity of the reflection from the standard oriented nickel sample.

Figure 6.10 compares texture coefficients of Ni and GPL/Ni coatings. It can be observed that all the coatings show the preferred orientations at (200) and the introduction of GPLs results in a decrease of the texture coefficient at the preferred orientation and significant increases at orientations of (111) and (22 0).

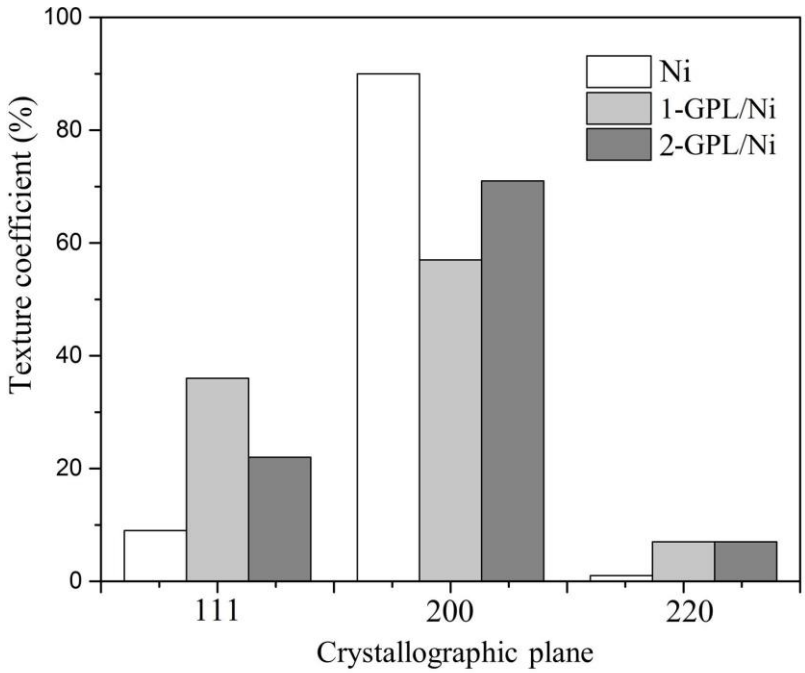

Figure 6.10. Texture coefficients of the pure Ni and GPL/Ni coatings.

It is suggested that reactions (1)-(4) would happen in the electroplating bath and $Ni(OH)_2$ is likely to be formed and absorbed onto the cathode surface, leading to a decrease of the texture coefficient at the preferred orientation (200) [217]. On the other hand, Ni^{2+} and $Ni[B(OH)_4]^+$ cations can be absorbed on GPLs which shield the Ni growth centres from the cations of the electrolyte and inhibit the further growth of grains [217]. Therefore, it is highly possible that renucleation would occur and the preferred nucleation orientations are on (1 1 1) and (2 2 0). However, the renucleation is more likely to take place around GPLs and not all grains in the composite coatings will be affected by the GPLs. This may explain why the (200) orientation shows the highest texture coefficient in all of the coatings and the coefficient in all of the coatings and the coefficient of (111) and (220) orientations are increased due to the introduction of GPLs.

$$Ni + H_2O \rightarrow Ni(H_2O) \quad (1)$$

$$Ni(H_2O) \rightarrow Ni(OH)^+ + H^+ + 2e^- \quad (2)$$

$$Ni(OH)^+ + OH^- \rightarrow Ni(OH)_2 \quad (3)$$

$$B(OH)_3 + H_2O \longleftrightarrow [B(OH)_4]^- + H^+ \quad (4)$$

The Vickers hardness of Ni and GPL/Ni composite coatings was examined and shown in Figure 6.11. It is noticed that the GPL/Ni composite coatings show a greater degree of hardness than the electrodeposited Ni coating and the higher percentage of GPLs result in greater hardness.

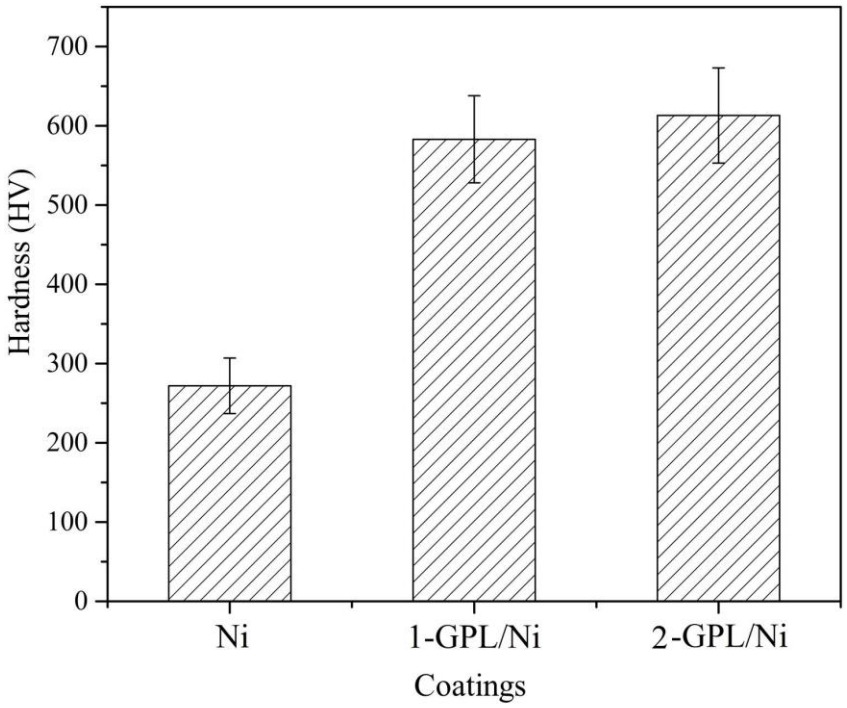

Figure 6.11. Hardness of the pure Ni and GPL/Ni coatings.

It is reported that the strengthening effect induced by interaction between the dispersed particulate phase in the matrix and edge dislocations can be expressed as follows [218]:

$$\Delta\boldsymbol{\sigma_p} = \frac{\boldsymbol{\beta_{OR}\mu b M (f_v)^{1/2}}}{\boldsymbol{d_p}} \qquad (6.3)$$

In which, μ is modulus of the matrix materials, b is Burger's vector, f_v is the volume fraction of the particulate phase, d_p is the size of the particulate phase and M is the Taylor factor with a value of 1.5-2. β_{OR} can be described by the following equation:

$$\boldsymbol{\beta_{OR}} = \frac{\boldsymbol{1}}{\boldsymbol{2\pi}}\boldsymbol{ln}\left[\frac{\boldsymbol{d_p}\left(\frac{\boldsymbol{\pi}}{\boldsymbol{6f_v}}\right)^{\boldsymbol{1/2}}}{\boldsymbol{b}}\right] \qquad (6.4)$$

As indicated by the equation (6.3), the strengthening effect of the particulate phase is significantly influenced by the particulate phase. In addition, the smaller the size of the particulate phase, the more effective the strengthening effect. In this research, GPLs are used as the particulate phase and are of a very small size and large specific surface. Therefore, it is expected that the introduction of a small percentage of GPLs would effectively strengthen the Ni matrix, leading to appreciable enhancement in micro hardness of the Ni matrix. On the other hand, grain refining effect caused by GPLs is believed to contribute the high micro hardness of the GPL/Ni composite coating. The introduction of GPLs results in smaller grain size and more grain boundaries, which obstruct the motion of dislocations and resists plastic flow [212]. Meanwhile, the inherent high mechanical strength of graphene sheets might be another cause of the increment in micro hardness [212].

6.3.4 Corrosion resistant properties of the electrodeposited coatings

The polarization curves of the mild steel, Ni and GPL/Ni composite coatings are shown in Figure 6.12. Table 6.2 gives the corrosion potentials (E_{ccor}) and corrosion current densities (I_{ccor}) of electrodeposited coatings obtained from the polarization curves. It can be clearly observed that pure Ni and GPL/Ni composite coatings present significantly higher corrosion potentials and lower corrosion current densities than the mild steel, indicating better resistance to corrosion for the electrodeposited coatings. In addition, a relatively higher amount of GPLs in the GPL/Ni composite coating results in higher corrosion potential and better corrosion resistance.

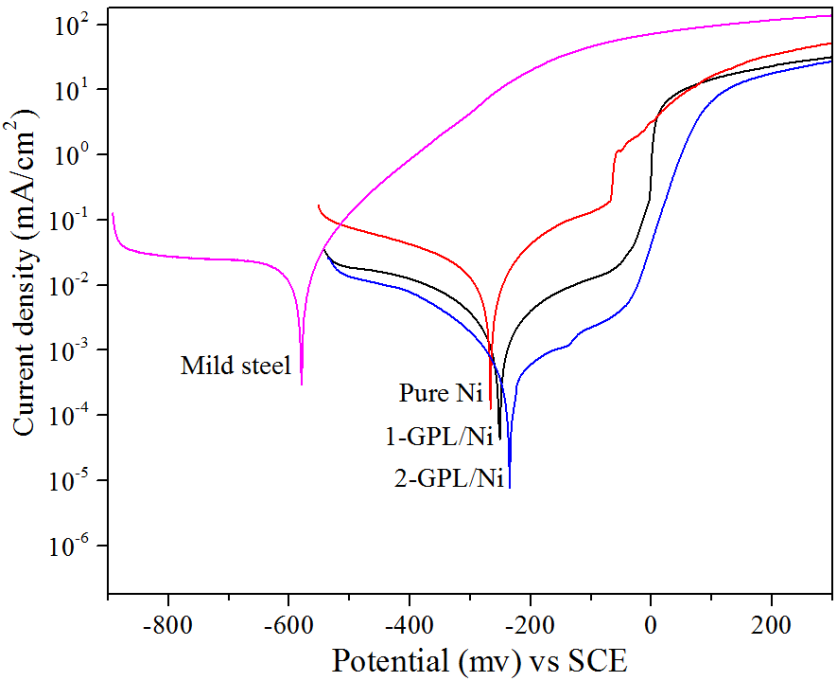

Figure 6.12. Polarization curves of the pure Ni and GPL/Ni coatings.

Table 6.2. Corrosion potentials and corrosion current densities of the electrodeposited coatings

Sample	Mild steel	Ni	1-GPL/Ni	2-GPL/Ni
E_{ccor} (mv)	-579.4	-266.5	-251.2	-234.6
I_{ccor} ($\mu A/cm^2$)	38.9	19.1	3.02	0.398

Several factors can be responsible for the enhancement of corrosion resistant properties of GPL/Ni composite coatings. Firstly, the GPLs are uniformly distributed in the Ni matrix (Figure 6.13 a) and can act as an inert physical barrier, leading to the inhabitation of the localized corrosion and occurrence of homogeneous corrosion across the surface of the composite coatings [218]. Secondly, GPLs can fill the crevices, gaps and micron holes in the Ni matrix (Figure 6.13b), preventing the initiation and development of defect corrosion [218]. Thirdly, the introduction of GPLs considerably decreases the grain size of the Ni matrix and

increases the grain boundary density, which causes the formation of continuous and protective passive films such as NiO and $Ni(OH)_2$ and better corrosion resistance [219, 220].

It is believed that the better corrosion resistance of GPL/Ni coatings is largely dependent on the distribution of GPLs in the Ni matrix. A homogeneous dispersion of GPLs during the electrodeposition process would certainly help contribute to good corrosion resistance. It is noted that GPL aggregates (Figure 6.13 c and d) are found on the GPL/Ni composite coatings when electroplating baths with a high concentration of GPLs are used. These aggregates imply that a better dispersion process is required to further improve corrosion resistance of the composite coatings.

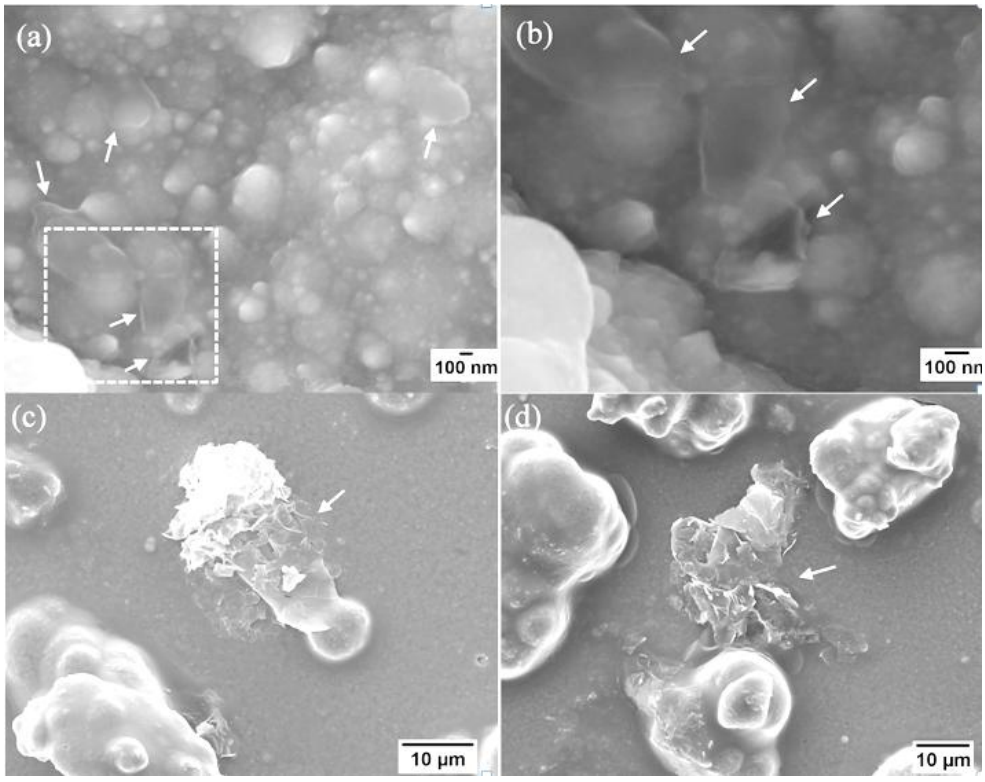

Figure 6.13. Surface morphologies of the GPL/Ni coatings. (b) is the magnified part of the square area in (a). White arrows indicate GPLs.

Electrochemical impedance tests were carried out to evaluate the corrosion resistant properties of the coatings. Figure 6.14 shows the Nyquist plots of the mild steel, pure Ni and the GPL/Ni coatings. It can be seen that pure Ni and GPL/Ni composite coatings exhibit considerable higher impedance compared to mild steel and the impedance of pure Ni is increased by introducing GPLs. Meanwhile, the acquired impedance spectra of the Ni and GPL/Ni composite coatings exhibit depressed semicircles. The diameter of the semicircle decides the corrosion resistance of the coatings and larger diameters imply higher corrosion resistance [221]. Clearly, the GPL/Ni composite coating deposited in the bath containing 0.2g/L GPLs has the highest impedance and better corrosion resistance.

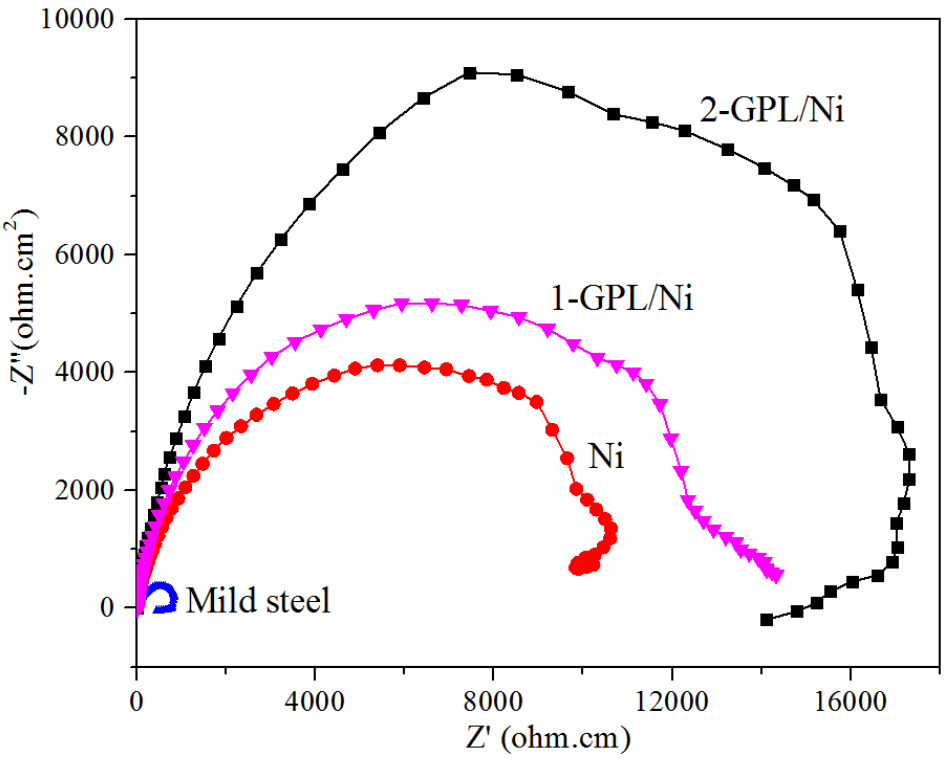

Figure 6.14. Impedance spectra of the mild steel, pure Ni and GPL/Ni coatings in 3.5% NaCl solution.

6.4 Summary

In the research of this chapter, pure Ni and GPL/Ni coatings were electrodeposited on the surface of the mild steel. The microstructures of the coatings were examined by SEM, XRD and EDS. The structures of the pristine GPL and GPLs in the coatings were characterized by the Raman spectroscopy. The polarization curves and corrosion resistances of the electrodeposited coatings were determined by electrochemical tests. The results obtained in the research can be summarized as follows:

1. Pure Ni and GPL/Ni coatings are successfully fabricated on the surface of the mild steel. GPLs are uniformly distributed within the Ni matrix. The introduction of GPLs causes the formation of bulges on the surface of the coating.

2. The introduction of GPLs results in the significant decrease in average grain size of the Ni matrix and considerable increase in hardness of the coatings. In addition, the GPL/Ni composite coatings with a relatively higher percentage of GPLs have smaller grain size and greater hardness.

3. Electrochemical tests have indicated that compared to a pure Ni coating, GPL/Ni composite coatings have higher corrosion potential and impedance, which implies significantly improved corrosion resistance. Additionally, better corrosion resistance can be obtained by introducing a relatively higher percentage of GPLs.

4. The Raman spectra and the observed SEM images of the GPLs suggest agglomeration of GPLs occurs during electrodeposition, implying a better dispersion process is required to form a more homogenous distribution of GPLs in the Ni matrix.

The research in this chapter shows the potentiality of GPLs as nano fillers for fabrication of composite coatings with good corrosion resistances and advanced composite coatings containing GPLs may open up opportunities for various engineering applications.

Chapter 7: Conclusions and future work

7.1 Introduction

This PhD thesis is aimed at exploring GPLs as nano fillers for preparation of Al_2O_3 matrix composites and Ni matrix composites with enhanced fracture toughness or corrosion resistant properties. The research covers fabrications and characterizations of GPL-reinforced ZTA composites, GPL-reinforced Al_2O_3 composites and GPL- SiC/Al_2O_3 composites prepared either using SPS or pressureless sintering. It also involves electrodeposition and characterization of the GPL/Ni coatings.

7.2 Contributions

The significant contributions of the research to the group of nanocomposites can be summarized as follows:

A. GPL/ZTA composites were fabricated using SPS and superior fracture toughness was achieved.

GPL/ZTA powder mixtures were successfully prepared by ball milling Al_2O_3 and GPLs powders using a high ball-to-powder ratio and DMF as the solvent. Dense GPL/ZTA bulk ceramic composites with improved fracture toughness have been successfully fabricated using SPS. A wide dispersion of GPLs in the ZTA matrix was achieved with the aid of ultrasonication and the ball milling process.

B. GPL/Al_2O_3 and GPL-SiC/Al_2O_3 composites were fabricated using SPS and enhanced flexural strength and fracture toughness were achieved.

GPL/Al_2O_3 and GPL-SiC/Al_2O_3 powder mixtures were successfully prepared by ball milling using a low ball-to-powder ratio. Dense GPL/Al_2O_3 bulk ceramic composites with improved flexural strength and fracture toughness have been successfully fabricated using SPS. Improvements in hardness, flexural strength and fracture toughness of the Al_2O_3 matrix were successfully achieved by introducing dual fillers of GPLs and SiC nanoparticles.

C. GPL/Al_2O_3 composites were fabricated using pressureless sintering and improved flexural strength and fracture toughness were achieved.

GPL/ Al_2O_3 powder compacts were successfully prepared using CIP. For the first time dense GPL/ Al_2O_3 bulk ceramic composites with improved flexural strength and fracture toughness were successfully sintered using a pressureless method.

D. Ni and GPL/Ni coatings were fabricated using an electrodeposition technique and improved corrosion resistance was achieved.

Ni and GPL/Ni coatings have been successfully electrodeposited on mild steel. Better corrosion resistance was achieved for GPL/Ni composite coatings.

7.3 Conclusions

The following conclusions can be drawn from the research:

1. The optimum sintering temperature for consolidating the GPL/ZTA bulk composites is 1550 ˚C. At this temperature, nearly fully densified GPL/ZTA samples with significantly improved fracture toughness can be obtained. The addition of only 0.81 vol% GPLs into ZTA ceramic matrix results in a 40% increase in fracture toughness.

2. GPLs are well distributed in the ceramic matrix and result in a decrease in grain size of the matrix microstructures. Higher content of GPLs leads to smaller grain size of ceramic matrices. The addition of SiC nanoparticles together with GPLs causes further refinement of the ceramic matrix microstructures. The refined microstructures contribute to the hardness and flexural strength of the GPL-reinforced ceramic composites and enhance the toughening effect of GPLs.

3. The content of GPLs has significant effects on the mechanical properties of the GPL-reinforced composites and there is an optimum content of GPLs where the mechanical properties of ceramic composites can be considerably improved. For GPL/Al_2O_3 composites, the maximum flexural strength and fracture toughness are obtained by adding 0.38 vol% GPLs. Compared to the pure Al_2O_3 sample, approximately a 31% and a 27% increase in flexural strength and fracture toughness have been achieved respectively.

4. The addition of GPLs leads to a slight decrease in hardness of the Al_2O_3 matrix. Both hard and tough Al_2O_3 ceramic composites can be obtained by adding dual nano fillers of GPLs and SiC nanoparticles. Approximately a 36 % increase in hardness, a 40% increase in flexural strength and a 50% increase in fracture toughness have been achieved by adding GPLs and SiC nanoparticles into the Al_2O_3 ceramic matrix.

5. The optimum processing paramters for pressureless sintering of GPL/Al_2O_3 composites are: heating rate: 5 ℃/min, sintering temperature: 1650 ℃, sintering time: 3h, sintering atmosphere: forming gas and flowing rate: 8L/minl.The obtained fracture toughness and flexural strength of the Al_2O_3 composites reinforced with 0.28 vol% GPLs are appoximately 70% and 60% higher than those of pure Al_2O_3.

6. Raman studies show that GPL aggregates are formed during the ball milling process and a higher content of GPLs is likely to cause the formation of thicker GPL aggregates. Thinning of GPLs during the SPS process occurs because of the interaction between the GPLs and ceramic matrix at high temperature. The shifting of G bands and 2D bands takes

place after ball milling and SPS processing. Structural damage of GPLs occurs during pressureless sintering due to the interaction between oxygen and GPLs and the interfacial reactions between the GPLs and ceramic matrix.

7. Toughening mechanisms such as pull-out, crack deflection and crack bridging are induced by GPLs and responsible for the significant improvement in fracture toughness.

8. The introduction of GPLs during the electrodeposition process increases nucleation sites and decreases the grain size of the Ni matrix. The hardness of the Ni matrix has been significantly improved by introducing GPLs and the GPL/Ni composite coatings show much better corrosion resistance than a pure Ni coating.

Based on the experimental and analysis work presented in this thesis, GPLs have been proven very effective nano fillers for fabrication of composite materials with enhanced mechanical and corrosion resistant properties. Thus the project aims have been successfully met. The methodology and analysis in the research are adequate in leading to the research aims.

7.4 Suggestions for future work

This thesis presents research effort to explore a ceramic or metal matrix composite reinforced with GPLs. The results obtained in the research can be regarded as a solid foundation for

further work. Future effort is needed either to extend the related research or to complete the works initiated in this PhD thesis which have not yet been completed.

The following is a list of further research topics:

1. The apparent fracture toughness of GPL/Al_2O_3 or GPL/ZTA has been investigated in the research. However, these composite materials may exhibit R-curve behaviour, which indicated that the fracture toughness would increase with the extension of the cracks. Further studies can be carried out to understand the R-curve behaviour of the ceramic composites reinforced with GPL.

2. The carbon fillers have been proven very effective lubricants for wear resistance purposes [222, 223]. Research effort can be carried out to investigate the effects of GPLs on the wear resistance of the ceramic composites.

3. Although GPL/Al_2O_3 and GPL/ZTA show improved mechanical properties, advanced composite materials for demanding applications require matrix materials with higher strength and toughness than Al_2O_3 and ZTA. In this case, Si_3N_4 is more desirable to be the matrix material because of its excellent mechanical properties and further work can be done to investigate the effects of GPLs on the mechanical properties of the Si_3N_4 matrix sintered using a pressureless method. The author has carried out some preliminary work of sintering Si_3N_4 using a conventional furnace. Figure 7.1 shows the comparison of powder compacts prepared by CIP before and after sintering. The relative density of the sintered sample is higher than 90%.

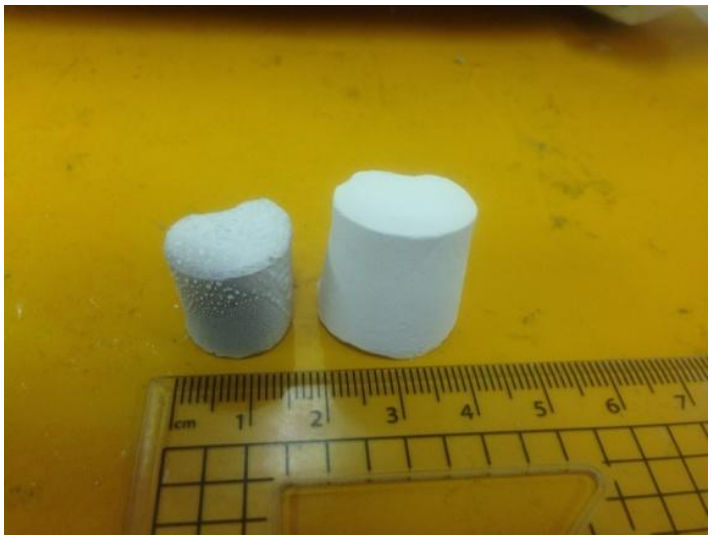

Figure 7.1. Images of sintered sample (left) and the green compact (right).

4. The Micro-engineering and Nano-technology Research Group at the University of Birmingham developed a soft lithography technique and powder metallurgy process to produce micro components [224]. In this thesis, it has been presented that GPL-reinforced ceramic composite can be successfully fabricated using pressureless sintering. Future effort can be made to employ the micro fabrication technique to produce micro components with improved fracture toughness. The authors have done some preliminary work and fabricated Al_2O_3 micro gears shown in Figure 7.2.

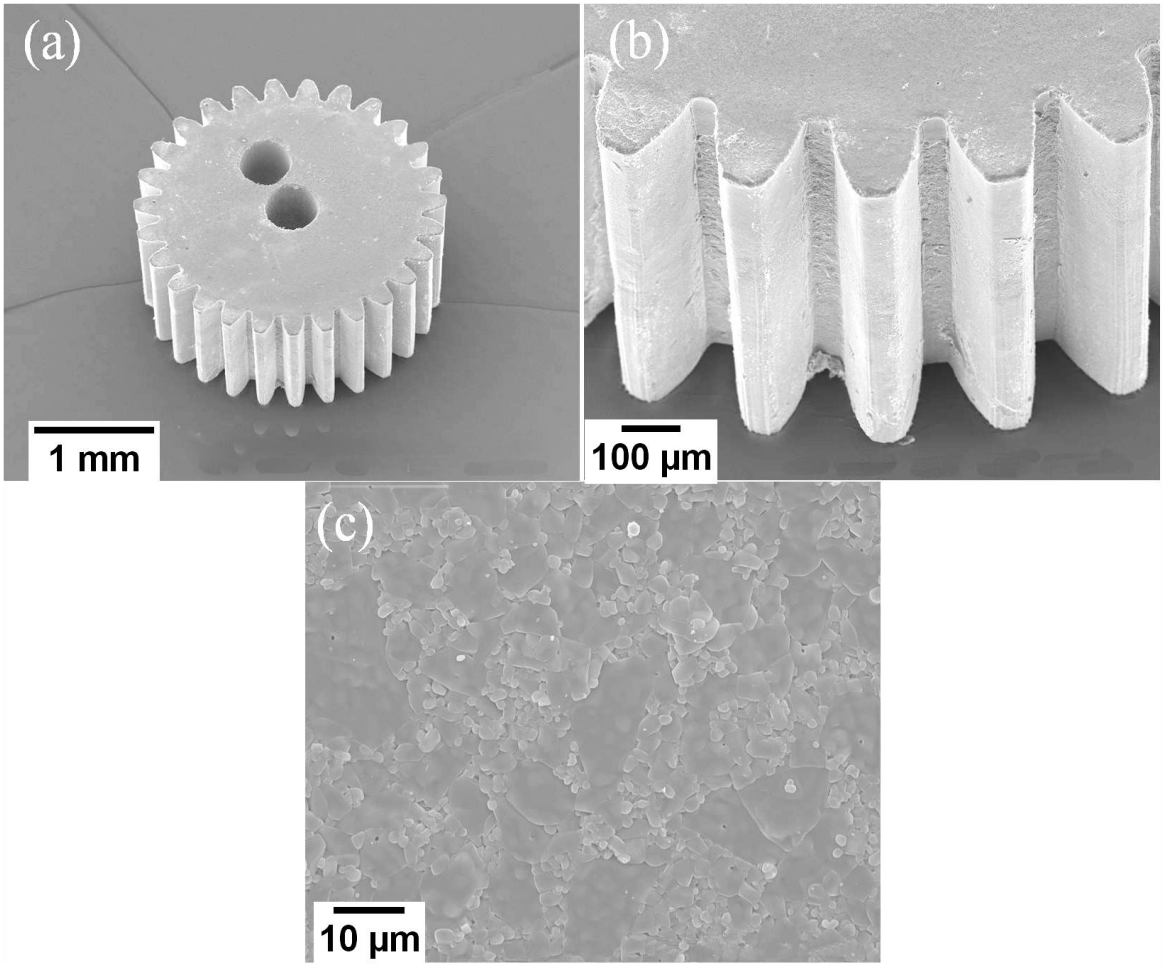

Figure 7.2. SEM images of the Al_2O_3 micro gear (a-b) and the surface morphology (c) of the micro gear.

5. In this thesis, the electrodeposition technique was used to fabricate GPL/Ni composite coatings onto mild steel for corrosion resistance application. However, this method is limited to produce metal or conductive coatings. Future work can be carried out to use other deposition techniques such as electrophoretic deposition to fabricate nonconductive coatings with better mechanical and corrosion resistant properties

References

[1] Liu J, Yan HX, Jiang K. Mechanical properties of graphene platelet-reinforced alumina ceramic composites. Ceram Int. 2013;39(6):6215-21.

[2] Frank IW, Tanenbaum DM, Van der Zande AM, McEuen PL. Mechanical properties of suspended graphene sheets. J Vac Sci Technol B. 2007;25(6):2558-61.

[3] Geim AK, Novoselov KS. The rise of graphene. Nat Mater. 2007;6(3):183-91.

[4] Liu J, Yan HX, Reece MJ, Jiang K. Toughening of zirconia/alumina composites by the addition of graphene platelets. J Eur Ceram Soc. 2012;32(16):4185-93.

[5] Van Lier G, Van Alsenoy C, Van Doren V, Geerlings P. Ab initio study of the elastic properties of single-walled carbon nanotubes and graphene. Chem Phys Lett. 2000;326(1-2):181-5.

[6] Reddy CD, Rajendran S, Liew KM. Equilibrium configuration and continuum elastic properties of finite sized graphene. Nanotechnology. 2006;17(3):864-70.

[7] Poot M, van der Zant HSJ. Nanomechanical properties of few-layer graphene membranes. Appl Phys Lett. 2008;92(6).

[8] Lee C, Wei XD, Kysar JW, Hone J. Measurement of the elastic properties and intrinsic strength of monolayer graphene. Science. 2008;321(5887):385-8.

[9] Gomez-Navarro C, Burghard M, Kern K. Elastic properties of chemically derived single graphene sheets. Nano Lett. 2008;8(7):2045-9.

[10] Yu CH, Shi L, Yao Z, Li DY, Majumdar A. Thermal conductance and thermopower of an individual single-wall carbon nanotube. Nano Lett. 2005;5(9):1842-6.

[11] Berber S, Kwon YK, Tomanek D. Unusually high thermal conductivity of carbon nanotubes. Phys Rev Lett. 2000;84(20):4613-6.

[12] Chen SS, Wu QZ, Mishra C, Kang JY, Zhang HJ, Cho KJ, et al. Thermal conductivity of isotopically modified graphene. Nat Mater. 2012;11(3):203-7.

[13] Balandin AA. Thermal properties of graphene and nanostructured carbon materials. Nat Mater. 2011;10(8):569-81.

[14] Pop E, Varshney V, Roy AK. Thermal properties of graphene: Fundamentals and applications. Mrs Bull. 2012;37(12):1273-81.

[15] Balandin AA, Ghosh S, Bao WZ, Calizo I, Teweldebrhan D, Miao F, et al. Superior thermal conductivity of single-layer graphene. Nano Lett. 2008;8(3):902-7.

[16] Nika DL, Balandin AA. Two-dimensional phonon transport in graphene. J Phys-Condens Mat. 2012;24(23).

[17] Charlier JC, Eklund PC, Zhu J, Ferrari AC. Electron and phonon properties of graphene: Their relationship with carbon nanotubes. Top Appl Phys. 2008;111:673-709.

[18] Singh V, Joung D, Zhai L, Das S, Khondaker SI, Seal S. Graphene based materials: Past, present and future. Prog Mater Sci. 2011;56(8):1178-271.

[19] Novoselov KS, Geim AK, Morozov SV, Jiang D, Katsnelson MI, Grigorieva IV, et al. Two-dimensional gas of massless Dirac fermions in graphene. Nature. 2005;438(7065):197-200.

[20] Morozov SV, Novoselov KS, Katsnelson MI, Schedin F, Elias DC, Jaszczak JA, et al. Giant intrinsic carrier mobilities in graphene and its bilayer. Phys Rev Lett. 2008;100(1).

[21] Bolotin KI, Sikes KJ, Jiang Z, Klima M, Fudenberg G, Hone J, et al. Ultrahigh electron mobility in suspended graphene. Solid State Commun. 2008;146(9-10):351-5.

[22] Kim SR, Parvez MK, Chhowalla M. UV-reduction of graphene oxide and its application as an interfacial layer to reduce the back-transport reactions in dye-sensitized solar cells. Chem Phys Lett. 2009;483(1-3):124-7.

[23] Lu GH, Ocola LE, Chen JH. Reduced graphene oxide for room-temperature gas sensors. Nanotechnology. 2009;20(44).

[24] Deville S, El Attaoui H, Chevalier M. Atomic force microscopy of transformation toughening in ceria-stabilized zirconia. J Eur Ceram Soc. 2005;25(13):3089-96.

[25] Eda G, Fanchini G, Chhowalla M. Large-area ultrathin films of reduced graphene oxide as a transparent and flexible electronic material. Nat Nanotechnol. 2008;3(5):270-4.

[26] Wang HL, Cui LF, Yang YA, Casalongue HS, Robinson JT, Liang YY, et al. Mn3O4-Graphene Hybrid as a High-Capacity Anode Material for Lithium Ion Batteries. J Am Chem Soc. 2010;132(40):13978-80.

[27] Liao AD, Wu JZ, Wang XR, Tahy K, Jena D, Dai HJ, et al. Thermally Limited Current Carrying Ability of Graphene Nanoribbons. Phys Rev Lett. 2011;106(25).

[28] Dusza J, Morgiel J, Duszova A, Kvetkova L, Nosko M, Kun P, et al. Microstructure and fracture toughness of Si3N4 + graphene platelet composites. J Eur Ceram Soc. 2012;32(12):3389-97.

[29] Rafiee MA, Rafiee J, Srivastava I, Wang Z, Song HH, Yu ZZ, et al. Fracture and Fatigue in Graphene Nanocomposites. Small. 2010;6(2):179-83.

[30] Wang DH, Kou R, Choi D, Yang ZG, Nie ZM, Li J, et al. Ternary Self-Assembly of Ordered Metal Oxide-Graphene Nanocomposites for Electrochemical Energy Storage. Acs Nano. 2010;4(3):1587-95.

[31] Zhou GM, Wang DW, Li F, Zhang LL, Li N, Wu ZS, et al. Graphene-Wrapped Fe3O4 Anode Material with Improved Reversible Capacity and Cyclic Stability for Lithium Ion Batteries. Chem Mater. 2010;22(18):5306-13.

[32] Sutter P. EPITAXIAL GRAPHENE How silicon leaves the scene. Nat Mater. 2009;8(3):171-2.

[33] Mallet P, Varchon F, Naud C, Magaud L, Berger C, Veuillen JY. Electron states of mono- and bilayer graphene on SiC probed by scanning-tunneling microscopy. Phys Rev B. 2007;76(4).

[34] Peng T, Lv HF, He DP, Pan M, Mu SC. Direct Transformation of Amorphous Silicon Carbide into Graphene under Low Temperature and Ambient Pressure. Sci Rep-Uk. 2013;3.

[35] Li XS, Cai WW, Colombo L, Ruoff RS. Evolution of Graphene Growth on Ni and Cu by Carbon Isotope Labeling. Nano Lett. 2009;9(12):4268-72.

[36] Bae S, Kim H, Lee Y, Xu XF, Park JS, Zheng Y, et al. Roll-to-roll production of 30-inch graphene films for transparent electrodes. Nat Nanotechnol. 2010;5(8):574-8.

[37] Park S, Ruoff RS. Chemical methods for the production of graphenes (vol 4, pg 217, 2009). Nat Nanotechnol. 2010;5(4):309-.

[38] Kalaitzidou K, Fukushima H, Drzal LT. Mechanical properties and morphological characterization of exfoliated graphite-polypropylene nanocomposites. Compos Part a-Appl S. 2007;38(7):1675-82.

[39] Liu YG, Zhou JQ, Shen TD. Effect of nano-metal particles on the fracture toughness of metal-ceramic composite. Mater Design. 2013;45:67-71.

[40] Evans AG, Cannon RM. Toughening of Brittle Solids by Martensitic Transformations. Acta Metall Mater. 1986;34(5):761-800.

[41] Bao G, Hui CY. Effects of Interface Debonding on the Toughness of Ductile Particle Reinforced Ceramics. Int J Solids Struct. 1990;26(5-6):631-42.

[42] Yang H, Wu S, Hu JA, Wang ZY, Wang R, He HM. Influence of nano-ZrO2 additive on the bending strength and fracture toughness of fluoro-silicic mica glass-ceramics. Mater Design. 2011;32(3):1590-3.

[43] Garvie RC, Hannink RH, Pascoe RT. Ceramic Steel. Nature. 1975;258(5537):703-4.

[44] Kuntz JD, Zhan GD, Mukherjee AK. Nanocriletalline-matrix ceramic composites for improved fracture toughness. Mrs Bull. 2004;29(1):22-7.

[45] Ji Y, Yeomans JA. Processing and mechanical properties of Al2O3-5 vol.% Cr nanocomposites. J Eur Ceram Soc. 2002;22(12):1927-36.

[46] Chen RZ, Tuan WH. Pressureless sintering of Al2O3/Ni nanocomposites. J Eur Ceram Soc. 1999;19(4):463-8.

[47] Chae JH, Kim KH, Choa YH, Matsushita J, Yoon JW, Shim KB. Microstructural evolution of Al2O3-SiC nanocomposites during spark plasma sintering. J Alloy Compd. 2006;413(1-2):259-64.

[48] Choi SM, Awaji H. Nanocomposites - a new material design concept. Sci Technol Adv Mat. 2005;6(1):2-10.

[49] Ohji T, Jeong YK, Choa YH, Niihara K. Strengthening and toughening mechanisms of ceramic nanocomposites. J Am Ceram Soc. 1998;81(6):1453-60.

[50] Levin I, Kaplan WD, Brandon DG. Effect of Sic Submicrometer Particle-Size and Content on Fracture-Toughness of Alumina-Sic Nanocomposites. J Am Ceram Soc. 1995;78(1):254-6.

[51] Sekino T, Niihara K. Fabrication and mechanical properties of fine-tungsten-dispersed alumina-based composites. J Mater Sci. 1997;32(15):3943-9.

[52] Awaji H, Choi SM, Yagi E. Mechanisms of toughening and strengthening in ceramic-based nanocomposites. Mech Mater. 2002;34(7):411-22.

[53] Pirouz P, Lawlor BF, Geipel T, BildeSorensen JB, Heuer AH, Lagerlof KPD. On basal slip and basal twinning in sapphire (alpha-Al2O3) .2. A new model of basal twinning. Acta Mater. 1996;44(5):2153-64.

[54] Jin XJ. Martensitic transformation in zirconia containing ceramics and its applications. Curr Opin Solid St M. 2005;9(6):313-8.

[55] Ma LF. Fundamental formulation for transformation toughening. Int J Solids Struct. 2010;47(22-23):3214-20.

[56] Evans AG. Perspective on the Development of High-Toughness Ceramics. J Am Ceram Soc. 1990;73(2):187-206.

[57] Li P, Chen IW, Pennerhahn JE. Effect of Dopants on Zirconia Stabilization - an X-Ray-Absorption Study .3. Charge-Compensating Dopants. J Am Ceram Soc. 1994;77(5):1289-95.

[58] Butler EP. Transformation-Toughened Zirconia Ceramics. Mater Sci Tech Ser. 1985;1(6):417-32.

[59] Gupta TK, Bechtold JH, Kuznicki RC, Cadoff LH, Rossing BR. Stabilization of Tetragonal Phase in Polycrystalline Zirconia. J Mater Sci. 1977;12(12):2421-6.

[60] Hannink RHJ, Kelly PM, Muddle BC. Transformation toughening in zirconia-containing ceramics. J Am Ceram Soc. 2000;83(3):461-87.

[61] Mcmeeking RM, Evans AG. Mechanics of Transformation-Toughening in Brittle Materials. J Am Ceram Soc. 1982;65(5):242-6.

[62] Rauchs G, Fett T, Munz D, Oberacker R. Tetragonal-to-monoclinic phase transformation in CeO2-stabilized zirconia under multiaxial loading. J Eur Ceram Soc. 2002;22(6):841-9.

[63] Claussen N. Fracture Toughness of Al-2 O-3 with an Unstabilized Zro-2 Dispersed Phase. J Am Ceram Soc. 1976;59(1-2):49-51.

[64] Tsukamoto H, Kotousov A. Micromechanical approach to transformation toughening in zirconia-enriched multiphase composites. J Mech Mater Struct. 2007;2(5):937-50.

[65] Tsukamoto H, Kotousov A. Transformation toughening in zirconia-enriched composites: Micromechanical modeling. Int J Fracture. 2006;139(1):161-8.

[66] Kobayashi K, Kuwajima H, Masaki T. Phase-Change and Mechanical-Properties of Zro2-Y2o3 Solid Electrolyte after Aging. Solid State Ionics. 1981;3-4(Aug):489-93.

[67] Tang DX, Lim HB, Lee KJ, Lee CH, Cho WS. Evaluation of mechanical reliability of zirconia-toughened alumina composites for dental implants. Ceram Int. 2012;38(3):2429-36.

[68] Huang XW, Wang SW, Huang XX. Microstructure and mechanical properties of ZTA fabricated by liquid phase sintering. Ceram Int. 2003;29(7):765-9.

[69] Aguilar-Elguezabal A, Bocanegra-Bernal MH. Alumina Toughened Zirconia Nanocomposite Incorporating Al2O3 Whiskers. Int J Appl Ceram Tec. 2013;10(2):215-23.

[70] Ma WM, Wen L, Guan RG, Sun XD, Li XK. Sintering densification, microstructure and transformation behavior of Al2O3/ZrO2(Y2O3) composites. Mat Sci Eng a-Struct. 2008;477(1-2):100-6.

[71] Basu B, Vleugels J, Van Der Biest O. ZrO2-Al2O3 composites with tailored toughness. J Alloy Compd. 2004;372(1-2):278-84.

[72] Claussen N. Stress-Induced Transformation of Tetragonal Zro2 Particles in Ceramic Matrices. J Am Ceram Soc. 1978;61(1-2):85-6.

[73] Heuer AH, Claussen N, Kriven WM, Ruhle M. Stability of Tetragonal Zro2 Particles in Ceramic Matrices. J Am Ceram Soc. 1982;65(12):642-50.

[74] Lange FF. Transformation Toughening .1. Size Effects Associated with the Thermodynamics of Constrained Transformations. J Mater Sci. 1982;17(1):225-34.

[75] Clegg WJ, Kendall K, Alford NM, Button TW, Birchall JD. A Simple Way to Make Tough Ceramics. Nature. 1990;347(6292):455-7.

[76] Clegg WJ. Design of ceramic laminates for structural applications. Mater Sci Tech Ser. 1998;14(6):483-95.

[77] Tomaszewski H, Weglarz H, Wajler A, Boniecki M, Kalinski D. Multilayer ceramic composites with high failure resistance. J Eur Ceram Soc. 2007;27(2-3):1373-7.

[78] Munch E, Launey ME, Alsem DH, Saiz E, Tomsia AP, Ritchie RO. Tough, Bio-Inspired Hybrid Materials. Science. 2008;322(5907):1516-20.

[79] Kovar D, Thouless MD, Halloran JW. Crack deflection and propagation in layered silicon nitride boron nitride ceramics. J Am Ceram Soc. 1998;81(4):1004-12.

[80] Prakash O, Sarkar P, Nicholson PS. Crack Deflection in Ceramic/Ceramic Laminates with Strong Interfaces. J Am Ceram Soc. 1995;78(4):1125-7.

[81] Marshall DB, Morgan PED, Housley RM. Debonding in multilayered composites of zirconia and LaPO4. J Am Ceram Soc. 1997;80(7):1677-83.

[82] Davis JB, Kristoffersson A, Carlstrom E, Clegg WJ. Fabrication and crack deflection in ceramic laminates with porous interlayers. J Am Ceram Soc. 2000;83(10):2369-74.

[83] Ma J, Wang HZ, Weng LQ, Tan GEB. Effect of porous interlayers on crack deflection in ceramic laminates. J Eur Ceram Soc. 2004;24(5):825-31.

[84] Clegg WJ. The Fabrication and Failure of Laminar Ceramic Composites. Acta Metallurgica Et Materialia. 1992;40(11):3085-93.

[85] Orlovskaya N, Kuebler J, Subbotin V, Lugovy M. Design of Si3N4-based ceramic laminates by the residual stresses. J Mater Sci. 2005;40(20):5443-50.

[86] Zhang XH, Zhou P, Hu P, Han WB. Toughening of laminated ZrB2-SiC ceramics with residual surface compression. J Eur Ceram Soc. 2011;31(13):2415-23.

[87] Zhou P, Hu P, Zhang XH, Han WB. Laminated ZrB2-SiC ceramic with improved strength and toughness. Scripta Mater. 2011;64(3):276-9.

[88] Song GM, Li Q, Wen GW, Zhou Y. Mechanical properties of short carbon fiber-reinforced TiC composites produced by hot pressing. Mat Sci Eng a-Struct. 2002;326(2):240-8.

[89] Fei JJ, Wang Wm, Rem AC, Yu J. Mechanical properties and densification of short carbon fiber-reinforced TiB2/C composites produced by hot pressing. J Alloy Compd. 2014;584:87-92.

[90] Sciti D, Silvestroni L. Processing, sintering and oxidation behavior of SiC fibers reinforced ZrB2 composites. J Eur Ceram Soc. 2012;32(9):1933-40.

[91] Ostertag CP. Influence of fiber and grain bridging on crack profiles in SiC fiber-reinforced alumina-matrix composites. Mat Sci Eng a-Struct. 1999;260(1-2):124-31.

[92] Hansson T, Warren R, Wasen J. Fracture-Toughness Anisotropy and Toughening Mechanisms of a Hot-Pressed Alumina Reinforced with Silicon-Carbide Whiskers. J Am Ceram Soc. 1993;76(4):841-8.

[93] Yamamoto G, Omori M, Hashida T, Kimura H. A novel structure for carbon nanotube reinforced alumina composites with improved mechanical properties. Nanotechnology. 2008;19(31).

[94] Ahmad I, Cao HZ, Chen HH, Zhao H, Kennedy A, Zhu YQ. Carbon nanotube toughened aluminium oxide nanocomposite. J Eur Ceram Soc. 2010;30(4):865-73.

[95] Bocanegra-Bernal MH, Echeberria J, Ollo J, Garcia-Reyes A, Dominguez-Rios C, Reyes-Rojas A, et al. A comparison of the effects of multi-wall and single-wall carbon nanotube additions on the properties of zirconia toughened alumina composites. Carbon. 2011;49(5):1599-607.

[96] Zhang SC, Fahrenholtz WG, Hilmas GE, Yadlowsky EJ. Pressureless sintering of carbon nanotube-Al2O3 composites. J Eur Ceram Soc. 2010;30(6):1373-80.

[97] Zhan GD, Kuntz JD, Wan JL, Mukherjee AK. Single-wall carbon nanotubes as attractive toughening agents in alumina-based nanocomposites. Nat Mater. 2003;2(1):38-42.

[98] Wang XT, Padture NP, Tanaka H. Contact-damage-resistant ceramic/single-wall carbon nanotubes and ceramic/graphite composites. Nat Mater. 2004;3(8):539-44.

[99] Meng YH, Tang CY, Tsui CP, Chen DZ. Fabrication and characterization of needle-like nano-HA and HA/MWNT composites. J Mater Sci-Mater M. 2008;19(1):75-81.

[100] Balani K, Zhang T, Karakoti A, Li WZ, Seal S, Agarwal A. In situ carbon nanotube reinforcements in a plasma-sprayed aluminum oxide nanocomposite coating. Acta Mater. 2008;56(3):571-9.

[101] Duszova A, Dusza J, Tomasek K, Morgiel J, Blugan G, Kuebler J. Zirconia/carbon nanofiber composite. Scripta Mater. 2008;58(6):520-3.

[102] Thomson KE, Jiang D, Lemberg JA, Koester KJ, Ritchie RO, Mukherjee AK. In situ bend testing of niobium-reinforced alumina nanocomposites with and without single-walled carbon nanotubes. Mat Sci Eng a-Struct. 2008;493(1-2):256-60.

[103] Estili M, Kawasaki A, Sakamoto H, Mekuchi Y, Kuno M, Tsukada T. The homogeneous dispersion of surfactantless, slightly disordered, crystalline, multiwalled carbon nanotubes in alpha-alumina ceramics for structural reinforcement. Acta Mater. 2008;56(15):4070-9.

[104] Walker LS, Marotto VR, Rafiee MA, Koratkar N, Corral EL. Toughening in Graphene Ceramic Composites. Acs Nano. 2011;5(4):3182-90.

[105] Wang K, Wang YF, Fan ZJ, Yan J, Wei T. Preparation of graphene nanosheet/alumina composites by spark plasma sintering. Mater Res Bull. 2011;46(2):315-8.

[106] Guo SQ, Sivakumar R, Kagawa Y. Multiwall carbon nanotube-SiO2 nanocomposites: Sintering, elastic properties, and fracture toughness. Adv Eng Mater. 2007;9(1-2):84-7.

[107] Ye F, Liu LM, Wang YJ, Zhou Y, Peng B, Meng QC. Preparation and mechanical properties of carbon nanotube reinforced barium aluminosilicate glass-ceramic composites. Scripta Mater. 2006;55(10):911-4.

[108] Huang Q, Gao L, Sun J. Effect of adding carbon nanotubes on microstructure, phase transformation, and mechanical property of BaTiO3 ceramics. J Am Ceram Soc. 2005;88(12):3515-8.

[109] Fan JP, Zhuang DM, Zhao DQ, Zhang G, Wu MS, Wei F, et al. Toughening and reinforcing alumina matrix composite with single-wall carbon nanotubes. Appl Phys Lett. 2006;89(12).

[110] Ramirez C, Miranzo P, Belmonte M, Osendi MI, Poza P, Vega-Diaz SM, et al. Extraordinary toughening enhancement and flexural strength in Si3N4 composites using graphene sheets. J Eur Ceram Soc. 2014;34(2):161-9.

[111] Yadhukulakrishnan GB, Karumuri S, Rahman A, Singh RP, Kalkan AK, Harimkar SP. Spark plasma sintering of graphene reinforced zirconium diboride ultra-high temperature ceramic composites. Ceram Int. 2013;39(6):6637-46.

[112] Kvetkova L, Duszova A, Kasiarova M, Dorcakova F, Dusza J, Balazsi C. Influence of processing on fracture toughness of Si3N4 + graphene platelet composites. J Eur Ceram Soc. 2013;33(12):2299-304.

[113] Zhang L, Liu WW, Yue CG, Zhang TH, Li P, Xing ZW, et al. A tough graphene nanosheet/hydroxyapatite composite with improved in vitro biocompatibility. Carbon. 2013;61:105-15.

[114] Hungria T, Galy J, Castro A. Spark Plasma Sintering as a Useful Technique to the Nanostructuration of Piezo-Ferroelectric Materials. Adv Eng Mater. 2009;11(8):615-31.

[115] Hulbert DM, Anders A, Dudina DV, Andersson J, Jiang D, Unuvar C, et al. The absence of plasma in "spark plasma sintering". J Appl Phys. 2008;104(3).

[116] Hulbert DM, Anders A, Andersson J, Lavernia EJ, Mukherjee AK. A discussion on the absence of plasma in spark plasma sintering. Scripta Mater. 2009;60(10):835-8.

[117] Makino Y. Characteristics of sintering process by pulsed large-current electrification. Nyu Seramikkusu. 1997;10(10).

[118] Nanko M, Maruyama T, Tomino H. Neck growth on initial stage of pulse current pressure sintering for coarse atomized powder made of cast-iron. J Jpn I Met. 1999;63(7):917-23.

[119] Munir ZA, Anselmi-Tamburini U, Ohyanagi M. The effect of electric field and pressure on the synthesis and consolidation of materials: A review of the spark plasma sintering method. J Mater Sci. 2006;41(3):763-77.

[120] Zhou Y, Hirao K, Yamauchi Y, Kanzaki S. Effects of heating rate and particle size on pulse electric current sintering of alumina. Scripta Mater. 2003;48(12):1631-6.

[121] Shen ZJ, Johnsson M, Zhao Z, Nygren M. Spark plasma sintering of alumina. J Am Ceram Soc. 2002;85(8):1921-7.

[122] Hong JS, Gao L, Torre SDDL, Miyamoto H, Miyamoto K. Spark plasma sintering and mechanical properties of ZrO2(Y2O3)-Al2O3 composites. Mater Lett. 2000;43(1-2):27-31.

[123] Harada YH, Uekawa N, Kojima T, Kakegawa K. Fabrication of Y3Al5O12-Al2O3 eutectic materials having ultra fine microstructure. J Eur Ceram Soc. 2008;28(1):235-40.

[124] Lee YI, Lee JH, Hong SH, Kim DY. Preparation of nanostructured TiO2 ceramics by spark plasma sintering. Mater Res Bull. 2003;38(6):925-30.

[125] Mukhopadhyay A, Basu B. Consolidation microstructure property relationships in bulk nanoceramics and ceramic nanocomposites: a review. Int Mater Rev. 2007;52(5):257-88.

[126] Shahzad K, Deckers J, Boury S, Neirinck B, Kruth JP, Vleugels J. Preparation and indirect selective laser sintering of alumina/PA microspheres. Ceram Int. 2012;38(2):1241-7.

[127] Bertrand P, Bayle F, Combe C, Goeuriot P, Smurov I. Ceramic components manufacturing by selective laser sintering. Appl Surf Sci. 2007;254(4):989-92.

[128] Meng FC, Fu ZY, Zhang JY, Wang H, Wang WM, Wang YC, et al. Rapid densification of nano-grained alumina by high temperature and pressure with a very high heating rate. J Am Ceram Soc. 2007;90(4):1262-4.

[129] Lei LW, Fu ZY, Zhang JY, Wang H, Niihara K. Low field magnetoresistance of La0.7Ca0.3MnO3 ceramics fabricated by fast sintering process. J Alloy Compd. 2012;530:164-8.

[130] Agrawal DK. Microwave processing of ceramics. Curr Opin Solid St M. 1998;3(5):480-5.

[131] Sutton WH. Microwave Processing of Ceramic Materials. Am Ceram Soc Bull. 1989;68(2):376-86.

[132] Oghbaei M, Mirzaee O. Microwave versus conventional sintering: A review of fundamentals, advantages and applications. J Alloy Compd. 2010;494(1-2):175-89.

[133] Ritzhaupt-Kleissl HJ, Link G. Millimeter wave sintering of ceramics. Cfi-Ceram Forum Int. 1999;76(1-2):28-32.

[134] Grossin D, Marinel S, Noudem JG. Materials processed by indirect microwave heating in a single-mode cavity. Ceram Int. 2006;32(8):911-5.

[135] Johnson DL. Microwave and Plasma Sintering of Ceramics. Ceram Int. 1991;17(5):295-300.

[136] Brosnan KH, Messing GL, Agrawal DK. Microwave sintering of alumina at 2.45 GHz. J Am Ceram Soc. 2003;86(8):1307-12.

[137] Deng ZY, Shi JL, Zhang YF, Jiang DY, Guo JK. Pinning effect of SiC particles on mechanical properties of Al2O3-SiC ceramic matrix composites. J Eur Ceram Soc. 1998;18(5):501-8.

[138] Reveron H, Zaafrani O, Fantozzi G. Microstructure development, hardness, toughness and creep behaviour of pressureless sintered alumina/SiC micro-nanocomposites obtained by slip-casting. J Eur Ceram Soc. 2010;30(6):1351-7.

[139] Porwal H, Tatarko P, Grasso S, Khaliq J, Dlouhy I, Reece MJ. Graphene reinforced alumina nano-composites. Carbon. 2013;64:359-69.

[140] Chakravarty D, Bysakh S, Muraleedharan K, Rao TN, Sundaresan R. Spark plasma sintering of magnesia-doped alumina with high hardness and fracture toughness. J Am Ceram Soc. 2008;91(1):203-8.

[141] Dong YL, Xu FM, Shi XL, Zhang C, Zhang ZJ, Yang JM, et al. Fabrication and mechanical properties of nano-/micro-sized Al2O3/SiC composites. Mat Sci Eng a-Struct. 2009;504(1-2):49-54.

[142] Cesari F, Esposito L, Furgiuele FM, Maletta C, Tucci A. Fracture toughness of alumina-zirconia composites. Ceram Int. 2006;32(3):249-55.

[143] Echeberria J, Ollo J, Bocanegra-Bernal MH, Garcia-Reyes A, Dominguez-Rios C, Aguilar-Elguezabal A, et al. Sinter and hot isostatic pressing (HIP) of multi-wall carbon nanotubes (MWCNTs) reinforced ZTA nanocomposite: Microstructure and fracture toughness. Int J Refract Met H. 2010;28(3):399-406.

[144] Li SF, Izui H, Okano M, Zhang WH, Watanabe T. Microstructure and mechanical properties of ZrO2 (Y2O3)-Al2O3 nanocomposites prepared by spark plasma sintering. Particuology. 2012;10(3):345-51.

[145] Bartolome JF, De Aza AH, Martin A, Pastor JY, Llorca J, Torrecillas R, et al. Alumina/zirconia micro/nanocomposites: A new material for biomedical applications with superior sliding wear resistance. J Am Ceram Soc. 2007;90(10):3177-84.

[146] Fan JP, Zhao DQ, Wu MS, Xu ZN, Song J. Preparation and microstructure of multi-wall carbon nanotubes-toughened Al2O3 composite. J Am Ceram Soc. 2006;89(2):750-3.

[147] Zhan GD, Mukherjee AK. Carbon nanotube reinforced alumina-based ceramics with novel mechanical, electrical, and thermal properties. Int J Appl Ceram Tec. 2004;1(2):161-71.

[148] Echeberria J, Rodriguez N, Vleugels J, Vanmeensel K, Reyes-Rojas A, Garcia-Reyes A, et al. Hard and tough carbon nanotube-reinforced zirconia-toughened alumina composites prepared by spark plasma sintering. Carbon. 2012;50(2):706-17.

[149] Baghery P, Farzam M, Mousavi AB, Hosseini M. Ni-TiO2 nanocomposite coating with high resistance to corrosion and wear. Surf Coat Tech. 2010;204(23):3804-10.

[150] Benea L, Bonora PL, Borello A, Martelli S. Wear corrosion properties of nano-structured SiC-nickel composite coatings obtained by electroplating. Wear. 2001;249(10-11):995-1003.

[151] Pompei E, Magagnin L, Lecis N, Cavallotti PL. Electrode position of nickel-BN composite coatings. Electrochim Acta. 2009;54(9):2571-4.

[152] Allahkaram SR, Golroh S, Mohammadalipour M. Properties of Al2O3 nano-particle reinforced copper matrix composite coatings prepared by pulse and direct current electroplating. Mater Design. 2011;32(8-9):4478-84.

[153] Zhu XB, Cai C, Zheng GQ, Zhang Z, Li JF. Electrodeposition and corrosion behavior of nanostructured Ni-TiN composite films. T Nonferr Metal Soc. 2011;21(10):2216-24.

[154] Lekka M, Kouloumbi N, Gajo M, Bonora PL. Corrosion and wear resistant electrodeposited composite coatings. Electrochim Acta. 2005;50(23):4551-6.

[155] Xiao XF, Liu RF. Effect of suspension stability on electrophoretic deposition of hydroxyapatite coatings. Mater Lett. 2006;60(21-22):2627-32.

[156] Farrokhi-Rad M, Shahrabi T. Effect of triethanolamine on the electrophoretic deposition of hydroxyapatite nanoparticles in isopropanol. Ceram Int. 2013;39(6):7007-13.

[157] Besra L, Liu M. A review on fundamentals and applications of electrophoretic deposition (EPD). Prog Mater Sci. 2007;52(1):1-61.

[158] Corni I, Neumann N, Novak S, Konig K, Veronesi P, Chen QZ, et al. Electrophoretic deposition of PEEK-nano alumina composite coatings on stainless steel. Surf Coat Tech. 2009;203(10-11):1349-59.

[159] Wang YH, Chen QZ, Cho J, Boccaccini AR. Electrophoretic co-deposition of diamond/borosilicate glass composite coatings. Surf Coat Tech. 2007;201(18):7645-51.

[160] Askari E, Mehrali M, Metselaar IHSC, Kadri NA, Rahman MM. Fabrication and mechanical properties of Al2O3/SiC/ZrO2 functionally graded material by electrophoretic deposition. J Mech Behav Biomed. 2012;12:144-50.

[161] Sudagar J, Lian JS, Sha W. Electroless nickel, alloy, composite and nano coatings - A critical review. J Alloy Compd. 2013;571:183-204.

[162] Tahy K, Xing HL, Jena D. Graphene nanoribbon FETs for digital electronics: experiment and modeling. Int J Circ Theor App. 2013;41(6):603-7.

[163] Trauzettel B, Bulaev DV, Loss D, Burkard G. Spin qubits in graphene quantum dots. Nat Phys. 2007;3(3):192-6.

[164] Becerril HA, Mao J, Liu Z, Stoltenberg RM, Bao Z, Chen Y. Evaluation of solution-processed reduced graphene oxide films as transparent conductors. Acs Nano. 2008;2(3):463-70.

[165] Li D, Muller MB, Gilje S, Kaner RB, Wallace GG. Processable aqueous dispersions of graphene nanosheets. Nat Nanotechnol. 2008;3(2):101-5.

[166] Li XL, Zhang GY, Bai XD, Sun XM, Wang XR, Wang E, et al. Highly conducting graphene sheets and Langmuir-Blodgett films. Nat Nanotechnol. 2008;3(9):538-42.

[167] Pang SP, Tsao HN, Feng XL, Mullen K. Patterned Graphene Electrodes from Solution-Processed Graphite Oxide Films for Organic Field-Effect Transistors. Adv Mater. 2009;21(34):3488-+.

[168] Eda G, Lin YY, Miller S, Chen CW, Su WF, Chhowalla M. Transparent and conducting electrodes for organic electronics from reduced graphene oxide. Appl Phys Lett. 2008;92(23).

[169] Tung VC, Chen LM, Allen MJ, Wassei JK, Nelson K, Kaner RB, et al. Low-Temperature Solution Processing of Graphene-Carbon Nanotube Hybrid Materials for High-Performance Transparent Conductors. Nano Lett. 2009;9(5):1949-55.

[170] Yin ZY, Wu SX, Zhou XZ, Huang X, Zhang QC, Boey F, et al. Electrochemical Deposition of ZnO Nanorods on Transparent Reduced Graphene Oxide Electrodes for Hybrid Solar Cells. Small. 2010;6(2):307-12.

[171] Wu JB, Agrawal M, Becerril HA, Bao ZN, Liu ZF, Chen YS, et al. Organic Light-Emitting Diodes on Solution-Processed Graphene Transparent Electrodes. Acs Nano. 2010;4(1):43-8.

[172] Wang X, Zhi LJ, Mullen K. Transparent, conductive graphene electrodes for dye-sensitized solar cells. Nano Lett. 2008;8(1):323-7.

[173] Li SS, Tu KH, Lin CC, Chen CW, Chhowalla M. Solution-Processable Graphene Oxide as an Efficient Hole Transport Layer in Polymer Solar Cells. Acs Nano. 2010;4(6):3169-74.

[174] Yin ZY, Sun SY, Salim T, Wu SX, Huang XA, He QY, et al. Organic Photovoltaic Devices Using Highly Flexible Reduced Graphene Oxide Films as Transparent Electrodes. Acs Nano. 2010;4(9):5263-8.

[175] Liu Q, Liu ZF, Zhang XY, Zhang N, Yang LY, Yin SG, et al. Organic photovoltaic cells based on an acceptor of soluble graphene. Appl Phys Lett. 2008;92(22).

[176] Robinson JT, Perkins FK, Snow ES, Wei ZQ, Sheehan PE. Reduced Graphene Oxide Molecular Sensors. Nano Lett. 2008;8(10):3137-40.

[177] Fowler JD, Allen MJ, Tung VC, Yang Y, Kaner RB, Weiller BH. Practical Chemical Sensors from Chemically Derived Graphene. Acs Nano. 2009;3(2):301-6.

[178] Sundaram RS, Gomez-Navarro C, Balasubramanian K, Burghard M, Kern K. Electrochemical modification of graphene. Adv Mater. 2008;20(16):3050-3.

[179] Lu GH, Ocola LE, Chen JH. Gas detection using low-temperature reduced graphene oxide sheets. Appl Phys Lett. 2009;94(8).

[180] Yang SB, Feng XL, Ivanovici S, Mullen K. Fabrication of Graphene-Encapsulated Oxide Nanoparticles: Towards High-Performance Anode Materials for Lithium Storage. Angew Chem Int Edit. 2010;49(45):8408-11.

[181] Wu ZS, Ren WC, Wen L, Gao LB, Zhao JP, Chen ZP, et al. Graphene Anchored with Co3O4 Nanoparticles as Anode of Lithium Ion Batteries with Enhanced Reversible Capacity and Cyclic Performance. Acs Nano. 2010;4(6):3187-94.

[182] Wang DH, Choi DW, Li J, Yang ZG, Nie ZM, Kou R, et al. Self-Assembled TiO2-Graphene Hybrid Nanostructures for Enhanced Li-Ion Insertion. Acs Nano. 2009;3(4):907-14.

[183] Liu Q, Liu ZF, Zhong XY, Yang LY, Zhang N, Pan GL, et al. Polymer Photovoltaic Cells Based on Solution-Processable Graphene and P3HT. Adv Funct Mater. 2009;19(6):894-904.

[184] Li ZF, Xie J. Graphene-based composites as electrochemical supercapacitors. Abstr Pap Am Chem S. 2013;246.

[185] Wu ZS, Ren WC, Wang DW, Li F, Liu BL, Cheng HM. High-Energy MnO2 Nanowire/Graphene and Graphene Asymmetric Electrochemical Capacitors. Acs Nano. 2010;4(10):5835-42.

[186] Wu ZS, Wang DW, Ren W, Zhao J, Zhou G, Li F, et al. Anchoring Hydrous RuO2 on Graphene Sheets for High-Performance Electrochemical Capacitors. Adv Funct Mater. 2010;20(20):3595-602.

[187] Chen S, Zhu JW, Wu XD, Han QF, Wang X. Graphene Oxide-MnO2 Nanocomposites for Supercapacitors. Acs Nano. 2010;4(5):2822-30.

[188] Wang DW, Li F, Zhao JP, Ren WC, Chen ZG, Tan J, et al. Fabrication of Graphene/Polyaniline Composite Paper via In Situ Anodic Electropolymerization for High-Performance Flexible Electrode. Acs Nano. 2009;3(7):1745-52.

[189] Vivekchand SRC, Rout CS, Subrahmanyam KS, Govindaraj A, Rao CNR. Graphene-based electrochemical supercapacitors. J Chem Sci. 2008;120(1):9-13.

[190] Wang Y, Shi ZQ, Huang Y, Ma YF, Wang CY, Chen MM, et al. Supercapacitor Devices Based on Graphene Materials. J Phys Chem C. 2009;113(30):13103-7.

[191] Stoller MD, Park SJ, Zhu YW, An JH, Ruoff RS. Graphene-Based Ultracapacitors. Nano Lett. 2008;8(10):3498-502.

[192] Kalaitzidou K, Fukushima H, Drzal LT. Multifunctional polypropylene composites produced by incorporation of exfoliated graphite nanoplatelets. Carbon. 2007;45(7):1446-52.

[193] Bao YW, Jin ZZ, Li XR. Evaluation of K(1c) Depending on Sample-Size for Ceramics. Eng Fract Mech. 1994;48(1):85-90.

[194] Park S, An JH, Jung IW, Piner RD, An SJ, Li XS, et al. Colloidal Suspensions of Highly Reduced Graphene Oxide in a Wide Variety of Organic Solvents. Nano Lett. 2009;9(4):1593-7.

[195] Boccaccini AR, Acevedo DR, Brusatin G, Colombo P. Borosilicate glass matrix composites containing multi-wall carbon nanotubes. J Eur Ceram Soc. 2005;25(9):1515-23.

[196] Aman Y, Garnier V, Djurado E. Spark Plasma Sintering Kinetics of Pure alpha-Alumina. J Am Ceram Soc. 2011;94(9):2825-33.

[197] Chaim R, Marder R, Estournes C, Shen Z. Densification and preservation of ceramic nanocrystalline character by spark plasma sintering. Adv Appl Ceram. 2012;111(5-6):280-5.

[198] Cha SI, Kim KT, Lee KH, Mo CB, Hong SH. Strengthening and toughening of carbon nanotube reinforced alumina nanocomposite fabricated by molecular level mixing process. Scripta Mater. 2005;53(7):793-7.

[199] Wei T, Fan ZJ, Luo GH, Wei F. A new structure for multi-walled carbon nanotubes reinforced alumina nanocomposite with high strength and toughness. Mater Lett. 2008;62(4-5):641-4.

[200] Bakshi SR, Musaramthota V, Virzi DA, Keshri AK, Lahiri D, Singh V, et al. Spark plasma sintered tantalum carbide-carbon nanotube composite: Effect of pressure, carbon nanotube length and dispersion technique on microstructure and mechanical properties. Mat Sci Eng a-Struct. 2011;528(6):2538-47.

[201] Damani R, Gstrein R, Danzer R. Critical notch-root radius effect in SENB-S fracture toughness testing. J Eur Ceram Soc. 1996;16(7):695-702.

[202] Ahn BK, Curtin WA, Parthasarathy TA, Dutton RE. Criteria for crack deflection/penetration criteria for fiber-reinforced ceramic matrix composites. Compos Sci Technol. 1998;58(11):1775-84.

[203] Ahmad K, Pan W, Qu ZX. Multifunctional Properties of Alumina Composites Reinforced by a Hybrid Filler. Int J Appl Ceram Tec. 2009;6(1):80-8.

[204] Kubler JJ. Fracture toughness of ceramics using the SEVNB method: From a preliminary study to a standard test method. Am Soc Test Mater. 2002;1409:93-106.

[205] Kun P, Tapaszto O, Weber F, Balazsi C. Determination of structural and mechanical properties of multilayer graphene added silicon nitride-based composites. Ceram Int. 2012;38(1):211-6.

[206] Gleiter H. Nanostructured materials: Basic concepts and microstructure. Acta Mater. 2000;48(1):1-29.

[207] Gustafsson S, Falk LKL, Liden E, Carlstrom E. Pressureless sintered Al(2)O(3)-SiC nanocomposites. Ceram Int. 2008;34(7):1609-15.

[208] Xu YR, Zangvil A, Kerber A. SiC nanoparticle-reinforced Al2O3 matrix composites: Role of intra- and intergranular particles. J Eur Ceram Soc. 1997;17(7):921-8.

[209] Currie M, Caldwell JD, Bezares FJ, Robinson J, Anderson T, Chun HD, et al. Quantifying pulsed laser induced damage to graphene. Appl Phys Lett. 2011;99(21).

[210] Sarkar S, Das PK. Statistical analysis of mechanical properties of pressureless sintered multiwalled carbon nanotube/alumina nanocomposites. Mater Chem Phys. 2012;137(2):511-8.

[211] Nieto A, Lahiri D, Agarwal A. Synthesis and properties of bulk graphene nanoplatelets consolidated by spark plasma sintering. Carbon. 2012;50(11):4068-77.

[212] Kumar CMP, Venkatesha TV, Shabadi R. Preparation and corrosion behavior of Ni and Ni-graphene composite coatings. Mater Res Bull. 2013;48(4):1477-83.

[213] van Huis MA, Fedorov AV, van Veen A, Falub CV, Eijt SWH, Kooi BJ, et al. Structural properties of Au and Ag nanoclusters embedded in MgO. Nucl Instrum Meth B. 2002;191:442-6.

[214] Ramalingam S, Muralidharan VS, Subramania A. Electrodeposition and characterization of Cu-TiO(2) nanocomposite coatings. J Solid State Electr. 2009;13(11):1777-83.

[215] Chen L, Wang LP, Zeng ZX, Xu T. Influence of pulse frequency on the microstructure and wear resistance of electrodeposited Ni-Al2O3 composite coatings. Surf Coat Tech. 2006;201(3-4):599-605.

[216] Muresan L, Oniciu L, Froment M, Maurin G. Inhibition of Lead Electrocrystallization by Organic Additives. Electrochim Acta. 1992;37(12):2249-54.

[217] Qu NS, Zhu D, Chan KC. Fabrication of Ni-CeO2 nanocomposite by electrodeposition. Scripta Mater. 2006;54(7):1421-5.

[218] Khabazian S, Sanjabi S. The effect of multi-walled carbon nanotube pretreatments on the electrodeposition of Ni-MWCNTs coatings. Appl Surf Sci. 2011;257(13):5850-6.

[219] Qin LY, Lian JS, Jiang Q. Effect of grain size on corrosion behavior of electrodeposited bulk nanocrystalline Ni. T Nonferr Metal Soc. 2010;20(1):82-9.

[220] Badea GE, Dzitac S, Porumb C, Popper L, Badea T. Nitrate Ion Effects on the Nickel Corrosion and Passivation Behaviour in 0.5 M H2so4 Solutions. Rev Roum Chim. 2010;55(4):263-+.

[221] Balaraju JN, Selvi VE, Rajam KS. Electrochemical behavior of low phosphorus electroless Ni-P-Si3N4 composite coatings. Mater Chem Phys. 2010;120(2-3):546-51.

[222] Lim DS, You DH, Choi HJ, Lim SH, Jang H. Effect of CNT distribution ontribological behavior of alumina-CNT composites. Wear. 2005;259(1-6):539-44.

[223] Gonzalez-Julian J, Schneider J, Miranzo P, Osendi MI, Belmonte M. Enhanced Tribological Performance of Silicon Nitride-Based Materials by Adding Carbon Nanotubes. J Am Ceram Soc. 2011;94(8):2542-8.

[224] Zhu ZG, Hassanin H, Jiang K. A soft moulding process for manufacture of net-shape ceramic microcomponents. Int J Adv Manuf Tech. 2010;47(1-4):147-52.